Methyl-coenzyme M reductase: Expressing active recombinant enzyme in *M. maripaludis,* and investigating the activation process, and the mechanism of inhibition of 3-nitrooxypropanol

and

Studying the effect of Ionic liquids on the mononuclear rearrangement of heterocycles using QM/MM method

By
Robel Zeray Ghebreab

A dissertation submitted to the Graduate Faculty of
Auburn University
in partial fulfillment of the
requirements for the Degree of
Doctor of Philosophy

Auburn, Alabama
August 3, 2019

Approved by
Eduardus Cornel Duin, Chair, Professor of Chemistry and Biochemistry
Holly Renee Ellis, Professor of Chemistry and Biochemistry
Steven Omid Mansoorabadi, Associate Professor of Chemistry and Biochemistry
Anne Elizabeth Vivian Gorden, Associate Professor of Chemistry and Biochemistry
Yi Wang, Assistant Professor of Biosystems Engineering

Abstract

The study of the biosynthesis of methane is appealing from both its potential role in biofuel production and environmental perspectives. Methane is the main component of natural gas, and it is also a potent greenhouse gas as it is the second most abundant greenhouse gas after CO_2. Methane is produced through geothermal processes and through the action of microorganisms known as methanogenic Archaea. Methanotrophic Archaea on the other hand are involved in the biological oxidation of methane. Together with aerobic methanotrophs, methanotrophic Archaea play an essential role in preventing the release of methane to the atmosphere which otherwise could have a serious contribution to global warming and climate change.[1–3] Methyl-coenzyme M reductase (MCR) is the key enzyme in both the biological formation and the anaerobic oxidation of methane.[4] MCR catalyzes the terminal step in methane formation and first step in the oxidation of methane. MCR catalyzes the reversible reaction of methyl-coenzyme M and coenzyme B to produce methane and the corresponding heterodisulfide. The catalytic activity of MCR depends on its unique nickel-containing tetrapyrrole core, coenzyme $F_{430,}$ which can exist in three different oxidation states. MCR exhibits nickel-based EPR signals when the nickel center is either in the oxidation state +1 or +3. This enzyme is active in the oxidation state +1 and exhibits an axial EPR signal, called MCR-red1. In the presence of coenzyme M and coenzyme B, the enzyme exhibits a rhombic signal, MCR-red2. Two other paramagnetic states of the enzyme can be detected, MCR-ox1 and MCR-ox2. The Nickel center has an oxidation state of +3 in these states. The ox states are

inactive, but can be converted *in vitro* to the active state of the enzyme, MCR-red1, by treating it with Ti(III) citrate.[5]

Near its active site, MCR has five post-translational modifications (PTMs). Four of these five modifications are methylations, including 2-(S)-methylglutamine, 5-(S)-methylarginine, 3-methylhistidine, S-methylcysteine, and the fifth modified amino acid is a thioglycine in which the backbone carbonyl oxygen is replaced with sulfur. The exact roles of these PTMs are not known, but the amino acids are believed to have some role in the catalytic mechanism of the enzyme. Moreover, a large multi protein complex is required for the activation of MCR in a process that involves both electron bifurcation and ATP hydrolysis. The research reported here was aimed at getting a more thorough understanding of the expression, activation, and inhibition of MCR.

A general introduction is presented in chapter one. The second chapter describes the expression and characterization of recombinant MCRs in *Methanococcus maripaludis*. The main reason to use *M. maripaludis* as a host for expressing MCR was that MCR requires several genes to correctly express including, but not limited to, genes needed for PTMs, genes required for activating MCR, and genes required for the biosynthesis of F_{430}. Most of them are not yet known. Thus, there could be a higher chance of success when expressing MCR in Archaea which contain all the machinery for getting mature and active MCR. MCR from *Methanothermococcus okinawensis* and from *M. maripaludis* were cloned and expressed in *M. maripaludis*. Surprisingly, the recombinant MCR from both organisms were purified into two distinct fractions. One set of fractions was without F_{430} and yet contains McrD. The function of McrD is not known, thus we proposed it may be involved in the insertion of F_{430}

to apo-MCR. The second fraction contained the expected MCR with F_{430}, but no McrD was detected in this fraction. This raised several questions and the chapter presents some of them in detail.

The third chapter “Activation system of MCR” describes the investigation of the MCR activation system from *M. marburgensis.* In vivo, MCR is activated by a large complex referred to as A3a. This chapter extends the investigation of this activating complex.

In the fourth chapter the inhibitory mechanism of 3-NOP on MCR is investigated. Large quantities of methane are produced and escaped to the atmosphere from dairy cows and other ruminal livestock. This not only is a burden to the atmosphere, but also a significant amount of nutrition is lost during methane biosynthesis. This loss could be reduced by inhibition of MCR. The chapter discusses the inhibitory mechanism of 3-NOP, a small molecule of MCR inhibitor developed by DSM.

Chapter five briefly intoduces the computational chemistry. The following chapter then presents computationally obtained data on the effect of ionic liquids on the mononuclear rearrangement of heterocycles (MRH). Mixed quantum mechanics/molecular mechanics (QM/MM) combined with free-energy perturbation theory (FEP) and Monte Carlo (MC) sampling was used to investigate the nature of the rate enhancement in ionic liquids in this type of reaction. The geometry and activation energy barrier of rearrangement of the Z-phenylhydrazone of 3-benzoyl-5-phenyl-1,2,4-oxadiazole into 4-benzoyla-mino-2,5-diphenyl-1,2,3-triazole in the 1-butyl- 3-methylimidazolium tetrafluoroborate [BMIM] based ionic liquid as well as in conventional organic solvents, methanol, and acetonitrile were computed for both uncatalyzed and general base catalyzed reactions. Detailed analysis is also presented to explain the origin of rate enhancement observed in [BF_4] ionic liquid. A significant difference in the activation barriers were observed, not only between conventional solvent and ionic liquids, but also among the two ionic liquids used for this study. The rate enhancement observed in [BMIM][BF_4] could not be attributed to the physical properties of the solvents used, (i.e., to the polarities or viscosity of the solvent) as the two ionic liquid have comparable properties. The computational results and analysis of structure and energetics of the reaction suggest that the difference in rate enhancement lies in the geometric arrangement of the ionic liquids at the transition state. A favorable π^+-π interaction between the imidazolium ring of the BMIM cation and the bicyclic quasi-aromatic 10π oxadiazole/triazole transition state region of the substrate was observed. This imposed a pre-ordered geometric arrangement that stabilize the transition structure, lowering the activation barrier, and thereby enhancing the rate of the rearrangement reaction. A coplanar orientation of the phenyl rings that maximized the electronic effects exerted on the reaction route together with site-specific electrostatic stabilization between the ions and the MRH substrate in [BMIM][BF_4] as compared to [BMIM][PF_6] could explain the rate enhancement observed in [BMIM][BF_4].

Acknowledgment

Praise be to the almighty God who bestowed me with patience and strength to finish these research projects successfully.

I would like to dedicate this work to my late beloved father who have been and is my inspiration and the reason for being who I am now. My in-depth gratitude goes to my beloved mother and my siblings for their support and encouragement during my study.

I would like to extend my in-depth gratitude and appreciation for my mentor and advisor professor Evert Duin. His expertise, assistance, and patience throughout the study as well as during writing this thesis was incredible. This work would have not been completed if it was not for him. I would also want to thank Dr. Orlando Acevedo for his advice and mentorship during my first two years of study in computational chemistry.

I would like to express the deepest appreciation to my committee members, Professors Steven Mansoorabadi, Holly Ellis, Anne Gorden, and Yi Wang, for their support, constructive suggestions, and more than all for their precious time.

I would like to take this opportunity to thank Professor Barny Whitman for his expertise and his willingness to come to our lab and teach us how to cultivate *M. maripaludis*. I was honored to see his expertise and his kindness personally.

My appreciation and thanks go to my current and former lab colleagues; Carly, Bryan, Cathrine (Kari), Theophila, Shadi, Selam, Symon, Bin Li, Brittany, and Nicole. I would also like to thank for the undergraduate students; Rachel, William, Jacob, and Ned whom I worked

with. Their support, help, and company were crucial during my studies. Thank you all for showing me love and kindness.

I would like to finish my acknowledgment my thanking the Department of Chemistry and Biochemistry at Auburn University, for allowing me to pursue my dream of obtaining a PhD degree.

Table of Contents

List of Tables

List of Figures

List of Abbreviations

MCR	Methyl coenzyme-M reductase
McrC	Methyl coenzyme M reductase I, operon protein C
McrD	Methyl coenzyme M reductase I, operon protein D
Isf	Predicted Iron Sulfur Flavoprotein
Mmp	Methanogenic marker protein
HDS	Heterodisulfide
M-CoM	Methyl Coenzyme M
CoB	Coenzyme B
CoM	Coenzyme M
CW	Continuous wave
IPTG	Isopropyl-β-D-thiogalactoside
EPR	Electron paramagnetic resonance spectroscopy
ENDOR	Electron nuclear double resonance
NMR	Nuclear magnetic resonance spectroscopy
IR	Infrared resonance
GC	Gas Chromatography
FPLC	Fluid pressure liquid chromatography
UV-Vis	Ultraviolet-Visible spectroscopy
MS	Mass spectroscopy
SDS-PAGE	Sodium dodecyl sulfate-polyacrylamide gel electrophoresis

PCR	Polymerase chain reaction
CD	Circular dichroism
WT	Wild-Type
3-NOP	3-Nitrooxypropanol
BES	2-Bromoethanesulfonate
BPS	3-Bromoprpanesulfonate
ANME	anaerobic methanotrophs
QM	Quantum mechanics
MM	Molecular mechanics
LCAO	Linear combination of atomic orbitals
DFT	Density Functional Theory
QM/MM	Mixed Quantum Mechanical/Molecular Mechanical
MC	Metropolis Monte Carlo
ILs	Ionic liquids
FEP	Free-energy perturbation theory
MRH	Mononuclear rearrangement of heterocycles

Chapter One: Background and Significance

1.1 Introduction

1.1.1 Methane and its significance

Methane is the primary component of natural gas which is an important form of clean and renewable energy.[6] The use of natural gas has been increasing significantly in recent years.[7] Natural gas has been used in power plants and other form of energy like fuel cells. Methane can be trapped from landfills and used to generate power. Methane could also be catalytically converted to CO_2 and H_2.[8] The catalytic conversion of methane to methanol or compounds with longer carbon chains could be economically and environmentally attractive.[6]

Unfortunately, methane is a potent greenhouse gas. It is the second most abundant greenhouse gas after carbon dioxide.[2] Though methane`s lifetime is shorter than the lifetime of CO_2, it has more radiation trapping power (34 times more than CO_2 over a century period of time) which renders it to have a significant impact on climate change.[2] Methane is produced by both anthropogenic activities and natural processes. Increased human activities in sectors like agriculture, cattle breeding in particular, and oil production and fracking are the main sources of the global increase in the emission of methane to the atmosphere.[6] Methane is also emitted from natural sources such as wetlands, termites, wild ruminants, oceans and methane hydrates.[9]

Methanogenic Archaea are anaerobic microorganisms that produce methane in different anoxic environments, including in the rumen of some animals, termites, landfills, rice paddies, and wetlands.[6,10] The actual production of methane is catalyzed by the enzyme methyl-coenzyme M reductase. Only small amounts of methane produced from the deep in the ocean escape to the atmosphere due to the function of methanotrophic Archaea and bacteria that consume most of methane produced.[11] Methanogens as well as methanotrophic Archaea follow similar biochemical pathways in the biogenesis and oxidation of methane, respectively.[11]

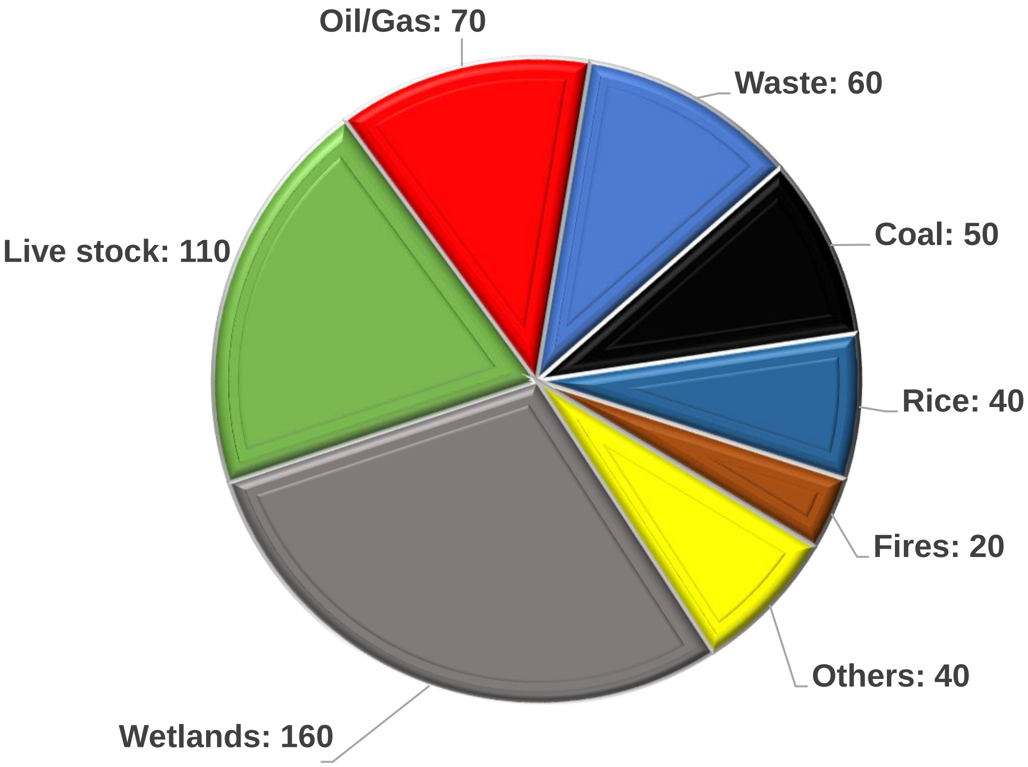

Figure 1.1. Global methane emission in Tg/year. Adapted from reference 13

1.1.2 The global methane cycle (Global Atmospheric Methane budget)

The current global atmospheric methane concentration is estimated to be 1800 ppb. During the last 250 years the amount of methane in the atmosphere has increased more than two-fold compared to the pre-industrial period where the methane level was estimated to be around 700 ppb.[10,12]During the pre-industrial era the natural sources were the main source of methane emission and were balanced through the action of natural methane sinks. An unknown sink has caused the level of atmospheric methane to be stagnant for almost a decade starting in the 1990s, which then continued in 2007.[6] This increase in atmospheric methane concentrations could be either due to an increase in the methane sources and/or due to declining methane sinks. Below the sources and sinks of methane are briefly discussed.

1.1.2.1 Natural Sources

Wetlands are the largest natural source of atmospheric methane.[6,10,13] The emissions of methane from such sources are estimated to be more than 100 Tg annually (1 Tg = 10^6 tones).[13] Methanogenic microbes produce methane by anaerobic decomposition of organic materials. Methane produced in the sediments is transported to the surface either through diffusion, ebullition or via transport through the plants themselves. Termites are another source of methane with an estimated emission of 15-20 Tg/year.[13] Methane is produced by the action of methane-producing bacteria on the organic material consumed by the termites. Approximately 10 Tg of methane are estimated to come from the oceans. Methane is produced at seepage areas in the seabed with organic-rich sediments. The quantities trapped in the form of methane hydrates are estimated to be close to 10000 Gt (10000000 Tg!).[14] Methane hydrates are rigid water cages surrounding methane molecules. Stability of hydrates requires high pressure and cold temperatures. Methane emission from hydrates is considered minor at present. Hydrates are subject to destabilization from climate warming and this destabilization could result in the release of an enormous amounts of methane.[14]

1.1.2.2 Anthropogenic Sources

The increase in the level of methane in the atmosphere relative to the preindustrial time is mainly due to the human activities. Rice Cultivation is estimated to account for 10% (~30-60 Tg) of the total annual methane emission. Methanogens produce methane by anaerobic decomposition of organic materials in the flooded field of rice farms. Livestock estimates to contribute about 120 Tg methane per year.[10,15] Non-dairy cattle and dairy cows together contribute about 75% of the total methane source from animals while water buffalo, sheep, goats, pigs, camels, and horses accounts for the remaining 25%. Another major anthropogenic source of methane emission is fossil fuel and about 80-120 Tg are emitted during fossil fuel processing.[16] Methane is the main component of Natural gas and coal contains significant amount methane. Coal mining and processing, as well as natural gas exploration, extraction, venting and flaring at oil and gas wells, transmission, and distribution leak a significant amount of methane to the atmosphere. Methane in fossil fuels is produced either from microbes or through geothermal processes. Another source is biomass burning which accounts to an estimated ~10-50 Tg of methane per year. Yearly 30-70 Tg of methane emission is estimated to come from landfills. Decomposition of biodegradable organic material in landfills produces both carbon dioxide and methane, the two potent greenhouse gases.[16]

1.1.2.3 Methane sink

The main atmospheric methane sink is the OH (hydroxyl) which accounts for about 90% of the global methane sink.[13,14] The oxidation reaction of the methane-OH mostly occurs in the troposphere, is the first step of a cascade of reactions that eventually leads to compounds that are readily removed from the atmosphere. About 500 Tg of methane are estimated to undergo this reaction yearly.[9,11] Although this process could reduce the level of methane in the atmosphere it indirectly affects the atmosphere negatively.[14] The process reduces the oxidation power of OH towards other compounds, produces CO_2 and also ozone in the troposphere during the chain of methane oxidation reactions.[13] A small portion of the formed methane is oxidized back to CO_2 in the atmosphere and anoxic environments by ANME and aerobic bacteria.[17] This biological methane degradation is carried out at about 0.6 Gt per year by aerobic bacteria and to a slightly lesser extent by anaerobic methanotrophs (ANME).[18]

1.1.3 Methanogenesis and Methanogenic Archaea

Methanogens are strictly anaerobic unicellular Archaea, taxonomically classified as a third phylogenetic domain of life.[5] They are mostly inhabitants of anaerobic environments. Methanogens are found in lake sediments, deep in the oceans, landfills, rice fields, digestive tracts of animal, ruminants and other anoxic environments where the availability of molecular oxygen is extremely low or absent. Some methanogens live under extreme conditions such as in temperatures above boiling, very high salt concentrations, or very acidic environments.[19,20]

Methanogenic Archaea play an important role in this environment by scavenging the end products of organic matter, H_2 and acetate, thereby facilitating the decomposition to completion. Methanogens are phylogenetically divergent orders of the domain Archaea (phylum euryarchaeota) which produce methane from simple substrates. They are taxonomically classified into five orders: Methanobacteriales, Methanococcales, Methanomicrobials, Methanosarcinales, and Methanopyrales.[5,21]

1.1.4 Biochemistry of methanogens

Methanogenic Archaea derive their metabolic energy from the conversion of only a certain number of substrates to methane and they cannot grow under physiological conditions without producing methane.[22] Depending on the substrate they utilize, methanogens are classified into three classes.[23] The first type of substrate most methanogens can use is CO_2. The major electron donors for the reduction of CO_2 to CH_4 are H_2 and formate (Figure 1.2, pathway in black). The microorganisms that utilize CO_2 as sole substrate are called hydrogenotrophic Archaea. *Methanococcus maripaludis, Methanothermococcus okinawensis* and *Methanothermobacter marburgensis* belong to this class. Formate can also be converted to methane through this pathway. It acts both as a source of carbon and reducing potential. The second type of substrates for methanogens includes C1, these compounds contain a methyl-group carbon bonded to O, N, or S (Figure 1.2, pathway in red). Compounds of this type include methanol, monomethylamine, dimethylamine, trimethlyamine, tetramethlyammonium, dimethylsulfide, and methane thiol. Microorganisms that belong to this class are called methylotrophic Archaea. Methylotrophic Archaea can use H_2 as an electron source, but the name hydrogenotrophic is exclusively reserved for those that reduced CO_2 to methane. The third class is called acetoclastic as they use acetate as a sole source of carbon (Figure 1.2, pathway in blue). In this reaction, the methyl (C-2) carbon of acetate is reduced to methane using electrons obtained from oxidation of the carboxyl (C-1) carbon.[24] This reaction is called acetoclastic because it results in the splitting of acetate into methane and CO_2. More than two third of the methane production is through this pathway mainly by *Methanosarcina* and *Methanosaeta*.[24]

During hydrogenotrophic methanogenesis, the CO_2 is first reduced to formylmethanofuran (CHO-MFR) (Figure 1.2). The formyl group is then transferred from methanofuran (MFR) to tetrahydromethanopterin (H$_4$MPT) which upon cyclization yields methylene-H$_4$MPT (HC≡H$_4$MPT). Two subsequent reduction processes yield methyl tetrahydromethanopterin (H$_3$C-H$_4$MPT). The methyl group is then transferred from H$_4$MPT onto coenzyme M (2-thioethanesulfonate) producing methyl-coenzyme M (CH$_3$-S-CoM) which is ultimately reduced to methane in the presence of MCR.[5,25]

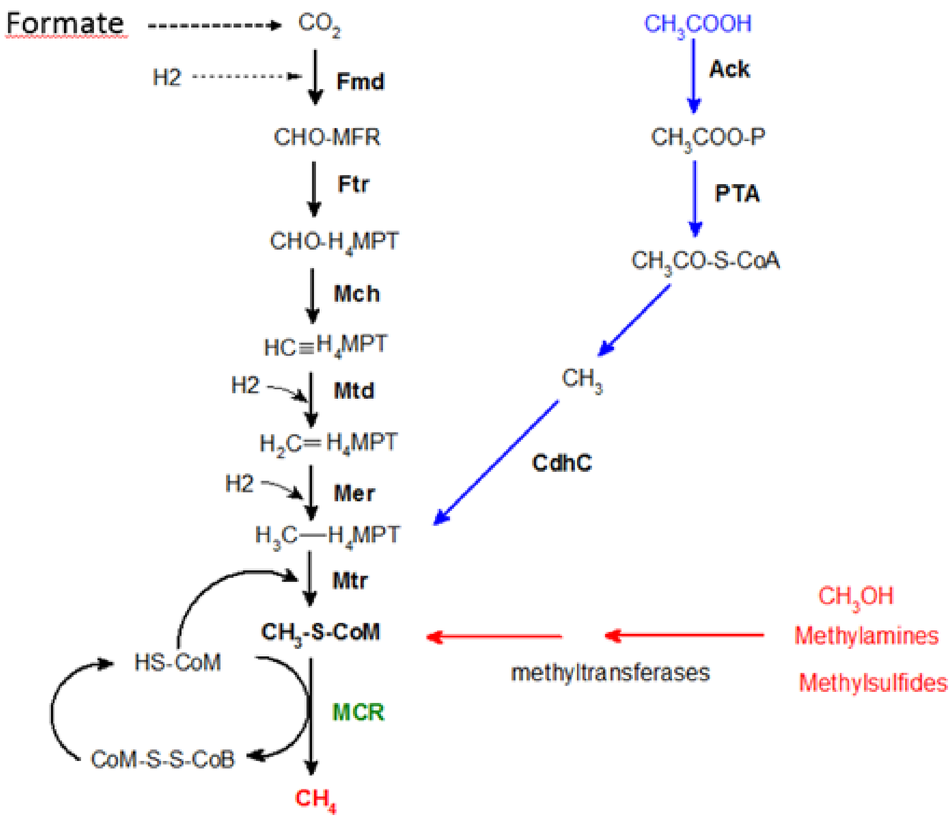

Figure 1.2. The three main methanogenic pathways. Abbreviations: Fmd, formylmethanofuran dehydrogenase; Ftr, formylmethanofuran:H$_4$MPT formyl transferase; Mch, methenyl-cyclohydrolase; Mtd, F$_{420}$-dependent methylene-H$_4$MPT dehydrogenase; Mer, methylene-H$_4$MPT reductase; Mtr, methyl-H$_4$MPT: coenzyme M methyl transferase; MCR, methyl-coenzyme M reductase; Ack, acetate kinase;

PTA, phosphate acetyl transferase; Cdhc (CODH/ACS), CO dehydrogenase/acetyl-CoA synthase complex.[5,21]

1.1.5 Methyl-Coenzyme M Reductase (MCR)

MCR is central to all methanogenic pathways; whether methane is produced from CO_2, methyl groups, or the acetoclastic reaction (Figure 1.2). During the forward reaction methyl-coenzyme M (CH_3-S-CoM) is reduced by the thiol coenzyme B (HS-CoB). Methane and the mixed disulfide (heterodisulfide, CoM-S-S-CoB) are formed in the process (Scheme 1.1). The first substrate, CH_3-S-CoM is enzymatically synthesized through the action of methyltranferase, and the second substrate, coenzyme B, is produced through the reduction of heterodisulfide by heterodisulfide reductase.[23,26] The second product of heterodisulfide reduction, coenzyme M enters the cycle of methanogensis to accept a methyl group and form methyl-coenzyme M. The MCR reaction is highly exothermic ($\Delta G^{o'}$ = -30 kJ/mol).[27,28]MCR can also catalyze the reduction of a non-natural substrate, ethyl-coenzyme M to produce ethane while larger chain alkane propane is inhibitory.[29] The product, heterodisulfide (HDS), inhibits the reaction, however, *in vivo* inhibitory effect is alleviated by the action of heterodisulfide reductase (Hdr). Ti (III) citrate (~ -600 mV) can also reduce HDS and is routinely used in the *in vitro* reaction assay to prevent product inhibition by HDS during turnover.

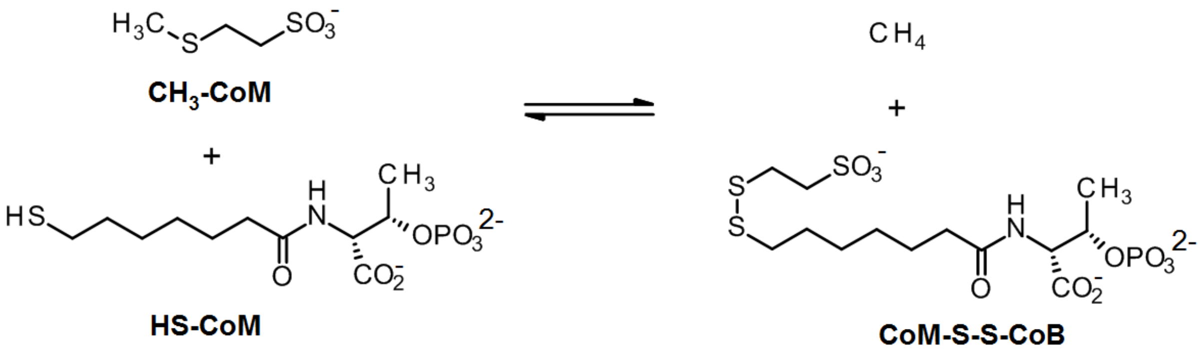

Scheme 1.1. Reaction Catalyzed by Methyl-Coenzyme M Reductase.[5]

MCR is a dimer of heterotrimers with a molecular weight close to 300 kDa. It is composed of three subunits in an $(\alpha\beta\gamma)_2$ stoichiometry. The enzyme contains a catalytic active coenzyme F_{430} as a prosthetic group tightly bounded to each monomer.[28] F_{430} is a nickel containing tetrapyrrole. The Nickel metal center in F_{430} cycles through three different oxidation states, 1+, 2+, and 3+. For the enzyme to initiate its catalytic activity, the Nickel in the F_{430} should be in the Ni(I) oxidation state.[30] Several crystal structures of MCR have been solved up to 1.16 Å resolution. Most of these are in its inactive Ni(II) state.[7,31,32] The structural characterization has revealed that the enzyme is a dimer of trimers with a C2 symmetry (see Figure 1.3).

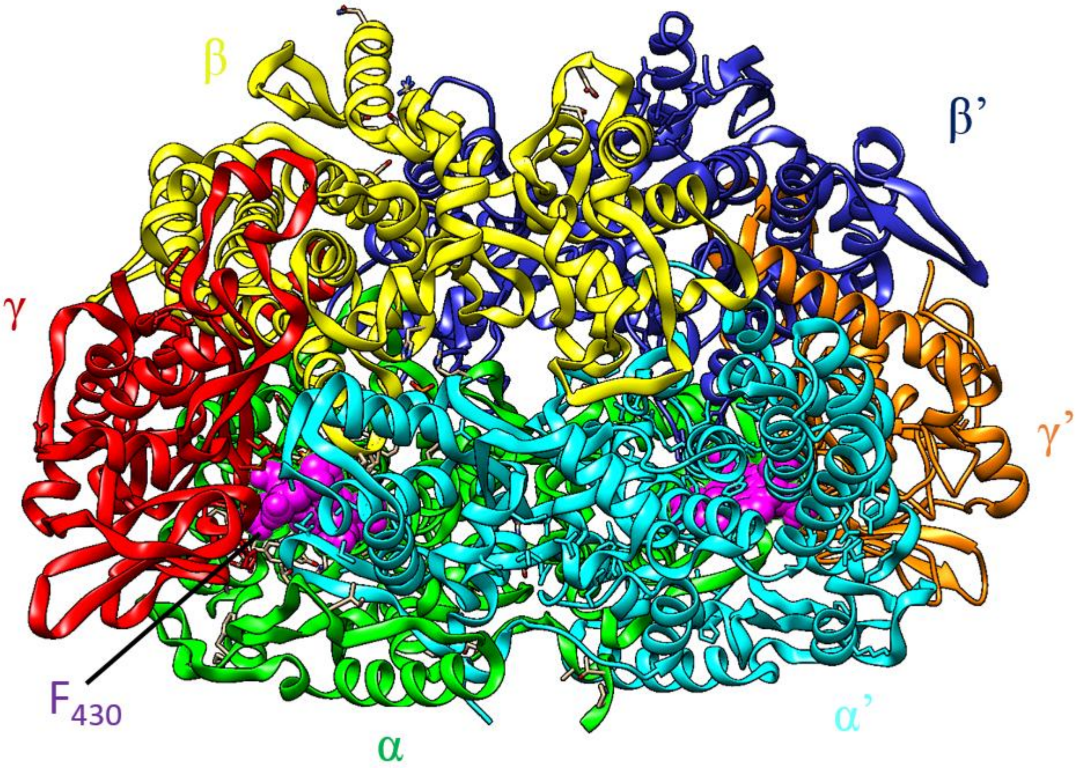

Figure 1.3. The structure of MCR

Deep inside the enzyme two independent F_{430} harboring active sites separated by roughly 50 Å are present. In all of the crystal structures reported, the oxygen of a Gln residue is axially coordinated to the nickel center of F_{430} (Figure 1.4).

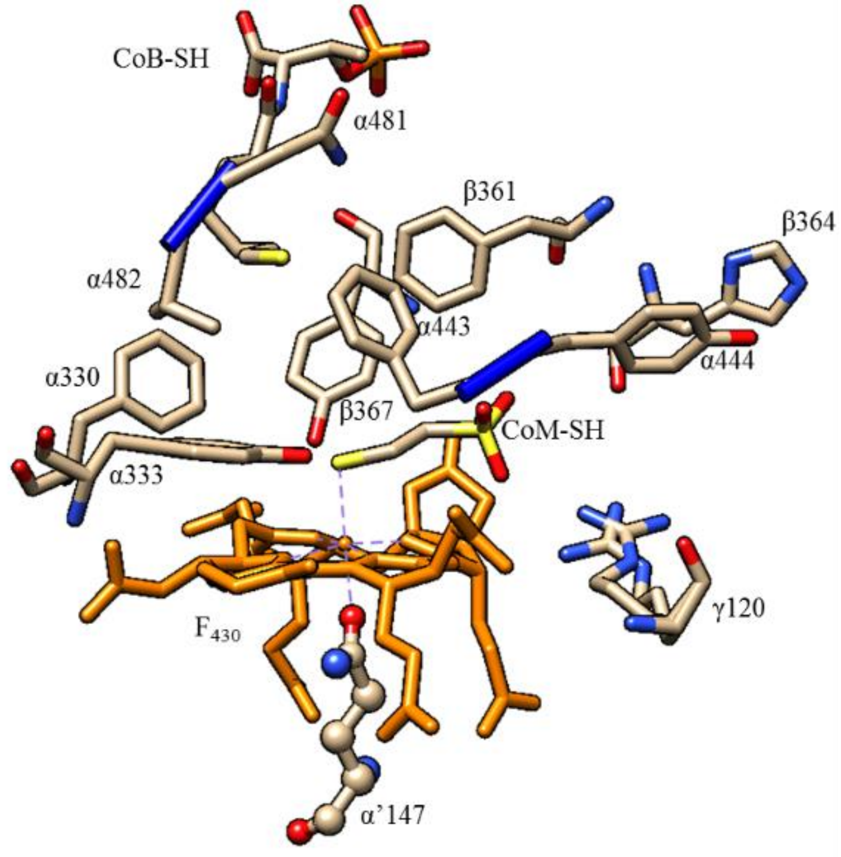

Figure 1.4. The residues in the active site of MCR

Each protomer of the enzyme MCR contains a long and narrow hydrophobic channel that extends from the surface of the enzyme to the hydrophobic pocket where the F_{430} resides. The substrates enter and bind to the active site through this 50 Å long channel, first CH_3-S-CoM followed by HS-CoB.[32] The channel and the active sites are formed by residues of subunits α, α', β and γ (and α', α, β' and γ'). Each active site is assembled in a ring type arrangement of Phe[330], Tyr[333], Phe[443], Phe[361], and Tyr[367] lined further by additional hydrophobic and aromatic residues (Figure 1.4).[25]These amino acids are all completely conserved in MCR. The phosphate group of HS-CoB is positioned by ionic interactions with MCR residues located halfway down the channel with its thiol group located 8.7 Å from the nickel. The binding site of HS-CoM/CH_3-S-

CoM) is more deeply buried within the enzyme. The CH_3 group of CH_3-S-CoM was shown to be able to get as close as 3.4 Å to the nickel ion of the enzyme, indicating that the CH_3-S-CoM enters first in the reaction mechanism followed by HS-CoB.[33] Kinetic studies showed that a ternary complex is formed involving both substrates. Binding of HS-CoB in the active site is believed to induce a conformational change that moves the substrates even closer to the nickel center of coenzyme F_{430}.[33]

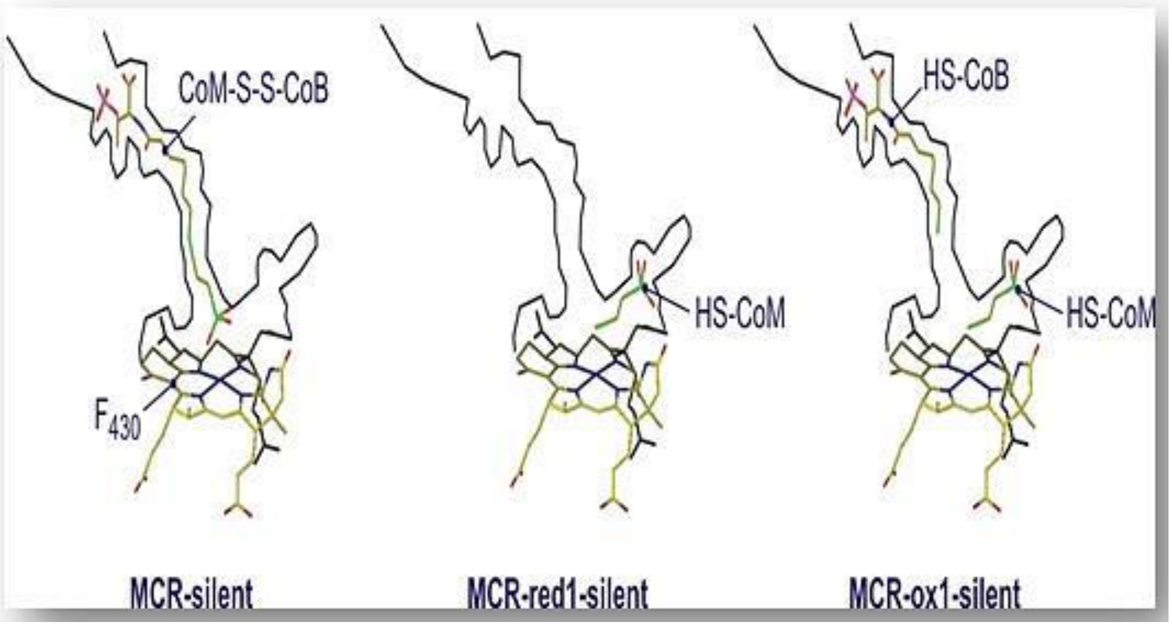

Figure 1.5. The channel and the binding site of the substrates, substrate analogs, and product of MCR.[32] Adapted from reference 29

1.1.5.1 Post translational modifications (PTMs)

The crystal structure of *M. marburgensis* revealed five modified amino acids within the active site residing on the α-subunit. Some of these modifications are unusual and uncommon. Four of these modifications are methylations: 2-(S)-methylglutamine (Me-Gln400, *M. marburgensis* numbering), 5-(S)-methylarginine (Me-Arg271), 3-methylhistidine (Me-His257), and S-methylcysteine (Me-Cys452). The methyl group of all four amino acids is believed to be derived from the methyl group of methionine, most likely via S-adenosyl-L-methionine (SAM).[34,35] The fifth modification is the insertion of sulfur into the backbone carbonyl group of a glycine residue forming a thioglycine (TGly445).[24, 25] All of these modifications are in the α subunit, and they are believed to be introduced after the gene translation as no unusual codon was found at the position of the modified amino acids. It is not known if all these five modifications are present in all methanogenic Archaea. For example, the modification of cysteine is not present in *M. okinawensis* and *M. maripaluids* while the other four modifications are present, however, all of these modified amino acids are conserved in the MCR of all methanogens.[34] The function of the five modifications is not known though several hypotheses have been proposed. Forexample, methylhistidine is involved in coordination of HS-CoB through the imidazole ring and is believed to be involved in influencing the affinity of MCR for its substrate.[37] The thioglycine may be involved in the catalytic mechanism directly.[32] The thioglycine was proposed to facilitate the deprotonation of HS-CoB by reducing the pKa of the sulfhydryl group.[32]Horng, and co-workers, suggested that thioglycine may serve as an intermediate electron carrier for oxidation of a heterodisulfide anion radical intermediate.[38]Goenrich, and co-workers, suggested a role of cis-trans isomerization of the thioamide during catalysis in coupling the two active sites via a previously proposed two-stroke mechanism for the enzyme.[39]

Recently, the genes encoding for some of these modifications were identified. Nayak, and co-workers, identified two genes named tfuA and ycaO (previously designated as methanogenesis marker protein 1, Mmp1) that are responsible for post translational insertion of sulfur generating thioglycine. Knock out of both genes or ycaO alone from *Methanosarcina* *acetivorans* resulted in an unmodified glycine suggesting the role of these genes in modification of glycine to thioglycine.[36] Furthermore, phenotypic results from this mutation study suggests a role of thioglycine in maintaining the structural conformation of residues near the active site rather than direct involvement in the catalytic mechanism. It is worth nothing that this argument was based on whole cell studies since no active purified enzyme was obtained. Thus, further studies need to be done to confirm this argument.

The gene encoding for methylarginine, *MMP1554*, has been under investigation.[40] This gene which encodes the methanogenesis marker protein 10 (Mmp10) was deleted and its effect on the *in vivo* MCR activity was tested in *M. maripaludis*. Mmp10 mutant resulted in the specific loss of the 5-(S) methylarginine PTM of residue 275 in the McrA. Moreover, a 40~60 % reduction in the maximal rates of methane formation by whole cells was observed with mutant strains. This result implies the role of Mmp10 and the methyl-Arg PTM on MCR activity (unpublished result). However, as argued in the above paragraph the activity of MCR was only assessed in *in vivo,* and further studies with purified MCR is necessary to get a better insight on the function of this PTM. Furthermore, Radle et al., recently, reported the role of Mmp10 for methylation of argining. They showed that Mmp10 from *M. acetivorans* catalyzes the methylation of Arg in a peptide, an Arg equivalent to Arg-285 in MCR from *M. acetivorans,* in the presence of cobalamin.[41]The role of Arg modification on the activity of purified MCR was not tested in his studies.

1.1.6 Methanotrophic Archaea and anaerobic methane oxidation

One of the main sinks for methane is anaerobic oxidation of methane (AOM) by methanotrophic Archaea referred as ANaerobic MEthane-oxidizing Archaea (ANME). AOM controls, at least partially, the emission of methane from anaerobic environments such as deep oceans. ANME are phylogenetically related to methanogeneic Archaea. Three classes of ANME have been discovered; ANME-I, ANME-II and ANME-III. ANME-I are phylogenetically related to the orders of *Methanomicrobiales* while ANME-II and ANME-III are related to *Methanosarcinale*.[7,42] ANME Archaea have been found in close association with sulfate-reducing bacteria and others.[11,42,43] ANME are believed to undergo AOM via reverse methanogenesis. This hypothesis is not, however, universaly accepted. All genes involved in methanogenesis pathways have been found in ANME, except one gene, the N_5,N_{10}-methylene-tetrahydromethanopterin (methylene-H_4MPT) reductase (Mer), which catalyzes the reaction from methylene-H_4MPT to methyl-H_4MPT, thus suggesting that the reverse reaction may not necessarily involve all the enzymes of methanogenesis.[44]

Furthermore, Proteomic analysis showed the presence of at least two different MCR homologs, designated as proteins I and II, which were later attributed to the ANME-I and ANME-II Archaea, respectively. These findings support the hypothesis of ‘reverse methanogenesis’ that propose ANME Archaea anaerobically oxidize methane to CO_2 using very similar enzymes following the same catalytic steps as methanogens, but in the reverse direction.[11] Jaun and Thauer first demonstrated that under the right conditions, the MCR from *M. marburgensis* can catalyze the reverse reaction oxidizing methane to methyl-SCoM.[45]

1.1.7 Different forms (states) of MCR

Several forms of MCR have been characterized using crystallography and spectroscopy techniques.[31,32] Figures. 1.6 and 1.7 give an overview of the Uv-vis and EPR spectra, respectively, of the most relevant states of MCR.[46] The MCRred1, MCRred2, MCRsilent and MCRox1 state can be detected *in vivo* and *in vitro* under different conditions. The enzyme is active in its MCRred1 forms. At this state the enzyme is coordinated by four Ni-ligands of F_{430}

and a fifth O-ligand from the Gln-residue of the enzyme. The six ligand position of the enzyme is unoccupied and it is believed to be the site of substrate binding during initiation of the catalytic reaction.[31]The red2 state can be induced *in vitro* by incubating MCRred1with both coenzyme M and coenzyme B. The EPR signal of MCRred2 is a mixture of two species, MCRred2-axial and MCRred2-rhombic that are in thermal equilibrium. In the MCRred2-rhombic form, the thiol sulfur of coenzyme M is bound to the nickel. In the MCRred2-axial species, a hydride is bound.

Adding of polysulfide or sulfide can convert MCRred2 into MCRox1 while addition of sulfite converts MCRred2 into the MCRox2 form. MCRox3 can be induced by exposing MCRred2 to oxygen.[47] The Active form of MCR, MCRred1, can be obtained in vitro by incubating MCRox1 or MCRox3 with the reductant Ti(III) citrate. MCRred2, MCRox2, and MCRox3 are light sensitive.[47]

Gassing the hydrogenotrophic methanogens, cells that utilize CO_2 and hydrogen as an electron donor, with 100 % H_2 before harvesting induces the MCRred forms. Both MCRred1 and MCRred2 are detected in cell extract after purging with 100% H_2**.** In the MCRred form, the cofactor is in Ni^{1+} (d^9) state and is a paramagnetic species**.** Purifying the enzyme anaerobically with buffers containing either substrate CH_3-CoM or HS-CoM yields exclusively the MCRred1 forms. Two MCRred forms can be obtained during purification. The $MCRred1_c$ is the form that obtained in the presence of coenzyme M and the $MCRred1_m$ is obtained in the presence of methyl coenzyme M. Both MCRred forms are stable in the presence of their respective molecule**.** A more resolved hyperfine-splitting pattern in EPR spectra of $MCRred1_m$ is observed in comparison to the EPR spectra of $MCRred1_{c,}$ due to weak interaction between Ni(I) center and the thioether sulfur atom of methyl-coenzyme M, which is at a Ni-S distance of 3.94 Å. Electron nuclear double resonance (ENDOR) measurements with labeled methyl-coenzyme M showed that in this from there is a weak interaction between them. A third uncommon and unstable form, of MCRred1$_a$ is detected in the absence of both HS-CoM and CH_3-CoM.[48]

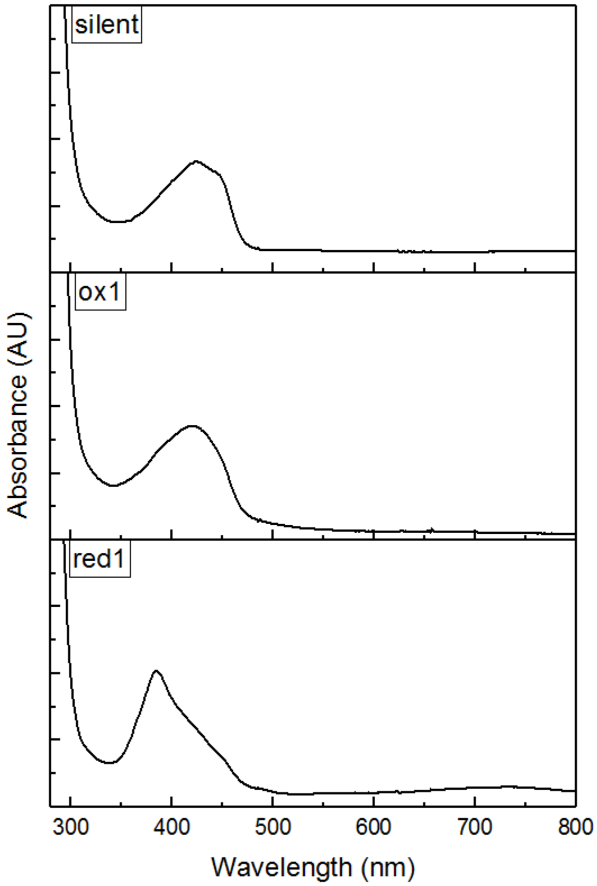

Figure 1.6. Uv-Vis spectra of methyl-coenzyme M reductase in its three major forms.

MCRox1 can be detected in cell extract after purging with N_2/CO_2. In the MCRox1 form, the cofactor is in the Ni^{3+} (d^7) state and is EPR active. Another state of MCR is the inactive and EPR silent form referred to as MCRsilent. In MCRsilent the cofactor Ni is in the 2+ (d^8) form and cannot be detected with EPR spectroscopy as it is a paramagnetic (S =1) species.

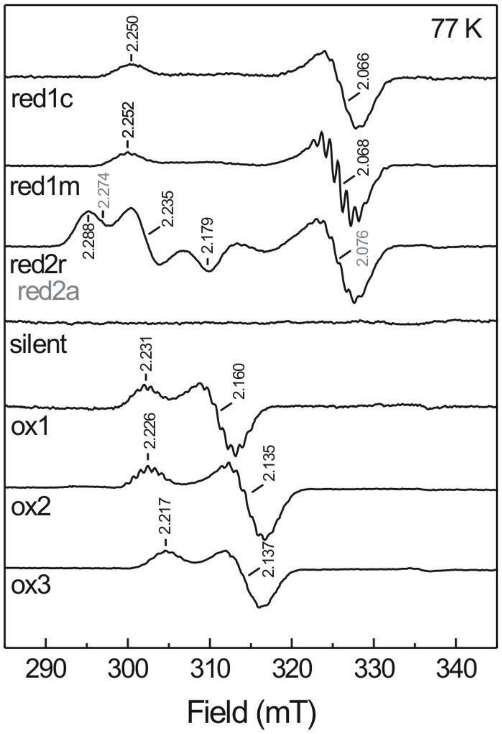

Figure 1.7. EPR spectra of methyl-coenzyme M reductase in different forms.

Unique EPR spectra have also been obtained when MCR binds or reacts with inhibitors.[49] The most commonly used inhibitors are bromopropane sulfonate (BPS), bromoethane sulfonate (BES).[50,51] Figure 1.8 depicts the interconversion of different MCR forms. All the relevant forms of MCR can convert spontaneously into the MCRsilent form. This form is the most stable forms and reluctant to be converted back to either the MCRred1 or MCRox1 form of the enzyme. As of today, there has not been a chemical approach that can convert the silent form to either the ox1 or red1 state.

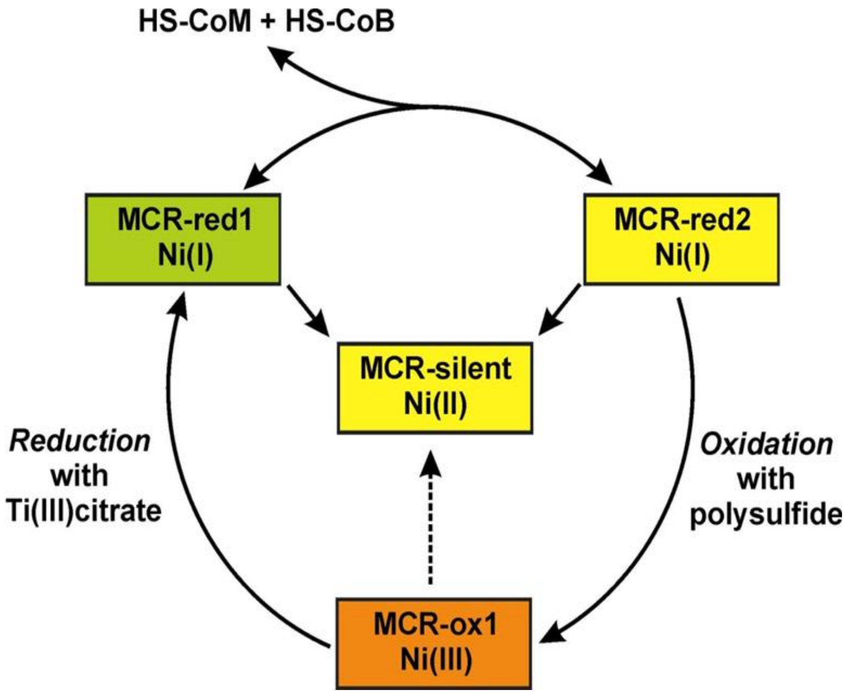

Figure 1.8. In vitro conversion of different forms of MCR

1.1.8 Purification of highly active enzyme

To purify MCR in its active form strictly anaerobic conditions are required throughout the harvesting and purification process. A special method for this purpose was developed by Thauer and coworkers.[48] The protocol was developed for the cells of the organism *M. marburgensis* which can only grow on 20% CO_2/80% H_2. Prior to harvesting the cell culture is treated with 100% H_2 for 20 min, quickly cooled to ~10^{o}C, and harvested anaerobically. The cells are then sonicated inside a tent, and the cell debris is removed by centrifugation using air tight ultracentrifugation cups. The MCR is then semi purified using ammonium sulfate precipitation steps. Finally, pure MCR is be obtained using a Q-sepharose chromatography step which separates the two isoenzymes MCR-I and MCR-II and a few proteins that are still present.

It is necessary to add HS-CoM or CH_3-CoM during each purification steps in order to stabilize the active MCRred1 state which otherwise spontaneously inactivates to the silent form. If this protocol is followed carefully, a highly active MCR can be obtained. We routinely obtained MCR with ~90% MCRred1 by following this protocol. The red1 form can also be obtained indirectly from the ox1 form induced using a treatment with Na_2S. This protocol will be discussed in chapter 2.

1.1.9 Proposed catalytic mechanisms of MCR

The reaction mechanism of MCR is not fully known. Several reaction mechanisms of MCR have been proposed based on the spectroscopic analysis of different state of the enzyme and computational studies.[29,32,38,52,53] The reaction of CH_3-CoM with HS-CoB catalyzed by MCR involves the breaking of the C-S bond of CH_3-CoM and the S-H bond of HS-CoB and subsequent S-S and C-H bond formation to produce heterodisulfide and methane, respectively. Two competing catalytic mechanisms for MCR have been extensively studied and are described below (Figure 1.9). These two mechanisms differ in the nature of the first intermediate in the catalytic cycle.

In mechanism I, it has been proposed that the reaction is initiated by a nucleophilic attack of the Ni(I) on the methyl group of methyl-SCoM to generate a methyl-Ni(III) intermediate. The Ni(III) intermediate then abstracts an electron from coenzyme M to form methyl-Ni(II) and a coenzyme M thiyl radical. Finally, a proton is abstracted by the methyl group of the Ni(II) complex and methane is formed while the coenzyme M thiyl radical reacts with HS-CoB to liberate the heterodisulfide anion radical which ultimately gives its excess electron to the Ni(II) complex to regenerate the active enzyme for the next turnover cycle.[54] Mechanism I is based on mechanistic work done with F_{430} model complexes characterizing the location of substrates in the active site of inactive Ni(II) MCR structures, and on mechanistic and crystallographic studies on the active Ni(I) enzyme with 3-bromopropanesulfonate (BPS) and methyl halide.[45,49,55,56] An enantioselectivity study of the enzyme with ethyl-coenzyme M as a substrate supports this mechanism. In this study an inversion of configuration to give chiral ethane was reported suggesting an exclusion of methyl radical formation as an intermediate which is proposed to occur in mechanism two.[29]

Mechanism II begins with the nucleophilic attack of Ni(I) on the sulfur atom of methyl-SCoM. This leads to the homolytic cleavage of the methylsulfur bond and generation of a methyl radical ($\bullet CH_3$) and a Ni(II)-thiolate complex. The transient methyl radical is then transformed to methane by withdrawing a hydrogen atom from the sulfhydryl group of HS-CoB. The coenzyme B thiyl radical reacts with coenzyme M thiolate to form the heterodisulfide radical anion. Finally, the excess electron goes to the Ni(II) complex and regenerates the active forms of the enzyme.[54] This mechanism is based on density functional theory (DFT) calculations and on isotope effects studies of the reaction of MCR with CH_3-SCoM and homologous substrate C_2H_5-SCoM.[49,55,57,58] A recent report from the Ragsdale group using transient kinetics, spectroscopic, and computational methods supports mechanism II. In this study, they identified a Ni(II)-thiolate species as the first intermediate using magnetic circular dichroism spectroscopy.[59] The actual methyl-radical species has not been detected.

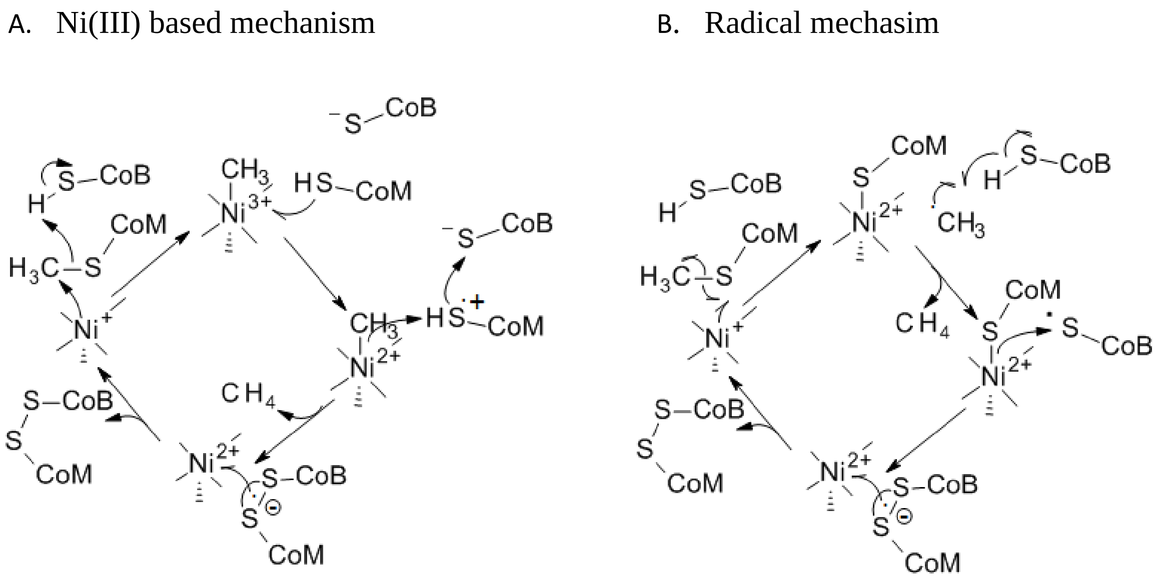
A. Ni(III) based mechanism

B. Radical mechasim

Figure 1.9. Proposed catalytic mechanism of MCR. Panel A, mechanism I; panel B mechanism II. Adapted from reference 58

The precedent available in experimental and computational arguments do not adequately take in to account the enzyme environment. Thus, it is still of interest to investigate the mechanism considering residues in the active site that are believed to play an important role in mechanism. F_{430} by itself is unreactive towards CH_3-SCoM, and if we want to design a Ni-based catalyst for the activation of CH_4, it is important to understand the role of this specific protein environment. Making fully active recombinant MCR would highly useful in characterizaing this mechanism and elucidate the role of PTMs and other conserved aminoacids of MCR.

1.1.10 Introduction to Electron Paramagnetic Resonance (EPR) spectroscopy

Electron Paramagnetic Resonance (EPR) spectroscopy, also known as Electron Spin Resonance (ESR) spectroscopy is one of the most powerful spectroscopic techniques used to characterize metalloproteins and organic radicals. EPR is commonly used to detect a paramagnetic species, a molecule or atom with unpaired electrons.[33,60–62] EPR has been widely used as a qualitative and quantitative technique to determine the structure and dynamics of transition metals that have a prominent role in catalysis. The utilization of EPR could even extend in investigating compounds through "Spin labeling" (e.g. Nitroxide spin labels attached to the protein) which is a useful approach for compounds that are not inherently paramagnetic species.[63,64]This approach provide valuable information related to the structure and dynamics of proteins.[65]

In EPR measurements, the sample in an EPR tube is subjected to a very strong magnetic field and an electromagnetic (EM) radiation is applied.[66] In the absence of external magnetic field, the electron spins are randomly oriented, and the two energy levels are degenerate i.e. they have equal energy. Once an external magnetic field is applied to the sample, the electron spins, S, orient themselves either parallel or anti-parallel to the direction of magnetic field. As a result, the energy levels split and are no more degenerate. The splitting depends linearly on the applied magnetic field and this splitting of the two energy states is called electron Zeeman interaction (Figure 1.10).[66,67]

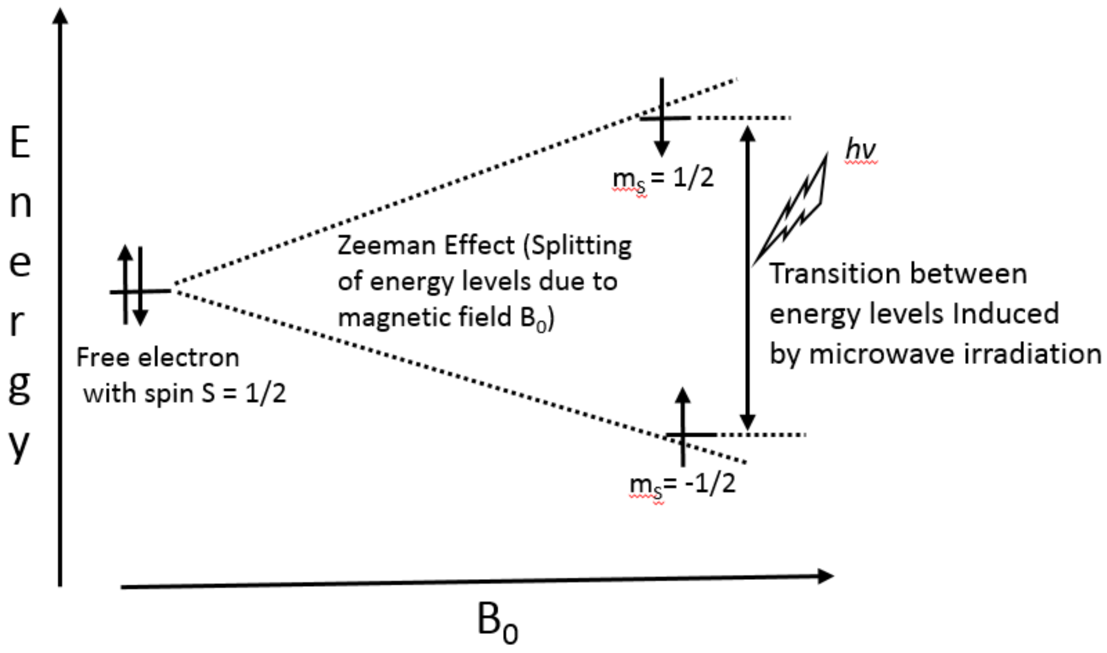

Figure 1.10. Splitting of an energy level of an electron

The energy difference between the two states is given by:

$$\Delta E = E\left(ms = +\frac{1}{2}\right) - E\left(ms = -\frac{1}{2}\right) = g\beta eBo$$

Where: g is the g-factor. (g-value for a free electron is ~ 2.0023[61] (g_e), predicted by quantum electrodynamics), βe is the Bohr magneton = $e\hbar/2me$ and Bo is magnetic induction.[62,66,67]

Once the energy difference between the two magnetic spin number (m_s) is reached by irradiating a frequency, electrons can exit from the less energetic m_s = -1/2 to the higher energy state m_s = +1/2, i.e the spin can be flipped from one orientation to the other. Under such condition an overall absorption of energy occurs, and the resonance condition is said to be fulfilled.[62] The relative population of the two-energy state (m_s ½ and m_s -1/2) can be obtained from Boltzmann distribution.[66]

1.1.8.1 Anisotropy in EPR

For most compounds, the actual measured g-factor is different from that of the free electron (~2.0023) which arises from spin angular momentum-orbit angular momentum interactions. Orbitals are oriented themselves in the molecule they reside in, and hence the magnitude of the spin angular momentum and orbit angular momentum coupling is directional, or commonly referred to as anisotropic.[66] The g-factors measured along the principal axes are called the principal g-factors and are represented as g_x, g_y and g_z. Three types of anisotropy exist depending on the value of the principal g factor and the spectra obtained vary accordingly (Figure 1.11). If all of the principal *g* factors have the same value, the spectrum obtained is an isotropic type of spectrum. In an axial type spectrum, there is a unique axis that differs from the other two ($g_x = g_y \neq g_z$). The last type of spectrum is referred to as rhombic and is obtained when all the *g* factors differ.[66]

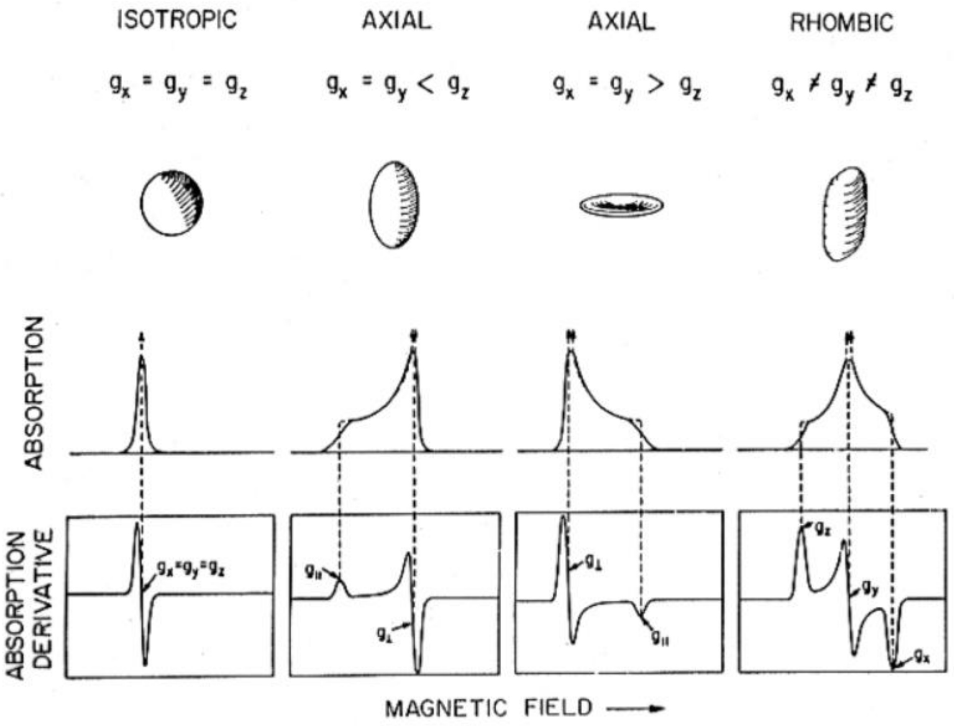

Figure 1.11. Schematic representation of the *g* tensor and the consequential EPR spectra adopted from reference 66.

1.1.8.2 Interaction with the nuclear spins

The intrinsic spin angular momentum of the nuclei is associated with a magnetic moment. In addition to the external magnetic field Bo, the electron spin can also experience the local magnetic field built up by a nuclear magnetic moment close to the unpaired electron. The interaction of the electron spin with the nuclear magnetic moments is called hyperfine interaction. For a given nuclear quantum number I a splitting into (2I + 1) energy levels is observed and provides important information in EPR spectroscopy. Additional information can also be obtained from the interaction of the unpaired electron with the set of equivalent nuclei that function as a ligand to the central nucleus. This results in further splitting of the signal and is referred as superhyperfine splitting.[66]

The superhyperfine and the hyperfine splitting are generally very small. Most of the time the (super)hyperfine splitting is unresolved but can be important for extracting valuable information regarding the environment around the paramagnetic species when it is detected. Hyperfine that is unresolved in CW EPR can often be detected with the techniques of ENDOR, ESEEM, and HYSCORE.[67]

1.1.8.3 Continuous-(micro)wave (CW) EPR

In CW EPR spectra measurement is performed by placing a sample into a MW irradiation field of constant microwave frequency while varying the external magnetic field B_0. Different frequency regions can be used to measure EPR spectra of a sample. The most common and important frequencies are S-band (~3 GHZ), X-band (~9 GHZ), Q-band (~35 GHz) and W-band (~ 90 GHz).[61,62,66]

1.1.8.4 Pulse EPR

In Pulse EPR, the spectra are measured by exciting a large frequency range simultaneously with a single high-power MW pulse of given frequency at a constant magnetic field B_0. An improved resolution of EPR spectra can be obtained in pulsed EPR which is otherwise is difficult to obtain from traditional CW EPR measurement.[67,68] However, the interpretation of pulse EPR spectra required technical equipment and a more advanced theoretical background and thus most of the EPR experiments are being carried out using CW EPR spectroscopy.[67]

1.1.11 Outline of the Project

1. Making active recombinant MCR

It is evident that MCR is critical for the methanogens and any attempt to do mutation on the enzyme MCR may severely affect the growth of the methanogens. Making mutant enzyme would provide valuable insight in understanding the catalytic mechanism of the enzyme as well as investigating the role of PTMs. Thus, it is of interest to make active recombine MCR first and make variant enzymes in order to test several hypotheses pertaining to the enzyme system. This project opens a way to the production of variant MCR by exploring a way to characterize and activate recombinant MCR from *M. okinawensis* and *M. maripaluids.*

2. Investigating the activating system of MCR

One of the main bottle necks in the study of MCR is the inherent nature of the enzyme to spontaneously inactivate and the difficulty to get MCR reactivated. Currently, there is no chemical method to activate the enzyme once the enzyme is inactivated. *In vivo,* however, the enzyme possesses an activating complex that can activate it. Although the complex has been discovered it is not fully clear what the role of each individual subunit are. Here we continue the characterization of the enzyme complex recently obtained by the Duin group.

3. Investigating the inhibitory mechanism of 3-NOP

MCR is responsible for the production of methane in different environments. One source of atmospheric methane is the gut of ruminant animals. Large amounts of methane escape from domestic cattle which adds to the greenhouse effect. In addition, up to 12% amount of food is wasted when feeding cattle as methanogens are using part of it for making methane. Thus, it is of interest from both economic and environmental perspectives to look for an inhibitor that can mitigate methane production from ruminal life stock. 3-NOP has been discovered and found to be effective in reducing methane production through the inhibitory action on MCR and thereby improving ruminant performance.[69] The exact mechanism of inhibition is not clear and is further investigated.

Chapter Two: Characterizing and activating recombinant Methyl-coenzyme M reductase (recMCR)

2.1 Introduction

Studying the biosynthesis of methane is quite appealing and attractive from both biofuel production and environmental perspectives. More than 90 % of methane is produced biologically as a byproduct of energy metabolism by methanogenic Archaea. Methanotrophic Archaea on the other hand are involved in the biological oxidation of methane. Together with aerobic methanotrophs, they play an essential role in preventing the release of methane to the atmosphere which otherwise could have a serious consequences on global warming and climate change.[1,2] Methyl-coenzyme M reductase (MCR) is the key enzyme in both the biological formation and the anaerobic oxidation of methane.[4] MCR catalyzes the terminal step in methane formation and the first step in the oxidation of methane. Its catalytic activity depends on the unique nickel-containing tetrapyrrole, coenzyme F_{430}. Near its active site, MCR from *M. marburgensis* has five post-translational modifications (PTMs). Four of these five modifications are methylations, including 2-(S)-methylglutamine, 5-(S)-methylarginine, 3-methylhistidine, S-methylcysteine, and the fifth modified amino acid is a thioglycine.[35] The exact roles of these PTMs are not known, but the amino acids are believed to have some role in the catalytic mechanism of the enzyme.

Expressing recombinant MCR (recMCR) in the active form is paramount for increasing our understanding of this enzyme system. Expressing MCR in *E. coli,* the most commonly used and thoroughly investigated organism for scientific studies, is not practical yet. This is mainly because a whole set of accessory genes are required to express mature and active MCR, and these genes need to be expressed together with MCR in order to express fully functional recombinant MCR. Unfortunately, these genes are not naturally present in *E.coli* and some of them are not even fully characterized hindering the utilization of *E.coli* as a host for expressing MCR. For this reason, it was decided to express MCR from similar organisms in *M. maripaludis*.

One of the main obstacles in research pertaining to the MCR system is obtaining active enzyme. Previous studies found that activity of MCR was quickly lost upon breaking the cells.[70] Several approaches were then established to obtain active MCR. Most of the work was done with *M. marburgensis* that grows on 80% H_2/20% CO_2, where H_2 provides electrons and is considered the reductant while CO_2, is the substrate, the oxidant for methanogenesis. *M. marburgensis* cultures are generally grown under a continuous supply of 80% H_2 and 20% CO_2. The inactive MCRsilent form is obtained when the cells are harvested and sonicated without any special pre-treatment. Changing the gas phase of the culture from 80%/20% H_2/CO_2 to 100% H_2 and purging the culture for 30 min before harvesting induces the reduced forms of the MCR. Both, MCRred1 and MCRred2, were detected in cell extract after this treatment.[47,48] When the enzyme is purified with CH_3-CoM/HS-CoM containing buffer, the protein could be obtained exclusively in the MCRred1 form. The MCRred2 is formed MCRred1 in the presence of coenzyme B which is lost during the purification procedure. MCRred1 is the active form of the enzyme, and the *M. marburgensis* enzyme can show specific activities as high as 100 units mg^{-1} of protein.[47]

Changing the gas phase of the culture to 80% N_2 and 20% CO_2 prior to harvesting induces the MCRox1 state. The MCRox1 form is not active but can be easily be converted into MCRred1 by treating it with Ti(III) citrate.[47,48] MCR can be interconverted from one forms to another *in vivo* as well as *in vitro*. Addition of coenzyme B to the MCRred1 form can induce the MCRred2 form. The red2 form can be converted into the ox1 form by oxidation with polysulfide. The ox1 form can be converted into the red1 form by reduction with Ti(III) citrate.

MCRred1, and MCRox1 are converted into the silent form upon contact with oxygen. The conversion of MCRred1 in particular is spontaneous and can be converted into the silent form completely within a few days even if the enzyme is stored in an anaerobic environment. MCRox1 on the other hand is relatively stable and can stay in this form for a long time without converting to the silent form. It is not possible to convert MCRsilent to either MCRred1 or MCRox1 form in vitro without the presence of the activating complex. This activating complex is discussed in more detail in chapter 3.

An alternative way of inducing the MCRox1 form was reported by Ragsdale and coworkers.[71] *Methanosarcina thermophila,* an acetoclastic methanogen grown on acetate or H_2/CO_2 at an optimum temperature of 50 °C was used for their study. After reducing the culture volume 2-3 times, 20 mM final concentration of sodium sulfide was added to the culture before harvesting. The Na_2S treated cell culture was further incubated at 50 °C for 1 h and cells were harvested, sonicated and the enzyme purified anaerobically. A significant amount of MCRox1 signal was detected and the activity of the purified MCR, after activating with Ti(II) citrate at pH 9.0, was up to 5 U/mg. The same protocol was tested for the *M. marburgensis* cells and the protocol works for *M. marburgensis* as well. They suggested that this protocol in principle should work for any methanogens regardless of their growth condition.

Now we have several methods to generate the MCRred1 form directly or indirectly. How the activation of MCR and the conversion of the different forms works in the cell, however, remains elusive for most of these estabilished protocols. MCR has been routinely purified in its active form mainly from *M. marburgensis* and most of the studies were performed with native MCR. Yet there are many key questions in the biochemistry of MCR, and these can only be addressed using recombinant enzyme.

M. maripaludis is one of the few methanogens with a well-developed genetic tool set. Methods were developed for enrichment of auxotrophic mutants similar to the penicillin selection in bacteria.[72] A selectable resistance marker called the *pac* cassette was created from the *Streptomyces* puromycin transacetylase gene and methanococcal transcriptional control elements to provide resistance to puromycine.[73]A neomycin resistance cassette was also created to provide a second selectable marker if necessary.[74] Several efficient transformation systems[75–77] and an expression vector were developed for *M. maripaludis*.[78,79]The genomic sequence of *M. maripaludis* S2, a robust N_2 -fixing strain, was completed.[80]A system was developed for constructing markerless deletions.[81]

M. maripaludis grows relatively rapidly compared to most other methanogens which is another advantage for use as an experimental organism. *M. maripaludis* has a generation time of two hours at 37 ^{o}C and a dense culture can be obtained overnight by culturing them in liquid mineral rich media. *M. maripaludis* is an obligate methanogen that can grow on formate rich media or on H_2/CO_2.[82] Amino acids and acetate supplemented to the medium are frequently stimulatory for growth. Nitrogen sources include ammonium, N_2 gas and alanine.[81] The ability to use alanine is distinctive for members of this species. They obtain the sulfur from sulfide and elemental sulfur. *M. maripaludis* is an irregular coccus, between 0.9 and 1.3 µm in diameter. It is a mesophilic organism, with an optimum growth temperature of about 37 ^{o}C and pH at around 8.[78,82]

Because MCR is essential for growth of the methanogens, mutations that may inactivate the enzyme and thust affect the growth of the organism must be performed on a second copy of MCR. However, if the second copy is identical to the host enzyme, it would be difficult to identify chimeric enzymes comprised of native as well as recombinant subunits. For this reason, the *MCR* operons (Figure 2.1) from a variety of other methanogens were expressed in *M. maripaludis* using a vector constructed for *methanococci*. This work was performed in collaboration with the lab of Barny Whitman at University of Georgia at Athens, GA. Several *MCR* operons with all five genes (Figure 2.1) from different organisms were cloned, and their sequences verified prior to transformation into *M. maripaludis*.[83] Because of the extensive biochemical studies, the MCR from *M. marburgensis* was the primary target. However, this operon proved to be toxic [unpublished observations]. Preliminary experiments showed that the toxicity was due to expression of *mcrA*, and the genes for the other subunits were expressed successfully either individually or in various combinations. For that reason, expression of MCR (recMCRok) from the methanogens that are more closely related to *M. maripaludis* were used, i.e. *Methanothermococcus okinawensis*.

Figure 2.1. MCR operon

The *MCR* operon from *M. maripaludis* (Mmp1555-1559) is typical of the *MCR* I operons from many methanogens. In addition to the genes encoding the structural components of MCR (*mcrB*, *mcrG*, and *mcrA*, shown in green), it also encodes two highly conserved *MCR*-associated genes, *mcrC* and *mcrD*, of unknown function (shown in orange).

2.2 Methods and Materials

2.2.1 Reagents

Most of the chemicals used in these experiments were either from Fisher Biotech (Pittsburg, PA) or from Sigma-Aldrich (St. Louis, MO). Fusion high fidelity DNA polymerase was purchased from Agilent Technologies (Clara, CA). The pET28b(+) vector was a generous gift from the Mansoorabadi group. The plasmid isolation and gel extraction kits were purchased from Qiagen (Valencia, CA). The primers were purchased from Integrated DNA Technologies (San Jose, CA) and the restriction enzymes were purchased from New England Biolabs (Ipswich, MA). Top10 chemically competent *E. coli* and BL21(DE3) competent *E. coli* were purchased from New England Biolab, Inc. Chemically competent cells were also made in our lab from the commercial competent cells. 3-[(3-cholamidopropyl)-dimethyl-ammonio]-1-propanesulfonate (CHAPS) was purchased from AMRESCO (Solon, OH). HS-CoM was from Merck. 7-Bromoheptanoic acid was purchased from Karl Industries Inc. Q-sepharose, S-300 Sephacryl, Phenol Sepharose and PD-10 columns were purchased from GE Healthcare. Centricon ultrafiltration units were from Millipore (Bedford, MA).

Anaerobic buffers were used for all purifications. Particles were removed by filtering through a 0.22 μm filter. Buffers were boiled under constant flow of nitrogen gas and stirred under vacuum for a period of 2-4 h. Buffers were stored in stoppered bottles and pressurized with N_2 or Ar gas and can stay oxygen free for 2-3 months. A 200 mM Ti(III) citrate solution was prepared by dissolving Ti(III) chloride powder in 250 mM sodium citrate under strictly anoxic conditions.

2.2.2 Synthesis of 2-Methylthioethane Sulfonate (Methyl-coenzyme M)

Methyl-coenzyme M was synthesized from commercially purchased coenzyme M (2-mercaptoethanesulfonate) by methylation with methyl iodide as described in the literature.[84] 3 mmol of coenzyme M was incubated for 12 h with 6 mmol of methyliodide in 5 mL of a 33% aqueous ammonia solution under a 100% N_2 atmosphere. After incubation for 12 h at room temperature the reaction mixture was evaporated to almost dryness and lyophilized. The dry yellow residue was dissolved in 10 ml distilled water. Aliquots of the solution of 5-mL were loaded on a Q-Sepharose column (volume 30 mL) and a linear gradient of 0 to 1 M ammonium carbonate was applied for elution. Ammonium carbonate was used instead of hydrochloric acid to elute methyl-coenzyme M from the Q-Sepharose column since methyl-coenzyme M in the non-dissociated sulfonic acid form and water produce an azeotropic mixture. Methyl-coenzyme M generally eluted from the column between 250-350 mM ammonium carbonate. Fractions containing methyl-coenzyme M were combined and lyophilized to remove the ammonium carbonate. Subsequently, the lyophilized powder was heated to 60 °C to remove remaining traces of iodine. Eluate was collected and tested for methyl-coenzyme M by thin layer chromatography (TLC) on Kieselgel 60 F_{254} with butanol/acetic acid/water (2:1:1) as the mobile phase. TLC plate was further developed with 1% $KMnO_4$ and Na_2CO_3. In the presence of developer, the whole plate turned purple with yellow band indicating the position of methyl-coenzyme M. Generally, 1.5 g of a dry white powder was obtained at the end of the procedure.

2.2.3 Strain and growth conditions

M. maripaludis strain S2 was grown at 37 ^oC. *M. okinawensis* strain IH1 was grown at 60 ^oC. Cell cultures were grown in mineral rich media (McFC, McF plus 10 mM sodium acetate and 2 g/l casamino acids) with 0.4 M sodium formate as the electron donor and buffered with glycylglycine pH 8 for *M. maripaludis* and pH 6.5 for *M. okinawensis*. The head space was pressurized to104 kPa with N_2/CO_2. 1.25 ug mL^{-1} or 2.5 ug mL^{-1} puromycine was added for recombinant strains.

2.2.4 Purification of native methyl-coenzyme M reductase

Wild-type *M. maripaludis* S2 was grown in 3.0 L of McFC medium anaerobically. Once the culture reached an absorbance of 0.8 measured at 600 nm, the bottles containing the culture were transferred into an anaerobic tent and cells were harvested anaerobically by centrifugation at 17,700 x g for 15 min at 4 ^{o}C. The pellets were suspended in an MCR buffer [10mM Ti(III) citrate, 10 mM coenzyme M, 0.1 mM methylviologen in 150 mM monosodium phosphate (pH 8.0)]. 2 ml of buffer was used for each gram of wet cells and suspended cells were stored at -20 ^{o}C if not used immediately for purification. The cells were thawed on ice, lysed by sonicated for a total of 3 min intermittently at 20 % amplitude on ice, and the mixture was centrifuged (30,000 rpm, 20 min) to remove cell debris. The supernatant was collected and 100% $(NH_4)_2SO_4$ was added slowly to make the solution 50%. The mixtue was then centrifuged for 20 min. Granular $(NH_4)_2SO_4$ was added to the supernatant on ice until 100% saturation. After centrifugation for 20 min at 30,000 rpm, the pellets were resuspended with 10 mM Tris-HCl plus 1 mM HS-CoM (buffer A) and loaded on an anion-exchange column (Mono-Q). The protein was eluted with a linear gradient of 0% to 50% buffer A containing 2 M NaCl (buffer B).

2.2.5 Heterologous expression and purification of recMCR

Cloning of MCR from *M. okinawensis* and *M. maripaludis* were carried out by the Whitman lab. The procedure of recMCR expression is presented below briefly.

The complete *mcrBDCGA* operon was amplified from the chromosomal DNA of *M. okinawensis* 1H1 using the primers 5’-GGGAAAATGCATGGTAAAGTATG AAAGTATGAAGATAAGATAAATTTGTATGA-3 (NsiI site is underlined) and 5’-GGGAAATCTAGATTAGTGATGGTGATGGTGATGATGTGCAGGAATGATTGGGTC-3’ (XbaI and 6 x His-tag are underlined). The product was cloned into PAW42 using NsiI/XbaI restriction sites. The coding region of *M. maripaludis* MCR operon was amplified using the primers 5’-GGGAAATCTAGA*AATAGGTGAAATGC*ATGGTAAAGTATGAAGATAAGATAAGTTTGTACG-3’ (*XbaI* site is underlined and ribosomal binding site (RB) is italicized) and 5’-GCAGCGGCCGCTTA*ATGGTGATGGTGATGGTG*TTTAGCAGGTAAGATAACGTCTCTTTCT-3’ (*Not*I site is underlined and 6 × his-tag is italicized). The product was cloned into PMEV4 using XbaI/NotI restriction sites, resulting in the expression plasmid pMEV4-MCR. The recombinant plasmid was confirmed by sequencing before being transformed into *M. maripaludis* S0001. After transformation, 0.6 to 2 ml of cells were spread on to McCv or McCF agar slabs in serum bottles containing 2.5 µg/ml of puromycin. The McCF bottles were pressurized to 104 kPa with N_2/CO_2 (4:1, v/v). After incubation at 37 ^{o}C for 5 days, puromycin-resistant colonies were picked into 5 ml of McCV or McCF medium supplemented with puromycin (2.5 µg/mL) in 28 mL Batch tubes. The McCV or McCF tubes were pressurized to 276 kPa with N_2/CO_2. The cultures were grown at 37 ^{o}C until an OD600 of 0.6 was reached. A 30 % (v/v) glycerol stock solution was prepared in a sterile centrifuge tube and stored at -80 ^{o}C until use.

2.2.6 Purification and fractionation of MCR from recombinant strain.

M. maripaludis S0001 hosting the recMCR was grown anaerobically in McCV medium containing 2.5 µl/mg puromycin. After the culture reached an OD600 of 0.6, the cells were harvested inside the tent. The cell pellets were resusupended in MCR buffer and lyzed by sonication as described above. The sonicated mixture was then centrifugation at 30,000 rpm for 30 min at 4 ^{o}C. The supernatant was filtered through a 0.2 µm syringe filter and loaded onto a 5 ml Ni-Sepharose column (GE Healthcare) connected to the Akta Pure FPLC system. The protein was eluted using a linear imidazole gradient from 0 % to 100% (100mM NaCl plus 500 mM imidazolium, pH 7.6). The fraction containing recMCR were pooled, collected, and washed with buffer A (100 mM NaCl, pH 7.6) and concentrated to 10 mL before loading onto a MonoQ column. The enzyme was then eluted with a linear gradient from 0 to 1 M NaCl in buffer A.

2.2.7 Characterizing recombinant MCR from *M. okinawensis* (recMCRok)

The fractions from the Mono-Q anion exchange were characterized using Uv-vis absorption spectroscopy. Moreover, CD spectroscopy was performed to see if there is any difference in two fractions obtained after the MonoQ column step. Furthermore, the purity of MCR in each fraction was assessed by SDS PAGE gel using Coomassie staining and the intensity and the ratio of the bands in the gel (subunits) were quantified using Image J.

At each step of the purification, protein concentrations were determined by a Bio-Rad protein assay based on the method of Bradford according to the manufacturer instructions. For colored fractions, the F_{430} content was measured from the absorbance using an extinction coefficient of 44,000 $M^{-1}cm^{-1}$ for MCR (the extinction coefficient of F_{430} is 22.000 $M^{-1}cm^{-1}$).

MALDI and LC MS/MS analysis of peptides

The MCR subunits were separated on SDS gel and stained with AcquaStain (Bulldog Bio) for 2 to 10 min until protein bands appeared. The gel was then washed with ddH_20, and a gel plug containing one of the methyl-coenzyme M reductase subunits was excised and destained twice in 30% of ethanol before being processed for mass spectrometry. After removing the supernatant, 80 µl of 755 acetonitrile was added for 15 min, and the plugs were placed in a 38 ^oC oven for 20 min. the plugs were next treated with DTT (80 µl of 8 mg in 1 mL of 20 mM ammonium bicarbonate) for 1 h at 38 ^oC. The supernatant was removed, and 80 µl of an iodoacetamide solution was added (18.3 mg of iodoacetamide in 1 mL of 20 mM ammonium bicarbonate). After incubating the mixture for 30 min at room temperature in the dark, the supernatants were removed, and the plugs were washed with 80 µl of 50 mM ammonium bicarbonate containing 50% methanol for 20 min and then 80 ul of 75 % acetonitrile for 20 min. The supernatants were discarded, and the plug was dried at 38 ^{o}C for 20 min.

For proteolytic digestion, either 0.3 µg mass spectrometry grade trypsin (Promega gold) in 30 µl of 20 mM ammonium bicarbonate or 50 ng of pepsin (Promega) in 25 µl of 40 mM HCl was added to the plugs in microfuge tubes. The tubes were incubated at 38 ^{o}C for 22 h (trypsin) or 48 h (pepsin). The supernatants were then removed and 50 µl of 50:50 acetonitrile: 0.1% trifluoracetic acid was added to the plugs. After 20 min, the supernatants were removed and pooled with previous supernatants, and 70 µl more of the 50:50 acetonitrile: 0.1 % trifluoroacetic acid solutions were added. After 20 min, the supernatants were again pooled.

For MALDI, the pooled supernatant solutions were brought to dryness in a SpeedVac and resuspended in 1-2 µl of 20% acetonitrile plus 1% formic acid prior to spotting on the plate. Matrix, 0.8 µl of 1.5 mg of DHB in 50:50 water: acetonitrile with 1% formic acid, was added, and the spot was allowed to dry. The samples were analyzed using a Bruker Daultonics Autoflex in reflection mode. The data was internally calibrated using trypsin autodigestion peaks if present, and if not, then a statistical calibration was applied. Mascot by MatrixScience was used to analyze the data by searching against the NCBInr data base with Cys carbamidomethylation selected as a fixed modification and Met oxidation as a variable modification. The peptide tolerance was set to 0.2 Da, and the number of missed cleavages was one.

For LC_MS/MS, following the elution from the gel plugs, the peptides were loaded onto a reversed-phase column (Dionex PepMap 100C8 or self-packed column/emitter with 200 A 5 uM Bruker MagicAQ C18 resin) with a Proxeon Easy NanoLC system (Waltham, MA) and directly eluted into a Thermo-Fisher LTQ Orbitrap Elite Mass Spectrometer at the Proteomics and Mass Spectrometry Facility, University of Georgia. Briefly, the two-buffer gradient elution (0.1% formic acid as buffer A and 99.9 5 acetonitrile with 0.1 formic acid as buffer B) started with 5 % B for 2 min, then increased to 2 % B in 60 min, 40 % B in 10 min, and 95% B in 10 min. A survey MS scan was acquired first, and then the top 5 ions in the MS scan were selected for Collision-induced dissociation (CID) and high-energy collisional dissociation (HCD) MS/MS analysis. When necessary, electron-transfer dissociation (ETD) was used instead of CID for better identification of post-translational modification (30). Both MS and MS/MS scans were acquired by Orbitrap at the resolution of 120,000 and 30,000, respectively. Data was acquired using Xcalibur software (version 2.2 Thermo Fisher Scientific). Protein identification and modification characterization were performed using Thermo Proteome Discovery (version 1.3/1.4) with Mascot (Matrix Science) or SEQUEST (Termo) programs. The spectra of modified peptides were inspected further to certify the accuracy of the assignments.

2.2.8 F_{430} extraction and analysis

M. maripaludis cells with and without the recMCR were grown in 1.5 L of McFC medium (formate medium containing casamino acid) in a 2 L Bottle. Once the absorbance at 600 nm reached 0.6 for *M. maripaludis* with the recMCR and 0.8, for wild type *M. maripaludis*, the cells were harvested anaerobically inside the tent. After sonication and centrifugation, the recMCR was purified using Ni-Sepharose as described above. Native MCR was separated from the flow through using the Amicon Ultra-4 centrifugal filter (100 kDa). MCR is about 300 kDa and thus could not pass through the filter and stays with the residue, while the free F_{430} passes through the Amicon Ultra-4 centrifugal filter. To dissociate F_{430} from other hypothetical chaperone proteins (other than MCR), and to remove small proteins, the flow through containing F_{430} was treated with methanol, ethanol, boiling, or methanol and boiling as described in the literature with some modifications.[74] The precipitated proteins were separated by centrifugation, and the supernatant containing free F_{430} was analyzed using HPLC coupled to a Uv-vis detector. Bound F_{430} was extracted from purified MCR using 100% methanol. 6 ml of 100% methanol was added to each mL of MCR solution and the precipitated enzyme was removed by centrifugation. The supernatant was concentrated using a continuous flow of nitrogen gas or by using a rotavapor at a temperature of 50 ^{o}C. The F_{430} was then analyzed on an HPLC.

High-performance liquid chromatography (HPLC)

Reversed-phase HPLC analysis was performed on an Agilent 1260 Infinity Quaternary LC System equipped with a Diode Array Detector (DAD) VL+ and an Agilent Poroshel 120 EC-C18 (4.6 x 150 mm, 2.7 um) column. The Agilent OpenLAB ChemStation Edition software was used for data analysis. The chromatography method utilized for characterization of the F_{430} biosynthesis consists the following gradient of water (solvent A) and acetonitrile (solvent B), each containing 0.5 % formic acid: 0% B for 2 min, 0-20% B over 3 min, 20% B for 5 min, 20-25% B over 5 min, 25% B for 5 min, 25-30% B over 5 min, 30-100% B over 5 min. The flow rate was set at 1.0 mL/min and the chromatogram was acquired following the absorbance at 400 nm.

2.2.9 Plasmid Construction for McrD and CfbE expression

The genomic DNA of *M. okinawensis* was extracted using a DNA extraction kit. The *mcrD* genes were amplified from the genomic DNA of *M. okinawensis*. Primers were from Sigma-Aldrich and their sequences are provided in Table 2.1. Phusion High-Fedelity DNA Polymerase (New England Biolabs) was utilized for all PCR reaction in accordance with the manufacturer's protocol.

	Forward primer	Reverse primer
cfbE	5′-ATATACATATGCTTATAATCGATGTAAATC-3′	5′-ATATACTCGAGTTAATTTATAGCTTTTCTATATATTATC-3′
mcrD	5′-ATATACATATGATAGAAATAGAAGTCTTCCCC-3′	5′-ATATACTCGAGTTACTTTTCTTTTTCATCCTTTTC-3′

Table 2.1 Primers used for PCR. The restriction enzymes site (*NdeI* and *XhoI*) are underlined

The PCR products were purified from an agarose gel and double digested using the appropriate restriction enzymes (NdeI/XboI, New England Biolabs). Likewise, the vector was cut at the restriction enzymes sites using the same restriction enzyme. The digested PCR product was cloned into the pET-28b(+) vector (Novagen) using T4 DNA ligase for heterologous expression in *E. coli*. The ligated product was transformed into TOP10 following the guidelines provide from the manufacturer (New England Biolab). The transformation mixtures were spread on a pre-warmed LB agar plates containing 50 µg/mL of kanamycin and incubated overnight at 37 ^{o}C. Kanamycin-resistant colonies were picked and placed into 5 ml of LB medium supplemented with Kanamycin (50 µg/mL) in 15 mL tubes and incubated overnight at 37 ^{o}C and the plasmid was prepared. The sequences of the cloned genes within each of the constructed plasmid were verified by sequencing by Eurofins Scientific. Each of the recombinant proteins thus produced contained a thrombin-cleavable 6-His-tag incorporated at the N-terminus for purification using immobilized Ni-sepharose chromatography (IMAC). The cultures were grown at 37 ^oC until an OD measured at 600 nm of 0.6 was reached. A 30 % (v/v) glycerol stock solution was prepared in a sterile centrifuge tube and stored at -80 ^oC until use.

2.2.10 Expression and Purification of McrD and CfbE

After confirming the inserts in the expression vector by sequencing, the plasmid DNA (*mcrD* and *cfbE* containing pET-28b(+) vector) were transformed to *E. coli* BL21 (DE3) following the protocol supplied by the company. The transformation mixture was then spread onto the selection plate (kanamycin plate) and incubated overnight at 37 ^oC.

The recombinant McrD and CfbE in BL21 *E. coli* were grown in LB medium containing 50 µg/mL Kanamycin at 37 ^oC in a shaker/incubator set to 250 rpm. After the culture reached an OD600 of ~ 0.4, the cells were induced using 40 µM isopropyl B-D-thiogalactoside (IPTG) and further incubated for 4-6 h or until the OD_{600} reached ~3.00. For CfbE expression the growth temperature was reduced to 18 ^oC after IBTG addition followed by overnight incubation. Moreover, the LB medium contained 10 % glycerol. When the culture reached the desired OD, the cells were harvested by centrifugation at 10,000 rpm, 4 ^oC for 20 min and stored at -80 ^oC until further use. The cell pellets were thawed on ice and resusupended in buffer containing 50 mM Tris HCl (pH 7.6) and lyzed by sonication at 70% amplitude for a total of 7 min. The sonicated mixture was then centrifugation at 30,000 rpm for 30 min at 4 ^oC. The supernatant was filtered through a 0.2 um syringe filter and loaded on a 5 ml Ni-Sepharose column (GE Healthcare) connected to the Akta Pure FPLC system. The protein was eluted using a linear imidazole gradient from 0% to 100% in buffer B (100 mM NaCl plus 500 mM imidazolium, pH 7.6). The fractions containing McrD *or* CfbE were pooled, collected, and washed with buffer A

(100 mM NaCl, pH 7.6) and stored at -30 ^{o}C. The purity of recombinant proteins was assessed by SDS-PAGE and concentration was measured using the Bradford protein assay.

2.2.11 Activation and activity of MCR

Treatment of cells with 100% H_2

The formate grown cells were treated with 100% H_2 before harvesting for 20 min. Once the cells were cooled to 4 ^{o}C they were harvested anaerobically. The pellets were resuspended in a small volume of growth medium, and an EPR sample was taken inside the tent. A methane assay was also performed with the cell extract.

Treatment of cells with formate

A similar protocol to the *100% H_2* treatment was followed to induce MCRred1using formate. 20 mM formate was added to the formate grown cells and incubated for 30 min or overnight. The cell culture was harvested, and the pellets were resusupended in small volume of growth medium. EPR samples were then taken anaerobically and methane production was measured with GC.

Treatment of cells with Na_2S

To induce the MCRox1 form and later activate to the MCRred1, *M. maripaludis* and *M. okinawensis* cells were grown in 3 L formate media. 20 mM (final concentration) of Na_2S was added to the culture before harvesting and further incubated for 1 h at 37 ^{o}C and 60 ^{o}C for *maripaludis* and *okinawensis* cells, respectively. The cell cultures were cooled on ice, transferred to the tent, and harvested anaerobically. The pellets were suspended in MCR buffer containing Ti(III) citrate and methyl-viologen (2 ml buffer was used for each g of wet cell).

MCRox1 Activation

MCRox1 was activated by incubating the cell extract or purified MCRox1 at 37 °C for MCR from *M. maripaludis* and 60 °C for MCR from *M. okinawensis* for 30 min in a solution (0.2 ml total volume) containing 200 mM CHES (pH 9.0). 20 mM Ti(III) citrate, and 20 mM CH_3-SCoM. The activation mixture was cooled to 4 °C and 0.14 mL of 2 M MOPS (pH 6.5) was added before the activity assay was performed.

2.2.12 Activity Assays

CfbE assay

The F_{430} was assayed by adding 40 µl of 1.4 mg/mL solution of CfbE, 1.0 µl of 200 mM solution of Mg-ATP, 2.5 µl of 500 mM solution of phosphoenol pyruvate (PEP), and 2 units of pyruvate kinase (PK) to 80 µl of 15,173-seco-F_{430}-173-acid reaction mixture and subsequent incubation for 12 hours at 55 °C. The reaction was carried out in a MBRAUN LABmaster Glove Box Workstation under a N_2 atmosphere containing less than 0.1 ppm O_2.[85]

McrD assay

No standard assay for McrD is available, however, the McrD was found to push forward the CfbE reaction in the biosynthesis of F_{430}. Thus, activity of McrD was assessed by adding 20 µl of 2.6 mg/mL solution of McrD to the CfbE reaction mixture and subsequent incubation for 12 hours at 55 °C. After the assays were completed, the reaction mixtures were quenched with an equal volume of methanol and centrifuged at 6,153 x g for 20 min. The pellets containing precipitated protein and insoluble material was discarded and the supernatants were saved for HPLC analysis. Seco- F_{430} was also used as standard.

2.2.12 Spectroscopic measurements

Uv-visible spectroscopy

UV-visible spectra of MCR were recorded with a diode array Uv-Vis spectroscopy (Agilant 8453)

Circular Dichroism (CD)

To test the difference in the folding pattern of the two forms of the recombinant MCRok, CD spectroscopy (Jasco J-810 spectropolarimeter Easton, MD) was performed. The CD Spectra for both fractions was recorded after exchanging the buffer from Tris-HCl to 10 mM potassium phosphate buffer (pH 8.0). CD data were collected from 190 to 300 nm. Each CD spectrum is the average of 8 runs.

EPR spectroscopy

Continues wave (CW) EPR spectra were measured at X-band (9 GHz) frequency on a Bruker EMX spectrometer, fitted with the ER-4119-HS high sensitivity perpendicular-mode cavity. The Oxford Instrument ESR 900 flow cryostat in combination with the ITC4 temperature controller was used for measurements in the 4 K to 300 K range using a helium flow. Most of the EPR spectra were performed at 77 K by fitting the cavity with a liquid nitrogen finger Dewar. A field modulation frequency of 100 kHz, modulation amplitude of 0.6 mT, and a frequency of 9.386 GHz were used for all measurements.

The EPR signal intensities were determined by measuring the respective EPR-active species under nonsaturating conditions. The signals in EPR spectra represent the first derivative of the absorption-type signal. The spectra were double integrated and compared with that of a 10 mM copper perchlorate standard (10 mM $CuSO_4$; 2 M NaClO4; 10 mM HCl) in order to calculate the concentration of EPR-active MCR. The amount of the EPR-inactive form, MCRsilent, was calculated as the difference between the concentrations of total MCR obtained from Uv-vis absorption spectroscopy and/or from Bradford protein determination and the concentration of paramagnetic species calculated from the double integration procedure for the MCRred1 or the MCRox1 signals.

Determination of methyl-coenzyme-M reductase activity

Activity of MCR was determined by methane production. Methane formation was detected by withdrawing 100 µl gas samples from the headspace of a sealed off bottle containing 600-800 µl assay solution. The solution contained 10 mM methyl-coenzyme M, 1 mM coenzyme B, 0.3 mM aquocobalamin, 30 mM Ti(III) citrate, and variable amounts of purified MCR. The assay solution was kept on ice until the reaction was initiated by placing the sample in a water bath with the desired temperature.

2.3 Result and Discussion

2.3.1 Synthesis of 2-Methylthioethane Sulfonate (Methyl-coenzyme M)

After separation on the Q-sepharose column, MCoM was detected by thin layer chromatography (TLC) plates Silica Gel 60 with butanol/acetic acid/water (2:1:1). TLC plates were developed with 1% $KMnO_4/Na_2CO_3$. Fractions containing CH_3-CoM were lyophilized and further analyzed by ^{1}H NMR (Figure 2.2). The purity and concentration of CH_3-CoM was measured as compared to an internal standard, 1,4-dioxane.

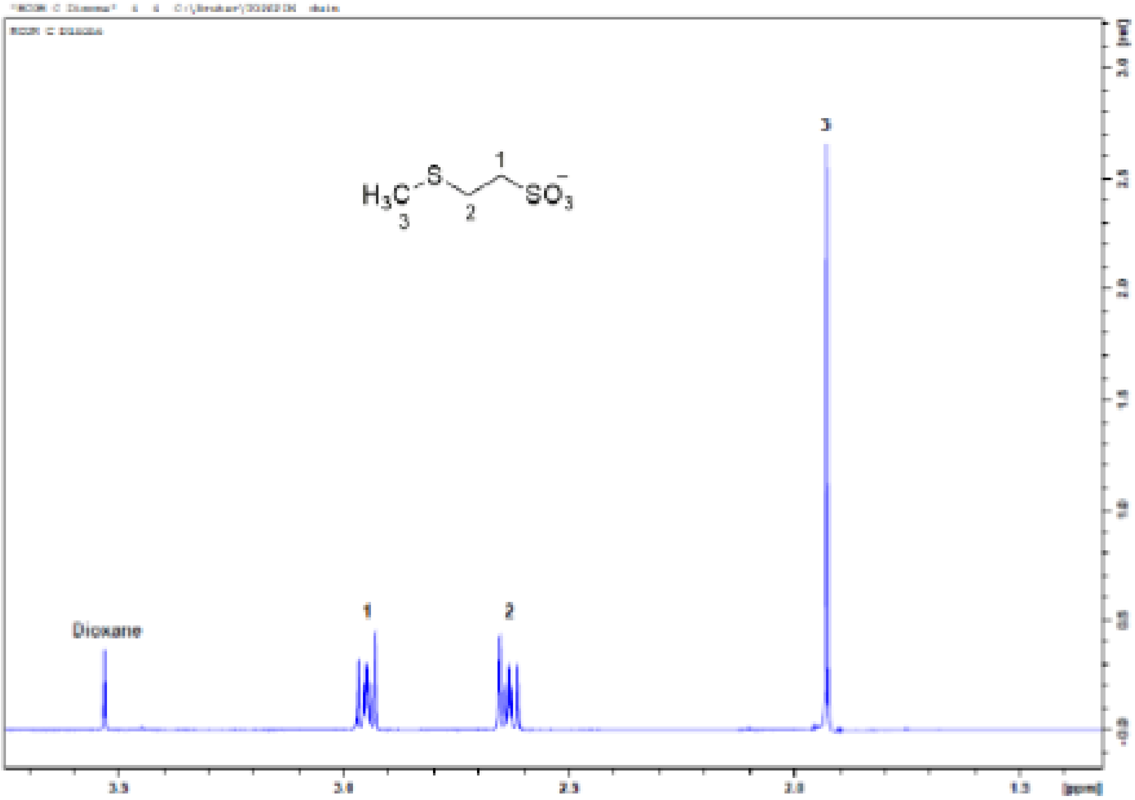

Figure 2.2. Proton NMR of Methyl-coenzyme M

2.3.2 Characterizing recombinant MCR_{ok}

The *M. okinawensis MCR* operon was cloned with a 6xhistidine tag at the C-terminus of *McrA*, as this site was exposed to the outer surface of the enzyme. The *M. okinawensis* gene is similar to the host gene from *M. maripaludis* with 65-87 % identity. It was first attempted to clone MCR from *M. marburgensis,* an organism that is extensively studied, however, the cloning was unsuccessful. Thus, a close relative of the host, *M. okinawensis*, was selected as an alternative, and MCRok was successfully cloned and overexpressed in *M. maripaludis.* The enzyme was purified on a Ni-Sepharose column. SDS-PAGE analysis of the Ni-Sepharose purified fraction revealed the presence of McrD (Figure 2.5) which normally is not tightly bound to the MCR complex and does not co-purify with wild type MCR.

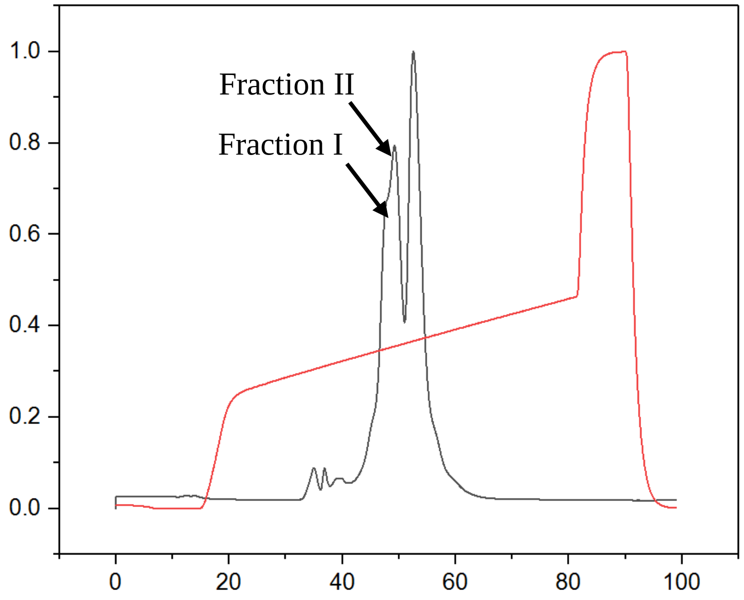

Figure 2.3. FPLC chromatogram for recMCRok on the MonoQ column

The fraction was then further purified on a MonoQ anion exchange column. The recMCRok eluted into two fractions (Figure 2.3). Figure 2.4 and Figure 2.5 show the UV-vis and the SDS-PAGE of the two MonoQ fractions of recMCR*ok*. One fraction (fraction II) contained the expected subunits of MCR. i.e. subunits A, B, and G with fully inserted F_{430} but not McrD. It should be noted that the faint McrD band in fraction II is probably a contaminant from the adjacent fraction as the two fractions overlapped in the purification profile (Figure 2.3). Fraction II was yellow in color due to the presence of F_{430} and it had an absorption maximum at around 430 (Figure 2.4). The other fraction (fraction I) was a colorless fraction and does not show a peak around 430 nm implying it lacks the cofactor F_{430}. Fraction I, however, contains McrD in addition to the expected three subunits of MCR (MCRABG) (Figure 2.5).

F_{430} has a typical absorption maximum at 420 nm when bound to MCR. The shape of the peak (with a shoulder at 445 nm) is particularly for the MCRsilent form of the enzyme which is the stable, but inactive form of the enzyme.

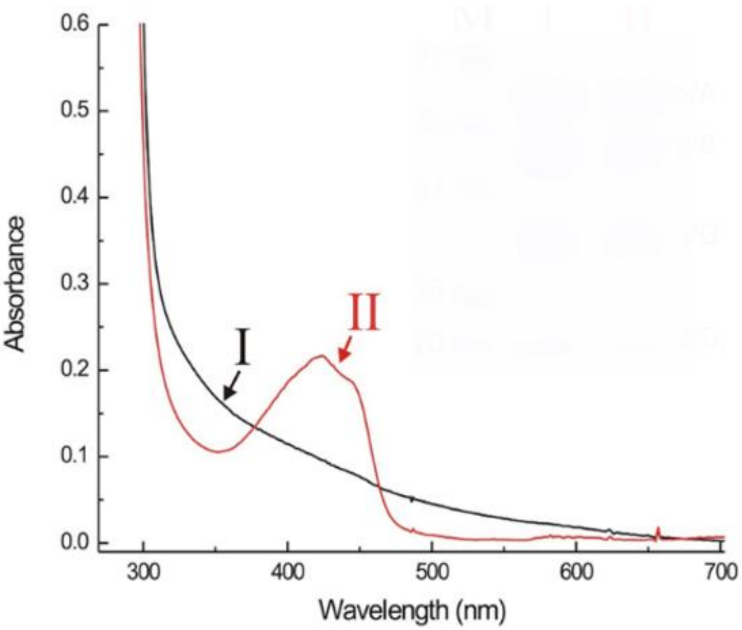

Figure 2.4. Absorption spectra for the recombinant MCR*ok* purified by nickel affinity and ion-exchange chromatography (MonoQ). The colorless fraction (I) and the colored fraction (II) were collected after the MonoQ column step

Analysis of the intensity of coomassie stained bands in the SDS-PAGE using image J, showed a stoichiometry ratio of A:B:G:D close to 1:1:1:0.5 for the fraction without the cofactor but containing McrD. The other fraction apparently have no McrD and as expected the ratio of A:B:G to the subunits are close to 1:1:1. Moreover Bradford protein concentration determination with Bovine serum albumin (BSA) standard gives almost similar values for both fractions. Usually around 3 mg of total recMCRok was purified from 3 L cell culture.

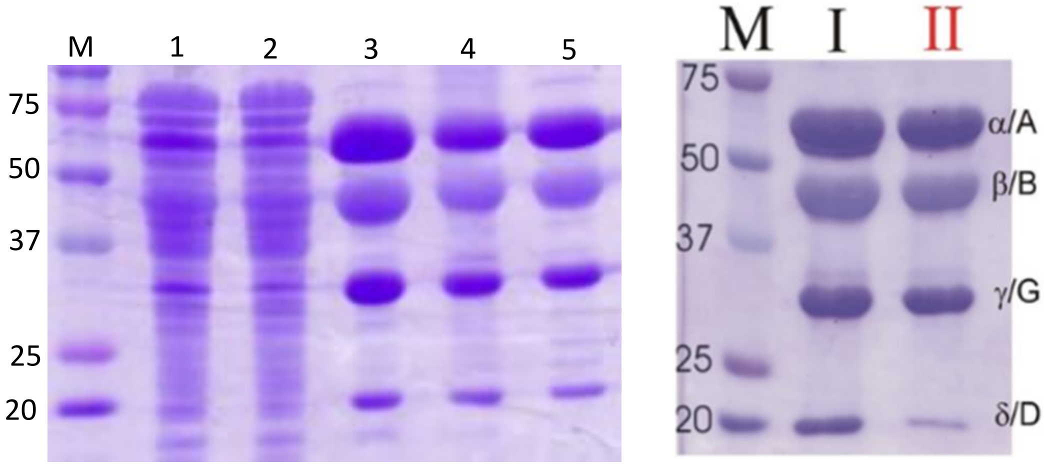

Figure 2.5. SDS-PAGE gel analysis of recMCRok. Left panel after Ni-sepharose and right pannel after MonoQ column. Lane 1; cell extract, 2; flowthrough, 3-5 Ni-column purified recMCR.

Circular dichroism (CD) spectroscopic measurements were also performed to see if the two fractions have different folding patterns. The CD result did not show significant difference in the pattern of folding between the two fractions (Figure 2.6). To our understanding this is the first time the recombinant halo enzyme is purified.

The above results rise several questions which some of them are discussed in the following paragraphs. Could there be a chimeric mixing of MCR from the host and the guest during transcription, translation, and/or maturation of the enzymes? Why did the enzyme purify in two forms, one with MCRABDG and one with MCRABG and F_{430}? What is the role of McrD and why did McrD show up in the fraction where coenzyme F_{430} was not present, but not in the other fraction? What is the reason for the lack of F_{430} in fraction I? Could it be a shortage of F_{430} in the host cell?

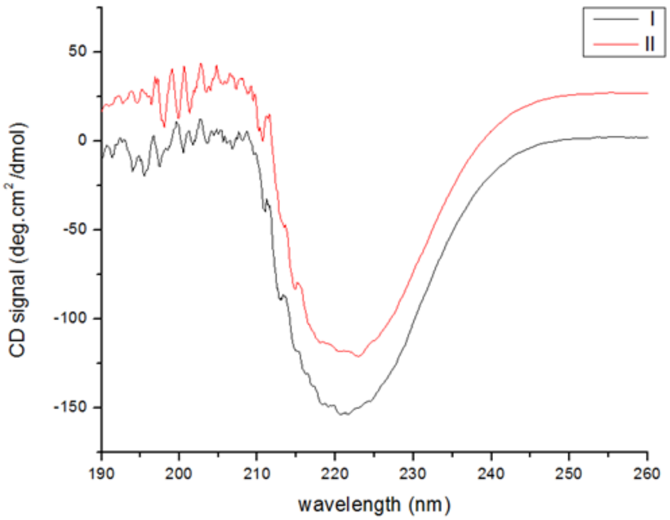

Figure 2.6. Circular dichroism spectra for the recMCR*ok* purified on Nickel-Sepharose and ion-exchange (MonoQ) column chromatography. The colorless fractions (I) and the colored fractions (II) collected after MonoQ step.

The result of MALDI MS of the purified recMCR is given in Figure 2.7 and Table 2.2 shows the summary of the PTMs result for the wild type and recombinant MCR. The presence of MCR subunits from *maripaludis* were negligible in $recMCR_{ok}$ implying recMCRok was assembled from co-transcribed and co-translated subunits. As shown in the table 2.2 the PTMs of wild type *M. maripaludis* and *M. okinawensis* are similar. All the four modification were present. Moreover, the modification of recMCRok was the same as that of wild type *M. okinawenis* MCR.

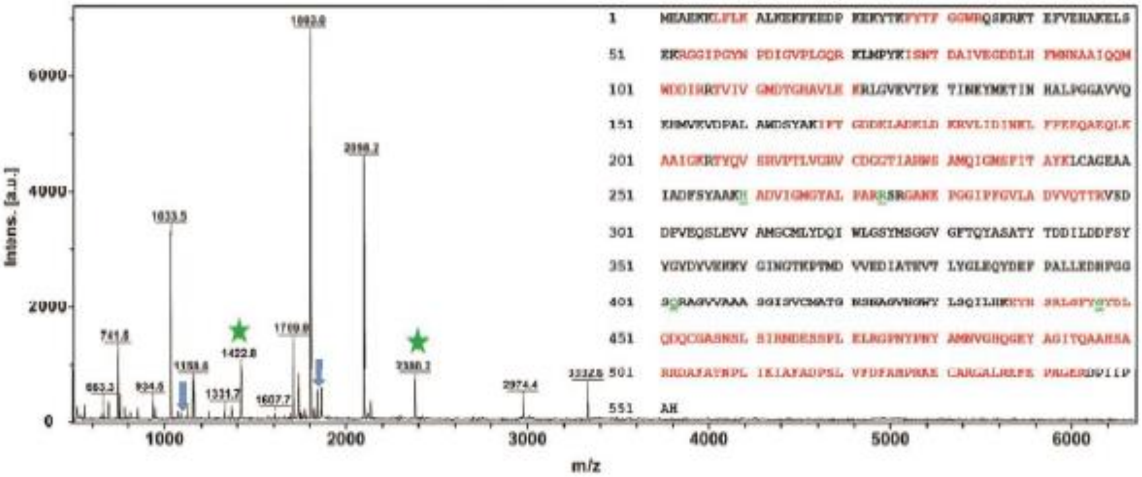

Figure 2.7. Analysis of the major PTMs, in the MCRA from *M. maripaludis* and *M. okinawensis* using LC MS/MS spectra of the digested peptides.[83]

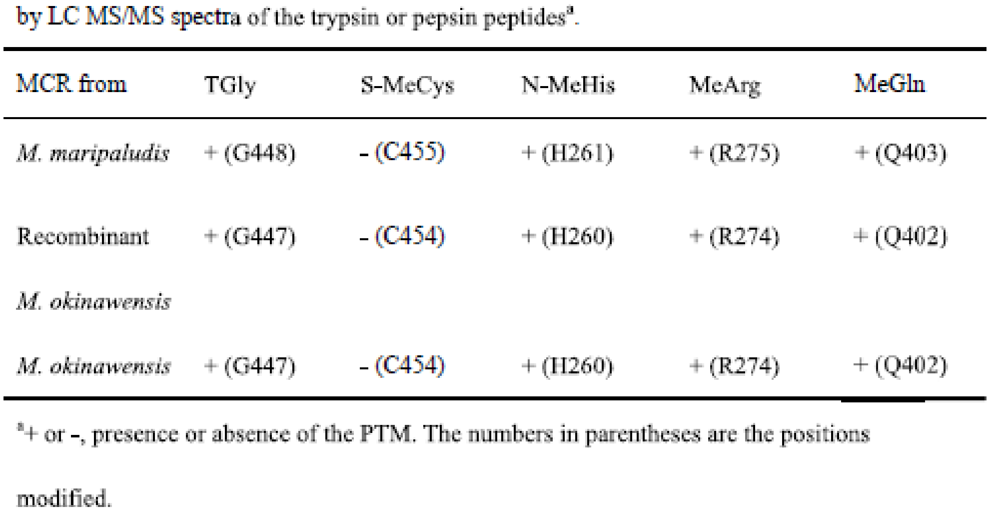

by LC MS/MS spectra of the trypsin or pepsin peptides[a].

MCR from	TGly	S-MeCys	N-MeHis	MeArg	MeGln
M. maripaludis	+ (G448)	- (C455)	+ (H261)	+ (R275)	+ (Q403)
Recombinant *M. okinawensis*	+ (G447)	- (C454)	+ (H260)	+ (R274)	+ (Q402)
M. okinawensis	+ (G447)	- (C454)	+ (H260)	+ (R274)	+ (Q402)

[a]+ or -, presence or absence of the PTM. The numbers in parentheses are the positions modified.

Table 2.2. Summary of the analysis of the PTMs, in the MCRA from *M. maripaludis* and *M. okinawensis* using LC MS/MS spectra of the digested peptides.[83]

When purified without exposure to O_2, the recMCR$_{ok}$ possessed very low activity in the methane production assay, 0.082 U/mg. The assay was performed by incubating recMCRok at

60 ^oC, which is the optimal temperature for *M. okinawensis* growth but well above the growth temperature range of the mesophilic *M. maripaludis*. This activity was much less than the expected specific activity for the fully active MCR of 100 U/mg (established activity of MCR from *M. marburgensis*). It should be noted, however, the activity of MCR in *M. okinawensis* may be different (lower than) from *M. marburgensis*. It is not known, to our knowledge, the activity of native MCR from *M. okinawensis*. Nevertheless, EPR failed to detect the MCRred1 signal. However, because MCR is notoriously unstable in its purified form, it was not possible to conclude that the recMCR$_{ok}$ was inactive *in vivo*. But the native MCR from *M. maripaludis* seems to have some activity as the cell extract showed substantial activity. The activity of cell extract increased with the addition of A2 from *M. okinawensis*, an ATP hydrolysis protein known to activate MCR together with the activating complex *in vivo*. Figure 2.8 also shows the activity from freshly purified and purified from frozen cells. No difference, however, was observed between the fresh and frozen cells. Furthermore, addition of recMCRok to the cell extract did not increase the production of methane. This implies that the recMCRok was not activated in this experiment by the cell extracts of *M. maripaludis* and all the activity observed in the cell extract is from the action of native MCR from *M. maripaludis* and not from recMCRok. Therefore, development of an activation protocol pertaining to the recMCRok will be necessary if we want to be able to study the effect of variant enzyme on enzyme activity.

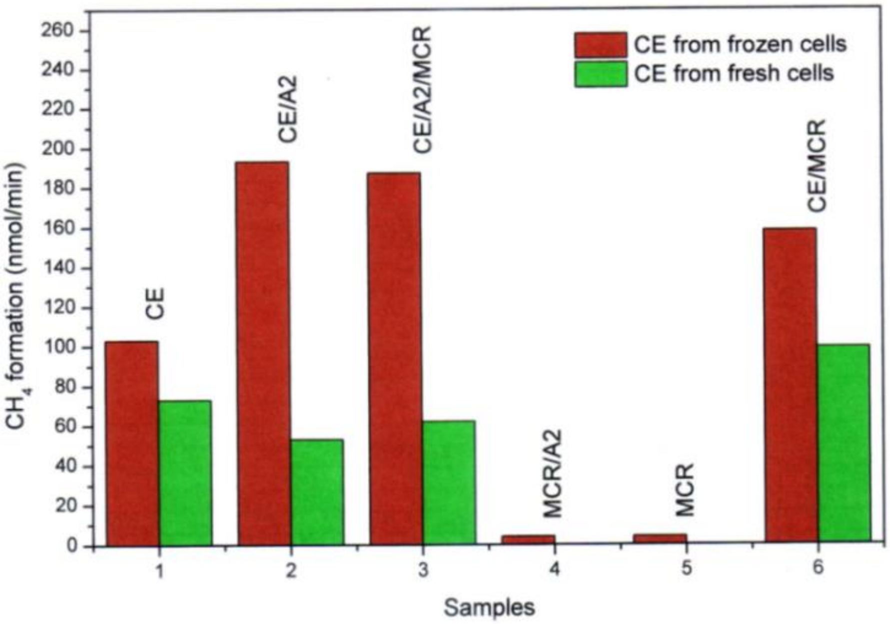

Figure 2.8. Methane production assay of CE and purified recMCRok.

2.3.3 Purification of component A2

The *M. okinawensis* A2 protein was overexpressed in *E. coli* and purified from the cell extract using a Ni-sepharose column. The purity of the protein was determined by SDS-PAGE which showed some additional bands. To get more pure protein, the Ni-Sepharose fractions of A2 were collected and further purified on Superdex (size exclusion) column (Figure 2.9). A single band was then obtained on the SDS-PAGE after this step. The protein concentration was determined by the Bradford assay and by using the extinction coefficient for (A_{280}) for the A2 protein (44,725 $M^{-1}cm^{-1}$).

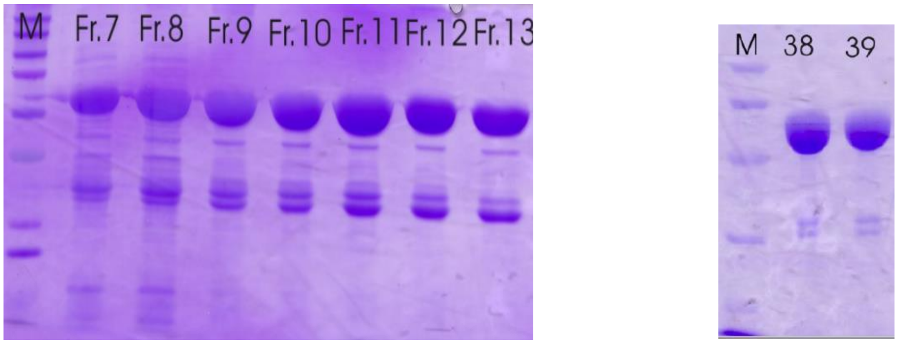

Figure 2.9. SDS-PAGE of A2 after Ni-sepharose (left) and superdex (right) column

2.3.4 *In vivo* and *in vitro* activation of recombinant MCRok

The purified recombinant MCRok contains about 50% F_{430}. Moreover, the recMCRok is properly assembled and contains all the PTMs found in the native enzyme from *M. maripaludis*. However, the enzyme shows very low activity even with strict exclusion of oxygen during harvesting and purification. This would hinder to perform studies related to the catalytic mechanism of the enzyme using the recombinant enzyme. Thus, in order to proceed with the studies, a significant amount of the recMCR has to be activated. Different approaches have been followed to activate the recombinant enzyme.

Thauer and coworkers developed a protocol to induce MCRred1from using the *M. marburgensis* strain, a well-studied Archaea grown on H_2/CO_2. They showed that MCRred1 could be induced by switching the gas phase from 80%/20% H_2/CO_2 to 100 % H_2 before harvesting and treating the cells with hydrogen for 20 min.[48] MCR is routinely purified from *M. marburgensis* in its active form using this procedure and can yield up to 90% MCRred1form if exclusively purified under a complete exclusion of oxygen and stabilized by adding HS-CoM to the buffers used to purify MCR. Purging the culture with 100 % H_2 before harvesting for 20 min floods the cells with electrons and provides a highly reduced environment which indirectly reduced MCR. The cell culture was quickly cooled close to 10 ^{o}C before harvesting and kept at low temperature during harvesting.

Here we repeated that procedure as a control with *M. marburgensis* cells. It was attempted to induce the MCRred1state by resuspending whole cells obtained after centrifugation step in growth medium and purging the suspension with 100% H_2. Samples were withdrawn from the sealed vials and transferred to EPR tubes and frozen in liquid N_2. The MCRred1form was induced within 10 min. The MCRred1 state formed within 10 min of purging the *M. marburgensis* cell suspension and the intensity increased with increasing purging time (Figure 2.10 panel A).

This approach was repeated for *M. maripaludis.* The formate grown cells were harvested anaerobically. The cell pellets were resuspended and treated with 100% H_2 the same way *M. marburgensis* cells were treated and samples were taken anaerobically with a needle and transferred to the EPR tubes without exposure to oxygen and immediately frozen in liquid N_2 for EPR analysis. As shown in the Figure 2.10 panel B, this protocol was not able to induce the MCRred1 state in *M. maripaludis* even after 30 min.

This procedure has been proved to be effective in inducing the MCRred1 state in *M. margurgensis* cells. Unfortunately, it seems to work for *M. marburgensis* only. For example, Ragsdale and coworker tested the effectiveness of this protocol by treating *M. thermophilia* culture, grown in acetate, with 100% H_2 prior harvesting. The protocol, however, failed to induce the MCRred1 form in *M. thermophila* cells.[71]

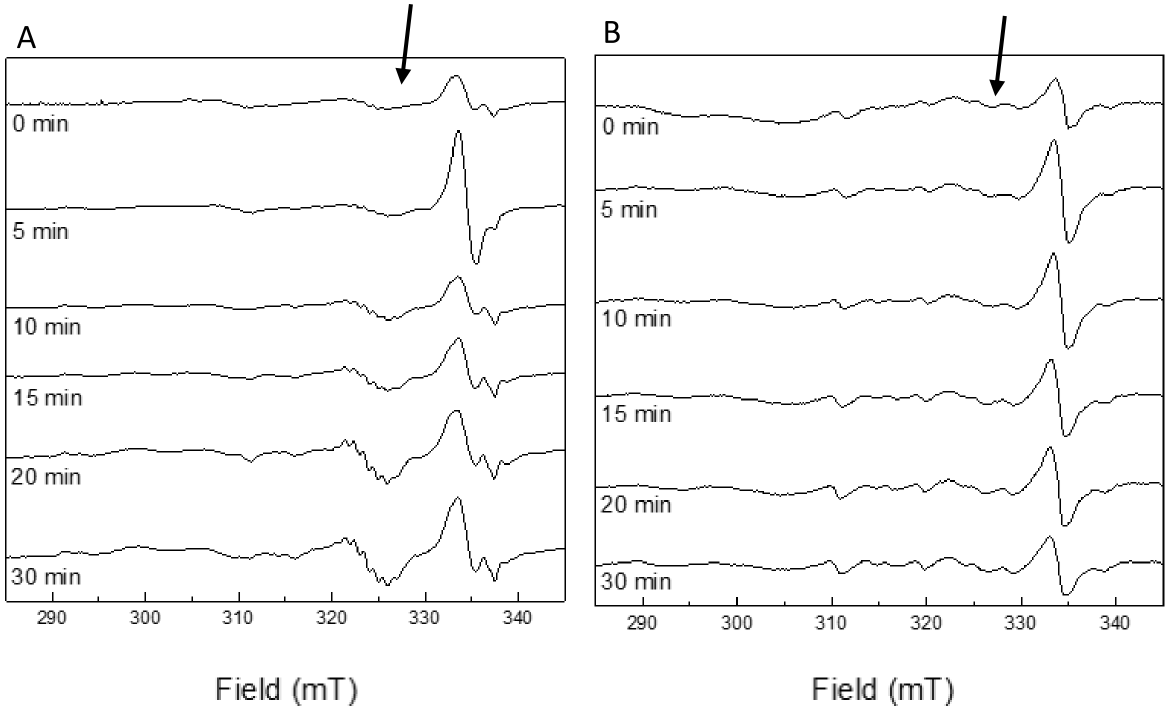

Figure 2.10. The effect of changing the gas phase to 100% H_2 for *M. marburgensis* cells (panel A) and for *M. maripaludis* cells (panel B). The MCRred1 is indicated by an arrow.

In our lab (Duin's lab) *M. maripaludis* cells are usually cultivated on formate medium, where formate acts as an electron donor and carbon source. But they can also grow on H_2 and CO_2, and they can be easily switched from a formate medium to a H_2/CO_2 culture within a couple of days. We though the failure for induction of the MCRred1forms using the above discussed protocol, i.e. treating the cells with 100% H_2 before harvesting, could be because the cells are grown on formate and might not expressing the necessary hydrogenase. Thus, to test the activation of MCR, *M. maripaludis* cells were grown on 80% H_2 and 20% CO_2, and the gas was changed to 100% H_2 and purged for 20 min before harvesting as described before. The cells were then harvested after cooling the media on ice. The EPR analysis of the whole cells, however, did not show the presence of the MCRred1signal (data not shown).

Formate may activate MCR in *M. maripaludis* cells the same way H_2 activate MCR in *M. margurgensis* cells as it is an electron donor during the methanogenesis on formate media. Thus, we tested activation of MCR in *M. maripaludis* with formate by incubating the cell suspension for 20 min and overnight. To fully reduce the extract of cells, Ti(III) citrate is added to the buffer when the cells are broken. Even then only about 5-10% of the whole cell activity is detected, and it quickly declines to 1% of the whole cell activity within one hour. Incubation of cell extracts with formate, and Ti(III) citrate triples the methanogenesis activity, but yet the activity was low (Figure 2.11).

Attempts to directly activate the enzyme to MCRred1form were not successful with 100 % H_2. Even though some activity was observed by incubating the cell extracts with formate overnight, the activity was not satisfactorily high enough that allows us to perform subsequent studies pertaining to mechanistic studies through site directed mutagenesis.

The MCRred1 form is extremely oxygen sensitive and even trace amount of oxygen at any step could inactivate the enzyme immediately. Considering low cell mass of *M. maripaludis* has been obtained we speculated that the condition may not have favored the MCRred1 form. Currently, there is not an established way to activate the silent form to the active form either enzymatically or with chemical treatment. Fortunately, the other form of the enzyme referred as MCRox1, was found to be more stable and it can be quantitatively converted to the active MCRred1forms by treatment with Ti(III) citrate at pH 9.0.

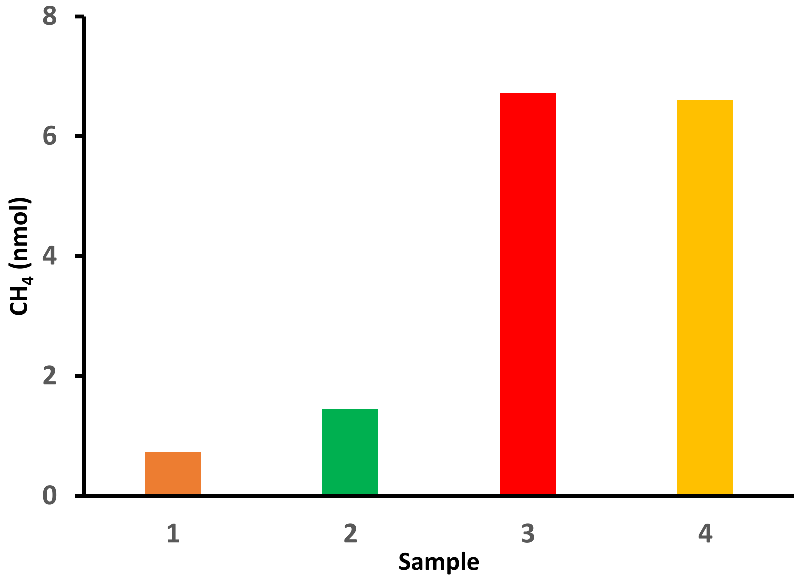

Figure 2.11. Activation of *M. maripaluids* wild type cell extracts with 20 mM Formate**.** Sample 1; CE as such, 2; CE + Ti(III) citrate, 3; CE treated with formate, and 4; CE treated with formate and Ti (III) citrate.

The MCRox1 state could be formed in vivo by switching the H_2/CO_2 gas (80%/20%) to N_2/CO_2 (80%/20%) and purging the *M. marburgensis* cell culture for 20 min prior harvesting.[48] To test if the same protocol would work for *M. maripaludis*, the culture was treated with N_2/CO_2 gas for 20 min before harvesting and EPR spectroscopy was measured for whole cell preparations. This protocol was, however, unsuccessful. It is not well understood how this protocol induce MCRox1 and its unclear why it did not work for *M. maripaludis* cells. It should be noted that the growth condition for *M. marburgensis* and *M. maripaludis* are different and the protocol might only be applicable for the cells grown in H_2/CO_2. Ragsdale and his coworkers tested this protocol for *M. thermopyla* by growing them in H_2/CO_2 and did not find MCRox1 induction upon treating cells with N_2/CO_2 before harvesting. MCRox1 induction using N_2/CO_2 was also unsuccessful for the *M. thermophila* cells grown on acetate.[71]

Since the above protocols failed to activate recombinant and wild type MCR in *M. maripaludis* an alternative method was considered. Ragsdale and coworker showed that in *M. thermophila* cells the ox1 form could be induced by the addition of Na_2S to the whole cells. They further proposed this procedure could be applicable to any methanogens regardless of the growth condition. Furthermore, Mahlert *et al*. showed *in vitro* conversion of MCRred2 state to MCRox1 state by incubating purified MCRred2 with polysulfide. Furthermore, they reported in vitro conversion of MCRred2 state into light sensitive MCRox2 state by adding sulfite.[47] Having these papers in mind, we tried if this protocol would work for *M. maripaludis* and *M. okinawensis* cells. For this, *M. okinawenisis* wild type was grown in formate at 60 ^{o}C and 6 mM Na_2S was added prior harvesting and incubated for 1 h at 60 ^{o}C. The culture was cooled to 4 ^{o}C on ice and transferred to the anaerobic tent and harvested and sonicated without exposing to oxygen. Figure 2.12 show the EPR spectra of the cell extract of *M. okinawensis*. Panel A in Figure 2.12 is the EPR signal of cell extract for untreated cells. Neither the ox1 signal nor the red1 signal were observed. On the other hand, significant amounts of the ox1 signal was detected in cell extracts after adding 6 mM sodium sulfide prior to harvesting (Figure 2.12, Panel B).

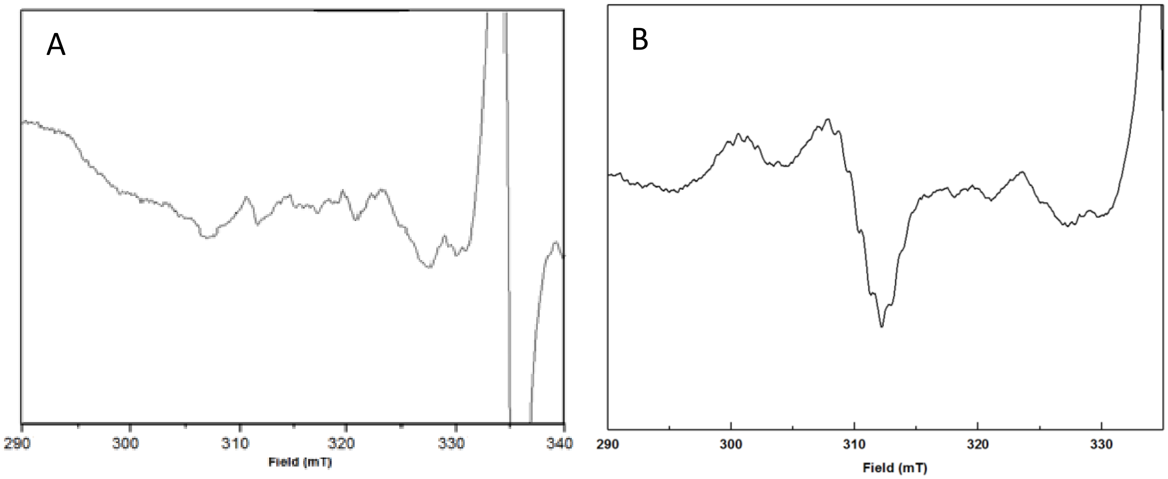

Figure 2.12. MCRox1 induction from *M. okinawensis* cell extract with Na_2S. Cell culture was grown in 3 L formate medium and treated with 20 mM Na_2S before harvesting. None treated cells (panel A) and treated cells (panel B).

The above result was promising, and it was repeated for the wild type *M. maripaludis* cell culture and *M. maripaludis* hosting MCR*ok*. As shown in the figure 2.13, the ox1 signal was detected in both *M. maripaludis* wild type and *M. maripaludis* hosting MCR*ok* cell extracts. This protocol was consistently able to induce the MCRox1 signal. Even though we were able to see the ox1 signal by incubating the cells with 6 mM Na_2S for 1 h prior harvesting, in order to get a higher activation/induction 20 mM Na_2S was used to induce MCRox1 state for most of part of the activation studies unless otherwise indicated.

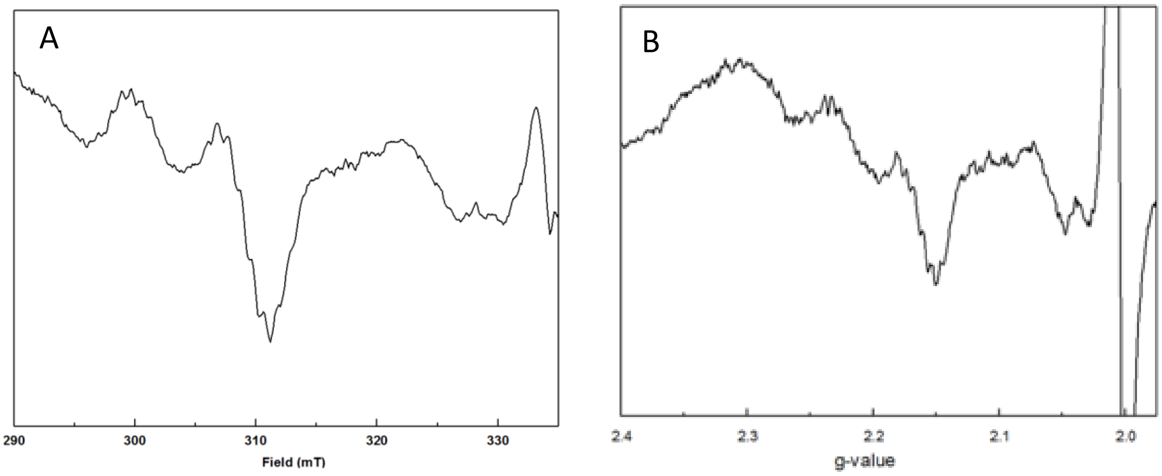

Figure 2.13. MCRox1 induction with 20 mM Na_2S of *M. maripaludis* wild type cell extract (panel A) and *M. maripaludis* expressing MCRok (panel B).

The next step is to activate the MCRox1 form using Ti(III) citrate. For this Na_2S treated *M. maripaludis* cell extract was incubated with 20 mM Ti(III) citrate at pH 9 for 20 min at 37 ^{o}C. The activation of the MCRox1 to the MCRred1was monitored by evaluating methane production using GC analysis. Ti(III) citrate has an intense signal which overlaps with the red1 signal and measuring EPR to monitor MCRred1was practically not possible. So it was more convenient and easier to performed the methane assay to test the activity of MCR. Figure 2.14 shows the result of Ti (III) activated cell extract after treatment with Na_2S. The activity of MCR as measured by methane production was significantly increased after activation with 20 mM Ti (III) citrate. The result implies MCRox1 is induced using Na_2S and it can be activated to the active MCRred1form of the enzyme by treating it with Ti(III) citrate. Consistent with the previos reports, the activation was higher when the activation of MCRox1 was performed at pH 9 and higher temperature (45 ^{o}C) even though the *M. maripaludis* optimum growth temperature is 37^{o}C.

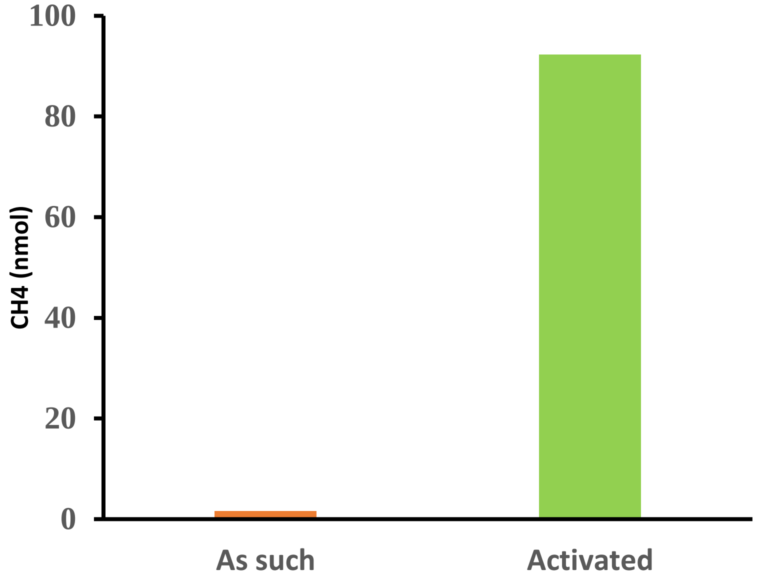

Figure 2.14. Activity assay for the cell free extracts of wild type *M. maripaludis*

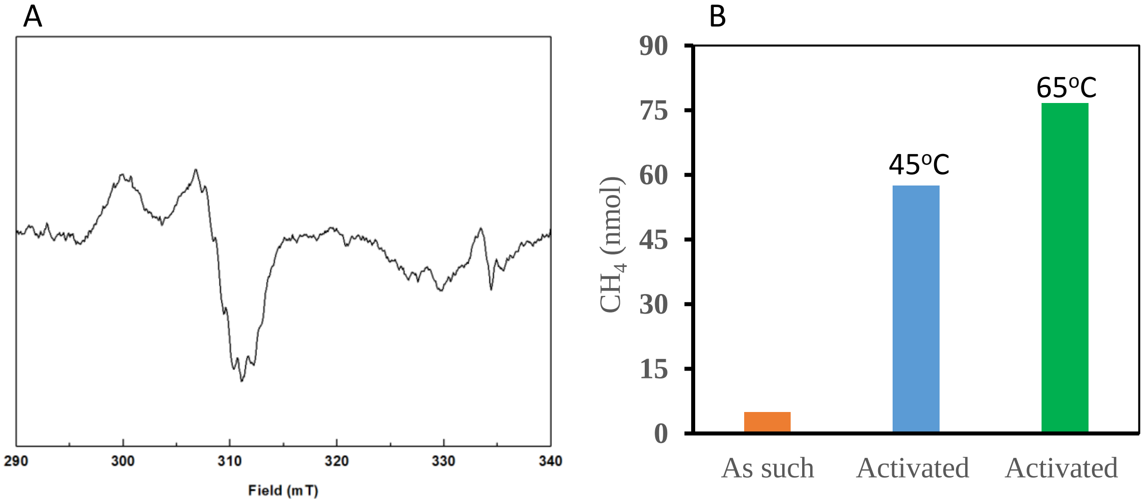

Figure 2.15. The EPR signal and the activity assay for the wild type purified MCR from *M. maripaludis* (MCRmmp). Activation was performed at 45 °C and 65 °C.

Of course the main objective to use this protocol is to be able to induce and purify MCRox in the recombinant MCR*ok* and later activate it to MCRred1state using Ti(III) citrate. Thus to test if the above procedure will work for this purpose, the *M. maripaludis* cells harboring recMCRok were treated with 20 mM Na_2S for 1 hr. An EPR sample was first taken before loading onto the Ni-sepharose column to see if MCRox1 signals were detected in cell extract. The ox1 signal was indeed detected in the cell extract (Figure 2.15, panel A). The next step was then to purify the recMCRok on the Ni-sepharose column and observe if the ox1 signal is detected. The ox1 EPR signal, however, was not detected in Ni-colummn purified recMCRok (data not shown). This implies that the ox1 signal obtained in cell extract was due to the induction of wild type MCR *M. maripaludis* (MCRmmp*)* and not the recMCRok or both wildtype and recMCRok. We propose that the activating system of *M. maripaludis* is not recognizing recMCRok1.

2.3.5 Characterization of recMCR*mmp*

One main hypothesis that we proposed based on the results obtained from the recMCRok was that the protein/chaperons of *M. maripaludis* are not properly recognizing the MCRok or McrD of *M. okinawenis* and as a consquence F_{430} is not fully inserted in some recMCR. Morover, its been found that the activation of MCRox1 was with the native MCR, but not recMCR*ok*. Therefore, to test this hypothesis, MCR were cloned from *M. maripaludis* in *M. maripaludis* by our collaborator Dr. Whitman. Since no *M. maripaludis* subunits were detected mixed in the recMCRok and ordered assembly of MCR was proposed. This means that only the subunits expressed in the same operon end up in the final enzyme form. Only when the genes were mixed on purpose was chimeric MCR detected.[83] Therefore, it should be possible to express recMCRmmp in *M. maripaludis.*

The Uv-vis absorption spectrum is shown in the Figure 2.16, panel A. Figure 2.16, panel B shows the SDS-PAGE of the recMCRmmp. As shown in the Figure 2.16, panel B the fraction from the Ni-Sepharose column reveals the presence of the expected three subunits of MCR as well as McrD.

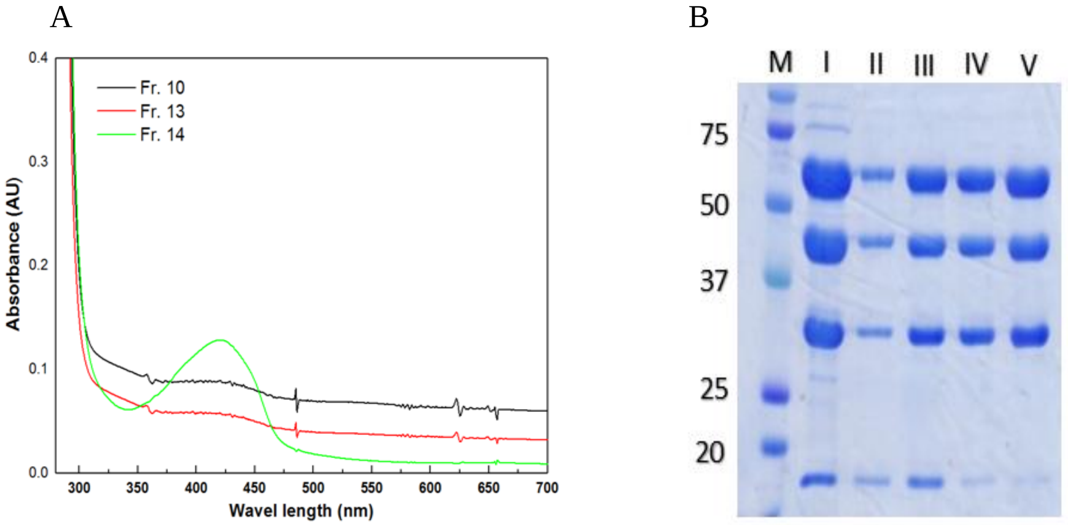

Figure 2.16. Absorption spectra (panel A) and the SDS-PAGE of recMCRmar. M; the molecular marker, I; Ni-column fraction, II-V; ion exchange (mono-Q) fractions.

This was similar to the result obtained after recMCRok purification. The fractions were then collected and further purified on Mono-Q. Two set of fractions were then obtained. One set was colorless and had McrD bound to it while the second set of fractions were without McrD and showed an absorption maximum at 420 nm characterstics of F_{430} bound MCR (Figure 2.16, panel A). This fraction was yellow in color. The results rule out one possible explanation for the results obtained with recMCR*ok*. Also in this case the F_{430} insertion cannot keep up with the MCR prodction, so both recMCRok and recMCR mmp are similarly recognized. The recMCR is expressed in two different forms, the reason could be the lack of F_{430} in the host cytosol (discussed in the next section), or timing issues since a ribosomal promotor is used for the recMCR expression. .

Figure 2.17 shows the ox1 signal of the purified recMCRmar. The signal was intense after Ni-column and persist even after the monoQ column albeit in low concentration. Now, the recombinant enzyme (recMCRmar) can be obtained in its ready form (ox1) and could be easily converted to the red1 form by treating it with Ti(III) citrate. This protocol has advantage as the ox1 is relatively more stable than the red1 form. However, it has also one disadvantage. Sodium sulfide is painfully pungent and is toxic. Therefore, it is not attractive to work with especially in large scale purification.

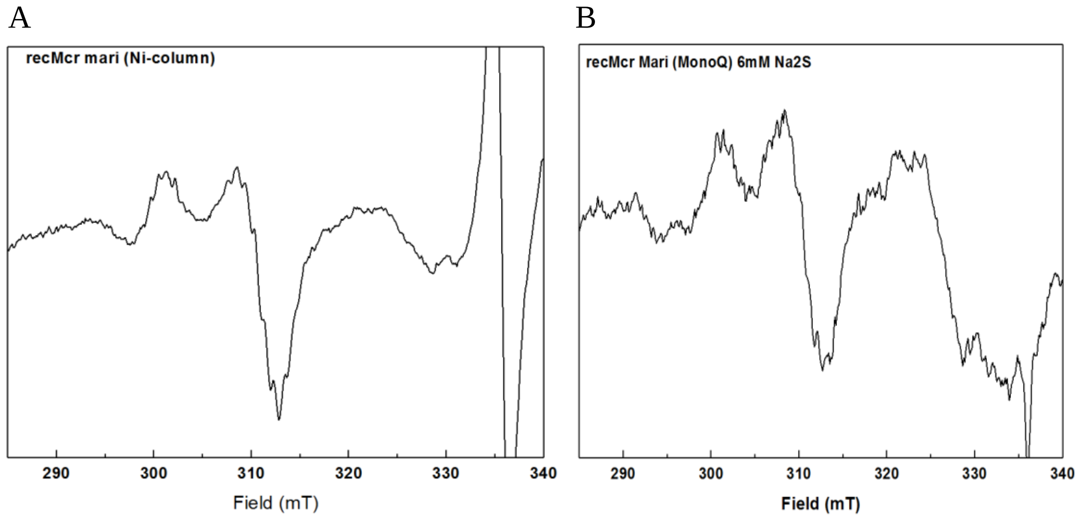

Figure 2.17. EPR spectra of the recombinant MCRmmp after Nickel-Sepharose column (panel A) and ion-exchange chromatography (MonoQ) (panel B). The Protein was purified after cells were induced with 20 mM Na_2S before harvesting for 1 h.

As discussed in the previous paragraph(s), direct activation of the MCRred1 in *M. maripaludis* was not successful. Two reasons can be attributed to this unsuccessful induction of the red1 form. First, *M. maripaludis* is grown on formate, and even though formate is an electron donor, it is also an oxidant. Most likely formate provides a different cell potential than growth on

H_2/CO_2. Second, hydrogenase may not be expressed in formate growth conditions. Whether the reason is first or second or even both, switching the media from formate to H_2/CO_2 could provide a solution. For this purpose, the cells were grown first on formate to an OD600 of 0.6-0.8 and then the gas phase was switched to 20%CO_2/80% H_2. The culture was further incubated for 2-3 days. The gas mix was switched to 100 % H_2 and purged for 1 h to induce the red1 signal. Both the ox1 and red1 signal were detected in cell extract and the 100% ammonium sulfate purification step. The ox1 signal persisted during the monoQ purification while the red1 signal was lost at that step (Figure 2.18, panel A). The activity assay was performed for both cell extract and ammonium sulfate fractions. The specific activity was calculated to be 1.4 U/mg and 1.5 U/mg for cell extract and ammonium sulfate fractions, respectively (Figure 2.18, panels B and C). Figure 2.19 shows the optimum concentration of MCR that can be used for the activity assay. It was found that 1-2 μM of enzyme is optimal for the activity assay.

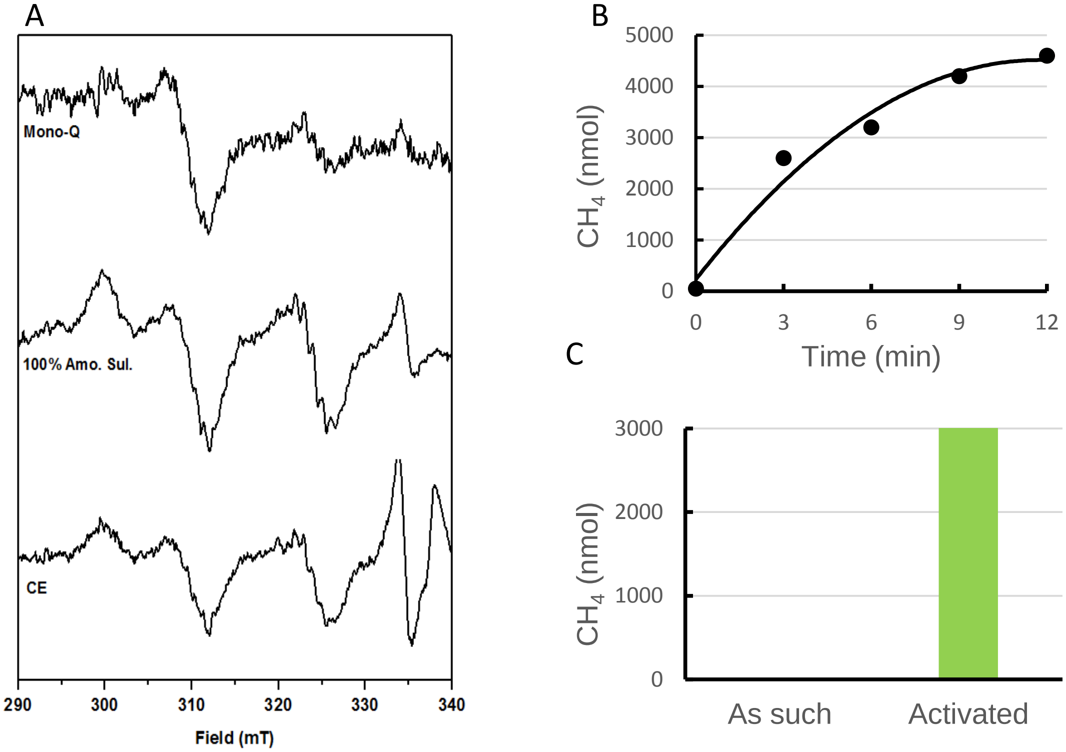

Figure 2.18. Activation and activity assay of *M. maripaludis* MCR with 100% H_2. Panel A; EPR spectra of CE, amonium sulfate and monoQ steps. Panel B; the activity assay from CE, and panel C; the activity assay after 100% ammonium sulfate purification step

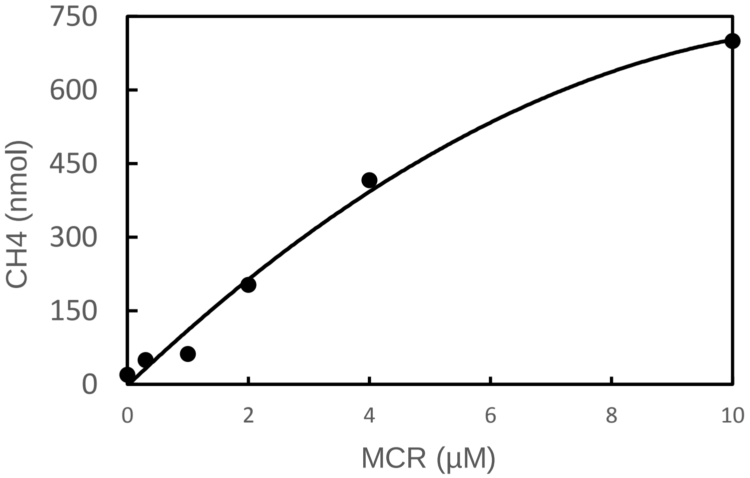

Figure 2.19. Optimization of MCR activity following its activation with 100% H_2

2.3.6 Determination of free and MCR-bound F_{430}

It has been reported that MCR comprises about 10-15% of the total protein content of the cell in methanogens that have been widely studied. In *M. marburgensis* 25% of the total F_{430} is bound to MCR, while the remaining 75% is freely available in the cytosol. The amount of free F_{430} available in *M. maripaludis* has not been determined. It is reasonable then to suggest that the scarcity of free F_{430} in *M. maripaluids* could be the reason for the lack of F_{430} in recMCRok. We proposed that the reason for the expression of MCRok without the cofactor could be either that there is not enough F_{430} available for wild type and recMCRok or that there may be unfavorable interaction among the proteins that are involved in the insertion of F_{430} to apoMCR. For example, the protein from *M. maripaludis* e.g. CfbE, which is the last protein in biosynethesis of F_{430} and a potential protein in the insertion of F_{430} to MCR may not be recognized by MCR and or McrD of *M. okinawensis*. However, expression of recMCRmmp in *M. maripaludis* also had low level of F_{430} bound, thus this may not be the case. The first hypothesis was tested by measuring the availability of free and bound F_{430} in *M. maripaludis* wild type and *M. maripaludis* expressing MCRok.

Different methods were used for extraction of free F_{430} from *M. maripaludis*, *M. okinawensis*, and *M. marburgensis*. For the wild type, cell extract was filtered through a 100 kDa filter to remove MCR as it is 300 kDa. The flow through that passed through the 100 kDa was subjected to different extraction methods discussed below.

The first method we followed was to treat the MCR-free flow through with methanol and boiling. A ratio of 1:6 (flow through: methanol) was used. This together with boiling will liberate any protein that might binds the F_{430} and ensures removal of any small proteins from the sample. The methanol solution was concentrated and HPLC was performed as described in the methods section. Figure 2.20 shows the result. An intense peak was observed around 7.5 min retention time (Figure 2.20 panel A). This retention time was similar to the retention time of authentic F_{430}. However, Uv-vis analysis of the peak show the compound has an absorption maximum around 390 nm and it's clearly different from the Uv-vis absorption spectra of F_{430} (Figure 2.20 panel B).

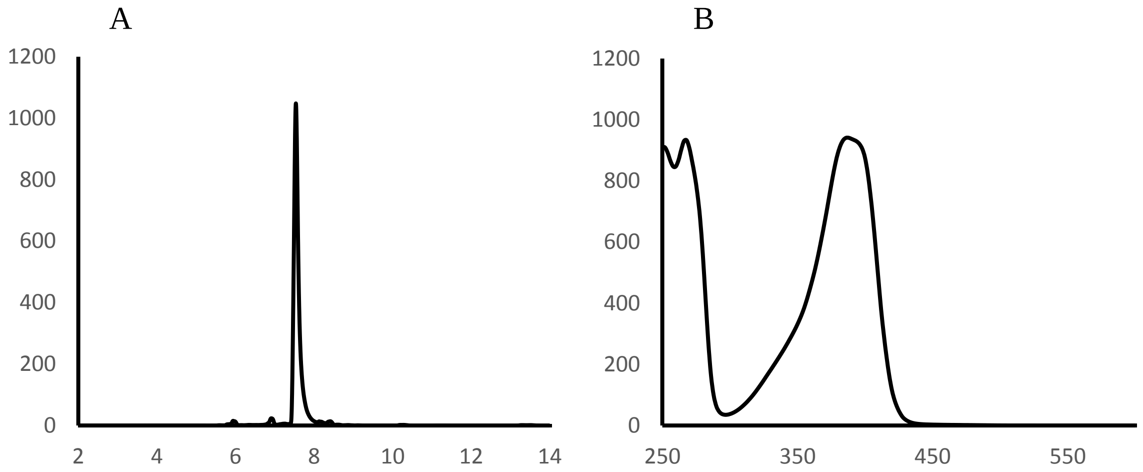

Figure 2.20. Extraction of free F_{430} from *M. maripaluids* hosting MCRok using Methanol and boiling. Panel A; the HPLC chromatogram and panel B; the Uv-vis spectra of the major peak

The spectrum, to our knowledge, was never been reported to our knowledge for any form of F_{430}. It has been reported, however, that F_{430} can be unstable in its free form and the product observed could be a degradation product of F_{430}. As our first method included boiling of the sample to denature proteins, it may also cause degradation of free F_{430}. Thus, to avoid a possible effect of boiling, the extraction was performed using methanol only with no heating step. The HPLC spectra and respective Uv-vis spectra are given in Figure 2.21. Once again one large peak was eluted at the retention time close to 7.4 min, close to the F_{430} retention time. The UV-Vis spectra of that main peak revealed an absorption maximum around 390 nm which is the same as the spectrum obtained with the methanol and boiling extraction protocol (Figure 2.20, panel B).

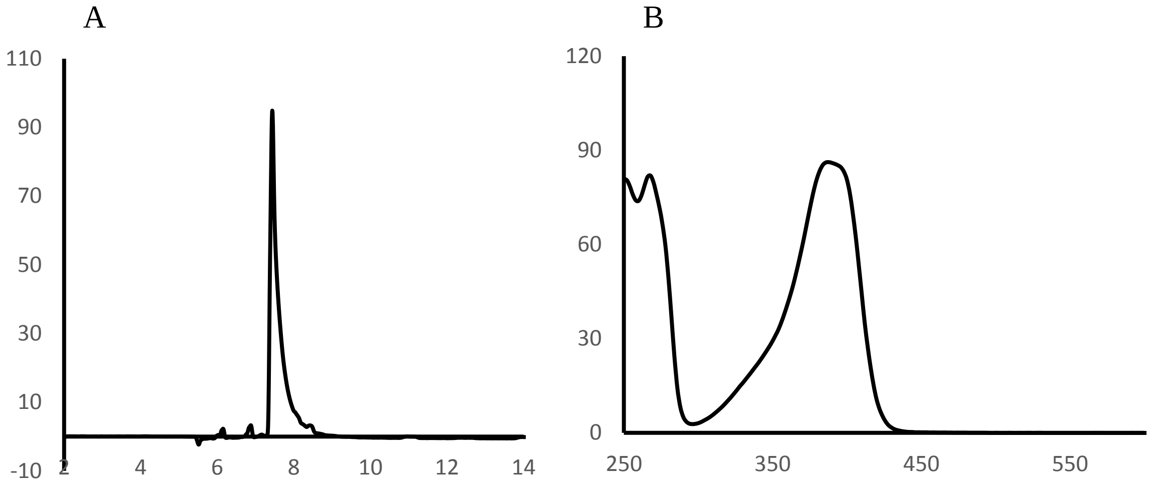

Figure 2.21. Methanol extraction of free F_{430} from *M. maripaludis* hosting MCRok. Panel A; the HPLC chromatogram and panel B; the Uv-vis spectra of the major peak

The extraction was also performed using cold methanol, but the result was the same as the result obtained with methanol and boiling.

At this point we decided to change the extraction method. One protocol described by Keltjens *et al*. uses cold ethanol and phosphate buffer.[74] They claimed that this method could be used to extract free and bound F_{430} (MCR bound). We followed the same procedure. A small amount of F_{430} was detected from the free F_{430} extraction part. This looked alluring at first; however, once we realized that the method did not release bound F_{430}, we suspected the result. The F_{430} detected in free form by this method could be the F_{430} extracted from MCR. The cold ethanol could denature MCR during the incubation time even though the authors argued that MCR is intact at this incubation time. It should be noted also that when this method was followed, the MCR was not separated by passing the cell extract through 100 kDa filter as the method did not specify doing so. Therefore, we decided to try the method with minor modifications. MCR was first separated using a filter and then the flow through was subjecting to cold Ethanol. The HPLC results are now identical to that of the previous methods (Figure 2.22).

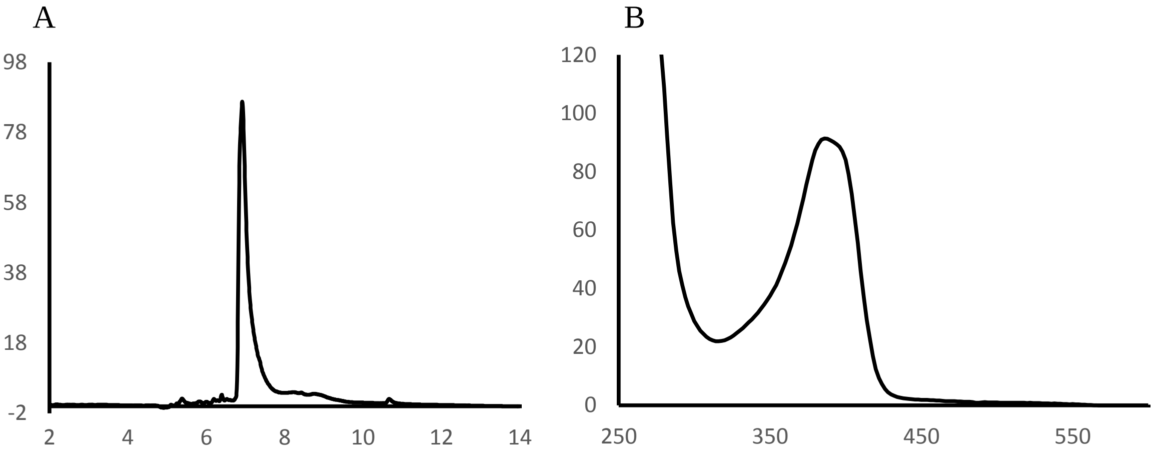

Figure 2.22. Extraction of free F_{430} from *M. maripaludis* hosting MCRok. Panel A; the HPLC chromatogram and panel B; the Uv-vis spectra of the major peak

It has also been suggested that F_{430} is unstable in the presence of oxygen and forms a didehydro-F_{430} oxidized at carbon 12 and 13. Since most of the extraction method was exposed at some point to air, we proposed that the product we are getting could be that form. So, the next experiment we performed in analyzing free F_{430} in *M. maripaludis* was to extract F_{430} from MCR free cell extract by treating it with methanol inside the tent and concentrating the sample with nitrogen gas without exposing to oxygen. The sample was taken anaerobically and only the HPLC part was performed under aerobic condition. Once again after analyzing the sample using HPLC the main peak was the one we found before. Cell extract was also purified using monoQ after MCR was removed through filtration. The yellow fraction was then collected and subjected to HPLC analysis. This protocol was done under exclusion of oxygen except the HPLC step. As shown in the figure the main peak was the peak with the maximum absorption at 390 nm, the same compound obtained with the other extraction methods (Figure 2. 23).

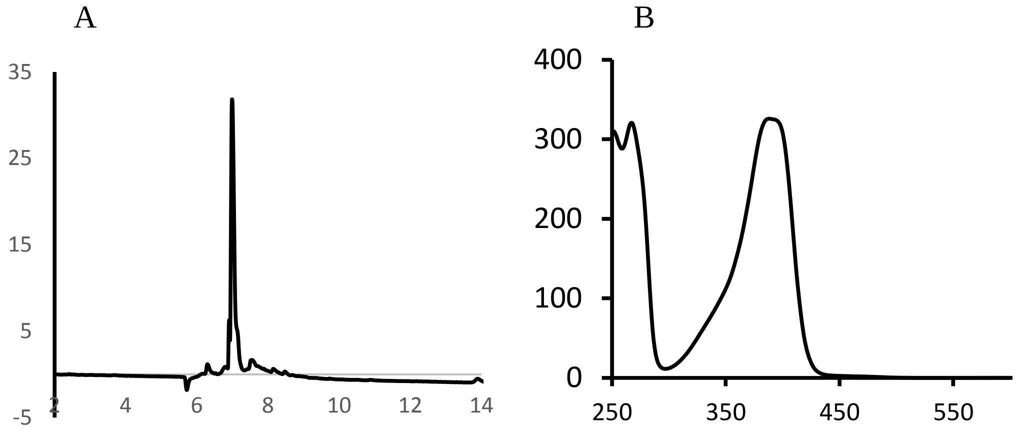

Figure 2.23. Extraction of F_{430} with methanol and monoQ. Panel A; the HPLC chromatogram and panel B; the Uv-vis spectra of the major peak.

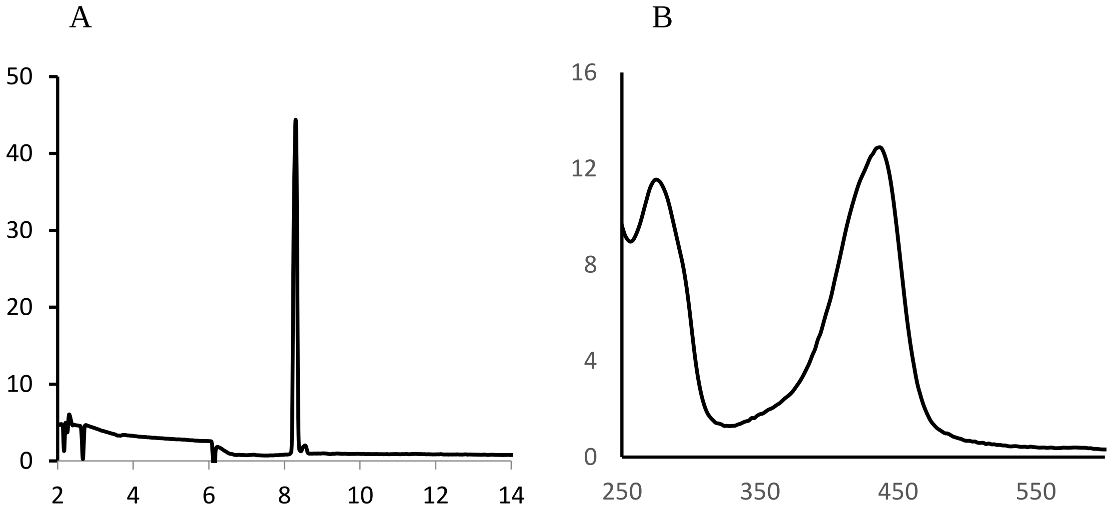

Figure 2. 24. Extraction of F_{430} from *M. maripaludis* MCR using methanol. Panel A; the HPLC chromatogram and panel B; the Uv-vis spectra of the major peak

It has been reported that *Methanocaldococcus jannaschii* and *M. maripaludis* contain more than one form of coenzyme F_{430}.[86] Thus, it is possible that only some forms of the coenzyme are available to bind to MCR. We hypothesized that the reason for the expression of 50% of the recMCR without F_{430}, may be because the available F_{430} forms are different in structure. To test this hypothesis LCMS was performed on the F_{430} extracted from cells (free F_{430}) and from purified MCR to determine if there is any difference in the structure between the free and MCR bound F_{430} in *M. maripaludis* and/or *M. marburgensis*. Indeed, there was difference in the forms obtained from freeF_{430} and the bound F_{430}. The main form consistently obtained in free forms found to be the didyhroF_{430} which has a molecular mass of 903.22, while the expected F_{430} was the main form in the bound MCR (Figure 2.25). Pure F_{430} should have a mass of 905 amu. The form, obtained from cell extract, however had a molecular mass of 903.22 (Figure. 2.25). Since this is 2 amu less than that of F_{430} it implies that this form represents a didehydro form. This form was dubbed F_{430}-4 in the paper by Allen *et al*.

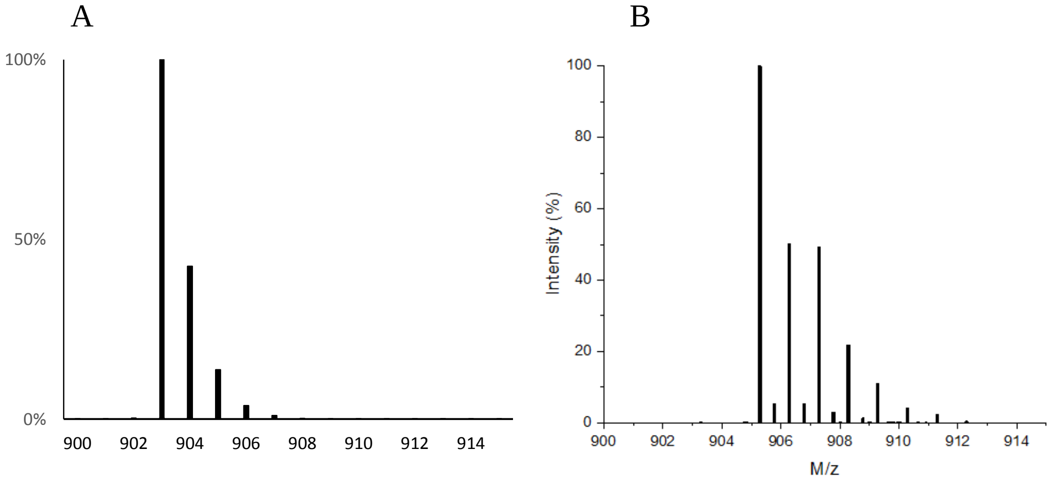

Figure 2. 25. LC MS spectra of free and bound F_{430} from *M. maripaludis* and *M. marburgensis*

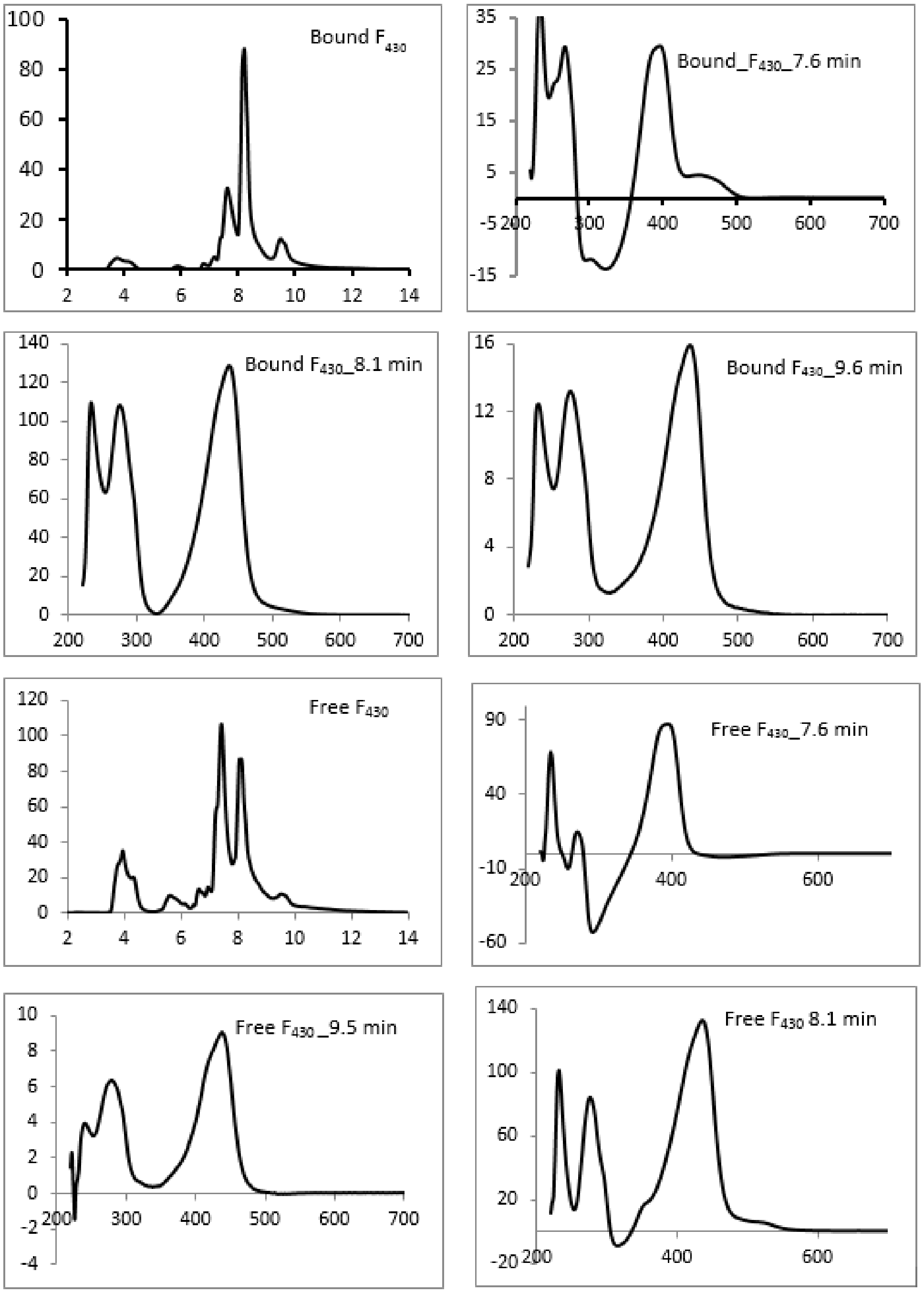

Figure 2. 26. Extraction of free-F_{430} and MCR-bound F430 from *M. marbugensis* using methanol

The F_{430} analysis was also performed with cell extract from *M. marburgensis*. Two different protocols were followed to see if there is an effect from the method employed on the result. In this case the methanol extraction was compared to the previously used perchloric acid extraction method. All steps were performed under aerobic conditions and samples were kept in dark as much as possible**.** ~8 g (wet weight) cells were resuspended in ~20 ml 50 mM Tris/HCl, pH 7.5. The cells were broken by sonication and the cell extract was collected by centrifugation and removal of cell debris. 10 ml CE was used for $HClO_4$ extraction while the remaining half was used for MeOH extraction. To the 10 ml CE the suspension $HClO_4$ (2 M) was added resulting in a white precipitate immediately. Once a pH value of 2 had been reached by the addition of $HClO_4$, the solution was stirred for 1h. The solution was centrifuged for 30 min at 10000 rpm and the supernatant was collected. The pellet was resuspended in ~ 1 ml of 10 mM $HClO_4$ and the stirred for 1h. The solution was centrifuged for 30 min at 10000 rpm and the supernatant was combined with the previous one. The pH was adjusted to 7.5 with 2 M NaOH. The solution was concentrated to ~3 ml using a rotavap. The suspension was filtered using a syringe filter to remove solid particles. The solution was concentrated using a N_2 flow to ~900 µl. The resulting extract was centrifuged to remove any remaining solid particles and the result sampl was subjected to HPLC assay.

The HPLC chromatograms obtained were almost identical for both methanol and perchloric acid extraction method suggesting the methods yield the same result (Figures 2.27 and 2.28). Visual inspection of the methanol and perchloric extractions detected an orange/purple color, rather than the expected yellow color similar to the sample from *M. maripaludis*. The darker color most probably is due to a small amount of resazurin still present in the extract. The absorption spectra of some of the peaks are presented in Figures 3 and 4. At the retention time of 7.06 min ($HClO_4$ extraction) 7.76 min (methanol extraction) and an abortion spectrum is obtained with a band at 390 nm indicating that the didehydro-F_{430} is also present in *M. marburgensis* regardless of the methods used for extraction. Moreover, LC/MS confirmed the mass of this form as 903.27 (Figure 2.25 B.) the same mass obtained for the compound extracted from *M. maripaludis*. The HPLC and LC/MS results also indicates the presence of authentic F_{430} from both extraction method at a retention time of 9.04 min ($HClO_4$ extraction) and 7.76 min (methanol extraction) (Figures 2.27 and 2.28).

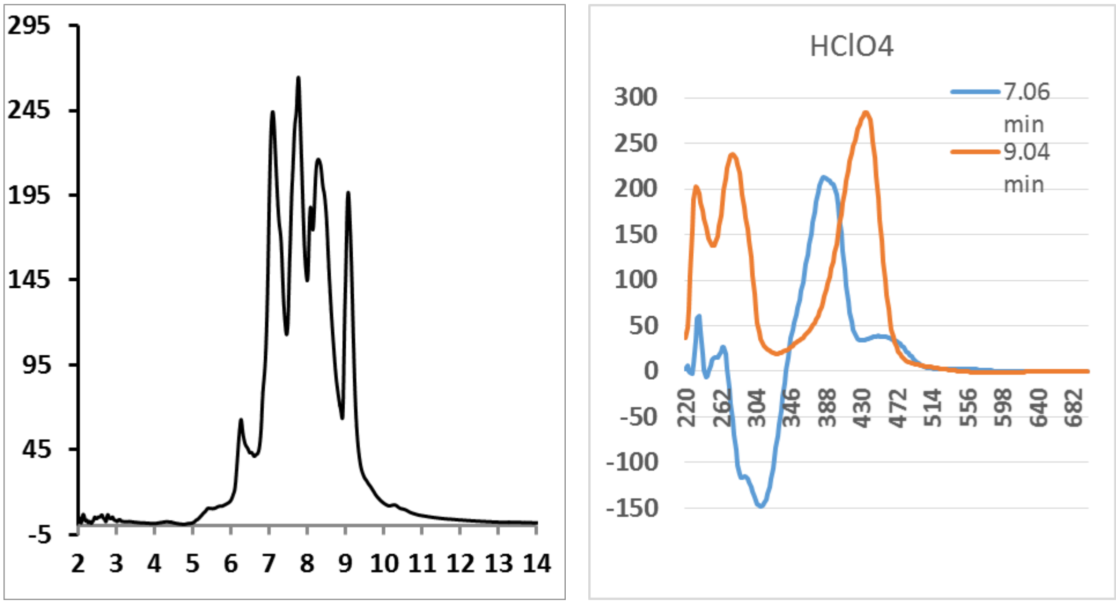

Figure 2.27. Extraction of F_{430} from *M. marburgensis* cell extract using 2M perchloric acid.

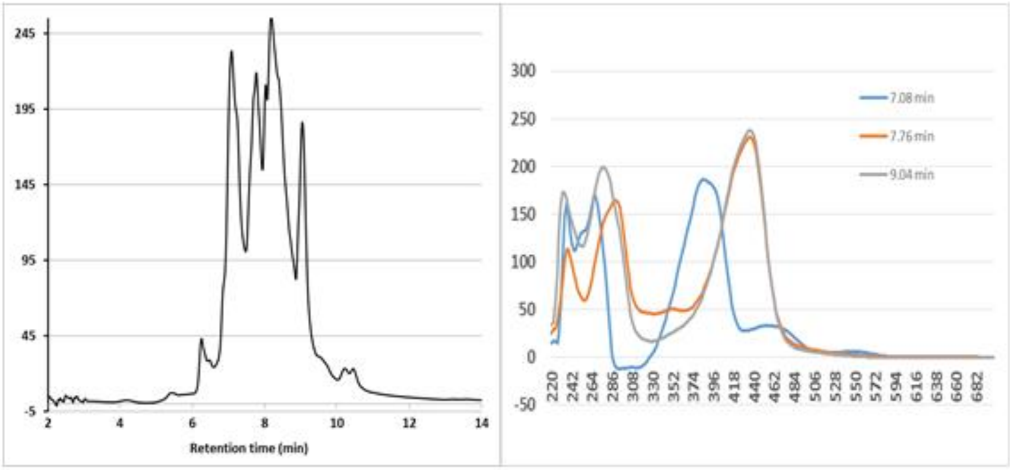

Figure 2.28. Extraction of F_{430} from *M. marburgensis* cell extract using methanol and heating

2.3.7 Role of McrD and CfbE in coenzyme F_{430} insertion to MCR

The *mcr* operon has 5 genes ABGCD. The A, B, and G genes encoded the α, β, γ subunits which form MCR. The function of McrC and McrD were not known until recently. McrC was found to be part of activating complex and is proposed to play a role in the activation of MCR.

The fraction we obtained with the recMCRok shines some light as to the function of McrD and suggest the potential role of McrD in the F_{430} insertion. As shown in the Figure 2.5 the SDS-PAGE of recMCRok reveals the presence of McrD in recMCRok. It is interesting that McrD was tightly bound to MCRok even after two purification steps. It is bound to the recMCRok fraction that was purified without its cofactor but not to the halo-MCRok fraction. McrD does not normally copurified with the MCR in *M. marburgensis*. This suggests that it perhaps is staying with apoMCR waiting for F_{430} to come and get inserted into MCR. After insertion of F_{430} in MCR the McrD is proposed to dissociate from the enzyme complex. Explaining why it was not detected in the SDS-PAGE of the fraction that contains F_{430} (Figure 2.4). Indeed, this hypothesis was augmented with the recent report from Dr. Mansoorabadi's lab.[75] In their paper, the biosynthesis of F_{430}, McrD was found to supplement the enzymatic function of CfbE. CfbE is the last enzyme in the biosynthesis of F_{430}. It catalyzed the conversion of seco-F_{430} to F_{430}. What they observed was incomplete conversion to F_{430} with CfbE alone. But upon adding McrD to the assay a complete conversion of seco-F_{430} to F_{430} was obtained.[75] This implies that McrD might bind F_{430} thereby preventing a product inhibition. Since the next step should be the insertion of the cofactor after it was biosynthesized, it can be hypothesized that McrD accepts F_{430} from CfbE and inserts it into MCR. This hypothesis was tested in the presence of CfbE from *Methanosarcina acetivorans* and did not result in the insertion of F_{430} to recMCR. But since the CfbE was from *M. acetivorans*, it might not interact with the *M. okinewensis* protein. Thus, the experiment cfbE was cloned along with McrD from *the M. okinewensis* and the experiment was repeated (see next sections).

2.3.7.1 Cloning *McrD* gene from *M. okinawensis* in *E. coli*

The *mcrD* gene was amplified from the *M. okinawensis* genomic DNA by PCR using the forward primer; ATATACATATGATAGAAATAGAAGTCTTCCCC containing an *NdeI* (underlined) site and the reverse primer CTTTTCCTACTTTTTCATTGAGCTCATATA containing a *XhoI* (underlined) site with the high fidelity thermostable DNA polymerase fusion. The Agarose gel of the PCR amplified genes is given in Figure 2.24. The amplified PCR products were analyzed on a 1% agarose gel. The bands at ~0.5 kb (Figure 2.24) corresponds to the size of the *mcrD gene***.** The PCR product was double digested with *NdeI* and XhoI restriction enzymes. Likewise, the vector was double digested with *NdeI* and XhoI. The double digested *mcrD* genes were then ligated into a digested pET28b(+) vector using T4 ligase. The success of the ligation was confirmed by sequencing of the *McrD* insert using a universal T7-promoter primer of pET28b(+).

The sequencing profile shows the presence of the T7-promotor of the vector pQE-80L and the complete sequence of the insert *mcrD.*

2.3.7.2 Cloning CfbE genes from *M. okinawensis* in *E. coli*

CfbE genes were amplified from *M. okinawensis* genomic DNA by PCR using the forward primer; ATATACATATGCTTATAATCGATGTAAATC containing a *NdeI* (underlined) site and the reverse primer CTATTATATATCTTTTCGATATTTAATTGAGCTCATATA containing a *xhoI* (underlined) site with the high-fidelity thermostable DNA polymerase *fusion.* The amplified PCR product was analyzed on a 1% agarose gel. The band at ~1.5 kb (Figure 2. 26) corresponds to the size of the *CfbE* gene. The PCR product was double digested with *NdeI* and *xhoI*. The vector was also double digested with the *NdeI* and *XhoI* restriction enzymes. The ligation of the *CfbE* to the vector was not successful, however when the protocol was performed without the addition of phosphatase. Upon addition of phosphatase and subsequent purification of the digested products, the ligation was successful. The double digested *CfbE* genes were then ligated into a digested pET28b(+) vector with T4 DNA ligase. Before transforming to BL21 *E. coli* for expression the ligation of the insert to the vector was confirmed by sequencing of the *CfbE* insert using a universal T7-promoter primer of pET28b(+) and the *CfbE* was cloned intact without any point mutation (Data not shown).

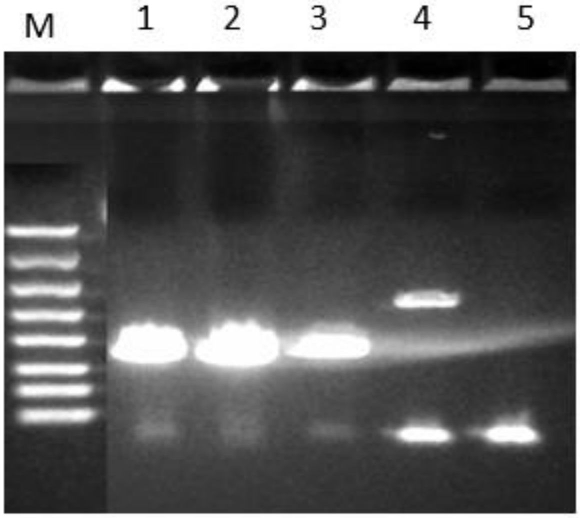

Figure 2.29. Agarose gel of *mcrD* and *CfbE* PCR amplified products. Lane 1, PCR marker (approximate molecular weights of the 101-5,000 bp marker are shown on the left of the gel); lane 2-4, *mcrD* (amplified at different temp); lane 5-8, *CfbE* (amplified at different temp). The small size products shown in lanes 5 and 6 are perhaps due to the non-specific binding of primers.

2.3.7.3 Purification and protein determination

McrD was purified on Ni-sepharose column. A prominent band around 20 KDa was obtained which corresponds to McrD (Figure 2.30, panel A). The numbers on the figure indicates the fraction obtained on the Ni-sepharose column. Those fractions that are pure are collected, combined and washed to remove the imidazole. The protein concentration was determined by the Bradford protein assay. The purification of CfbE was only possible when 10% glycerol was added to LB growth media and the temperature of culture was reduced to 25 ^{o}C. The routine growth and induction condition resulted in the presence of the protein in the inclusion bodies. The SDS-PAGE for CfbE is shown in Figure 2.30, panel B . The bands at around 35 kDa corresponds to CfbE and the concertation was determined with Bradford protein assay. Only the fraction which is relatively pure (fraction III) was used for the experiment.

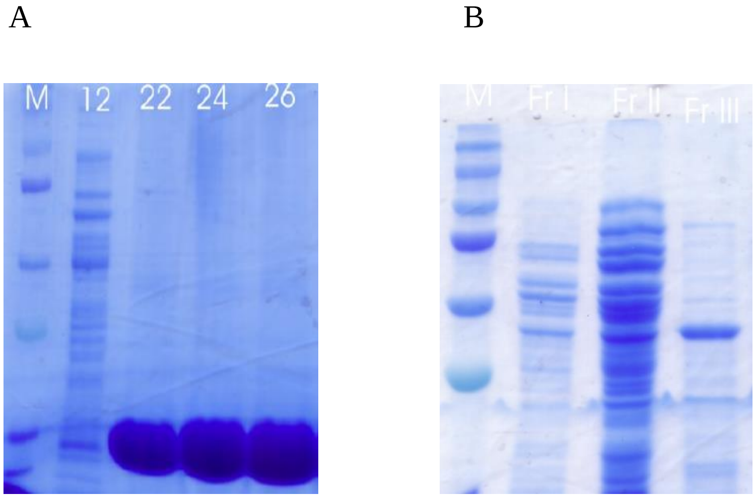

Figure 2.30. SDS-PAGE gel analysis of McrD (panel A) and CfbE (panel B)

Figure 2.31 shows the result of the CfbE activity assay. CfbE was found to catalyze an ATP dependent reaction of sec-F_{430} to F_{430}. The activity assay was performed by incubating seco-F_{430}, Mg-ATP, PK and PEP together with 2.0 g/mL CfbE. The incubation temperature was 55 °C for *M. okinawensis* CfbE. Higher temperature found to precipitate proteins. As a point of reference CfbE from *M. okinewensis* was also tested at 37 °C. The CfbE from both methanogens was found to convert seco-F_{430} to F_{430} to almost completion consistent with the previous report.[85]

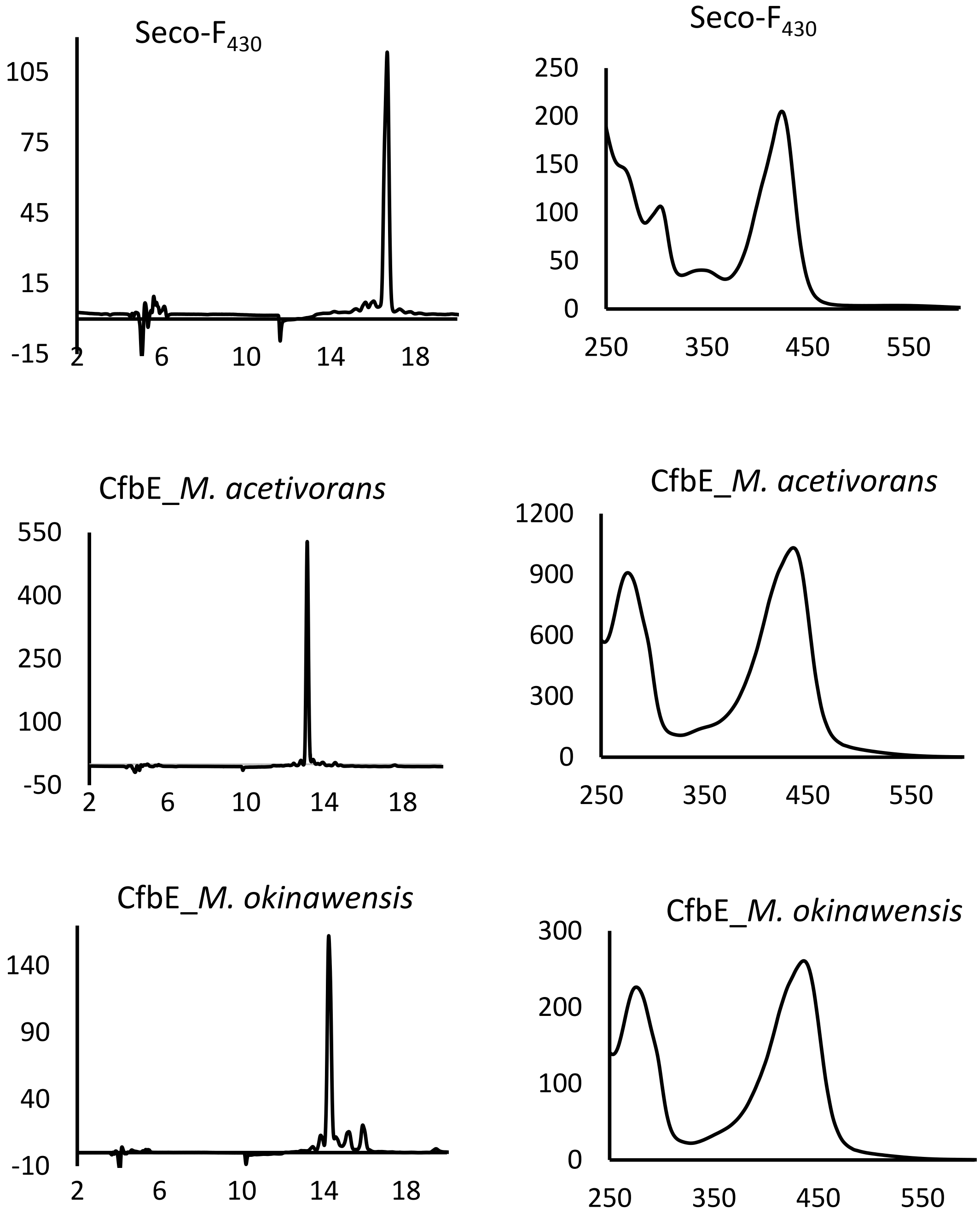

Figure 2. 31 Activity assay of CfbE from *M. okinawensis* and *M. acetivorans*

2.4 Discussion and conclusion

Here we presented the expression of the recombinant MCRok and MCRmmp. Interestingly the recombinant enzyme were purified in two set of fractions. One fraction contained a cofactor F_{430} (halo-enzyme) and the second fraction was purified as an apo-protein. MCR from *M. marburgensis* have previously expressed in *E.coli* and MCR from ANME was expressed in *Methanosarcina acetivorans.*[87,88] This is the first report, to our knowledge, that provides an insight to the assembly of MCR. The recMCRs expressed in *M. maripaludis* contain the same stoichiometry ratio of the subunits as that of native MCR. The holo-recMCR contain significant amounts of the coenzyme F_{430}. All the PTMs of the native enzyme were also detected in recMCRok and recMCRmmp. Moreover, McrD was found to associate with the apo-recMCR in half stoichiometry ratio relative to the other three subunits. This is the first time McrD copurified with MCR. Based on the results a model for the assembly of MCR (Figure 2.32) was proposed. Since the post-translationally modified residues are deeply buried in the active site of the enzyme it has been proposed that they are most likely modified prior to the binding coenzyme F_{430}. [83]

Figure 2.32. Order assembly of MCR.[83] See text for description of the model

The gene order of the subunits is highly conserved (BDGA) in the *mcr* operons. The gene present in order are usually cotranslated in the order for the correct assembly of the protein. Therefore we hypothesize that the *mcr* genes are translated in the order of transcribed. Thus, according to the working model given in Figure 2.32, McrB is translated first, and act as a scaffold for the assembly of the other subunits. McrD then binds to McrB followed by McrG.

McrG may have a role in facilitating the interaction of McrB and McrA or facilitating PTM of McrA (all the PTM are in McrA subunit). McrD may function in preventing the misfolding of McrA and/or in the insertion of F_{430}. McrD was found in the final biosynthesis of F_{430} helping the CfbE in the full conversion of sec-F_{430} to F_{430}.[85] McrC is not conserved in all MCR, but it has been proposed that it involves in the activation of MCR from *M. marburgensis*.[89]

Unfortunately, the activity of the purified recMCRok was very low hindering it from being used for further studies. This could be due to inability of the host's (*M. maripaludis*) activating system to activate recMCRok. Since the study of heterologous expression of recMCRok assures that there are no subunits mixing and an order assembly of subunits occur during maturation of MCR, homologous expression of recMCRmmp was performed in *M. maripaludis*. This was aimed to get active recombinant MCR. As the host gene and activating system in this case are the same, there should not be inability of host's activating system to activate the recMCRmmp. The recMCRmmp indeed was found to show some activity 1.4-2.0 U/mg.

In conclusion, recMCRok and recMCRmmp were successfully expressed in *M. maripaludis.* Detailed study pertaining to characterization and activation of the recMCRs have been presented in this chapter. This study lays a foundation for further studies that need to be conducted using the recombinant enzyme. There are several unanswered question regarding this enzyme system that need to be addressed. Interesting experiments such site directed mutagenesis can be conducted, and we believe this work opens a door for such kind of studies. Moreover, some additional experiments will be needed to provide a conclusive role for McrD in the insertion of F_{430} to apo-MCR.

Chapter Three: Investigating the Activation system of MCR

3.1 Introduction

MCR is the key enzyme in biological methane formation by methanogenic Archaea and in methane consumption by anaerobic methanotrophs. The enzyme can be found in different states of which the MCRred, MCRsilent, and MCRox are the most relevant. It must be in its reduced form (red1) in order to initiate the catalytic activity.[28,48]

MCRsilent is readily purified, but unfortunately it is catalytically inactive. MCRox1 can be induced *in vivo* following specially developed methods. The ox1is more stable than the red1 form. Like the silent form ox1 is also inactive. MCRox1 can be obtained by switching the 80%H_2/20%CO_2 growth media (gas) to 20%CO_2/80%N_2 before harvesting and can be converted into the MCRred1 form *in vitro* by reduction with Ti(III) citrate.[48] The ox1 is more stable than the red1 form, however, like the red1 from it also gets converted to the silent form if stored for a long time.

The MCRred1 can be purified in its active form following a specifically developed protocol.[48] This protocol has been routinely used to obtain the red1 form from *M. marburgensis*. For this purpose, the H_2/CO_2 grown cells are gassed with 100% H_2 before harvesting and the enzyme is subsequently purified under strict exclusion of oxygen. The protocol could yield up to 95% of the MCRred1 form of the enzyme. However, due to its low mid point potential of the Ni(II)/Ni(I) couple in F_{430} (estimated to be -650 mV vs Hydrogen electrode at pH 7) MCRred1 is prone to spontaneous deactivation even under an exclusive oxygen free environment making it difficult to keep it for a longer time.

Although there is a chemical method to activate the MCRox1 form to the red1 form, currently there is no any chemical method to activate the MCRsilent to MCRred1. It is inherently interesting to learn how the cells perform this task, but with the goal of using recombinant MCR to trap CH_4 in an engineered organism is imperative to obtain this knowledge. This project aims to understand and characterize the major components of the activating system of MCR. This work was performed together with Bryan Cronin.

Decades ago partial enzymatic reductive activation of MCRsilent was reported.[90,91] Robert Gunsalus and Ralph Wolfe found the first evidence for an activation system for MCR. In their chromatographic studies, they were able to resolve a cell free extract from *M. thermoautotrophicum* into three fractions which they named as component A, B, and C. They also showed that in the presence of hydrogen these components were able to reduce CH_3-S-CoM to methane. It was later found that fraction B was the second substrate of MCR i.e. HS-CoB while component C turned out to be MCR itself. Component A was further resolved into four fractions named as A1, A2, A3a, and A3b.[91] Back then the function of components A was not known, but it was evident that they were required for activation of MCR and were not replaceable by a chemical reductant like DTT. Later on, fraction A1 was found to be an F_{420}-reducing hydrogenase, A2 an ATP-binding protein; A3b, a methyl-viologen-reducing hydrogenase (F_{420}-non-reducing), and A3a, an uncharacterized iron-sulfur containing protein complex.[90]

Even though the components showed activity in methane assays, the activity was low and it cannot be excluded that the observed activity was due to a direct activation of MCRox1 to MCRred1 by Ti(III) citrate. Ti(III) citrate was present in the activity assay and it is known to directly activate MCRox1. Moreover, A3a was found to be a very large complex with a molecular mass greater than 700 kDa and was not further characterized.

To continue this work, the component A3a was purified by Divya in the Duin laboratory. A total of four purification steps were used, and the last step was a Superdex-200 gel-filtration column. A single peak was obtained after Superdex-200 gel-filtration step. The characterization of the different subunits as separated on a SDS-PAGE showed the presence of other larger complexes including ribosomal and proteasomal subunits. This presence makes it difficult to establish if some of the SDS-PAGE bands belong to A3a or to the other large complexes. (Figure 3.2).

To get a better separation of the components and rule out proteins that may not be part of the activating complex we modified the purification procedure. The column used in the fourth purification step (Superdex-200) was changed to a superose-6 column which could separate up to 5000 kDa. This column was expected to provide a better separation than the superdex-200 column used in the previous study. Purification of the first three column steps, sephacryl, phenyl sepharose, and Q-sepharose, were the same as previous experiments conducted by Divya. Nevertheless, A3a obtained previously was able to activate both the MCRox1 and MCRsilent forms in the presence of ATP, component A2, and an artificial electron donor dithiothreitol (DTT) (Figure 3.1).[89]

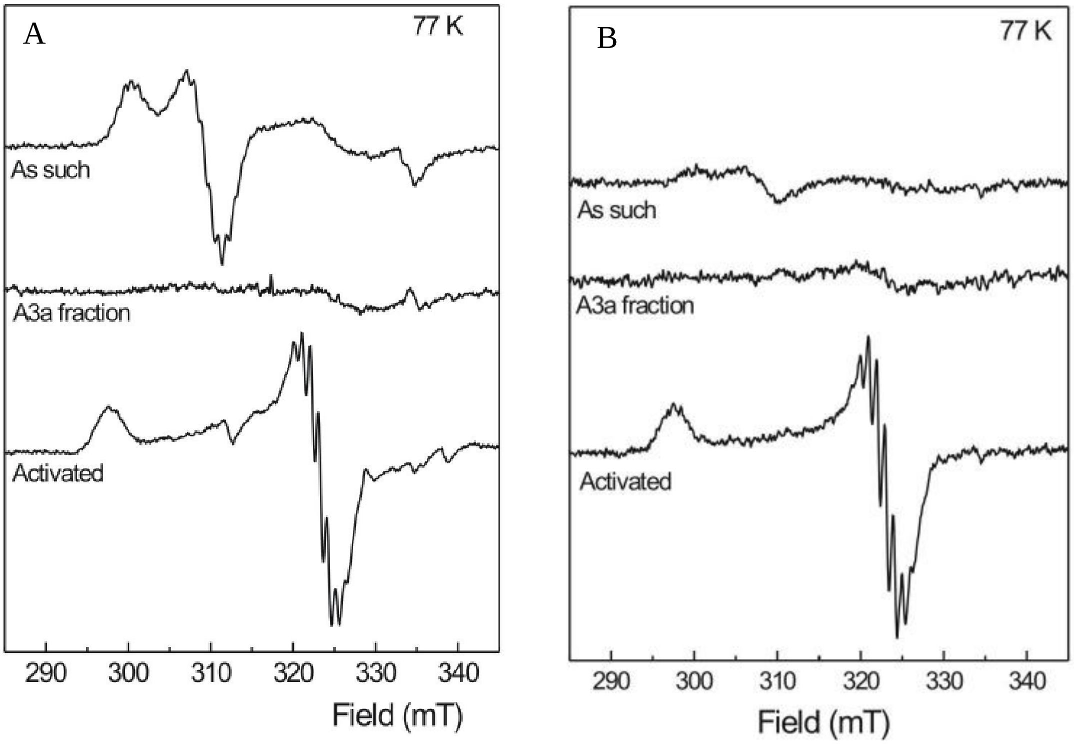

Figure 3.1 Activation of MCRox1 (panel A) and MCRsilent (panel B) in the presence of A3a activating component (Data obtained with permission from reference 78).

Application of the purified enzyme on SDS-PAGE and subsequent sequencing of the individual bands by mass spectrometry showed the presence of subunits from hydrogenases (Figure 3.2, panel A bands 3, 5, 6, 8, 9 and 12), heterodisulfide reductase (bands 2, 8, and 11), polyferredoxin (band 7), iron-sulfur flavoprotein (band 11), methanogenesis marker protein 7 (Mmp7) (band 8), McrC (band 11), and ATP-binding protein (band 10). From this result, a model was proposed for the activation of MCR (Figure 3.2, panel B). Hydrogenases would transfer the electrons from H_2 to the heterodisulfide reductase, which would utilize electron bifurcation to reduce both the heterodisulfide and (poly)ferredoxin.[89] This would lower the potential of the H_2 electrons from -400 mV to -500 mV. ATP hydrolysis coupled to electron transfer via [4Fe-4S] cluster(s) would lower the potential all the way to -650 mV needed to reduce F_{430}. Component A2 would be important for the delivery of ATP to the ATP-binding enzyme, which is a homolog to the Fe-protein important for activation of nitrogenases. The ATP hydrolysis would be coupled to electron transport through the iron-sulfur cluster containing subunits, iron-sulfur flavor protein (Isf) and possibly McrC. Methanogenesis marker protein 7 (Mmp7) could function as a chaperone in this process.

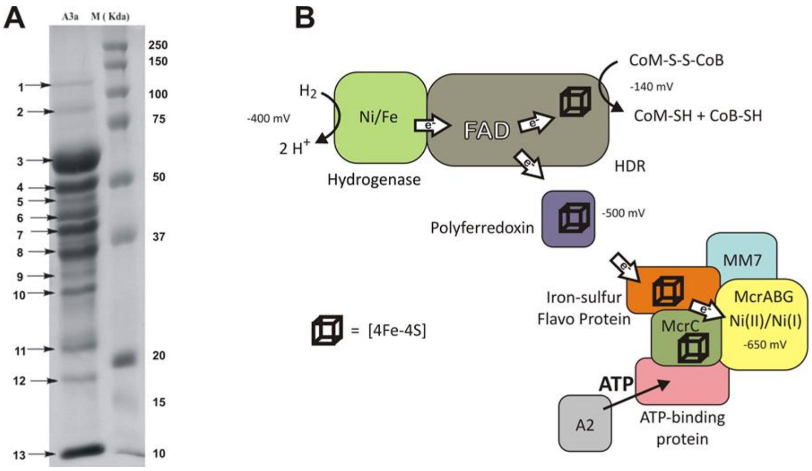

Figure 3.2 Activating complex A3a. A) SDS-PAGE of the purified complex. Individual bands are indicated by number. B) Hypothetical model for the activation of MCR by the A3a complex. (Data obtained with permission from reference 78)

To test this hypothesis, the five core proteins were overexpressed in *E. coli*. In all cases, a 6xHis-tag was added for ease of purification. The core activating components were expressed and could be purified using Ni-Sepharose chromatography except Isf which was expressed in inclusion bodies and could not be purified as a soluble protein. Thus, Isf was expressed as a thioredoxin fusion protein (Isf-Trx).

Figure 3.3, panel B shows that in the presence of the core activating enzymes, component A2, MgATP and Ti(III) citrate, the MCRsilent form from *M. marburgensis* was activated. A stronger reductant Ti(III) citrate, but not DTT was used in the activation assay because the midpoint potential of Ti(III) citrate was similar to the midpoint potential of (poly)ferredoxine (-500 mV). DTT, however, was used in the activation assay when used to measure EPR (Figure 3.1). This was mainly due the fact that Ti(III) citrate is EPR active and has very pronounced peak that overshadow the spectra of the red1 form and made EPR analysis difficult. In Figure 3.3, panel B, the preparation also contained small amounts of the MCRox1 form that was activated with Ti(III) citrate alone, explaining the low level of activity observed in the absence of the activation system. The additional activity obtained in this experiments was only 1-2 % of the expected full activity of MCR. The low activity could most likely be due to the following reasons. 1) Protein(s) may not have folded correctly or may not have a full set of cofactors. 2) It is also possible that not all essential components of the activation system were present in the activation experiments. Therefore, the work presented here was to optimize the activation system. The first aim was to optimize the expression procedures to obtain fully active, cofactor containing enzyme. We emphasis mainly on developing an approach to obtain soluble and stable Isf by itself.

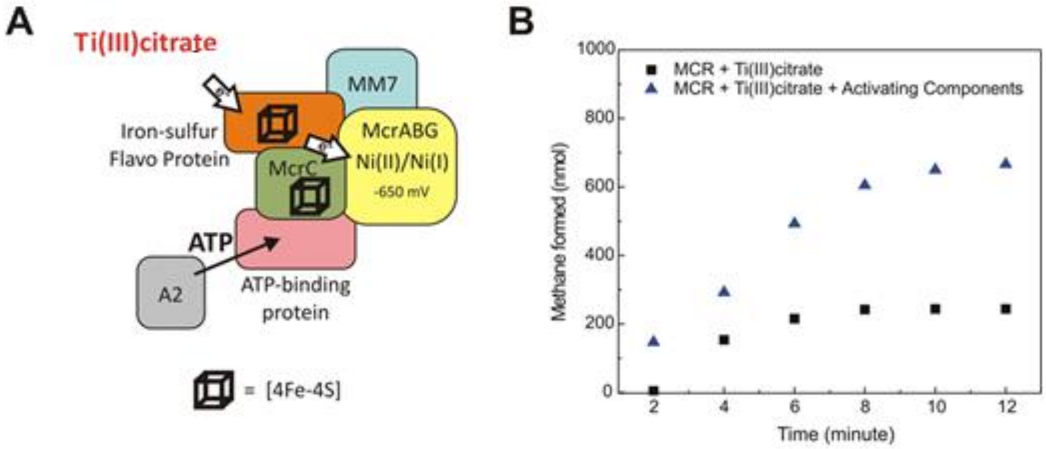

Figure 3.3 Overview of the core activating enzymes (panel A) and their function in the activation of MCR (panel B). In the presence of only Ti(III) citrate, the small amount of MCRox1 present in the sample is activated. In the presence of the activating components, the MCR silent form is also activated.

3.2 Materials and Methods

3.2.1 Purification of MCR

M. marburgensis cells were grown at 65°C in a 13 L glass fermenter (New Brunswick) containing 10 L of growth medium as described in the literature.[92]The fermenter and the media did not need sterilization as the organism has the highest growth rate and practically dominates any other organism that might grow under these growth conditions. The growth medium contained 65 mM KH_2PO_4, 50 mM NH_4Cl, 30 mM Na_2CO_3, trace elements (0.5 mM nitrilotriacetic acid, 2 mM $MgCl_2$, 50 μM $FeCl_2$, 1 μM $CoCl_2$, 1 μM Na_2MoO_4, 5 μM $NiCl_2$) and 20 μM resazurin. The resazurin was added to the medium to indicate when sufficient anoxic conditions were reached. It changed from blue to colorless once the media is anoxic. The medium was gassed with a mixture of 80% H_2/20% CO_2/~1% H_2S. The culture was agitated at 1000 rpm using a stirring motor. Once the medium was anaerobic (~2 h), 200-300 ml of cell culture was inoculated, and the culture was allowed to grow for another 15 h. Once the cell density reached an OD_{570} of 4-6 the cells were harvested.[92]

To get MCR in the MCRsilent state no growth gas switch was necessary. The overnight grown cell culture was cooled down over a 10 min period to 10°C under continuous gas flow. The cells were subsequently harvested anaerobically using a flow-through centrifuge (Hettich, centrifuge 17 RS). Approximately 60 g of wet cells are generally obtained using this procedure.

After the cells were collected, the rotor was brought into the anaerobic chamber (Coy). The cell pellet was collected and resuspended in 50 ml 10 mM Tris-HCl buffer (pH 7.6), and sonicated in a sonication beaker placed on ice for three 3.5 min cycles (pulse 0.5 s ON/0.5 s OF, 70 % power), followed by ultracentrifugation at 35,000 rpm (RCF= 95834, Beckman Ti45 rotor) for 20 min at 4°C. The supernatant was collected and subjected to a 70% ammonium sulfate precipitation step. A 100% Ammonium sulfate solution was added slowly (2.33x the volume of the supernatant) while stirring the mixture on ice inside the chamber. MCR stays in solution under these conditions while most proteins are precipitated. Precipitated proteins were removed by ultracentrifugation at 35,000 rpm for 20 min at 4°C and the supernatant was collected. Again, the collected supernatant was kept in an ice cooled beaker and solid ammonium sulfate was added to make the 100% ammonium sulfate solution. The 100% precipitation step separates MCR from small cofactors present in the cell extract. After the 100% precipitation step, the pellet containing MCR was resuspended in 100 ml 10 mM Tris-HCl (pH 7.6) and loaded onto a Q-Sepharose anion exchange column. Buffer A contains 50 mM Tris-HCl (pH 7.6) and 10 mM HS-CoM. Buffer B contains 50 mM Tris-HCl (pH 7.6), 2 M NaCl, and 10 mM HS-CoM. A step gradient of buffer B (0%, 18%, 20%, 22%, 24%, 26%, 30 %, and 100%) was used to elute the enzymes from the column. Fractions containing MCR were collected and concentrated to 3-5 mL using an Amicon Stirred Cell (Millipore) with a filter with a molecular mass cutoff of 100 kDa. The protein concentration was determined by measuring the absorbance of oxidized enzyme (MCRsilent) at 420 nm using $\varepsilon = 44{,}000\ M^{-1}\ cm^{-1}$ for a molecular mass of 300 kDa.

3.2.2 Amplification, cloning, and expression of gene encoding component A2.

The gene (*atwA)* encoding for component A2 was amplified by PCR from the genomic DNA of *M. marburgensis.* The sequence of the primers are as follows: forward primer CATG<u>GATCC</u>ATGTCT TTCATAAAGCTGGAAAACG (*Bam*HI restriction site is underlined) and reverse primer CATA<u>AGCTT</u>GGTTAT TCCCTGAGCATCCCCC (*Hin*dIII restriction site is underlined). The PCR product and pQE-80L vector were digested with *Bam*HI and *Hin*dIII prior ligation using T4 ligase. To express the gene encoding A2, pQE-80L containing the insert was transformed into *E. coli* strain DH10B after sequence conformation. The cloned fragment has six histidine residues tagged at its N-terminus for ease of purification. *E. coli* DH10B cells harboring a pQE-80L-*atwA* plasmid were grown at 37°C in Luria-Bertani (LB) medium containing 100 mg ampicillin per liter while shaking at 250 rpm. The *E. coli* cells were grown to an OD_{600} of 0.4-0.6. Once the desired OD was reached the gene was induced from the T5 promoter with 1 mM (final concentration) of isopropyl-β-D-thiogalactopyranoside (IPTG). After 5-6 h of post induction growth, the cells were harvested by centrifugation at 5000 rpm for 20 min at 4^oC. The cell pellets were then stored at -80^oC until further use.

3.2.3 Purification of component A2

All sonication and purification steps were performed anaerobically inside a tent (COY anaerobic chamber) filled with 95% N_2 and 5% H_2. The cell pellet was resuspended in 80 ml buffer A (50 mM Tris-HCl, [pH 7.6], 100 mM NaCl) and lysed by sonication for three times (70% Amplitude, 3.5 min, 0.5 ON/OFF pulse). The lysates were centrifuged at 35,000 rpm for 20 min at 4^oC. The supernatant containing A2 was filtered using a 0.22 µm syringe filter and loaded on the 5 ml Ni-Sepharose column. A linear imidazole gradient from 0% to 100% buffer B (50 mM Tris HCl, [pH 7.6], 100 mM NaCl, and 500 mM) was used to elute the protein. The protein concentration was determined by the Bradford assay and the purity was determined by SDS-PAGE.

3.2.4 Amplification, cloning, and expression of genes encoding McrC, Mmp7, Flavoprotein, and ATP binding protein

The gene encoding for Isf, McrC, Mmp7, flavoprotein, and ATP-binding protein were amplified by PCR from genomic DNA of *M. marburgensis.* The sequences of the primers are presented in table 3.1

	Forward primer	reverse primer
A2 (AtwA)	CATG**GATCC**ATGTCTTTCATAAA GCTGGAAAACG	CATA**AGCTT**GGTTATTCCCTGAG CATCCCCC
isf	TCA CCA TCA C**GG ATC C**AT GAT ATC TGC AAG TCC AAG GA	TCA GCT AAT T**AA GCT T**TT ACT CCC CGC TTT GAA TCC
mcrC	TCA CCA TCA C**GG ATC C**AT GTA CGA AAC TTT AAC CTA TCA GGG	TCA GCT AAT T**AA GCT T**TC ACA GTA TGG AGC TTT CAG GTA G
mmp7	TCA CCA TCA C**GG ATC C**AT GAT CGG AAA GTG CAC TCA C	TCA GCT AAT TAA GCT TTC ATG CAC CTC CTA AAG CTA ACT
flavoprotein	TCA CCA TCA C**GG ATC C**AT GAC TGA AAA ACT GAC TGT TGC	TCA GCT AAT TAA GCT TTC ATT GAT CCT TGG GGT AGG
ATP-bindingprotein	TCA CCA TCA C**GG ATC C**AT GAC AAG AGT GAT TAC AGT CGC A	TCA GCT AAT T**AA GCT T**TC ACC TTC GCC CCA TCA A

Table 3.1. The primers used for amplification of the respected genes from genomic *M. marburgensis*. The restriction enzymes sites are in bold.

3.2.5 Purification of McrC, Mmp7, Flavoprotein, and ATP-binding protein

The purification of the above proteins was identical to the purification of component A2 described in the previous section.

3.2.6 The reconstitution of McrC and Isf

Reconstitution was performed as described in the literate with some modification. 5-10 mg of protein was added to 50 ml Tris buffer (pH 7.6). 300 µl of 60 mM sodium sulfide, 300 µl of 60 mM ferric chloride, and 30 µl of 15 mM FMN (for Isf) were then added stepwise at 10 min interval. The mixture was then incubated at 4^{o}C overnight. The next day, the mixture was concentrated using a 10 kDa filter and precipitated particles were removed using a 0.2 µl syringe filter or by centrifugation. The excess FMN and Fe, S were removed using a desalting column (PD10).

3.2.7 Purification of the A3a protein:

Four column steps were used to obtain A3a from *M. marburgensis*. The *M. marburgensis* cells were grown as described above. The cell extracts were routinely prepared from ~60-70 g (wet mass) of cells that had been freshly harvested under anoxic conditions without special pretreatment of the cell culture. The cells were suspended in ∼50 mL buffer A (50 mM TrisHCl, [pH 7.6]). Cells were lysed by sonication followed by centrifugation at 35,000 rpm (RCF= 95834) for 20 min at 4°C. The supernatant was concentrated to 10 ml using an Amicon Stirred Cell (Millipore) with a filter with a molecular mass cutoff of 100 kDa and loaded onto a Sephacryl S-300 column. The protein was eluted with buffer A (containing 50 mM TrisHCl, [pH 7.6] and100 mM NaCl). The fractions that showed activity were pooled and loaded to the Phenyl-Sepharose column. A decreasing step gradient of buffer B from 1 M to 0 M of NaCl in Buffer A was used to elute fractions from the phenyl-Sepharose column. The fractions that showed activity were combined and loaded onto a Mono-Q column. The fractions were eluted with an increasing salt gradient from 0 to 1 M NaCl in Buffer A. Finally fractions that showed activity from Mono-Q were further purified using a Superose-6 column equilibrated with buffer B after concentrating to 100 µL. The Superose-6 fractions were subjected to activity assays and the fractions with activity were analyzed using SDS-PAGE, UV-Vis, EPR, and MS

3.2.8 Activation of the MCRsilent form

100 µM MCR was incubated for 20 min at 60°C in the presence of component A2, the core components of A3a, 10 mM MgATP, 20 mM Ti(III) citrate, and 10 mM methyl-coenzym M in a total volume of 800 µl. The activated sample was then assayed for MCR activity as described below.

3.2.9 Determination of methyl-coenzyme-M reductase activity

Activity of MCR was determined as described before (chapter two). Methane formation was detected by withdrawing a gas sample from the headspace of a closed 8 ml serum vial containing 800 µl assay solution. The solution contained 10 mM methyl-coenzyme M, 1 mM coenzyme B, 0.3 mM aquocobalamin, 20 mM Ti(III) citrate. The gas phase was 95% N_2/5 % H_2. The activity assay was started by heating the assay mixture to 65°C. Gas samples from each vial were withdrawn and injected into the gas chromatography every 2-3 min. The methane production was quantified using a 1% methane standard for each set of runs.

3.2.10 EPR Spectroscopy

CW EPR spectra were measured at X-band (9 GHz) frequency on a Bruker EMX spectrometer, fitted with the ER-4119-HS high sensitivity perpendicular-mode cavity. The Oxford Instrument ESR 900 flow cryostat in combination with the ITC4 temperature controller was used for measurements in the 4 K to 300 K range using a helium flow. Measurements at 77 K were performed by fitting the cavity with a liquid nitrogen finger Dewar. All spectra were recorded with a field modulation frequency of 100 kHz, modulation amplitude of 0.6 mT, and a frequency of 9.386 GHz.

3.3 Result and Discussion

3.3.1 Purification of Methyl Coenzyme M reductase (MCR):

Both MCR I and MCR II can be obtained after Ammonium sulphate and Q-Sepharose purification steps. The purification profile is shown in Figure 3.4. Both pure MCR I and II can be obtained with this procedure, but only MCR I was used for this study. MCR I elutes down at 24-

26 % buffer B (2 M NaCl) and the fractions are yellow in color and can be easily identified by eye. MCR II elutes a little earlier than MCR I and has a yellow color (Figure 3.4).

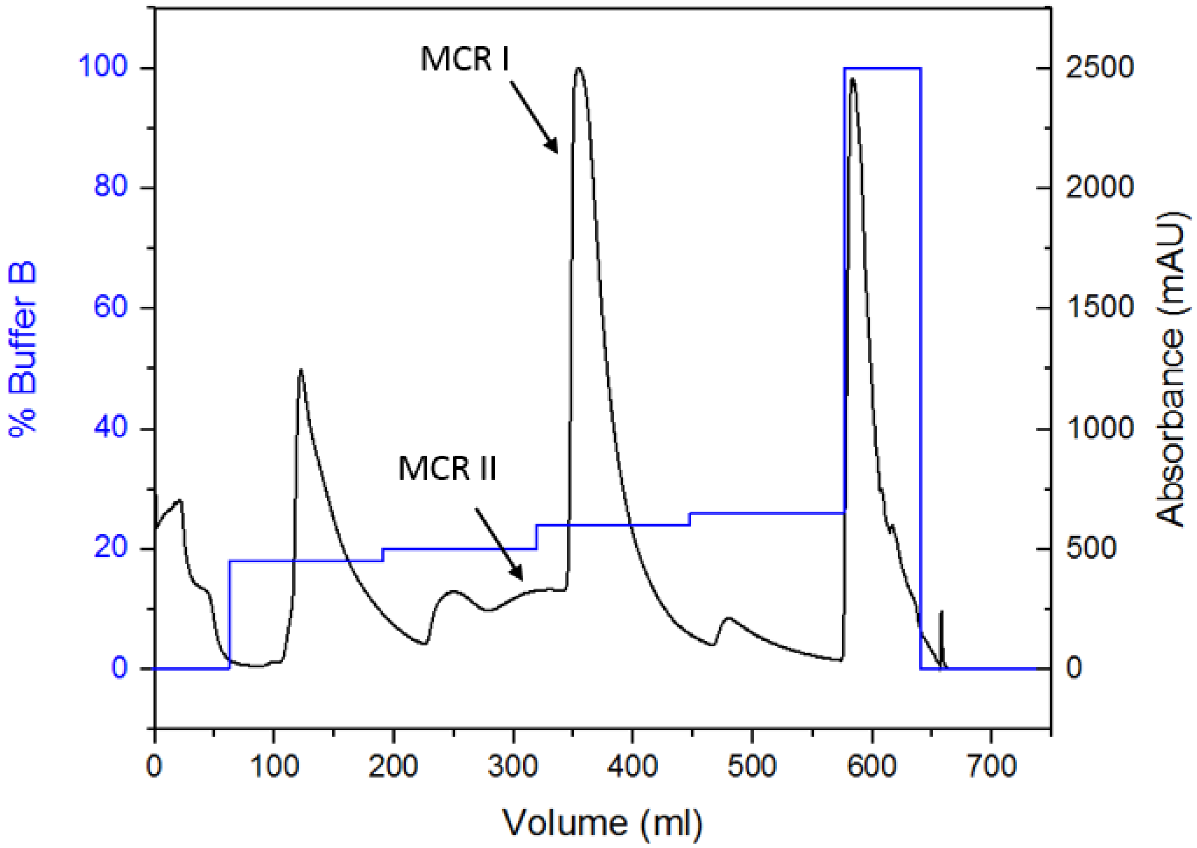

Figure 3.4 The purification profile for the Q-sepharose column.

The absorption spectrum of MCR is shown in the Figure 3.5.

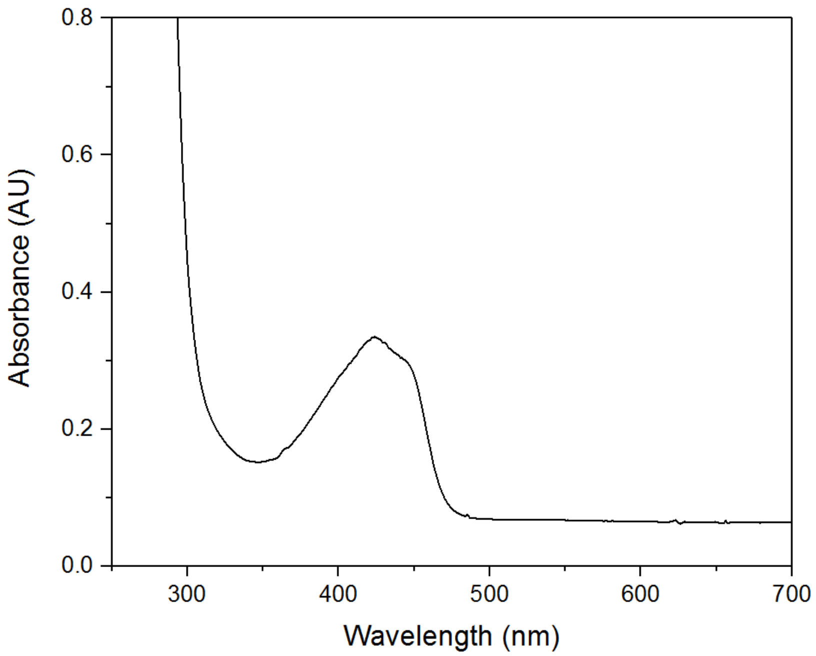

Figure 3.5 Uv-Vis absorption spectra of MCRsilent.

3.3.2 Purification and characterization of Isf

Previous attempts to purify Isf failed as it ends up being expressed in the inclusion bodies. The Isf was extracted from the inclusion bodies using 8 M urea and sonication with subsequent purification on a Ni-sepharose column. However, urea needed to be washed before the enzyme was used in the activation experiments through dialysis (buffer exchange). The protein precipitated during dialysis even if the dialysis was performed at lower temperature (4^{o}C).

To help solubilize Isf, the protein was expressed with a thioredoxin (trx) tag. The trx tagged Isf was soluble and purified on a Ni-column. However, since trx could interfere with the activity assay, the trx needed to be cleaved with an enterokinase prior the activation experiment. And this attempt was not successful as the protein was not recovered after cleavage of the trx tag. This experiment was done by Dr. Divya Prakash.

Due to the above-mentioned problems associated mainly with getting soluble Isf, the activation system studies lagged. Thus, it was necessary to look for a protocol that can yield soluble protein. Reducing the growth rate after induction and lowering the inducing agent may help to increase the solubility of recombinant proteins. This approach was used to express CfbE (chapter two) and was found to yield soluble protein. Thus, the same approach was performed for purifying Isf without the trx tag. For this purpose, cells containing Isf were grown in LB media containing 10% glycerol. The cells were incubated at 37^{o}C 250 rpm shaking until the OD reached 0.8. The temperature and the shaking were then reduced to 25^{o}C and 150 rpm prior to inducing the cells with IPTG. Furthermore, the concentration of IPTG was reduced from 1 mM to 200 μM and the cells were incubated overnight after induction. The Isf was found to be expressed as soluble protein in cytosol and the SDS-PAGE and Uv-Vis spectra of purified protein is shown in Figure 3.6 panel D.

The amino acid sequence of Isf reveals a cysteine motif, CxxCxxCxxxxxC which is typical for binding of an [4Fe-4S] cluster. Currently, there is no crystal structure for Isf. Thus, an I-TASSER (Iterative Threading ASSEmbly Refinement) was used to predict its structure from the primary amino acid sequencing. Consistent with the primary structure, the model obtained with I-TASSER predicts the binding of an [4Fe-4S] cluster with 4 cys on the flexible loop and at the coordination distances. Furthermore, the homologue study and the model suggest the presence of FMN as a cofactor for Isf thus molecular docking was performed to deduce the binding site of FMN on Isf (Figure 3.6 panel A).

Using the model predicted by I-TASSER as starting protein structure, FMN docking was performed. Autodock vina was used for this purpose. Autodock vina is an open source program developed by The Scripps Research Institution for molecular docking and virtual screening.

Polar hydrogen atoms were added to each residue and Gasteiger charges were assigned to every atom within the receptor (Isf). As the binding site is not known, it was first performed blind docking by search the whole protein site.

Up to nine possible docking sites were obtained along with their respective score (affinity). From this initial docking outcome, two possible binding sites were identified. Next, FMN was separately docked at each site by narrowing the search space and the results were compared. The one with higher affinity is shown in the Figure 3. 6, panel A. This pose was similar to the Isf homolog with known crystal structure. As shown in the Figure 3.6 FMN was docked on the surface of the protein.

Reconstitution of Isf

The purified Isf did not contain FMN. The Uv-vis absorbance and the visual color inspection of the protein did not indicate the presence of FMN. However, it is not uncommon to get recombinant protein without the cofactor (FMN). Thus, reconstitution was performed in the presence of FMN. The reconstitution was also aimed to reconstitute 4Fe-4S cluster as the protein is expected to contain the cluster. Figure 3.6 shows the absorption spectra of Isf before and after the reconstitution. Before reconstitution the spectrum shows a Heme characterizes by a sharp peak around 410 nm. (Figure 3.6 panel B). From the spectrum and visual inspection of the reconstituted Isf, it was clear that the FMN did not bind to the protein. Thus, FMN most likely is not a cofactor of Isf.

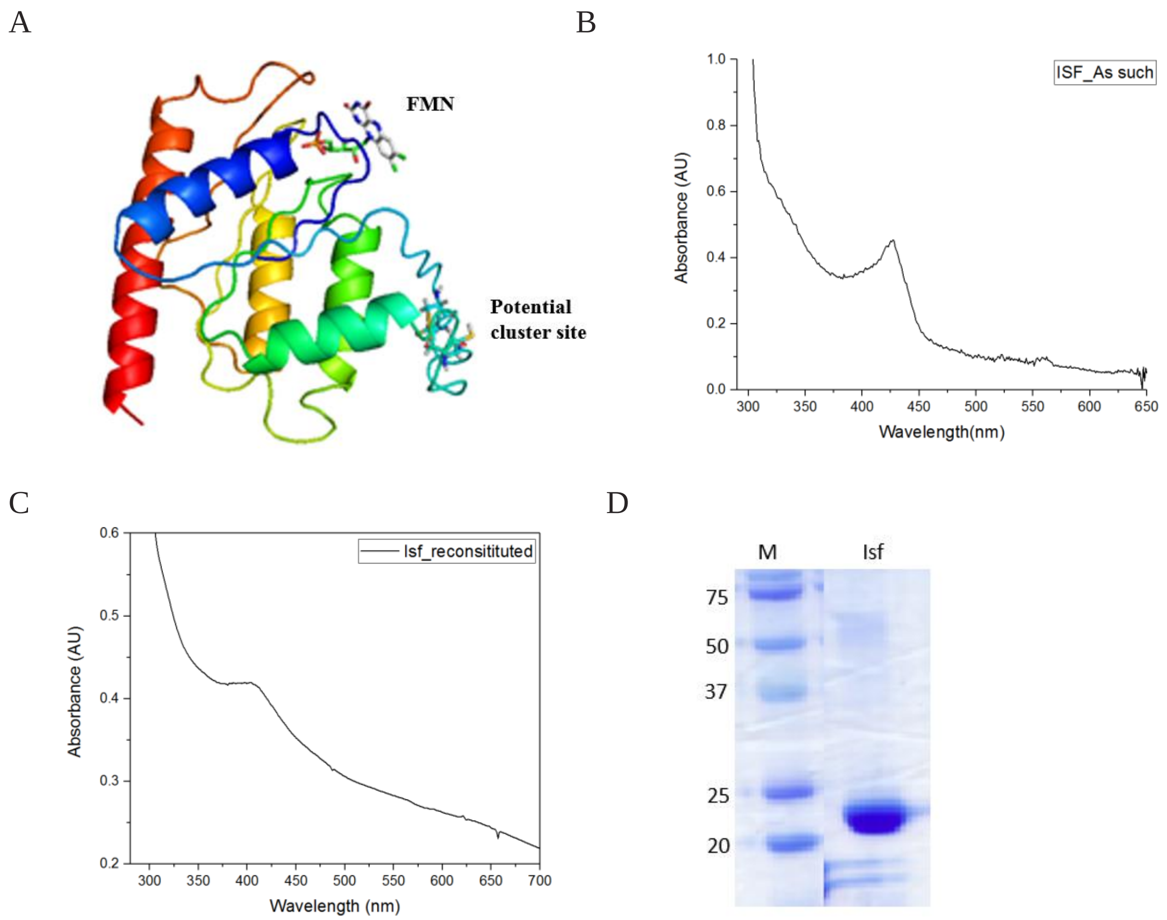

Figure 3.6. Uv-vis spectra (B and C, I-Tasser predicted structure (A), and the SDS-PAGE of Isf (D)

3.3.3 Characterization of McrC

McrC also contained a low amount of [4Fe-4S] clusters based on absorption and EPR experiments. The Uv-vis absorption spectrum of McrC, after reconstitution, is shown in Figure 3.7 panel A. The broad peak around 420 nm is typical of [4Fe-4S] cluster. Moreover, the cluster was reduced by treating with dithiothreitol (DIT). Furthermore, the EPR spectra of McrC suggests the presence of an [4Fe-4S] cluster. These spectroscopic results support that the McrC contains an [4Fe-4S] cluster. The primary sequencing of McrC does not indicate the usual cluster binding motif of [4Fe-4S] cluster which usually are characterized by a cysteine motif

(CxxCxxxCxxxxxC). However, two cys (shown by the two arrows on Figure 3.7 panel A) are present on the surface of the protein which may be involved in the binding of the cluster. We hypothesis that McrC may be is a dimer and the cluster might form a bridge between the two dimers. Reconstitution of the protein with the cluster gave up to 10-fold increase in cluster content (Table 3.2). The reconstitution was performed with and without supplement of cysteine, but there was no difference in the amount of the reconstituted cluster.

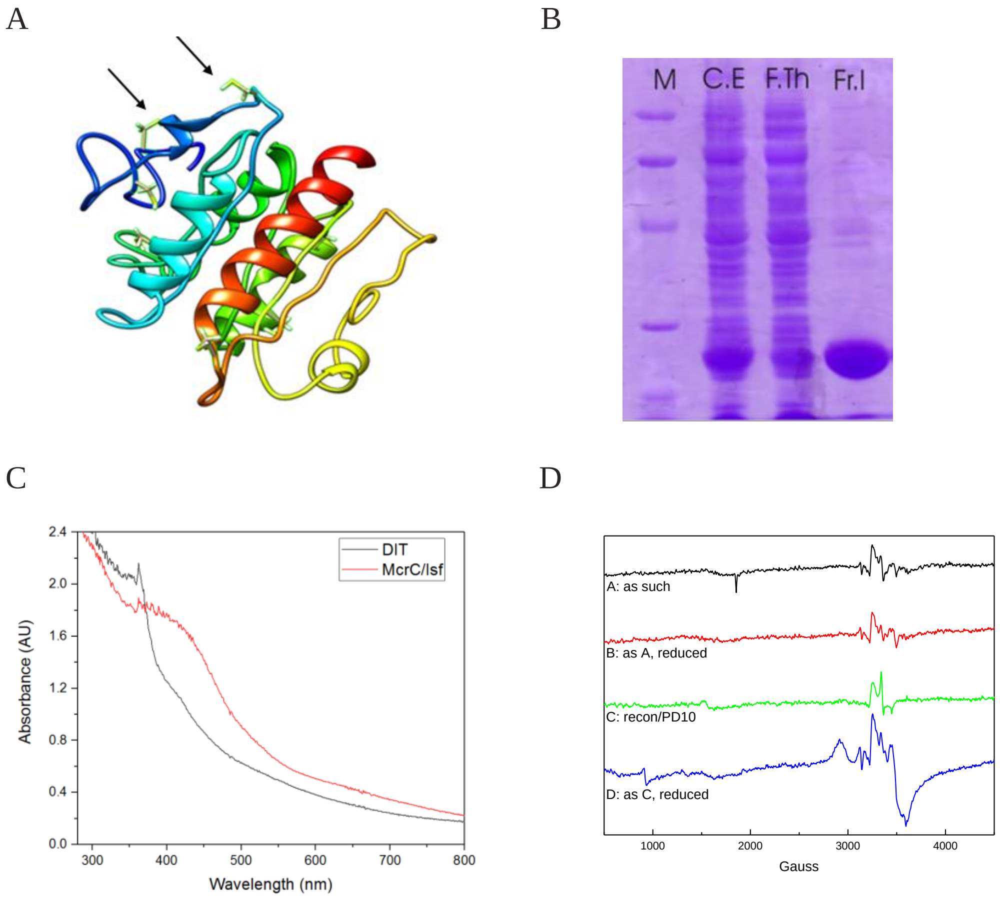

Figure 3.7 Characterization of McrC. The I-TASER predicted structure (A), the arrows indicate the position of two cys on the surface of the protein, SDS-PAGE of McrC (B), Uv-Vis spectra (C) and EPR spectra (D) of McrC

Fraction	% in vitro Reconstituted
As such	4.2
reconstituted	43.5

Table 3.2. The reconstitution of McrC

3.3.4 Optimizing the purification of component A3a

The activation of MCR in the presence of the core activating components was performed. However, the activity obtained was not high enough. Although the core components believed to comprise the activating system seemed to contain the expected cofactors, the result obtained in the current study was not satisfactory. Thus, it was necessary to look up if some proteins are missing from the core activating components. We made a small modification and repeated the experiment performed previously by Divya.

To get a clear separation of the components that may not be part of the activating complex, the column used in the fourth purification step was changed to a high-performace size exclusion, superos-6 column, which can separate molecules in the range of 5 kD to 5000 kDa. This column was expected to provide a better separation than the superdex column used in the previous study which can only separate upto 500 kDa.

After the superose purification step, four peaks were obtained (Figure 3.8 panel A). The activity assay was performed for each individual peaks and only one fraction, (Figure 3.8 panel A, the second peak from left) showed activity albeit in low amount. The EPR spectrum of the active fraction is shown in Figure 3.8, lower pannel. The EPR spectrum would indicate the presence of [4Fe-4S] cluster containing enzymes. (Figure 3.8 panel C).

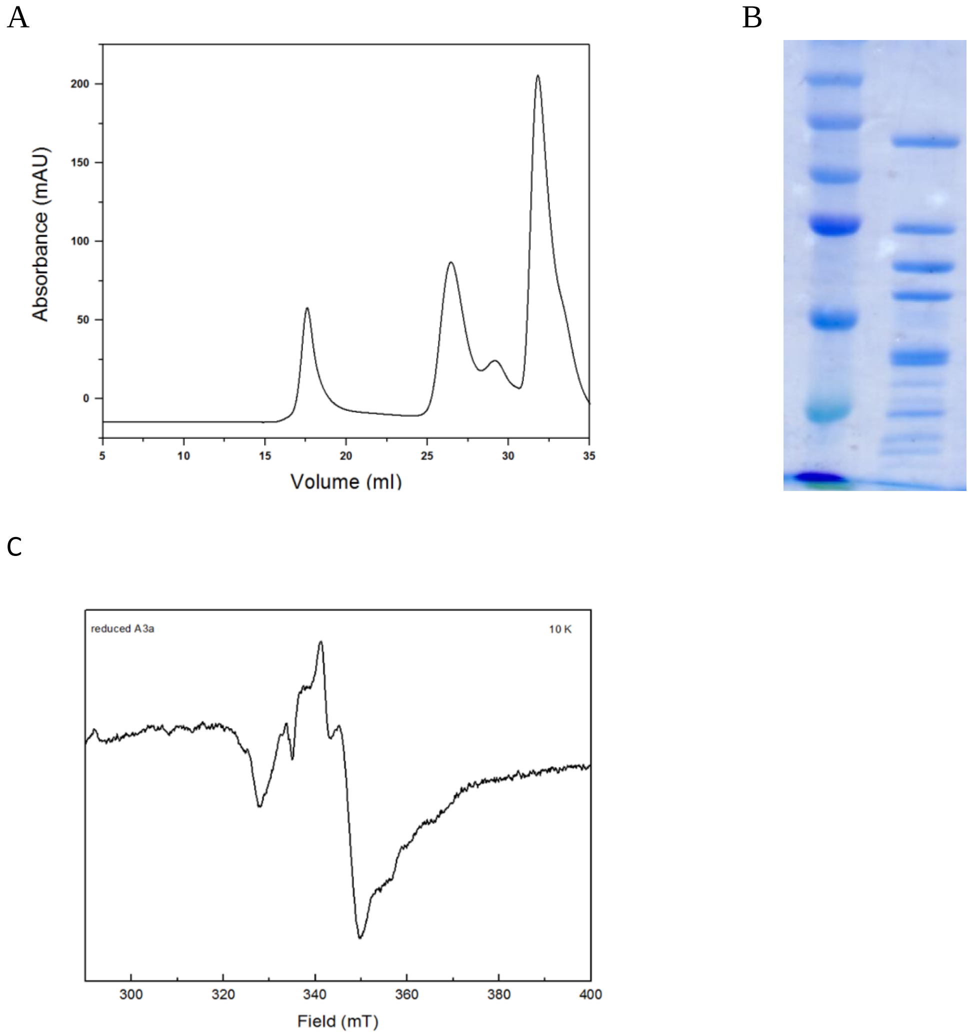

Figure 3.8 The purification profile (A), the SDS-PAGE (B), and the EPR spectrum (C) of the Superose fraction.

Some of the bands obtained after superpose-6 column step were sequenced. The F_{420} dependent hydrogenase was present in the band analyzed. The same protein was also detected in the previous result. However, since the sample obtained had low concentration and only faint bands were present on SDS-PAGE (Figure 3.8 panel B). Consequently, sequencing of all bands was not possible as this time. This experiment will be repeated with some modifications and optimizations. Once a good amount of protein and satisfactory activation are obtained, the individual components comprizing the complex will be sequeenced using MS. Individual component comprising the complex would then be cloned and expressed if there is a need to. This study is currently undergoing, and Bryan is working on it.

3.4 Discussion and conclusion

MCR is quite a stable enzyme, however, the most stable form of the MCR, so called MCRsilent form, is unfortunately inactive. Even though there are established protocols routinely used to obtain the active MCRred1 form, the enzyme is only stable for a few days even in an exclusive oxygen free environment. Moreover, currently, there are no chemical method(s) to activate MCRsilent to MCRred1. Luckily, the *M. marburgensis* contains an activating system involved in activating MCR *in vivo.* The activation system comprises of a large complex and is referred to as A3a. Its function depends on hydrolysis of ATP provided by component A2 and a transfer of electrons(s) through a series of [4Fe-4S] containing proteins.

The activating system of MCR was investigated and the components have been characterized. A working model was hypothesized based on the previous studies in Duin's lab. According to the model, a pair of electrons are derived from the oxidation of molecular hydrogen catalyzed by hydrogenase. The electrons undergo a Flavin based electron bifurcation in the Hdr complex resulting in a lower potential electron (-500 mV). The low potential electron then moves to polyferredoxin, Isf or McrC. The final transfer of electron to MCR is coupled to ATP hydrolysis.

In the current activation study, an artificial electron donor (Ti(III) citrate) was used. Since the potential of Ti(III) citrate is comparable to the cluster potentials of polyferredoxin (-500 mV) it is reasonable to assume it would replace polyferredoxin in providing electron to the [4Fe-4S] of Isf or McrC. Previous attempt in our lab to clone and express polyferedoxin was not successful. It is not clear if replacing the natural electron donor with an artificial donor could be one of the reasons for the low activity observed with recombinant core proteins of the activating complex. It is noteworthy also that polyferredoxin and Hdr and hydrogenases were copurified with the activating complex even in the final purification steps. Thus, it is fair to assume that some of these proteins may be directly involved in regulating the function of the activation complex during the activation of MCR. It would be interesting to express Hdr and polyferredoxin and add them to the core activating components and see if they can augment the activation of MCR. The hydrogenase:HDR complex is available in the lab, but polyferredoxin is currently not being purified.

One of the core activating proteins is Isf. No crystal structure is available for Isf, but the homologues protein and the I-TASSER prediction suggest that the protein contains both the FMN and [4Fe-4S] cofactors. However, the purification of Isf and subsequent reconstitution with the cluster and FMN did not result in the binding of FMN while the cluster content was slightly increased. This was not a surprise considering the possible role of FMN during an electron transfer in the MCR activation process. FMN has a mid-point potential of -277 mV while [4Fe-4S] has around -400 mV. According to the model described previously electrons from ferredoxin (-400 mV) are believed to be transferred to Isf and/or McrC. Considering the higher potential of FMN than the upstream (poly)ferredoxin, it is not favorable for electrons to be transferred from ferredoxin to FMN and then to the cluster in Isf. Rather the electrons would transfer directly to the cluster in Isf and subsequently to MCR (Ni(II)) with lower potential (-650 mV). Therefore, it would be reasonable to argue that FMN may not be required for Isf to function as an electron shuttle during the reductive activation of MCR. The role of this protein have not been assigned.

The low amount of activity observed made it difficult to determine if the protein plays a role or not.

The low level of activation obtained in the presence of core activating components could perhaps be due to the fact that some proteins are missing. Thus, further studies will be needed to get reasonable activation. Protein-protein interaction coupled with MS identification of the interacting proteins, for example, can provide valuable information regarding this interesting activating system.

Chapter Four: Investigating the Inhibition mechanism of 3-Nitrooxypropanol (3-NOP) on Methyl-Coenzyme M Reductase (MCR)

4.1 Introduction

Methane is a potent greenhouse gas and it is the second most abundant greenhouse gas just after carbon dioxide. Furthermore, methane is 28-30 times more power in trapping radiant energy than CO_2, making it an important greenhouse gas from an environmental perspective. Large portions of methane are emitted to the atmosphere from several sources, contributing significantly to the greenhouse effect and subsequent global warming. Ruminants (e.g., cattle, sheep, and goat) are one of the major anthropogenic sources of methane. Yearly, about 100 million tons of methane is emitted from the ruminants which corresponds to ~ 20% of the total global methane emission to the atmosphere.[2] Methane is produced in the gut of ruminants as a byproduct of methanogensis. A significant amount of energy available to the host is lost in the process of methane formation by methanogenic Archaea. Organic materials (cellulose) is decomposed to smaller molecules like butyrate, propionate, acetate, CO_2, and H_2 by mostly anaerobic bacteria. The methanogenic Archaea produce methane from acetate and/or CO_2 and H_2. This action facilitates the decomposition of plant materials. The methane production pathways, however, are responsible for the loss of up to 12% gross energy ingested by the ruminant.[9] Therefore, it is evident from both economic and environmental perspective that blocking methane production from ruminants, at least partially, is of a significant importance.

In the biogenesis of methane several enzymes are involved, and each enzyme could be a target for the inhibition of methane production. More than 30 proteins involved in the process of methanogenesis have been identified as a potential target for pharmacological intervention.[50]

Considering its key role in the biosynthesis of methane, MCR is an attractive target for the inhibition of methanogenesis in ruminants and other sources of methane.

Several inhibitors of methanogenesis have been identified.[42] Most of these compounds are structural analogues of methyl-coenzyme M, one of the MCR substrates. 2-Bromoethanesulfonate (BES) is one of the potent inhibitors of MCR that have been widely used for experimental purposes. It quenches MCRred1 signal and a radical species is formed.[51] The other potent inhibitor of MCR is 3-Bromopropanesulfonate (BPS). BPS reacts with MCRred1 and a Ni(III)-propanesulfonate (Ni(III)-BPS) is formed.[49] The Ni(III)-alkyl species formed in the reaction between MCRred1 and BPS is relatively stable with a half-life time of about 8 h. Bromomethane (Br-CH_3) can also reversibly inhibit MCR. Like the Ni(III)-BPS, a Ni(III)-methyl intermediate was detected when Br-CH_3 was reacted with MCRred1. This intermediate has shorter half-life (20 min) comparing to the Ni(III)-BPS.[93] A similar intermediates was also reported when I-CH_3 reacted with MCRred1.[94]

All inhibitors mentioned above, however, have an inherent drawback that prevent them from being authorized to be used as an additive for cattle feeding. Both BES and BPS are charged compounds (see Figure 4.1), and thus cannot easily diffuse through the hydrophobic membrane of methanogens. This is evident if you look the difference in the IC_{50} *in vivo* and *in vitro.* The *in vitro* IC_{50} of BES is 4 µM and for BPS is 0.05 µM (for MCR from *M. marburgensis*). On the other hand, the *in vivo* IC_{50} is reported as 1 mM for both inhibitors which is too high for pharmacological applications. Thus, these inhibitors are considered as poor inhibitors *in vivo*. Another main problem with these inhibitors is their unfavorable toxicological profiles which prevent them from being used as feed additive.[42,83] Therefore, it is empirical to search for some alternative inhibitors with better pharmacological profiles.

DSM Nutritional Products, a Switzerland based company have developed a small organic compound, called 3-nitrooxypropanol (3-NOP) using a 3D pharmacophore based virtual screening (the chemical structure of 3-NOP is shown in Figure 4.1). 3-NOP has been found to be effective in decreasing enteric methane emission from different livestock. It was found to partially block, at the concentration used for the study, the emission of methane from sheep[95], from cows[96], and from beef cattle.[49] Moreover, at the concentration tested, 3-NOP apparently had no side effects on the cattle. An increased body weight gain without negatively affecting feed intake was reported while the milk production and composition remained unaltered.[97] At the lower inhibition of methane, H_2 concentration in the rumen remains constant, even though its consumption by methanogens is reduced due to partial inhibition of methanogenesis. This could be due to that fact that the H_2 regulatory pathways are stimulated during the imbalance of H_2 concentration in the rumen.[98]

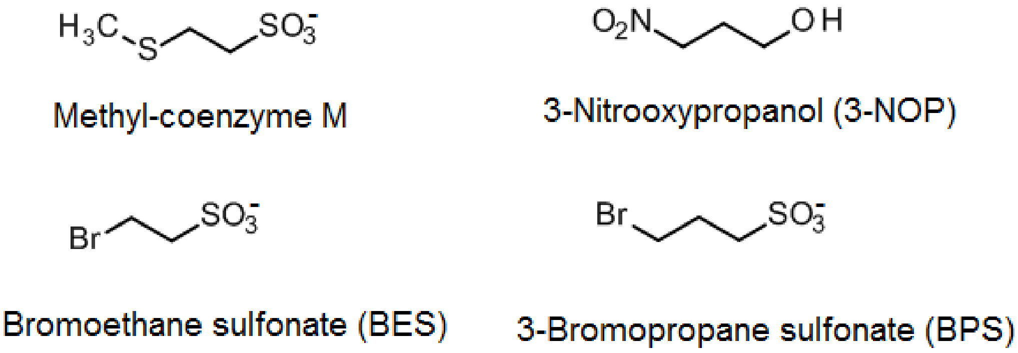

Methyl-coenzyme M

3-Nitrooxypropanol (3-NOP)

Bromoethane sulfonate (BES)

3-Bromopropane sulfonate (BPS)

Figure 4. 1. The molecular structural the inhibitor 3-NOP, and the natural MCR substrate CH_3-S-CoM.

Because the redox potential Eo′ of the F_{430} (Ni^{2+})/ F_{430} (Ni^{1+}) couple inside the enzyme is estimated to be -600 mV (Vs NHE), the enzyme is very susceptible to inactivation by oxidants. 3-NOP is a structural analogue to CH_3-S-CoM (Figure 4.1) and has a mild oxidizing potential. Figure 4.2 demonstrates the docking of 3-NOP and CH_3-S-CoM on the active site of MCR. The nitrate ester group of 3-NOP was positioned near the Ni(I) center of MCR and its hydroxyl group is coordinated to the Arg120 through a water molecule. Arg 120 is responsible in coordinating the sulfonate group of CH_3-S-CoM through a water molecule (Figure 4.2 panel B).[98]

Moreover, Duin et al reported the inhibitory effect of 3-NOP on methanogensis and on the purified MCR.[98]3-NOP was found to react with the MCRred1 form but not MCRox1 form (Figure 4.3). Nitrite, a possible product of the inhibition reaction was also found to inhibit the enzyme albeit at slow rate. Interesting both nitrite and nitrate was detected when 3-NOP was reacting with MCRred1. While 1,3-propanediol was also found in the *in vivo* experiments, this compound has not yet been detected in the *in vitro* studies.

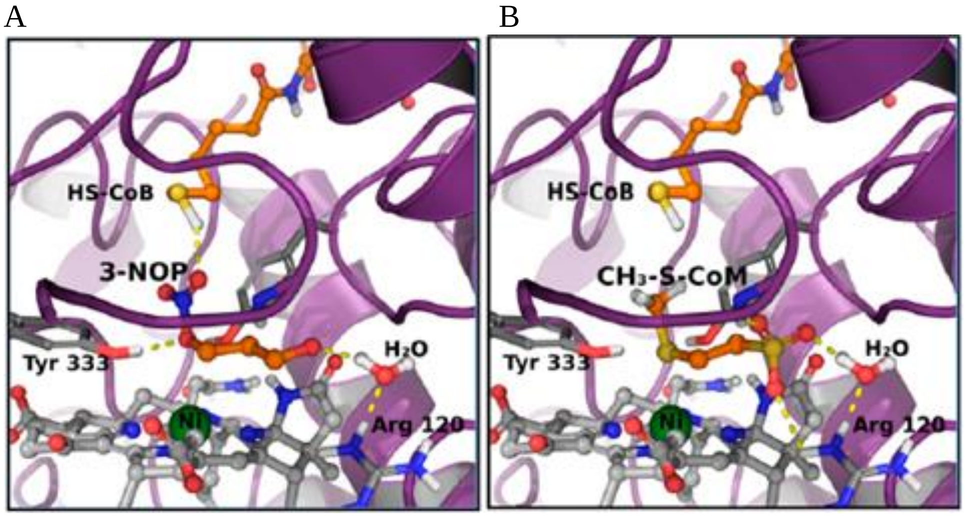

Figure 4.2. Docking of 3-NOP (panel A) and CH_3-S-CoM (panel B) on MCR. Obtained with permission from reference 97.[98]

The aim of the current study is to investigate the detailed mechanism of inhibition of 3-NOP on MCR. This work has been performed together with Bryan Cronin from the Duin laboratory.

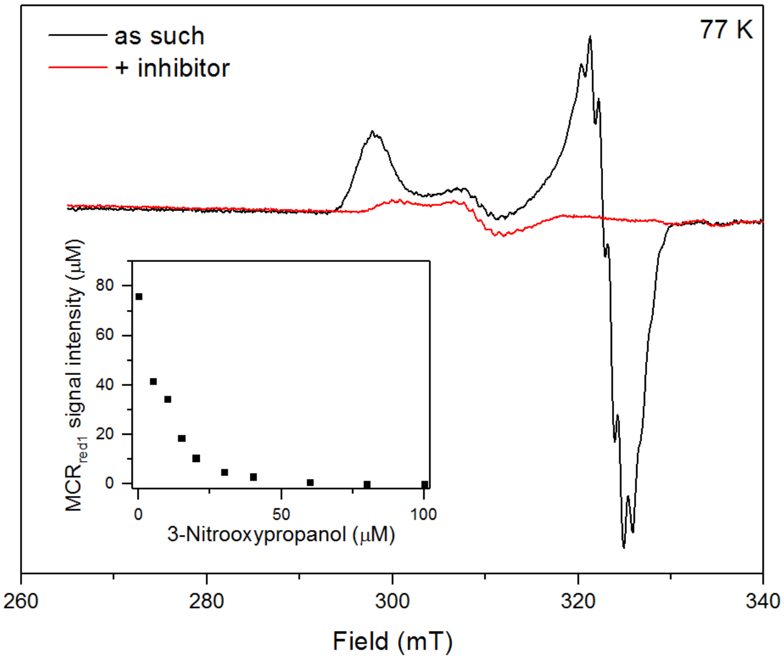

Figure 4.3. Effect of 3-NOP on MCRred1 and MCRox1.

4.2 Materials and Methods

4.2.1 Reagents

3-nitrooxypropanol (3-NOP) was provided by DSM Nutritional, Basel, Switzerland. Isopentane and other reagents were purchased from Sigma Aldrich.

4.2.2 Purification of MCRred1 state

M. marburgensis cells were grown anaerobically at 65°C in a 13 L glass fermenter (New Brunswick) containing 10 L of growth medium as described in chapter three.

To get the MCRred1 form, a growing cell culture was purged with 100% H_2 for 20 min by switching the gas supply from 80% H_2/20% CO_2 prior to harvesting. The culture was cooled immediately to around 10°C under continuous gas (100% H_2) flow. The cells were then harvested anaerobically and kept at 4°C for immediate use.

MCRred1 was purified as described in chapter three. To stabilize the MCRred1 form, HS-CoM was present during all purification steps. The concentration of the MCRred1 was determined from the spin integration of the EPR spectra against a 10 mM Cu(II)sulfate standard. The total enzyme concertation was quantified from the absorption spectra of the silent from using the extinction coefficient (44,000 $cm^{-1}M^{-1}$)

4.2.3 Measuring the reaction product of 3-NOP

The MCRred1 form was incubated with 3-NOP for 15 min. The reaction product(s) was separated from the inactive MCR using a 10 KDa filter. The filtrate was then analyzed using proton NMR.

4.2.5 Freeze quench experiment

A rapid freeze quench (RFQ) combined with EPR measurements was performed to trap and characterize any intermediates that may form after the reaction of 3-NOP and the MCRred1. For this purpose, a freeze quench apparatus shown in Figure 4.4 was used. The enzyme, MCRred1, was placed in one syringe and 3-NOP (the inhibitor) was placed on the second syringe. 3-NOP and MCR were then rapidly mixed and incubated for certain time before ejecting the reaction mixture through an aging tube into an EPR tube in cold isopentane (~ -140°C) to quench the reaction. The frozen reaction mixture particles in the funnel area were collected and pressed into an EPR tube. The reaction was quenched at different time interval (4.6 ms, 10 ms, 20 ms, 40 ms, 70 ms, 100 ms, 150 ms , 500 ms, 1 s, 5 s and 10 s) and the samples were analyzed by EPR spectroscopy.

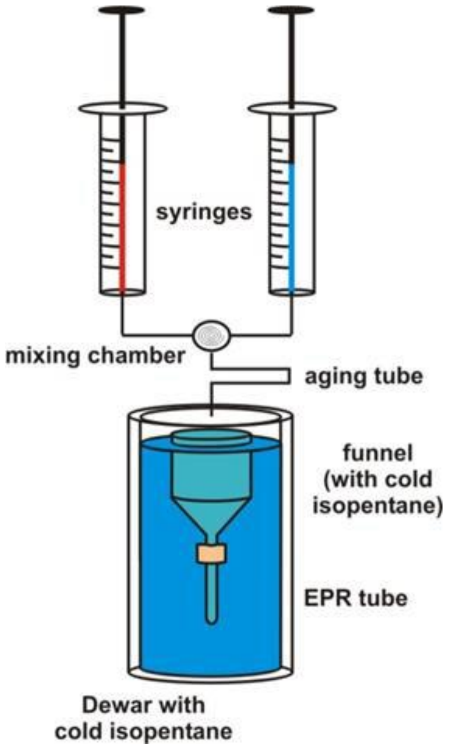

Figure 4.4. Schematic set up of freeze-quench experiment

4.2.6 EPR Measurements

All EPR measurement were performed on a Bruker EMX spectrometer fitted with an ER-4119-HS (high-sensitivity) perpendicular-mode cavity. Continuous-wave (CW) EPR spectra were measured at X-band (9-GHz) frequency at 77 K by fitting the cavity with a liquid nitrogen finger Dewar. The spectra were recorded with a field modulation frequency of 100 kHz, modulation amplitude of 0.6 mT, and frequency of 9.386 GHz. The EPR signal intensities were determined by measuring the respective EPR-active species under nonsaturating conditions. The spectra were double integrated, and area of each signal was compared with that of a 10 mM copper perchlorate standard (10 mM $CuSO_4$; 2 M $NaClO_4$; 10 mM HCl).

4.3 Results

4.3.1 Purification of MCRred1

The purification profile of MCR is presented in chapter three (Figure 3.) The red1 form can be easily distingushed from the silent and ox1 forms by its characteristics green color as well as by its distinct EPR and UV-vis spectra. The Uv-vis and EPR spectra of the red1 form is shown in Figure 4.5. 100-300 µM of MCR (upto 90% red1) are routinely obtained. Enzyme activity is lost upon overnight storage, therefore all of the experiments are performed with in 24 h of the purification step.

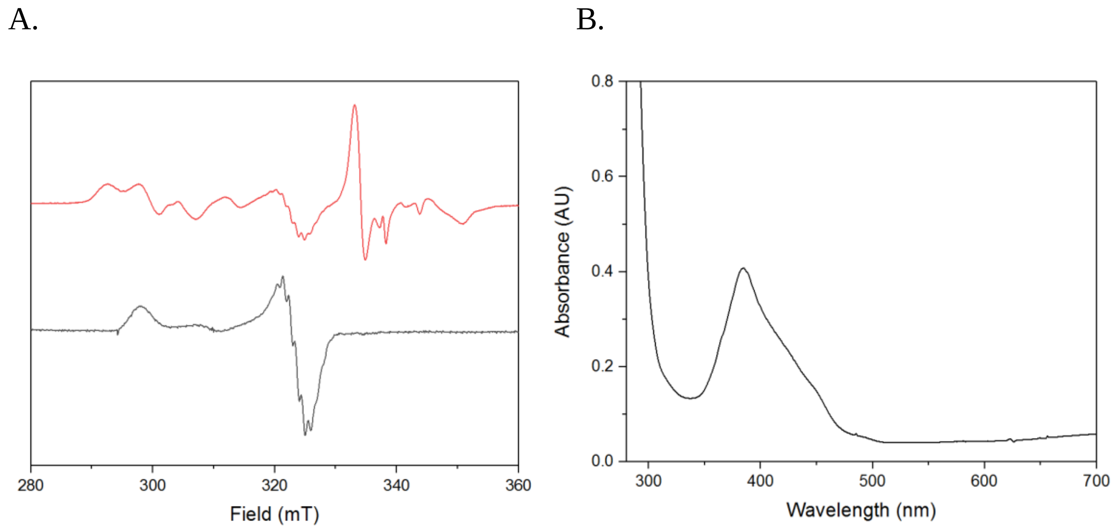

Figure. 4.5. (A) EPR spectra of cell free extract (upper trace) and purified MCRred1 form (lower trace). (B) Absorption spectrum of MCRred1

4.3.2 Rapid freeze quench experiments

To trap any EPR detectable intermediate(s) from the reaction of 3-NOP and MCRred1, rapid freeze-quench (RFQ) experiments were performed. Figure 4.6 shows the EPR spectra of the FQ experiment. An excess (5 mM) of 3-NOP was used to react with 50 µM of MCRred1 and the resulting reaction was quenched at defined time points. The 3-NOP almost immediately quenched the red1. As shown in the Figure 4.6 the red1 signal disappear and no new Ni based signal was observed, implying MCRsilent was the major form at the time points tested. It was expected a radical species will be detectable since Ni(I) (red1) is converted to Ni(II) (silent). Indeed, a radical signal was observed around 335 mT (Figure 4.6) when MCRred1 was incubated with 3-NOP albeit in low intensity. Since the samples were not packed well in this experiment, we thought the high noise observed could perhaps be due to poor packing of the reacted frozen mixture to the EPR tube. It could also be due to the low concentration of MCRred1 (50 µM) used during this experiment. Both could affect the intensity of the intermediate signal and we may even overlook some of the intermediates that may form after the inhibition reaction. Next, we performed RFQ experiment with higher concentration of MCRred1.

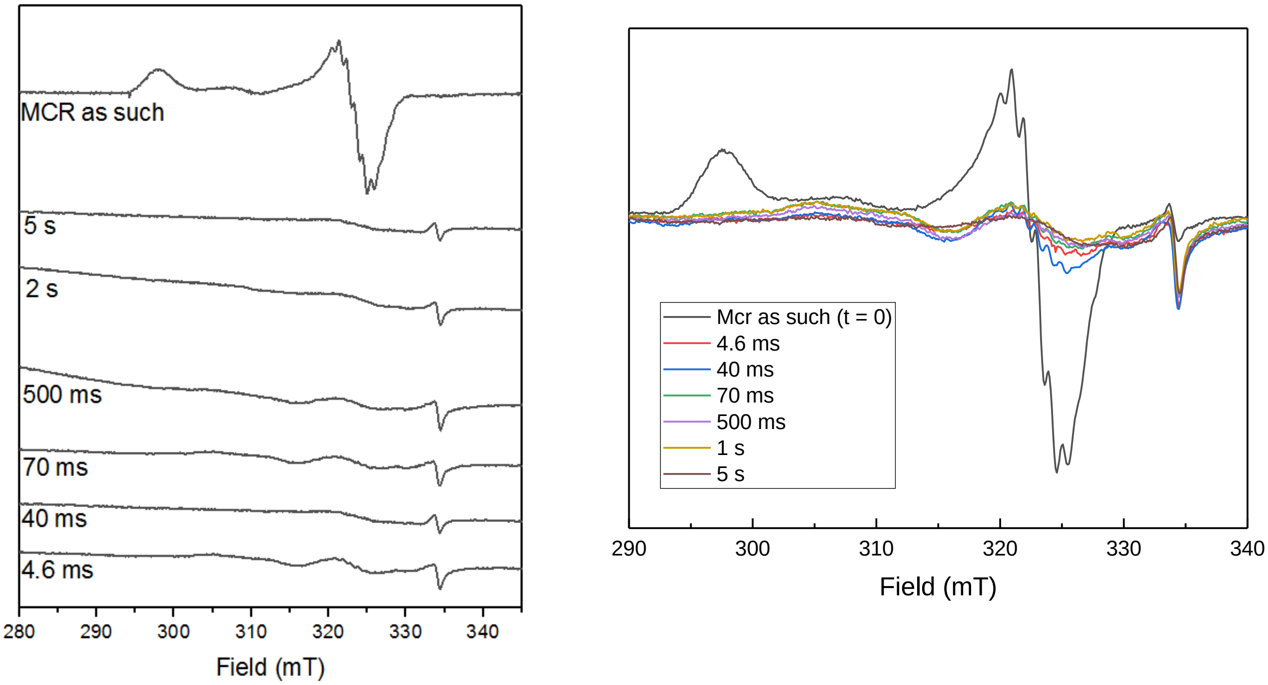

Figure 4.6. Freeze-quench experiment. 50 µM of MCRred1 form was incubated with 150 µl of 5 mM of 3-NOP. Samples were mixed and frozen 4.6 ms, 40 ms, 70 ms, 500 ms, 1 s, 2 s, sand 5 s.

Figure 4.7 shows the FQ experiment performed at a sub-saturation concentration of the inhibitor 3-NOP (at half the concentration of MCRred1). The as such red1 signal is not on scale with the rest of the measurements. As shown in the Figure, the reaction is quite fast and 3-NOP reacts instantly with the MCRred1. Within 4.6 ms, a signal typical of a radical was observed at around 335 mT. The radical signal was not observed on the as such sample (Figure 4.7). This suggests that the radical is indeed from the reaction of MCRred1 and 3-NOP.

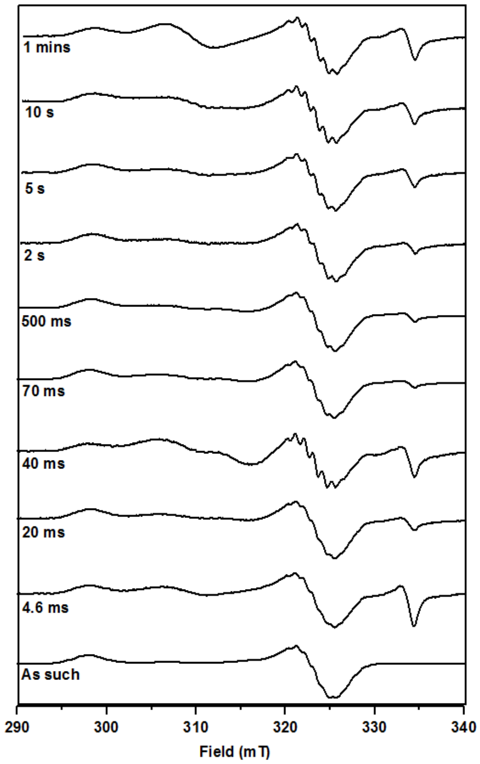

Figure 4.7. Freeze-quench experiment. 150 μM of MCRred1 form was incubated with 75 μM of 3-NOP.Samples were mixed and frozen 4.6ms, 20 ms, 40 ms, 70 ms, 500 ms, 2 s, 5 s, and 1 min

In addition to the radical signal observed in the FQ experiment, a new signal was also detected. This signal is prominent around 70 msec and apparently disappears at higher time points. To characterize this signal, a separate freeze quench experiment was performed with relatively high concentration of MCR (300 µM). This signal was used for simulation as depicted in Figure 4.8. The EPR signal was obtained from the reaction of 3-NOP with MCRred1at 70 msec and both simulated MCRred1 and MCRox1 were subtracted from the spectra. This results in a new spectrum shown in Figure 4.8 trace E. It is very similar to signals induced by treating the MCRred1 with either Br-CH_3 or bromopropane sulfonate (BPS) (see Figure 4.10 for the EPR spectra of BPS and MCRred1 reaction).[40] In both cases a Ni(III)-alkyl species is formed. Therefore we assign this new signal to a Ni(III)-3-NOP species. To make sure the spectrum in trace E has the correct proportions, the spectrum was simulated and an almost perfect fit between spectrum and simulation was obtained (trace E and F). In addition, the simulation was subtracted from the original 70 msec spectrum, resulting in a spectrum that just shows the red1 and ox1 spectra (trace G).

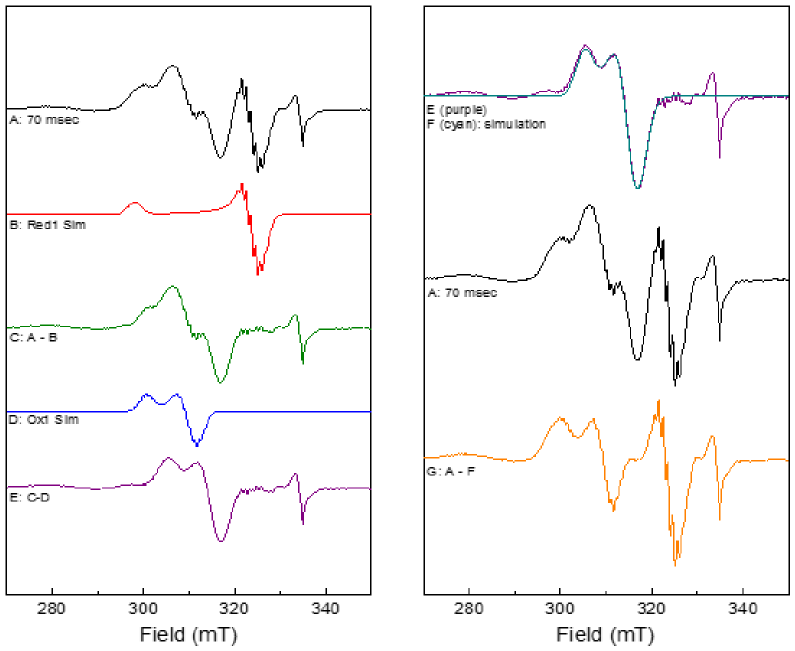

Figure 4.8. Trace A, shows the spectra obtained at 70 msec. The Ni(I)red1 signal was simulated (trace B) and subtracted (trace C). The amount of Ni(III)ox1 was estimated from the orginal spectrum at t = 0. A simulation of the Ni(III)ox1 signal (trace D) with the correct intensity was subtracted from trace C, resulting in trace E.

To get an insight in the reaction mechanism of 3-NOP, and to see if it somehow matches with the inhibition mechanism of the well know MCR inhibitors, BES and BPS, MCRred1 was reacted with these inhibitors. A freeze quench experiments coupled with EPR measurements were performed for the BES (Figure 4.9). To our knowledge, no RFQ was performed or reported for reaction between BES and MCRred1 and it is not known if BES forms a Ni-alkyl intermediate when reacted with MCRred1 though it is know that this inhibitor forms a radical intermediate. Nonetheless, no new signal that looks like the Ni(III)-alkyl was observed in the RFQ experiment (Figure 4.9) while a radical species was detected consistent with previous observations.

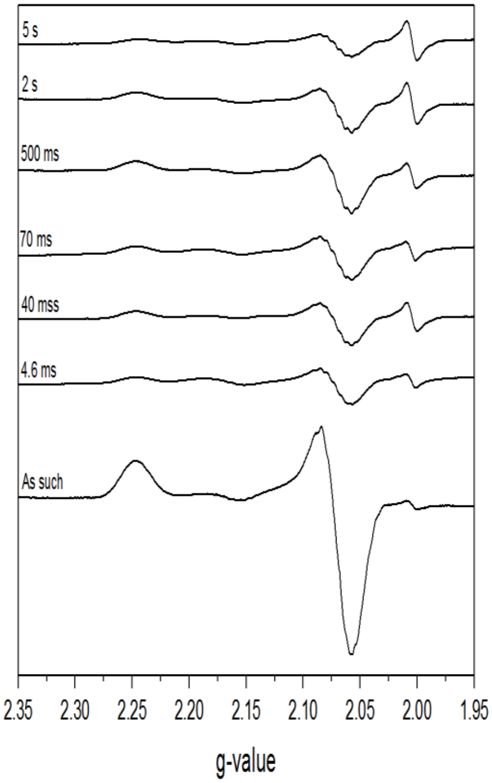

Figure 4.9. Freeze-quench experiment. 75 µM of MCRred1 form was incubated with 5 mM of BES. Samples were mixed and frozen at 4.6 ms, 40 ms, 70 ms, 500 ms, 2 s and 5 s.

Figure 4.10 shows the effect of HS-CoB on the reaction of MCRred1 with the inhibitors (BES, BPS, and 3-NOP). HS-CoB was found to have an effect on the intensity of the radical signals obtained when MCRred1 was reacted with BES and 3-NOP (Figure 4.10 panel D and E). The substrate HS-COB was found to found to have a higher effect on the BES than on the 3-NOP. Both the signal intensity and the shape of the spectra seems to be changed in the presence of the HS-CoB. As shown in the Figures 4.10 panels D and E, the signal increased. In addition a splitting of EPR signals were observed with both BES and 3-NOP. This kind of radical EPR signal is believed to originate from the residue of protein. There was no effect of HS-COB on the BPS and MCRred1 inhibition reaction (Figure 4.10 panel C).

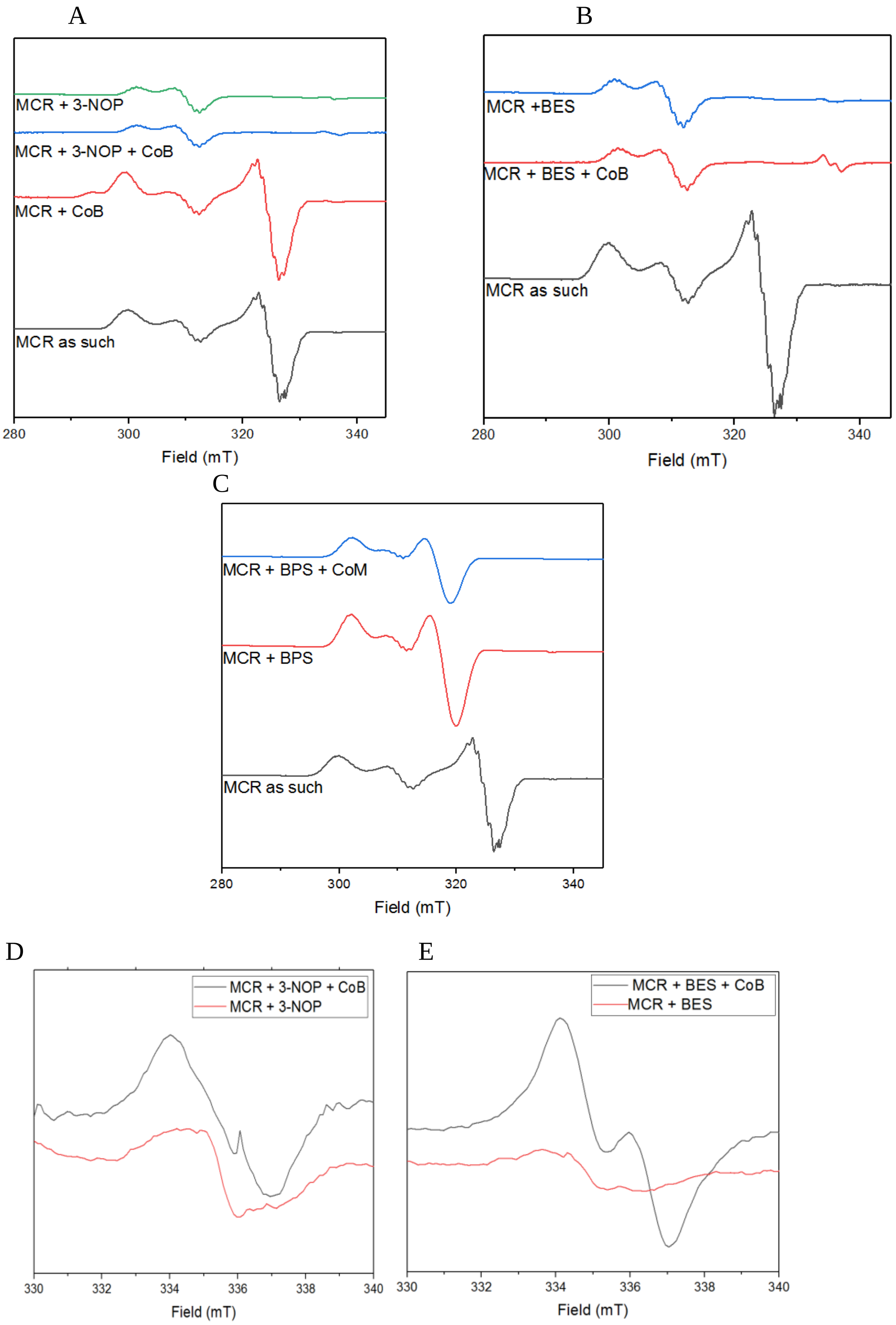

Figure 4.10. The effect of HS-CoB on the incubation of MCRred1 with inhibitors 3-NOP, BES, and BPS.

4.3.3 Determination of the other potential products formed in the inhibition reaction

To test the product(s) that could form after reaction of 3-NOP with MCRred1, NMR measurements were performed. Figure 4.11 shows the NMR spectra of the sample and the controls. 1 mM MCRred1 was incubated with equimolar concentration of 3-NOP for 20 min and the resulting products were analyzed with proton NMR. Both peaks 1 and 2 of 3-propanol (panel A) are absent in the inhibited sample (panel E) implying 3-propanol is not a product. Peak 2 in 3-NOP sample (Panel C) disappear in the inhibition reaction sample (panel E) and small peak appeared (marked by ?). Since the shift for peak 3 in 1.3-propandiol and 3-NOP are similar, we are not sure if the same peak showed in panel E is for 1,3-propanediol or for the unreactive 3-NOP. But careful observation of the peaks tells there are two overlapping peak which most probably could be due to both 3-NOP and 1,3-propanediol. The peaks marked by "x" (panels D and E) are most probably from the tris buffer as this peak did not appear in D_2O controls.

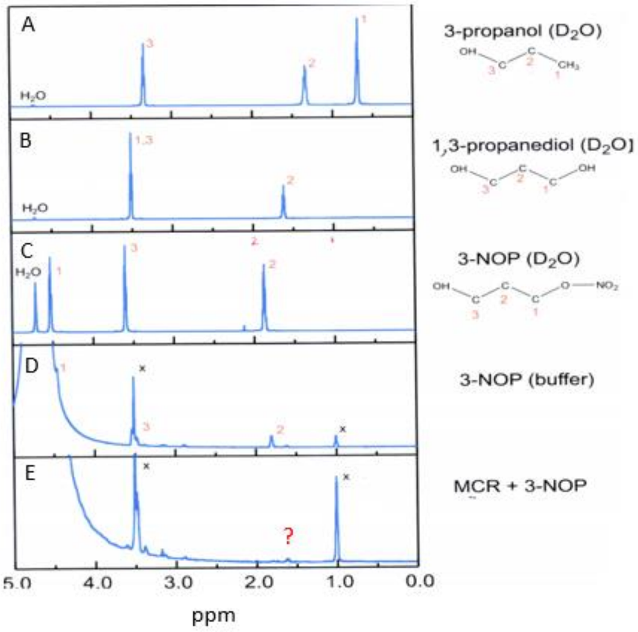

Figure 4.11. Panel A; shows the spectra obtained for 3-propanol in D_2O, B; 1,3-propanediol in D_2O, C; 3-NOP in D_2O, D; 3-NOP in Tris Buffer, E; sample after the reaction of 3-NOP and MCRred1.

4.4 Discussion and conclusion

The current study extends the previous investigation on the mode of inhibition of 3-NOP on MCR. 3-NOP reacts with MCRred1, but not with MCRox1 as the EPR signal of MCRox1 was not affected after reacting with 3-NOP even after long time incubation. The docking studies predicted the binding confirmation of 3-NOP on the active site of MCRred1. 3-NOP binds to MCR with its nitrate group close to the nickel center (According to docking study 3-NOP could bind to MCR through its hydroxyl group). This conformation of the inhibitor in the active site of the enzyme is favorable for the reaction to occur. 80 % of nitrate and 20 % of nitrite were also measured after the reaction of 3-NOP with MCRred1. Interestingly, the nitrite was also found to inhibit the enzyme while the nitrate does not have effect on the MCRred1. 1,3-propanediol was also detected in the *in vivo* studies using the ^{14}C labeled 3-NOP in the reaction and subsequently measuring the product with radio-HPLC.[98] Likewise, our *in vitro* product analysis with NMR indicates the formation of 1,3-propanediol. However, this experiment needs to be repeated due to the ambiguity of the NMR peaks which perhaps could be due to the low sensitivity of the NMR instrument. The production of 1,3-propanediol is consistent with the formation of nitrite.

In the RFQ experiments a radical species was observed. The EPR signal of the radical looks like radical signal observed in the BES inhibition reaction. Furthermore, a nickel-based intermediate was also detected in the RFQ experiment after the reaction of 3-NOP with MCRred1. This EPR signal is similar to the Ni(III) based EPR spectra obtained with BPS, Br-CH_3 and I-CH_3 inhibitors.[49,93,94] Two mechanisms have been proposed. In the first mechanism, Ni(I) of MCR attacks the carbon of 3-NOP to generate Ni(III)-alkyl intermediate and nitrate. The Ni(III)-alkyl intermediate then reacts with water to form 1,3-propanediol and a Ni(I). Mechanism II starts with nucleophilic attach of Ni(I) to the carbon of 3-NOP to generate Ni(III)-alkyl intermediate. A hemolytic cleavage of the intermediate then produce a Ni(II) and propanol radical which ultimatley forms 1,3-propanediol. In mechanism III, Ni(I) attacks the nitrogen of 3-NOP to generate Ni(III)-NO_2 intermediate and 1,3-propanediol anion. The 1,3-propanediol anion abstracts a proton and forms 1,3-propanediol whil the Ni(III)-NO_2 undergoes a hemolytic cleavage to produce Ni(II) and nitrite radical. Finally the nirite radical disproportionately react with water to produce both nitrite and nitrate. Additional spectroscopic experiments (ENDOR, for example) coupled with as isotope labeling ^{13}C and/or ^{17}O would be necessary to assign the intermediate conclusively.

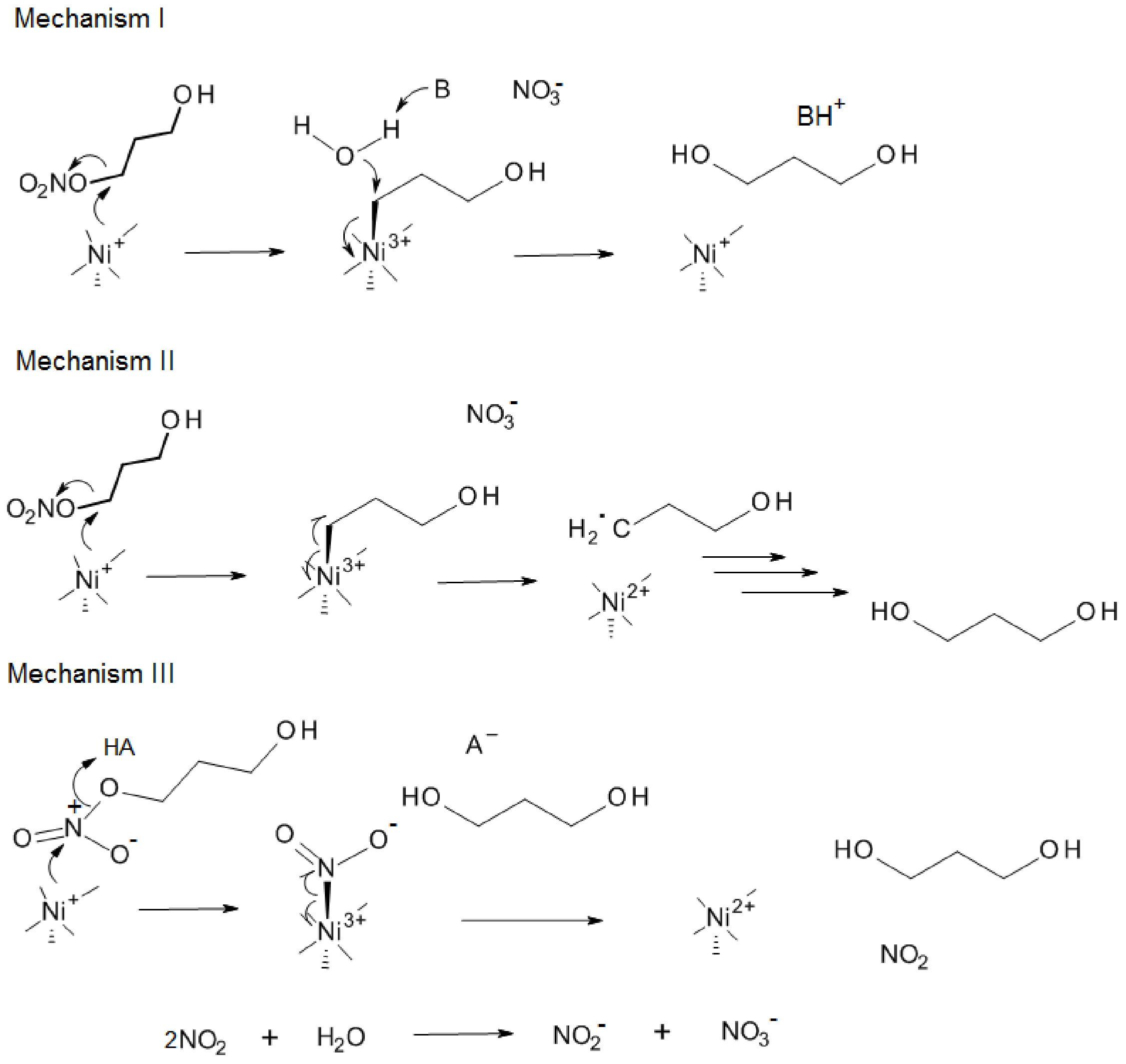

Figure 4.12. The proposed inhibition mechanism of MCR by 3-NOP

Chapter Five: Introduction to Computational Chemistry

5.1 Introduction

Computational chemistry also referred as molecular modeling is a branch of chemistry that has been widely used to investigating chemical problems using mathematical models and computer programs.[99] Computational methods are important methods that have been widely used as adjunct to experimental and/or as independent research tool. Experimental scientists are mainly concerned with gathering tangible information related to the physical states and dynamic processes of chemical occurrence. Computational chemistry on the other hand tries to look for possible explanations for the physical phenomena which otherwise are difficult to figure out only with the available experimental information.[99]

Computational methods have been used for studying various properties of a chemical system. Molecular geometry optimizations (bond lengths, angles, and dihedrals), transition structures, energy of activation, frequency calculations, the interaction of a substrate with an enzyme/protein (Docking), determining rate constants (kinetics), thermodynamic calculations, IR, UV, and NMR spectra are some of the properties of molecules a computational chemist investigates. Computational chemists model structure and reactions of molecules based on basic laws of physics. The methods can be used to model ground state, exited state, and even the short lived unstable intermediates and transition states.[99] Computational techniques provide valuable information about the structure and reaction of a molecule which sometimes is impossible to get from the conventional experiments. Computational methods could be used either as independent research to predict physical and chemical behavior of a system or as an adjunct to experimental studies. Ab initio, DFT, Semiempirical methods, molecular mechanics, and Molecular dynamics are the five main methods computational chemistry employs.[99] Combined with statistical mechanics, the above method could provide valuable information for real physicochemical properties of a system.

The heart of computational chemistry is to simulate the interaction of particles. The interaction between particles can be described in terms of either force or potential. Equation below describes the relationship between force and potential.

$$F(r) = \frac{-dV}{\mathrm{dr}} \tag{1}$$

Of the four main fundamental interactions, the weak interaction, the electromagnetic interaction, governs how particles interact at the atomic and molecular level.[99]

5.2 The Dynamic Equation

Particles are not completely stationary even at their lowest level of energy (ground state) rather they are in continuous motion. They have inherent motion associated with them, at least the ground state vibration. Therefore, they can be studied using dynamic equation. The dynamic equation (the equation of motion) describes the behavior of a system in terms of mass and velocity of the particles in the system. It is divided into four parts; the relativistic and non-relativistic classical mechanics and relativistic and non-relativistic quantum mechanics. Newtonian mechanics (non-relativistic classical mechanics) represented by Newton's second law applies for slow-moving particles. Relativistic effects (relativistic mechanics) provides description of a system when the velocity is comparable to the speed of light. Quantum mechanics (QM) described by Dirac and Schrödinger equations applies for light particles having both wave and particle characteristics.

An electron is a very light subatomic particle and exhibits a wave and a particle behavior. Thus, its property can be described by quantum mechanics. Atoms and molecules are considered heavy particles that behave essentially as a classical particles and are conveniently described by classical mechanics (molecular mechanics). In molecular mechanics (MM), Newton's equation is used to determine where the particle will be at a certain time point. The equations can be integrated over time either forward or backward, and the position of the particle can then be predicted at certain time point. Thus, molecular mechanics is deterministic in nature. In QM, on the other hand, the probability of finding a particle (electron) at a certain place is determined. QM is then probabilistic. The exact position and momentum of a particle cannot be determined at the same time (Heisenberg uncertainty).

$$F = \frac{-dp}{\mathrm{dt}} \tag{2}$$

The momentum p of the particle is the mass times the velocity and is given by the following equation at constant mass.

$$P = mv \tag{3}$$

$$F = \frac{dp}{\mathrm{dt}} = \frac{\mathrm{m}dv}{\mathrm{dt}} = ma \tag{4}$$

$$\frac{dV}{dr} = \frac{md^2r}{dt^2} \tag{5}$$

Force is the derivative of the potential (eq. 1), and the acceleration is the second derivative of the position r with respect to time. Solving this equation gives the position of each particle as a function of time.

Quantum mechanics is used to describe the behavior of a particles with small masses (electrons). At low velocities time-independent Schrödinger equation is relevant and can be written as follows

$$H\Psi = \frac{d\Psi}{\mathrm{dt}} \tag{6}$$

The Hamiltonian operator is given as a sum of kinetic and potential energy operators.

$$H = T + V \tag{7}$$

The solution to the Schrödinger equation gives the wavefunction as a function of time, and the probability of finding a particle at a position r and time *t* is given as the square of the wavefunction.[100]

Computational chemistry is mainly interested in time independent phenomenon, thus classical Newtonian and the time independent Schrödinger quantum mechanics are useful in describing chemical behaviors and are the discussed below.

5.3. Electronic Structure Methods (Quantum Mechanics Methods)

Electronic structure methods use the law of quantum mechanics (QM) as a basis of computations. QM is based on solving the Schrödinger equation.

$$\mathrm{H}\,\Psi = \mathrm{E}\,\Psi \tag{8}$$

Where Ψ is a many electron wavefunction. It is a function of the positions of all the particles (electrons and nuclei) describing the motion of the electrons. E is the total energy operator of the system and H is the Hamiltonian operator. The Hamiltonian operator is the composed of the kinetic (T) and potential (V) energy operators and are expressed by the following equations.[100]

$$H = T^{ele}(r) + T^{nucl}(R) + V^{nucl-ele}(R,r) + V^{ele}(r) + V^{nucl}(R) \tag{9}$$

$$H = \frac{1}{2}\sum_{i}^{ele} \nabla_i{}^2 - \frac{1}{2}\sum_{A}^{nucl} \frac{1}{M_A}\nabla_i{}^2 - \sum_{i}^{ele} \sum_{A}^{nucl} \frac{Z_A}{r_{iA}} + \sum_{i}^{ele} \sum_{j}^{ele} \frac{1}{r_{ij}} + \sum_{A}^{nucl} \sum_{B}^{nucl} \frac{Z_A Z_B}{R_{AB}} \tag{10}$$

where Z is the nuclear charge, MA is the ratio of mass of nucleus A to the mass of an electron, R_{AB} is the distance between nuclei A and B, r_{ij} is the distance between electrons i and j and r_{iA} is the distance between electron i and nucleus A. ∇ is the Laplace operator defined by the following equation

$$\nabla^2 = \left(\frac{\partial^2}{\partial x^2} + \frac{\partial^2}{\partial y^2} + \frac{\partial^2}{\partial z^2}\right) \tag{11}$$

The exact solution of Schrödinger equation is not yet possible for most systems except for the smallest system (Hydrogen atom or a one electron system). Thus, QM methods use several approximations to solve the Schrödinger equation for complex system (multi electrons). The approximations, some of them discussed below, provides significant improvement in the speed of computation by eliminating (ignoring) some of the integrals. There are three main classes of electronic structures methods: *Ab intio,* density functional theory (DFT), and semi-empirical methods.

5.3.1 Ab initio

Ab initio is a Latin word for “from the beginning”. This method compute solution to the Schrödinger equation using mainly the Born-Oppenheimer approximation (described below). An input of the number and positions of the atoms within the system are needed for *ab initio*-based simulation and no experimental parameters are needed for the computation unlike semi-empirical or molecular mechanics methods. Ab initio methods provide highly accurate quantitative predictions for broad range of molecular systems. It can compute the energetics and other properties of heavy atoms in quite a few minutes. It could also be used to study system containing up to hundreds of atoms using supercomputers with high accuracy.[101]

Born-Oppenheimer Approximation

As mentioned above, for most system the exact solution for the electronic Schrödinger equation cannot be obtained. Thus, QM methods uses several approximations to solve the Schrödinger equation in each time step to determine the potential energy of the particle. One of these approximations is the Born-Oppenheimer approximation which separates the nuclear motion from electronic motion.[102] Nucleus and electrons have opposite charge and attract each other with the same force and momentum. Nuclei are, however, much heavier than the electrons and their velocities can therefore be neglected during the computation of electronic Schrödinger equation. Thus, the second term in the equation 9 is set to zero. A nucleus is then assumed to be in stationary while the electrons revolve around it. Subsequently the equation is separated into two, the electronic and nuclear Schrödinger equation. The electronic Schrödinger equation describes the behavior of electrons when the position of nuclei is fixed, and its solution produce a potential that describes the effect of electrons on the interaction between the nuclei.

$$H^{ele} = -\frac{1}{2}\sum_{i}^{ele}\nabla_{i}^{2} - \sum_{i}^{ele}\sum_{A}^{nucl}\frac{Z_A}{r_{iA}} + \sum_{i}^{ele}\sum_{j}^{ele}\frac{1}{r_{ij}} \tag{12}$$

$$E = E^{ele} + \sum_{A}^{nucl}\sum_{B}^{nucl}\frac{Z_A Z_B}{R_{AB}} \tag{13}$$

Hartree-Fock Approximation

Here each electron is confined to a function (molecular orbitals). Each molecular orbital is determined by assuming that electron is moving within an average field of all the other electrons. The total wavefunction is then written in the form of a single slater determinant.[102]

$$\Psi = \frac{1}{\sqrt{N!}} \begin{vmatrix} \chi_1(1) & \chi_2(1) \cdots & \chi_n(1) \\ \chi_1(2) & \chi_2(2) \cdots & \chi_n(2) \\ \vdots & \vdots & \vdots \\ \chi_1(N) & \chi_2(N) \cdots & \chi_n(N) \end{vmatrix} \qquad (14)$$

LCAO Approximation

Linear combination of atomic orbitals (LCAO) is another approximation used to solve the Schrödinger equation. LCAOs yields a qualitative picture of molecular orbitals (MOs) by superimposing of individual atomic orbitals (wavefunctions). In this technique molecular orbitals are construct of LCAOs. If the superimposition of atomic orbital is constructive the bonding molecular orbital form. On the otherhand destructive superimposition leads to anti-bonding molecular orbital. Bonding and anti-bonding molecular orbital have different energies as they differ in the configuration of electron density in their respective orbitals.

The Hartree-Fock approximation together with LCAO approximations lead to the Roothaan-Hall equation given by the following general eigenvalue problems

$$FC = SCe \qquad (15)$$

Where the F is the Fock matrix, analogous to the Hamiltonian operator, C is MO-coefficient, S is the overlap matrix, a measure of the extent to which basis functions see each other, and e is the diagonal matrix containing the orbital energy.[102]

$$F_{\mu v} = H_{\mu v}^{core} + J_{\mu v} - K_{\mu v} \tag{16}$$

$H_{\mu v}^{core}$ is the core Hamiltonian given by equation (17), $J_{\mu v}$ is the coulomb and $K_{\mu v}$ is the exchange terms given by equation 18 and 19, respectively.

$$H_{\mu v}^{core} = \int \phi_0 (r) \left[-\frac{1}{2} \nabla^2 \sum_A^{nucl} \frac{Z_A}{\mathrm{r}}\right] \phi_0(r) dr \tag{17}$$

$$J_{\mu v} = \sum_{\lambda}^{basis} \sum_{\sigma}^{functions} P_{\lambda\sigma} (\mu v \,|\, \lambda\sigma) \tag{18}$$

$$K_{\mu v} = \frac{1}{2} \sum_{\lambda}^{basis} \sum_{\sigma}^{functions} P_{\lambda\sigma} (\mu\lambda \,|\, v\sigma) \tag{19}$$

5.3.2 Density Functional Theory (DFT)

The DFT methods are quite similar to ab initio methods in that they both are constructed from an SCF and the building blocks are molecular orbitals (single electron). However, unlike ab initio methods which depend on solving wavefunctions, DFT methods employ electron density ρ(r) to extract the energy and other properties of a system. DFT includes the effect of electron correlation. In this model electrons in a molecule react to one another’s motion and tries to move away from the motion of one another. In ab initio method, each electron sees and reacts on an average electron density. The DFT method treats the electron density as the central variable rather than the many-body wavefunction.[103]

$$E = E_T + E_V + E_J + E_{XC} \tag{20}$$

In DFT, the total energy (E) is written as a sum of the kinetic energy (E_T) the electronuclear interaction energy (E_V) the Coulomb energy (E_J) and the exchange/correlation energy (E_{XC}). All energy terms, except E_T, depend on the electron density, ρ(r). [104]

$$\rho(\mathrm{r}) = 2\sum_i^{orbital} |\Psi(r)|^2 \tag{21}$$

$$E_V = \sum_\mu^{basis}\sum_v^{functions} P_{\mu v}\sum_A^{nuclei}\int \phi_\mu(r)\left|\frac{Z_A}{|r-R_A|}\right|\phi_V(r)dr \tag{22}$$

$$E_J = \frac{1}{2}\sum_\mu^{basis}\sum_v^{functions}\sum_\lambda\sum_\sigma P_{\mu v}P_{\lambda\sigma}(\mu v|\lambda\sigma) \tag{23}$$

$$E_{XC} = \int f(\rho(r), \nabla\rho(r), \ldots.)dr \tag{24}$$

P is the density matrix, $(\mu v|\lambda\sigma)$ are the two-electron integrals, E_{XC} is the exchange and correlation functional. E_V and E_J are solved with Kohn-Sham orbitals which are analogous to the LCAO approximation using a set of single-electron spin orbitals solved by the SCF approach.

5.3.3 Semiempirical

In standard electronic structure methods, the molecular orbitals are approximated by a linear combination of atomic orbitals (basis functions). The HF theory considers all electrons in the atomic orbital. In semiempirical one electron and sometimes two electron integrals are neglected, and some empirical parameters are inserted.[105] This significantly reduce the computational cost associated with integrating the functions.

Semiempirical methods use parameters derived from experimental data (semi-empirical) or from low level QM calculations. Depending on the available parameters semi-empirical methods solve an approximate form of the Schrödinger equation for the chemical system of interest. It eliminates the core electrons and uses minimum basis set for the calculation. Only valence electrons are considered, and the core electrons are treated together with nuclei by reducing the nuclear charge. They are comparably inexpensive (faster than *ab initio).*[105,106]

A Nobel Prize laureate, professor Pople developed semiempirical methods; complete neglect of differential overlap (CNDO), intermediate neglect of differential overlap (INDO) and the neglect of diatomic differential overlap (NDDO).[107] Professor John A. Pople won the prize in chemistry 1998 along with Professor Walter Kohn, for developing the famous density-functional theory (DFT).

Zero Differential overlap (ZDO)

In implementing the ZDO (common approximation in semi-empirical methods), the overlap densities Qu*Qv with Qu and Qv being orbitals localized on different atoms are neglected.[105,108]

Complete neglect of differential orbital (CNDO), intermediate neglect of differential orbital (INDO) and neglect of differential-diatomic orbital (NDDO)

In CNDO the overlap distribution between two pairs of different atomic orbitals is neglected in the all-electronic-repulsion integrals.[107] This provides relatively small number of parameters in the integrals and subsequently lower computational cost incomparison to LCAO-SCF QM methods. The CNDO, nevertheless, has some limitations. The CNDO overestimated the dissociation energies and the equilibrium distance between two atoms were too short comparing to experimental results. This could be due to modeling two neutral atoms as having a high attraction for one another, even though the two atoms are separated by several angstroms.[105]

In INDO monoatomic differential overlap for atomic orbitals that are on the same atom is included to enables the interaction between the two electrons on that particular atom. However, there was not significant improvement over the CNDO while the computational cost increases significantly.

The NDDO method is less approximate. Only differential overlap between atomic orbitals on different atoms is neglected. Two electron repulsion integrals which depend on the overlapping of charge densities of different atomic orbitals are equal to zero. All remaining two electron interactions are of the two-center type, with one electron associated with each atom. This reduces the computational demand significantly comparing to corresponding INDO and CNDO methods.[105]

Modified Intermediate Neglect of Differential Overlap (MINDO/3), Modified Neglect of Differential Overlap (MNDO), Austin Model 1 (AM1) and Third Parameterization of Modified Neglect of Diatomic Overlap (PM3)

In the MINDO/3 approach, some or all the energy terms were set equal to parametric functions, which can be adjusted to fit experimental data. In addition, variables that were fixed in CNDO, INDO and NNDO calculations were permitted to vary during the parameterization.

The MINDO/3 method includes geometry optimizations, and this allowed for the initial starting configuration to be unrefined. However, for compounds with lone pairs of electrons on adjacent atoms the heats of formation were too negative and the corresponding bond lengths were too short. Moreover, heats of formation for aromatic hydrocarbons were too positive comparing to experimental result.

The Austin Model 1 (AM1) includes repulsive and attractive Gaussian functions. Attractive Gaussians were used to compensate for the excessive repulsions and were centered in the regions where these repulsions were greatest. Then repulsive Gaussians where added at small internuclear distances to reduce the repulsion at larger atomic distances. AM1 was better in modeling heats of formation for neutral closed-shell molecules, cations, radicals and anions over MINDO.[109]

PM3, the third parameterization of MNDO, was developed which includes two Gaussian functions per atom instead of four Gaussian functions as used in AM1. Both methods predict thermodynamic and structural properties to roughly the same level of accuracy.[110]

Pairwise Distance Directed Gaussian Third Parameterization of Modified Neglect of Differential Overlap (PDDG/PM3)

The most commonly used method in semiempirical QM calculation is PDDG/PM3. This semiempirical method provides more accurate heats of formation than the preceding developed semiempirical methods. The method includes a pairwise distance directed Gaussian (PDDG) modification to the core repulsion function (CRF) and uses the bond and groups equivalents scheme (BGE). Bond equivalents represent the bonding energy of the molecule and include most of the energy required to convert molecular energy into enthalpy. BGE, however, can only be used for molecules at stationary points on the potential energy surface that have conventional bonding.[111]

$$\mathrm{PDDG(A,B)} = \sum_A \sum_{B>A} \frac{1}{n_A + n_B} \times \Big[\sum_{i=1}^{2} \sum_{i=1}^{2} \big(n_A P_{Ai} + n_B P_{Bj}\big)\, e^{\left(-10\text{Å}^{-2}(R_{AB}-D_{Ai}-D_{Bj})^2\right)}\Big] \tag{25}$$

P_{Ai} and P_{Bj} are the pre-exponential factors, D_{Ai} D_{Bj} and are the distance.

5.4 Molecular Mechanics (MM)

Molecular mechanics uses classical physics to explain and interpret the behavior of atoms and molecules. MM models molecules as a collection of atoms and bonds (as opposed to nuclei and electrons in QM model).[99] In MM methods electrons are not considered as individual particles rather they are treated as unified atoms together with nuclei. Atom positions are adjusted to best match known structural data (bond lengths and angles), as well as to accommodate non-bonded interactions. If the bond length, angles and dihedral and the energy to stretch and bend the bond are known, which could be derived through parameterization from experimental result or from higher degree quantum mechanics calculation, one can calculate the energy of a given molecule. By changing the geometry of a molecule until the lowest energy (minima) is found enables to perform energy optimization. MM methods are based on implementing classical Newtonian law of motion which is way much simpler than solving the Schrödinger equation for electron motions and it is therefore MM calculations are faster than the corresponding QM calculations and are convenient for the study of large systems such as condensed phase of organic reaction or bimolecular systems. However, it requires description of "chemical bonding", as well as a large amount of information about the structures of molecules through parameterization.[99,112]

5.4.1 The Force Field Energy

The total force field energy is written as a sum of the four individual energies. The four essential components of interacting particle are bond stretching (E_{bond}), angle bending (E_{angle}), torsional rotations or the dihedral angle ($E_{torsional}$), and nonbonded interactions ($E_{nonbonded}$).

$$E_{FF} = E_{stretching} + E_{bending} + E_{torsional} + E_{nonbonding} \tag{26}$$

The stretching (Bond) Energy:

The energy of stretching (E_{str}) is the energy requires to stretch a bond between Atom A and B. It is described by a simple Tylor expansion around an equilibrium bond length (R_o)

$$E_{str}\,(R^{AB} - R_o{}^{AB}) = E(0) + \frac{dE}{dR}(R^{AB} - R_o{}^{AB}) + \frac{1d^2E}{2dR^2}(R^{AB} - R_o{}^{AB})^2 \tag{27}$$

The Eo is set to zero and the third term is also set to zero terminating the Tylor expansion at second order, thus the derivative of second terms gives eq 28, a form of harmonic potential where k^{AB} is the force constant for A-B.

$$E_{str}\,(R^{AB} - R_o{}^{AB}) = k^{AB}(R^{AB} - R_o{}^{AB})^2 \tag{28}$$

The bending (angle) Energy:

The energy of bending (E_{bend}) is the energy required for bending an angle formed by three bonded atoms A−B−C. Like the E_{bond}, E_{angle} is represented by simple harmonic potential.

$$E_{bend}\,(\theta^{ABC} - \theta_o{}^{ABC}) = k^{ABC}(\theta^{ABC} - \theta_o{}^{ABC})^2 \tag{29}$$

The torsional (dihedral) Energy:

The Energy of Torsion (E_{tors}) is the energy required to rotate a bond of the two central atoms in four bonded atoms. The torsional energy is periodic, i.e if the bond is rotated 360° the energy returns to the initial value and thus is given by periodic function (cosine series)

$$E_{tors}(\omega) = \sum_{n=1} V_n \cos(n\omega) \tag{30}$$

Where N is the multiplicity i.e the number of minima's in a 360° rotation, n = 1, for example describes a rotation that is periodic by 360°.

Non-Bonding Energy:

The non-bonded energy of the force field is described by a combination of Coulomb and Lennard-Jones terms. The electrostatic interactions between two charged particles are described by Coulomb potential. The interaction could be intermolecular interactions, which occur in most chemical systems of interest and/or intramolecular nonbonded interactions between two pairs of atoms separated by three or more bonds. The weak interactions, van der waals interactions, are modeled using Lennard-Jones 12-6 potential which describes the attractive and/or repulsive forces between two interacting particles. Most of the computational time goes in computing the non-bonded interaction and its extremely demanding. The van der Waals interactions vanished significantly with distance and thus a cutoff approach is used to compute the potential. It's not, however true with electrostatic interactions and using cutoff would produce an error in computing the energy.[99,112] Several methods are thus developed to compute long range interaction.

5.5 Long Range Interactions

Ewald summation, developed by Ewald is a method used for computing long-range interactions of particles in the periodic system.[113] It is the most widely used method for condensed phase simulations. In this method, each particle in the box interacts with all other particles in the box and with all of their images in an infinite periodic array. The electrostatics interactions among the particles inside the central box and all image boxes are used to compute the potential energy.

For a cubic box with lattice point n = $(n_x L, n_y L, n_z L)$, where $n_x n_y n_z$ are integers equation 2.7 can be applied using electrostatic potentials

$$V = \frac{1}{2}\sum_{|n|}\sum_{i=1}^{N}\ \sum_{j=1}^{N}\ \frac{q_i q_j}{4\pi\varepsilon_o|r_{ij}+n|} \tag{31}$$

Where:

$q_i\ and\ q_j$ are the nuclear charges, while all image boxes positioned at a cubic lattice point are expressed as |n|.

A cut-off method is employed to shorten a long-range interaction in the potential energy function. In this method, a potential is set to zero over some distance *r* beyond the cuff off, which usually is half of the box distance. As this method seems easy enough, it is not natural for the potential energy to instantly switch to zero; therefore a switching function is applied to obtain the type of potential truncation needed.[114]

5.6 Mixed Quantum Mechanical/Molecular Mechanical (QM/MM)

In the modeling of chemical systems, the number of atoms in the system dramatically influences the computational method utilized. In modeling organic reactions in a condensed phase medium using QM would be computationally unreasonable and expensive. On the other hand, treating the entire system with MM could cost the accuracy in describing the properties of the chemical system of interest. The same is true for modeling substrates in macromolecules (protein for example). Thus QM/MM provides a balance between accuracy and speed in modeling bond making and breaking.[115] It approaches the large chemical system of interest by dividing into two subsystems, i.e. QM and MM.

$$E_{total} = E_{QM} + E_{MM} + E_{QM/MM} \tag{32}$$

The total energy of the entire chemical system is calculated as the sum of three variables, EQM (energy of the QM region); EMM (energy of the MM region) and EQM/MM which represent the energy of interactions between the QM and MM. The QM region is a small region of the system where significant changes in electronic structure occur while the MM region is a larger portion, like a macromolecule or hundreds of solvent molecules. The larger portion of the system is treated by a force field described above.

$$E_{QM/MM} = \sum_{i}^{solute} \sum_{j}^{solvent} \left[\frac{\alpha {q_i}^{CMX} q_j e^2}{r_{ij}} + 4\varepsilon_{ij} \left[\left(\frac{\sigma_{ij}}{r_{ij}} \right)^{12} - \left(\frac{\sigma_{ij}}{r_{ij}} \right)^{6} \right] \right] \tag{33}$$

Where $\boldsymbol{\alpha}$ is the scaling factor of the charge model.[116]

In this study, QM/MM calculation was performed using BOSS developed by Jorgensen and coworker in the late 1970. BOSS, which stands for biochemical and organic simulation system is a molecular modeling software. BOSS can perform various calculations including; molecular mechanics (MM), semiempirical, Monte Carlo (MC) statistical mechanics simulations, and mixed QM/MM calculations.

5.7 Metropolis Monte Carlo (MC)

MC is one of the two methods (the other is molecular dynamics, MD) used to generate an ensemble.[117] In MC, configurations are generated randomly by perturbing the initial geometry (Figure 5.1). The energy of the new geometry is then calculated. If the energy is lower than the previous configuration the new configuration is accepted and become the starting point for the next move. If the new energy is higher than the previous configuration then a Boltzmann distribution (exp(-E/kT)) is computed and compared to a random number from 0 to 1 to decide whether to accept or reject the new geometry. If the Boltzman factor is larger than the number, the new configuration is accepted otherwise it is rejected. The old configuration is then added to the sampling and a new move is attempted.[118] This indeed is an advantage over molecular dynamics as it could lead to uphill trajectories and escape from a local minimum. Accepting higher energy states ensures the exploration of greater conformational space and allows multiple pathways to be generated along the PES.

The perturbing step size should not be too small or too big. Too small perturbation step provides high acceptance but changes the configuration a little. The explored space will be too little and is computationally costly. Too large step on the other hand, gives a low acceptance. Many configurations will be rejected and little progress across the PES occurs as the calculation will crash before converging. Usually MC simulation generates an *NVT* ensemble, (constant temperature, volume and particles). However, other ensemble like NPT can also be generated by MC methods.[115]

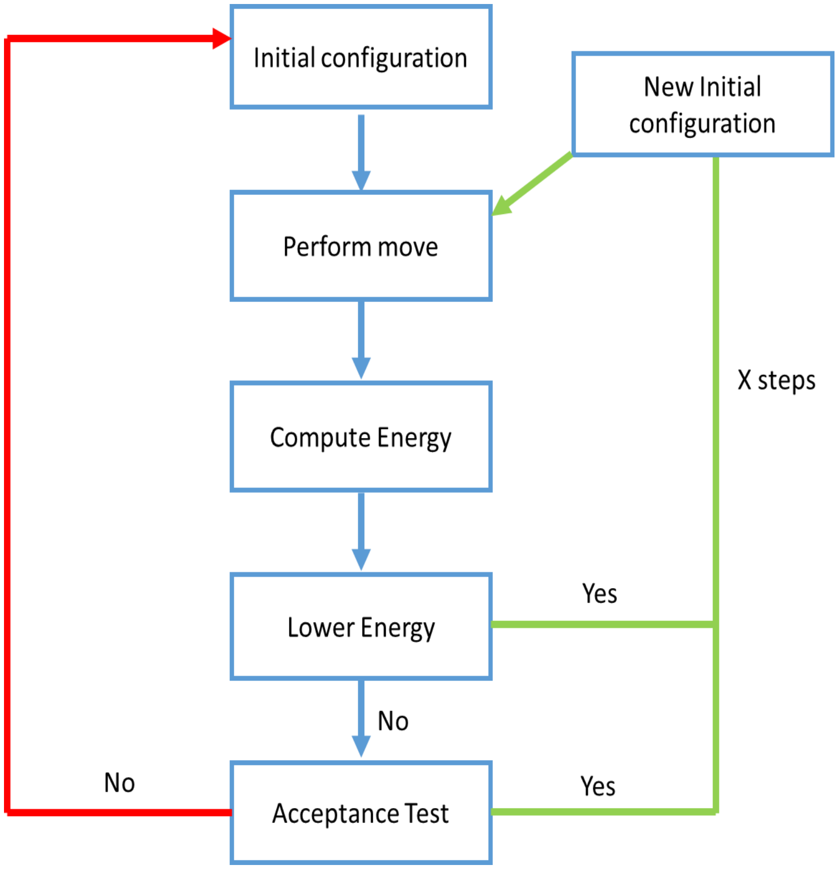

Figure 5.1 Monte Carlo Algorism

5.8 Periodic Boundary Conditions (PBC)

Periodic boundary conditions are employed to model for bulk solvent. PBC allows small number of solvent molecules to reproduce the properties of the bulk solvent. In PBC the few solvent molecules are enclosed in a box usually a cubic box. The Box is then replicated in all directions. This gives periodic array of solvent molecules (Figure 5.2) and prevents the outer solvent molecules from escaping out of the box to the vacuum. If one of the solvent molecules leave the box during simulation, it replaced simultaneously by the image solvent molecule entering from the opposite side of the box. Thus, the number of molecules within the box remains constant during simulation.[119]

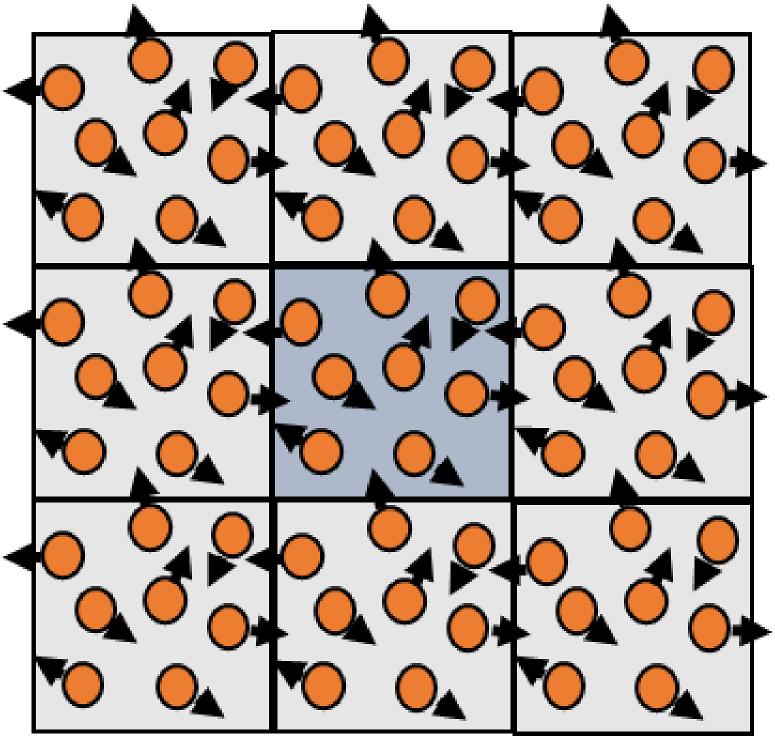

Figure 5.2 Periodic boundary conditions

During simulation, the solute molecule(s) are placed at the center of box and a solute-solvent cutoff is implemented to compute long range electrostatic interactions as discussed in the above paragraphs.[120]

5.9 Free Energy Calculations

Calculating free energy is one the main task of computational chemist. Computing free energy and constructing potential energy surface helps to characterize the reaction pathways and understand the chemical reactions. Free energy is a fundamental property of thermodynamics. Free energy is usually expressed as the Helmholtz free energy (A), or the Gibbs free energy (G). Calculating the exact free energy of a chemical system is difficult and thus methods were developed to compute the energy difference between two states of a system. One of the most popular method used to calculate the difference in free energy is free energy perturbation.

Computation of free energy difference of a system with the Free Energy Perturbation (FEP) method is based on mutation. One solute molecule (say system 0) is mutated into another solute molecule (system 1), the energy difference between the systems is then defined by an average function of their energy difference.[121]

$$\Delta A = A1 - A0 = -KBln[exp(\frac{-(E1-E0)}{KT})] \tag{34}$$

kB is the Boltzmann constant. E_1 and E_0 are the energies for the corresponding state.

In practice, the energy between the two states should be small enough in order to get proper convergence. Intermediates can be introduced between the two states. In fact multiple intermediates are used in computation, and simulation is carried put at each intermediate λ, which are referred to as windows (Fig 1.3). The chemical system is first equilibrated for the initial conditions of molecular species A with the corresponding initial λ chosen, (λi). Then the free energy difference is calculated at each step of $\lambda i \rightarrow \lambda i{+}1$ and the total free energy for λ = 0 to λ = 1 is given by summing up the free energy differences for all values of λi.[122]

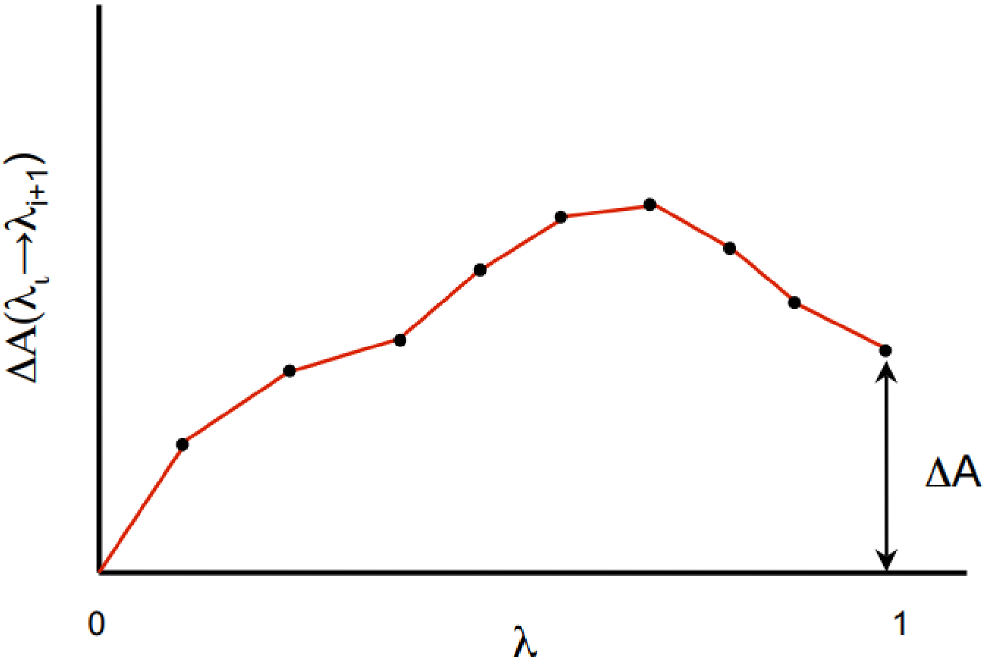

Figure 5.3 Free Energy Perturbation

5.10 Potential Energy Surfaces

Constructing a potential energy surface (PES) is the central part in simulating chemical systems. PES is a plot of potential energy as a function of reaction coordinates. PES plots provide valuable information about a chemical observable phenomenon. It helps to study the relationship between a molecular geometry, reactivity and their respective potential energy. The equilibrium structure and energetics of the reactant and products can be obtained from the position of the energy minima along the reaction coordinates in the PES. Thus, thermodynamics of the reaction can be extracted. It can also aid to locate and characterize the structure and energetics of the transition state and thereby exploit the kinetics of a chemical reaction. Overall, PES provides valuable information necessary to deduce the reaction mechanism(s) of a chemical system of interest.[112]

5.11 Ionic liquids

Ionic liquids (ILs) have been widely consider as a solvent of choice in different research areas owing to their unique characteristics. Generally, ILs are defined as fluids with low melting point, less than 100 ^{o}C and often some ILs have a melting point at or lower than room temperature.[11] These compounds are composed of at least two components, the cations and anions. This imparts them the flexibility to design to the choice of user, i.e their properties and composition can be adjusted to fit the objective of the system. For this unique property they are commonly referred as “designer solvents”.[123] Several application of ILs have been documented. They have been widely used in catalysis, separation process and in organic synthesis, electrochemistry, material science, and others. They are generally poor conductors of electricity, highly viscous, have low combustibility, and are thermally and chemically stable molecules. These together with the ability to recycle them make IL attractive solvents and advantageous over conventional organic solvent for chemical reactions.[124,125]

ILs possesses a high degree of structural order and organization. Several interactions, from Coulomb to hydrogen bond, quadrapole-pi and pi-pi staking plays a role in giving unique characteristics to ILs. Imidazolium-based ILs are considered as supramolecular polymer consisting of a highly extended network of hydrogen bonds linking anions and cations together. They are commonly referred as designer solvents due to the simplicity of modification of their ionic or cationic components. Ionic liquids are poorly miscible with most organic solvent which provides an easy separation from the reaction mixture and recycling.[123]

ILs have also been shown to affect the mechanism of reaction. The presence of IL in β-elimination reactions, for example, were found to change the reaction mechanism from an E1cB-like mechanism in methanol to a pure E2 mechanism.[126] Another reaction extensively studied in ILs is the mononuclear rearrangement of heterocycles (MRH).[127] Higher reactivity rate of rearrangement was reported in ILs for the amino-catalyzed rearrangement of the Z-phenylhydrazone of 3-benzoyl-5-phenyl-1,2,4-oxadiazole into 4-benzoylamino-2,5-diphenyl-1,2,3-triazole.[127] This rate enhancement was attributed to their organized structure of ILs rather than their polarities or viscosities. This research project presents detailed understanding of the MRH reaction in selective BMIM based ILs.

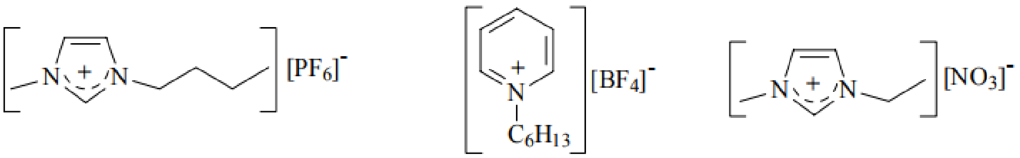

Figure 5.4 Typical Example of Ionic liquids[124]

Chapter Six: Investigating the origin of rate enhancement of Mononuclear Rearrangement of Heterocycles on ionic liquids using QM/MM computational method

Portions of this chapter are adapted with permission from Caley Allen, Robel Ghebreab, Brian Doherty, Bin Li, and Orlando Acevedo. *J. phys. Chem. B.* **2016**, *120* (41), 10786–10796. Copyright (2016) American Chemical Society.

6. 2 Introduction

Room-temperature ionic liquids have been attracting the attention of synthetic chemists owing to their unique solvent behaviors. Ionic liquids are found to influence not only the reactivity of a chemical reaction but also the selectivity of reactants.[127] Several ionic liquids have been designed and studied as a solvent for different organic reactions and rearrangement of heterocycles in particular. Heterocycles are extensively used in several areas of chemistry. They have been found in quite a large number of medicinal and biological products.[125,128] Nitrogen containing heterocycles in particular are of interest in synthesis chemistry as they tend to have better biological activities.[128] One way to synthesis heterocycles is through mononuclear rearrangement, also referred as Boulton-Katritzky rearrangement. The *Z*-phenylhydrazone of 3-benzoyl-5-phenyl-1,2,4-oxadiazole into 4-benzoylamino-2,5-diphenyl-1,2,3-triazole (Scheme 1) reported by D'Anna and coworkers is of specific interest to study the MRH reaction in different solvent.[127] The MRH of this reaction proceeds via an intramolecular nucleophilic substitution (S_{Ni}) that represents a special case of an S_N2 reaction (Scheme 6.1).[127,129,130]

It is well known that solvents play a key role in the reaction mechanism and affects the rate of a reaction through stabilizing or destabilizing the transition structure. The rate of rearrangement of heterocycles, for example, was found to be enhanced with increasing polarity of the solvent.[127] However, polarity only is not sufficient to describe the rate enhancement associated with ionic liquid. The rate of rearrangement of MRH was reported to be higher in [BMIM][BF_4] than those of conventional organic solvent, methanol and acetonitrile.[127,131] On the other hand the rate of rearrangement in [BMIM][PF_6] ionic liquid was comparable to the rate in methanol, acetonitrile and significantly lower when compared to [BMIM][BF_4]. Interestingly, the polarity of the two ionic liquids ([BMIM][PF_6] and [BMIM][BF_4]) are comparable (polarizability (π^*) values of 1.032 and 1.047 for [BMIM][PF_6] and [BMIM][BF_4], respectively).[132] Thus there should be a better explanation for this significant difference in the rate of enhancement observed in [BMIM][BF_4] ionic liquid other than polarity or viscosity as these two parameters failed to give a reasonable explanation for the trend of reactivity observed in MRH.[127] Furthermore, the E_T^N value (a measure of the ionizing power of solvents) for [BMIM][BF_4] is lower than that of methanol, 0.670 versus 0.762,[132] respectively, nonetheless the reaction proceeding faster in the ionic liquid than in the methanol.

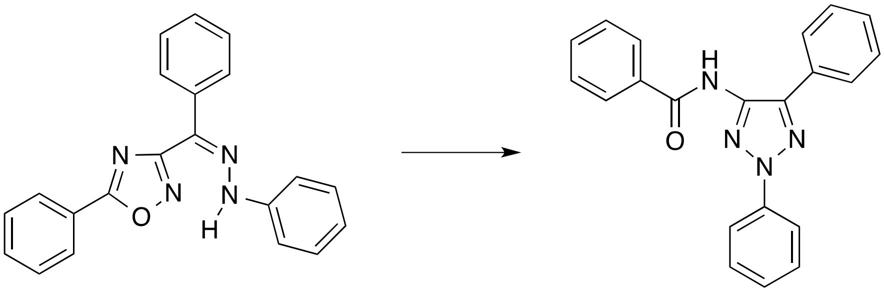

Scheme 6.1. Mononuclear rearrangement of heterocycles (MRH) for the Z-phenylhydrazone of 3-benzoyl-5-phenyl-1,2,4-oxadiazole into 4-benzoylamino-2,5-diphenyl-1,2,3-triazole.

The MRH reaction in polar protic, polar aprotic, and nonpolar aprotic proceed via different reaction pathways.[127,133,134]Two reaction mechanisms have been suggested for the MRH of Z-phenylhydrazone which solely depends on the type of solvent employed. In conventional polar solvents, such as acetonitrile or methanol, the rearrangement of *Z*-phenylhydrazone occurred with different kinetic laws implying a combination (or competition) between a base-catalyzed (specific or general) and an uncatalyzed mechanism (Scheme 6.2). In low polarity solvent (e.g benzene, toluene, and ethyl acetate) on the other hand, the MRH reactions proceeded exclusively via a base-catalyzed pathway. The reaction (where R = H in Scheme 2) was reported to proceed predominantly through an uncatalyzed pathway at a pS^+ range of 3.8-7.0 (pS^+ is an operational scale of proton concentration in the mixed solvent). At a $pS^+ \geq 8.0$, however, a base-catalyzed pathway was a dominant pathway. These reaction pathway differences suggest dependence of the reaction on the proton concentration. Furthermore, Density functional theory (DFT) study supported the solvent dependence of the MRH reaction. Bottoni et al. carried out the DFT calculation to compute the activation energies by adding two explicit water molecules to the transition state of the MRH and deduce from their computational results the dependence of the reaction on solvent.[135]

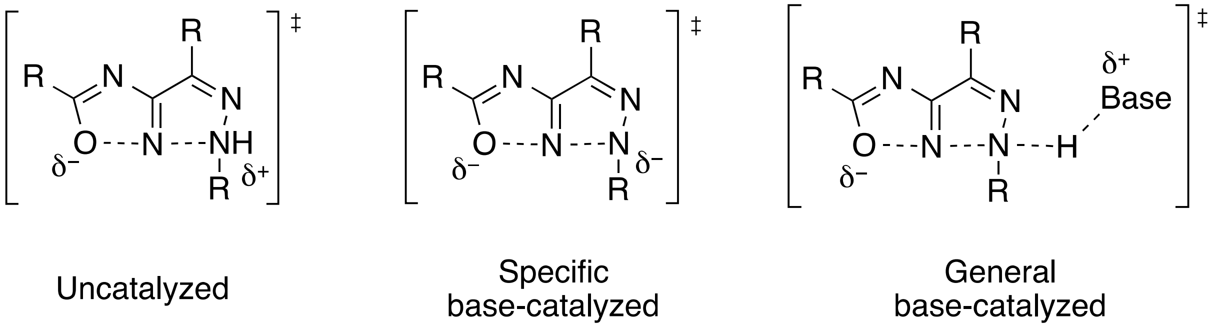

Scheme 6.2. Transition States for the Uncatalyzed and the Specific and General Gase-Catalyzed Mechanisms in the MRH reaction of the *Z*-phenylhydrazone of 3-benzoyl-5-phenyl-1,2,4-oxadiazole (R = Ph).

The MRH reaction (Scheme 6.1) in the [BMIM][BF_4] ionic liquid showed a simple first-order dependence on the piperidine concentration while a mixed first- and second-order dependence was observed for the reaction in conventional solvents.[127] No significant difference in the reactivity was observed when different bases were used, e.g. butylamine (primary amine), piperidine (secondary amine), and trimethylamine (tertiary amine), in multiple ionic liquids.

Another solvent's property that may alter the rate of a reaction is viscosity. Indeed, studies on bimolecular bond-forming reactions have reported a link between the rates of reactions and solvent viscosity, considering other solvent properties such as polarity are not taking into account for the results.[136] It is natural then to consider viscosity of the Ionic liquids to their influence in the rate of a reaction as they are known to be quite viscous. Nonetheless, D'Anna and coworkers could not find a good agreement between viscosity and reactivity of the current MRH reaction in ionic liquids.[127] It has also been hypothesized that the influence of the ionic liquids on the reactivity of the MRH reaction is due to an organizing ability derived from π-π interactions and the chemical nature of the cations and anions parts of the Ionic liquid. Atomic-level simulations, featuring hundreds of ionic liquid ions interacting with the MRH reaction, should help clarify many of the contradictions experimentally observed for the reactivity in ionic liquids as compared to conventional solvents.

In the current study, mixed quantum and molecular mechanical (QM/MM) calculations utilizing Monte Carlo statistical mechanics and free-energy perturbation theory (MC/FEP) was carried out for the *Z*-phenylhydrazone rearrangement of 3-benzoyl-5-phenyl-1,2,4-oxadiazole (Scheme 1) in [BMIM][BF_4] and [BMIM][PF_6] ionic liquids, acetonitrile (aprotic), and methanol (protic) solvents. Activation barriers and solute-solvent interactions have been computed for the uncatalyzed and specific base-catalyzed mechanisms (Scheme 6.2) to further explore the effect of solvent upon MRH reaction. The activation energy barrier for the MRH was significantly lower in [BF_4] based RTILs compared to [PF_6] based RTIL and conventional solvent, methanol and acetonitrile consistent with the experimental results reported previously. This rate enhancement of RTLIs is attributed to the substrate-substrate and solvent–substrate interaction which is favored in [BMIM][BF_4].

6.3 Computational Methods

QM/MM Calculations. Mixed QM/MM calculations were carried out for the MRH reaction (Scheme 1) in [BMIM][BF_4], [BMIM][PF_6], acetonitrile, and methanol for both specific base-catalyzed and uncatlyzed pathways. The starting geometry for the solute was determined by performing a Monte Carlo (MC) conformational search followed by geometry optimizations for the selected conformations and the conformer with the lowest energy was used as the starting geometry for the QM/MM calculations. Combined QM/MM methods allows modeling of bond making and bond breaking process of a chemical reaction. It permits to treat a system that is large enough where a QM alone can do the job.[136] The solutes, the key part of the reacting system were treated with the PDDG/PM3 semiempirical QM, which has been given excellent results for a wide variety of condensed-phase organic reactions.[111,115,137] Potentials of mean force (PMF) calculations coupled to Metropolis Monte Carlo (MC) statistical mechanics were used to build a free-energy profile for the rearrangement reactions at 25 °C and 1 atm. The solvents were represented explicitly using MM, OPLS-AA force field for ionic liquid and the united-atom OPLS (OPLS-UA) force field for methanol and acetonitrile.[138,139] In the current QM/MM methodology, the systems consisted of the reactants plus 395 conventional solvent molecules or 188 ion pairs for the ionic liquids. Periodic boundary condition was used for the reaction with the tetragonal boxes with long-range electrostatic interactions handled with Ewald summations. Solutes were inserted into the fully equilibrated ionic liquid boxes and re-equilibrated for minimally 100 million MC configurations. The computation of the QM energy and atomic charges is performed upon each attempted MC move of the solute, which occurred every 100 configurations. For electrostatic contributions to the solute-solvent energy, CM3 charges were obtained for the solute with a scaling factor of 1.14 for neutral molecules, to replicate experimental free energies of hydration and unscaled for charged species.[140,141] Furthermore, Lennard-Jones interactions between solute and solvent atoms were taken into account using OPLS parameters. This combination minimizes errors in the computed free energies. Free energy changes were calculated using the free energy perturbation theory (FEP) in conjunction with isothermal-isobaric (NPT) ensemble Metropolis Monte Carlo simulation. The free energy changes were computed as a function of intramolecular coordinates, the bond distance between nitrogen oxygen and nitrogen and nitrogen. The free energy calculation were broken into a series of intermediates steps referred to as windows. For each window, the system undergoes MC equilibration and averaging, and the result free energy difference is determined. The total free energy difference is the sum of all windows. A Double-wide sampling is used to double the efficiency of the calculation by simultaneously calculating $\lambda i \rightarrow \lambda i+1$ and $\lambda i \rightarrow \lambda i-1$ window.[136]

The BOSS program was used to simulate all QM/MM reactions in condensed phase.[138] The [BMIM] cations were fully flexible, i.e. all bond stretching, angle bending, and torsional motions were sampled. The anions were simulated as rigid molecules. The use of rigid anions in OPLS-AA has been shown to provide an accurate representation of ionic liquid physical properties, including use as a reaction medium for computed QM/MM Diels-Alder,[52] Kemp elimination,[46] β-elimination,[53] and S_NAr[54] reaction studies.[126,138,142,143] Solute-solvent and solvent-solvent intermolecular cutoff distances of 12 Å were employed for the tail carbon atom of each side chain (methyl and alkyl), a midpoint carbon on the alkyl chain, and the ring carbon between both nitrogens for imidazolium. Center atoms, i.e. B in BF_4^-, were used for the anions. If any distance is within the cutoff, the entire solvent-solvent interaction was included. Adjustments to the allowed ranges for rotations, translations, and dihedral angle movements led to overall acceptance rates of about 30% for new configurations. The ranges for bond stretching and angle bending were set automatically by the BOSS program on the basis of force constants and temperature.

Density Functional Theory. The transition structures geometries and energetics for the MRH reaction were also computed with M06-2X/6-311+G(d,p) geometry optimizations using Gaussian 09. The effect of solvent was explored by using the conductor-like polarizable continuum model (CPCM) with the UFF cavity. Frequency calculations were performed in order to verify all stationary points as minima for ground states or as saddle points for transition structures. All computations were carried out on a computer cluster located at the Alabama Supercomputer Center.

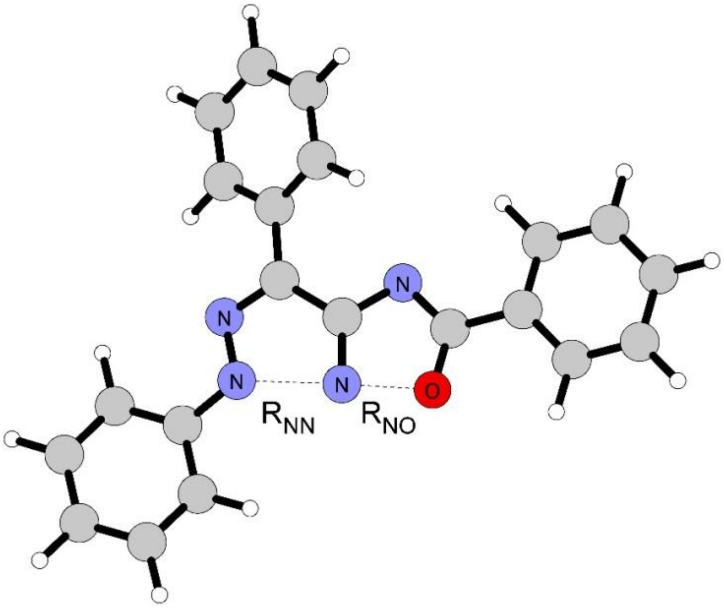

Figure 6.1. Reaction coordinates R_{NN} and R_{NO} for the MRH reaction of the *Z*-phenylhydrazone of 3-benzoyl-5-phenyl-1,2,4-oxadiazole.

6.4 Results and Discussion

The transition state and global minima were identified from the free energy maps constructed from the QM/MM/MC/FEP computation for both the specific base-catalyzed and uncatalyzed reaction pathways in [BMIM][BF_4], [BMIM][PF_6], acetonitrile, and methanol solvents. Free energy perturbation procedure was followed to obtain the energies at each window. The $\Delta G^{\ddagger}$ for the MRH reaction was computed by perturbing the bond distances between the nucleophilic nitrogen atom and the nitrogen in the oxadiazole ring denoted R_{NN} using 0.025 Å increments which represent bond formation of the reaction. A second perturbation denoted by, R_{NO}, which entailed the breaking of the oxadiazole ring at the N–O bond in 0.005 Å increments was also carried out. Figure 6.1 shows the typical reaction coordinates of the MRH reaction. It indicates a concerted bond breaking (R_{NO}) and bond making (R_{NN}) at the transition state. Combining the R_{NN} PMF, which runs along one reaction coordinate with the R_{NO} PMF in a second direction produced a two-dimensional (2D) PMF. Figure 6.2 depicts one representative of the 2D-PMF obtained from the computation. Each 2D-PMF calculation required extensive reorganization of the solvent for the ionic liquids with 80 million configurations of equilibration followed by 20 million MC steps of averaging per FEP window. For the reaction in methanol and acetonitrile, 2.5 and 5 million MC configurations of equilibration and averaging, respectively were performed.

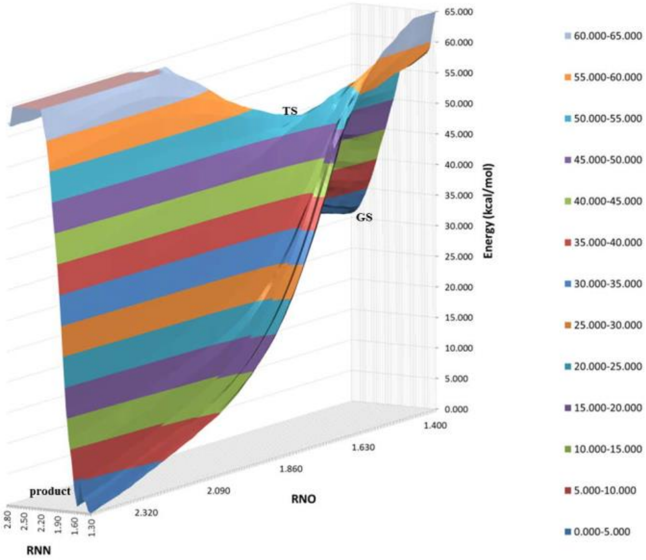

Figure 6.2. The free energy map (kcal/mol) computed for the MHR from QM/MM/MC simulations.

The computed geometries (bond length at the transition state) for the two perturbed bonds (R_{NN} and R_{NO}) of the MRH reaction on Ionic liquids and conventional solvents are given in Table 6.1. As shown in the table, no significance difference was found for bond making and bond breaking steps for both catalyzed and uncatalyzed reactions pathways. Neither was a significant difference in the bond making and breaking predicted for MRH transition structure in all the solvents tested. The $R_{NN,}$ a bond distance representing the nucleophilic attack, for the catalyzed reaction mechanism was computed in the range of 1.95-1.99 Å in the ionic liquids and the conventional solvents. For the uncatalyzed pathway the bond forming geometry was in the range 1.90-1.95 Å. Likewise, the R_{NO} which represents the opening of the 1,2,4-oxadiazole ring, was in the range of 1.73-1.84 Å and 1.73-1.78 Å for catalyzed and uncatalyzed pathways, respectively (Table 6.1). For all computed transition structure R_{NN} and R_{NO} geometries the error was ± 0.003 Å. Uncertainties in the free energy barriers were calculated by propagating the standard deviation (σ_i) on each individual ΔG_i. Smooth free energy profiles were obtained with statistical uncertainties (σ_i) of 0.01-0.03 kcal/mol in each window; thus, implying overall uncertainties in the $\Delta G^{\ddagger}$ of ca. 0.4 kcal/mol for the conventional solvents. The error bars in the ionic liquids simulations are estimated at ± 1 kcal/mol.

	CH_3OH		CH_3CN		[BMIM][BF_4]		[BMIM][PF_6]	
	R_{NO}	R_{NN}	R_{NO}	R_{NN}	R_{NO}	R_{NN}	R_{NO}	R_{NN}
Catalyzed	1.73	1.99	1.76	1.95	1.84	1.98	1.80	1.98
Uncatalyzed	1.74	1.90	1.78	1.93	1.73	1.95	1.76	1.95

[a] PDDG/PM3, MC/FEP, and Ewald summations.

Table 6.1. QM/MM calculated R_{NO} and R_{NN} Transition Structure Bond Distances (Å) for the MRH of the *Z*-phenylhydrazone of 3-benzoyl-5-phenyl-1,2,4-oxadiazole in Solution.[a]

Table 6.2 provides the energetics of the MRH reaction in methanol, acetonitrile, [BMIM][BF_4], and [BMIM][PF_6] for both specific base-catalyzed and uncatalyzed pathways. Experimental values are also given for comparison. The computed free energy activation value was 19.0 kcal/mol [BMIM][BF_4] and 20.4 kcal/mol in and [BMIM][PF_6], respectively, for the base-catalyzed route. For the uncatayzed pathway, the computed value was 30.8 kcal/mol and 31.8 kcal/mol in [BMIM][BF_4] and [BMIM][PF_6]. For the specific base-cataylzed MRH reaction, the activation energy was computed to be lower in [BMIM][BF_4] ionic liquid than in [BMIM][PF_6] by 1.4 kcal/mol. The activation barrier was also lower in [BMIM][BF_4] as compared to [BMIM][PF_6] in the uncatalyzed reaction by 1 kcal/mol. This prediction values and trend were consistent with previously reported experimental results (Table 6.2). Experimental activation barrier value of 20.6, 21.3, and 21.4 kcal/mol were reported for the MRH reaction in [BMIM][BF_4] when piperidin(Pip), trietylamine (TEA), and butylamine (BuA), respectively were used as a base. In [BMIM][PF_6] the activation energy was larger for the same bases used for the reaction in [BMIM][BF_4]. The value was 22.7, 22.6, and 23.8 kcal/mol in Pip, TEA, and

BuA, repectivley.[127] Base effect are subtle for the MRH reaction in ionic liquids as the experimental rations of reactivity are 1:1.2:1.4 for BuA/TEA/Pip in [BMIM][BF_4]. When the mechanism is believed to be general base catalyzed (low polarity solvent), a much larger reactivity range was observed.[134] In benzene for example the reactivity ratio was 1:66:188 for BuA/TEA/Pip.[127,144]This may suggest that the uncatalyzed mechanism is dominant in ionic liquids over the base-catalyzed route (Scheme 6.2) as differences in basicity between primary vs secondary vs tertiary amines should have a larger effect upon the rates. However, enhancement of the amines' basicity through decreased solvation in the ionic liquids has been reported and may play a key role.[142,144]

The QM/MM computed $\Delta G^\ddagger$ for the specific base-catalyze reaction in CH_3OH and CH_3CN were 20.7 and 20.4 kcal/mol, respectively, which is comparable to the [BMIM][PF_6] based ionic liquid (20.4 kcal/mol) and greater than in [BMIM][BF_4] (19 kcal/mol). The result was in agreement with the experimental results reported. On the other hand, the activation energy for the uncatalyzed reaction in CH_3OH and CH_3CN are 30.1 and 29.6 kcal/mol, higher than the catalyzed reaction, but lower than in the ionic liquids for the uncatalyzed reaction.

$\Delta G^\ddagger$	CH_3OH	CH_3CN	[BMIM][B	[BMIM][P
catalyzed	20.7	20.4	19.0	20.4
uncatalyzed	30.1	29.6	30.8	31.8
Exptl.	23^b	22^b	20.6^c	22.7^c

Table 6.2. Free Energies of Activation, $\Delta G^\ddagger$ (kcal/mol) at 25 °C for the MRH reaction in solutions. ^{b}Estimated using rate constant from Piperidine-catalyzed at 40 °C and Eyring equation. ^{c}Piperidine-catalyzed MRH reaction at 25°C.[127]

The rate of reaction in methanol is similar to [BMIM][PF_6]. For the base-catalyzed reaction, 20.7 kcal/mol (methanol) and 20.4 kcal/mol [BMIM][PF_6]. This unexpectedly higher rate in methanol could be due to the catalytic effect of a methoxide ion, which was present significantly in the basic solution. For example, the first order kinetic rate constant reported for the MRH reaction in CH_3OH depends on both the concentration of piperidine and methoxide ion.[127,133] This may indicate a competition between the two mechanisms, base catalyzed and uncatalyzed, were occurring when methanol is used as a solvent for the reaction. As strong methoxide ion is readily capable of abstracting the proton prior to the nucleophilic attack favoring the specific base catalyzed route, and the highly polar nature of methanol should provide a significant contribution for the uncatalyzed pathway.

Density functional theory calculations were also carried out using the M06-2X/6-311+G(d,p) method in methanol and acetonitrile by using the CPCM (The conductor-like polarizable continuum model) continuum solvent method. The transition structure bond distances (R_{NO} and R_{NN}) and the activation free energies for the specific base-catalyzed route are given in the Table 6.3. The DFT calculations for the specific base-catalyzed transition states gave transition structure distances for R_{NO} (1.8 Å for methanol and acetonitrile) and R_{NN} (2.10 Å for methanol and acetonitrile) that were in reasonable agreement with the values predicted by QM/MM/MC simulations (Tables 6.2 and 6.3). The same activation barrier for methanol and acetonitrile was predicted using DFT method, unlike the QM/MM and experimental methods (Table 6.2). The computed $\Delta G^‡$ for both methanol and acetonitrile was 16.9 kcal/mol. These values predicted by the DFT/CPCM calculations, however, are underestimated, relative to experimental values which were reported as approximately 23 and 22 kcal/mol in methanol and acetonitrile, respectively (Table 6.2). The inability of continuum solvent models to differentiate rates when comparing protic and aprotic solvents has been reported for a wide variety of chemical reactions.[137]A gas phase DFT mechanistic study of a MRH featuring the Z-hydrazone of 3-acyl-1,2,4-oxadizoles (where the phenyl was replaced with H in Scheme 6.2) was reported by Bottoni et al. They predicted an activation barrier of 34.2 kcal/mol for the uncatalyzed nucleophilic attack in gas phase.[135]

Catalyzed	$\Delta G^{\ddagger}$	R_{NO}	R_{NN}]
CH_3OH	16.9	1.81	2.10
CH_3CN	16.9	1.81	2.10

Table 6.3. MO6-2X/6-311+G(d,p)/CPCM Computed Free Energy of Activation, $\Delta G^{\ddagger}$ (kcal/mol), and transition structure geometries (Å) at 25 °C for the Specific base-catalyzed MRH of the Z-Phenylhydrazone of 3-Benzoyl-5-phenyl-1,2,4-oxadiazole.

A supermolecule approach by including two water molecules in the transition state calculation that participate via proton transfers lowered the barrier to 26.1 kcal/mol. From their computational results, Bottoni et al. conclude that the rearrangement should proceed through a concerted, asynchronous path where the nucleophilic attack of the hydrazonic nitrogen onto the oxadiozolic nitrogen and a water promoted proton shuffle from the hydrazonic nitrogen occur in the same kinetic step, but not simultaneously.[135]

The computed and experimental activation barrier for the MRH reaction for both specific base-catalyzed and uncatalyzed reaction mechanism was lower in [BMIM][BF_4] comparing to [BMIM][PF_6] (Table 6.2). However, the origin of this difference in the rate of reaction has been difficult to rationalize as no experimental trends relates the physical properties to the observed rate enhancement of [BMIM][BF_4]. The polarities and the viscosities of the two ionic liquids are, for example, comparable and could not explain for the rate difference between the two ionic liquids. D'Anna et al., proposed that the π^+-π interactions may play a large role. They suggested the π-stacking between the BMIM cation and the aromatic rings on 3-benzoyle-5-phenyl-1,2,4-oxadizole may impose a preordered geometric arrangement that ultimately enhance the rate of reaction.[127] Moreover, a coplanar orientation of the phenyl rings at the transition state should maximize the electronic effect exerted on the reaction route, similar to the previous ionic liquid studies of a base-induced β-elimination reaction and an S_NAr reaction.[126,142]

The potential π-π stacking of the MRH substrate phenyl rings and BMIM cations was monitored over the final 20 million MC steps of the simulation by using combined distribution function (CDF).[145,146] CDF monitors the angle between the normal vector across the oxadiozolic nitrogen and oxygen atoms and the distance between the oxadiozolic N and the geometrical center of BMIM as a function of the distance between the cation (BMIM) and the substrate transition structure (see the structure in Figure 6.3). The orientation of the imidazolium ring with respect to the 10π bicyclic region was assessed by using combined distribution functions (Figures 6.3 and 6.4). Angles near 0 or 180^o indicate that the imidazolium ring and the substrate transition state are stacked parallel to one another. Figure 6.3 shows significant π^+-π stacking occurring between BMIM and the transition structure for the uncatalyzed mechanism in both BF_4 and PF_6 with approximate distance of 4.5 Å and an angel near 0 deg. π^+-π staking was also observed in the specific base-catalyzed mechanism, but not as pronounced as in the uncatalyzed rout (Figure 6.4), suggesting that negative charge on the substrate may be better stabilized by specific site-directed electrostatic interactions with the cation protons.

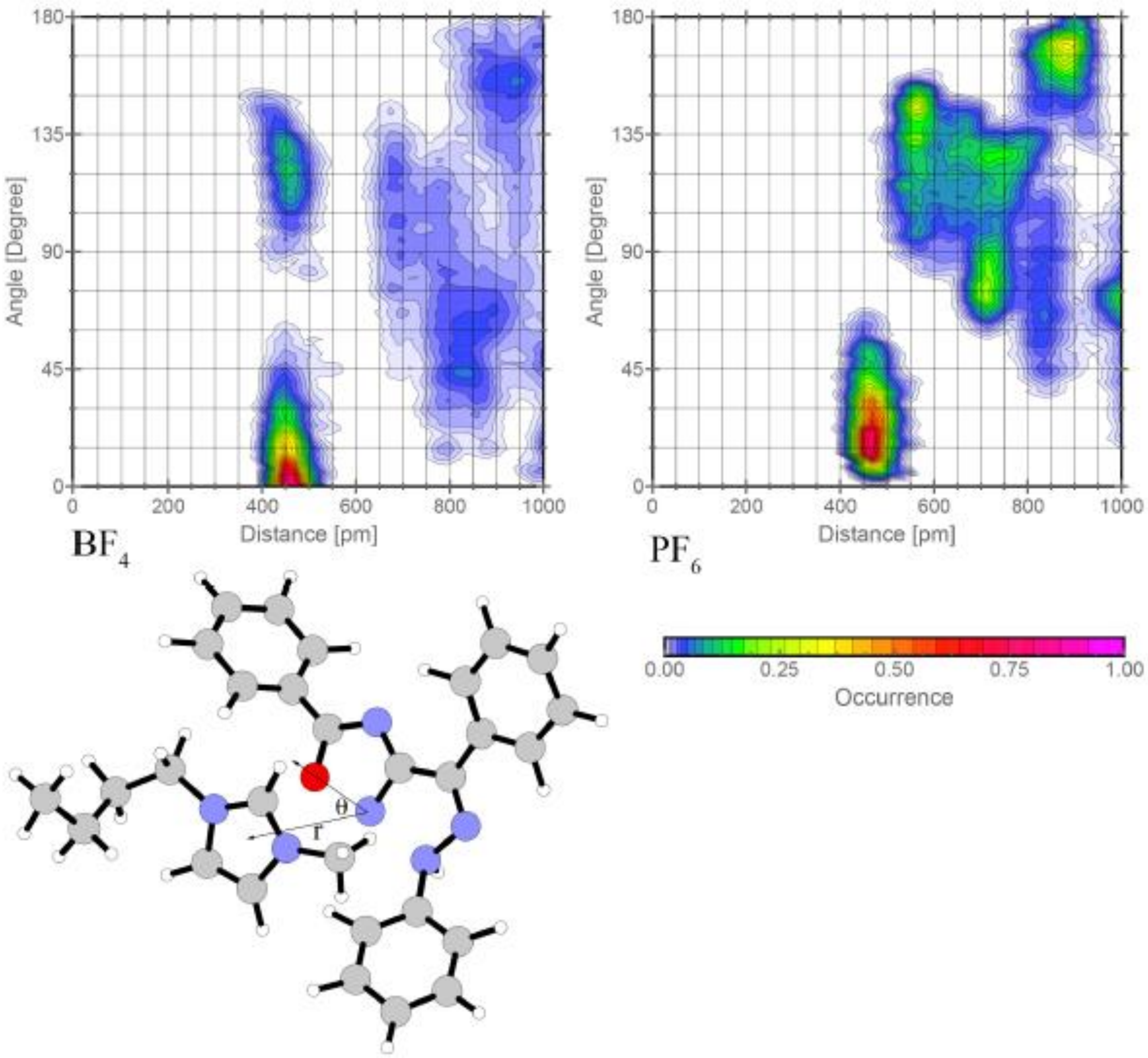

Figure 6.3. Angle (θ) between the normal to the oxadiazole N and O atoms and the line connecting the oxadiazole nitrogen to the geometric ring center of a given imidazolium ring as a function of the distance (r) between BMIM and the substrate transition structure for the uncatalyzed MRH reaction in [BMIM][BF$_4$] (left) and [BMIM][PF$_6$] (right).

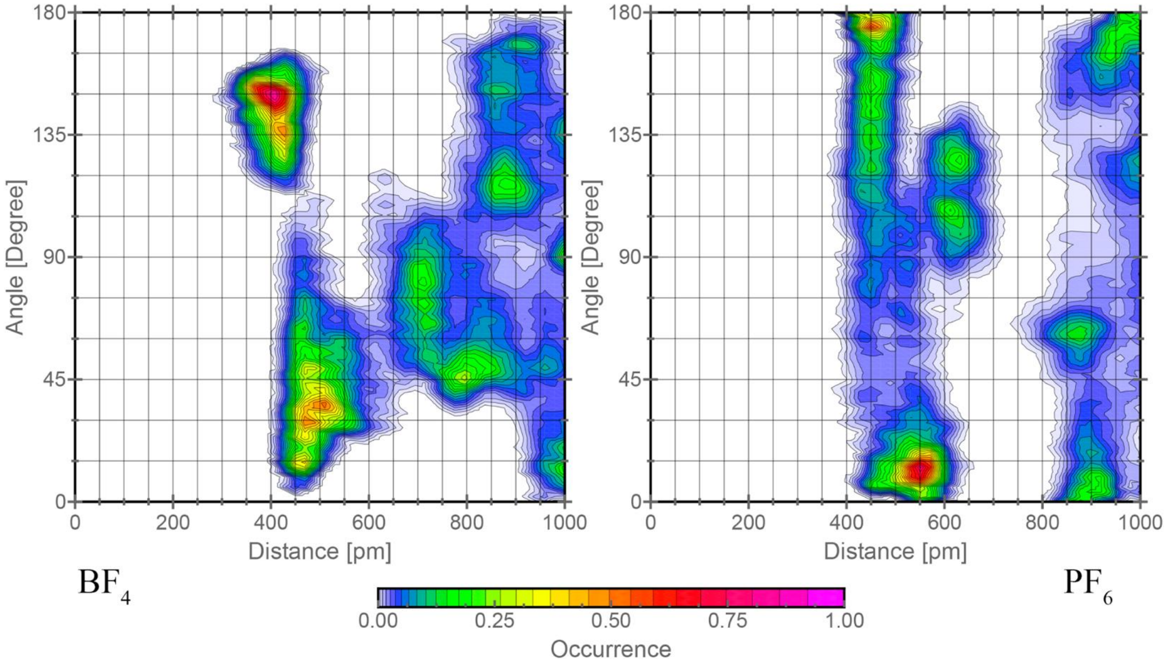

Figure 6.4. Angle (θ) between the normal to the oxadiazole N and O atoms and the line connecting the oxadiazole nitrogen to the geometric ring center of a given imidazolium ring as a function of the distance (r) between BMIM and the substrate transition structure for the specific base-catalyzed MRH reaction in [BMIM][BF_4] (left) and [BMIM][PF_6] (right).

Furthermore, CDF analysis was also performed to monitor the angle between a reference normal vector from the plan of the phenyl group and the vector between the geometrical centers of the phenyl and imidazolium rings as a function of the distance between the cation and the substrate at the ground state and transition state for both BF_4 and PF_6. Angels near 0 or 180 deg indicate that the imidazolium ring and the phenyl ring are stacked parallel to one another, an optimum geometry for favorable π^+-π stacking

Figure 6.5 to Figure 6.10 present the CDF plots between imidazolium ring of BMIM and the phenyl rings of the substrate (ring 1, ring 2 and ring 3) for the specific base-catalyzed and uncatalyzed at the ground and the transition states. The CDF highlight the significant π^+-π stacking occurring in the ionic liquids throughout the MRH reaction.

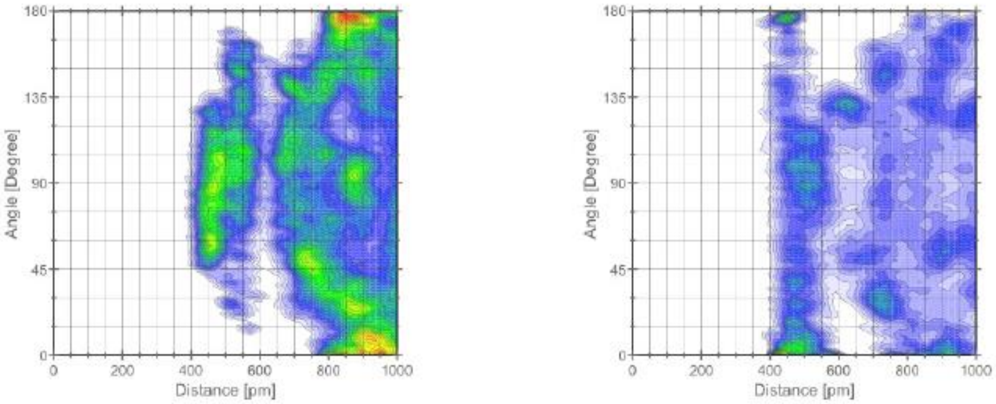

GS-Catalyzed GS-Uncatalyzed

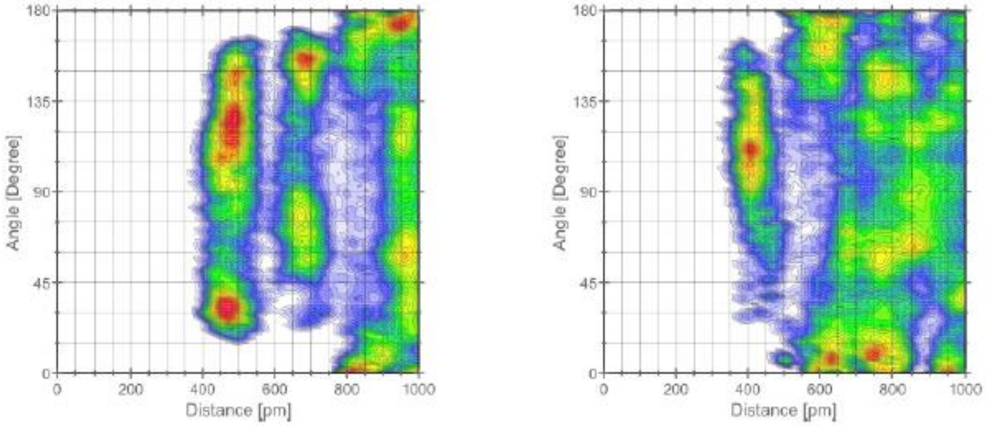

GS-Catalyzed GS-Uncatalyzed

Figure 6.5. CDF assessing the π^+-π stacking between the imidazolium cation and Ring 1 (R1) of the substrate in specific base catalyzed and uncatalyzed [BMIM][BF4] (upper) and [BMIM][PF_6] (lower) at the ground state.

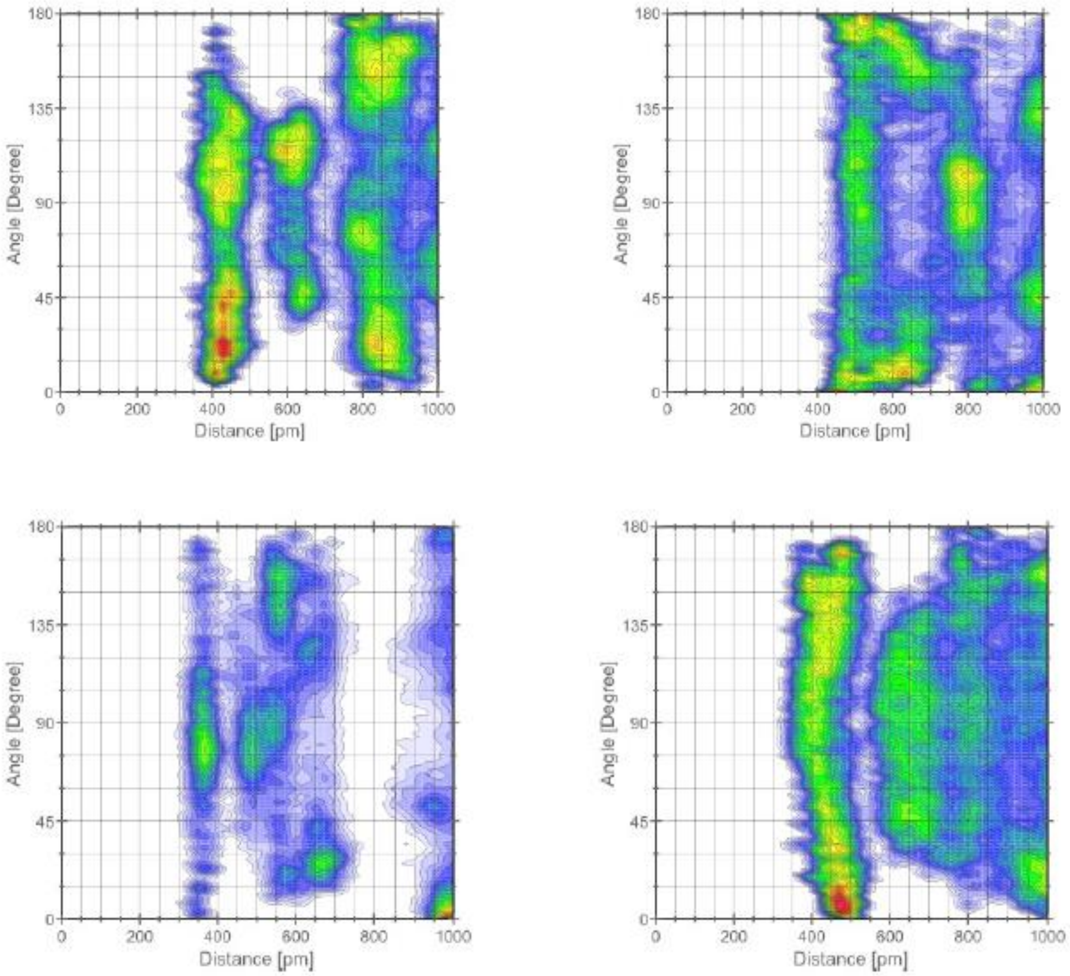

GS-Catalyzed **GS-Uncatalyzed**

Figure 6.6. CDF assessing the π^+-π stacking between the imidazolium cation and Ring 2 (R2) of the substrate in specific base catalyzed and uncatalyzed [BMIM][BF4] (upper) and [BMIM][PF_6] (lower) at the ground state.

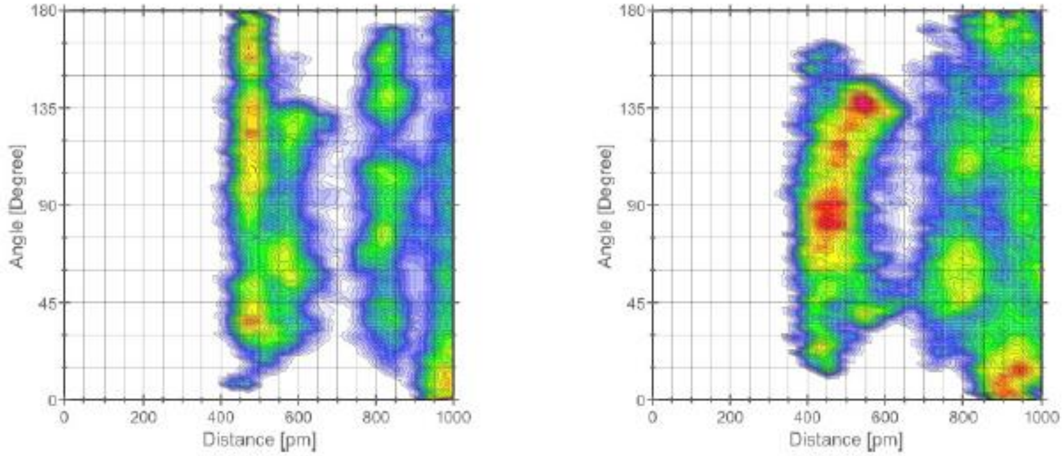

GS-Catalyzed **GS-Uncatalyzed**

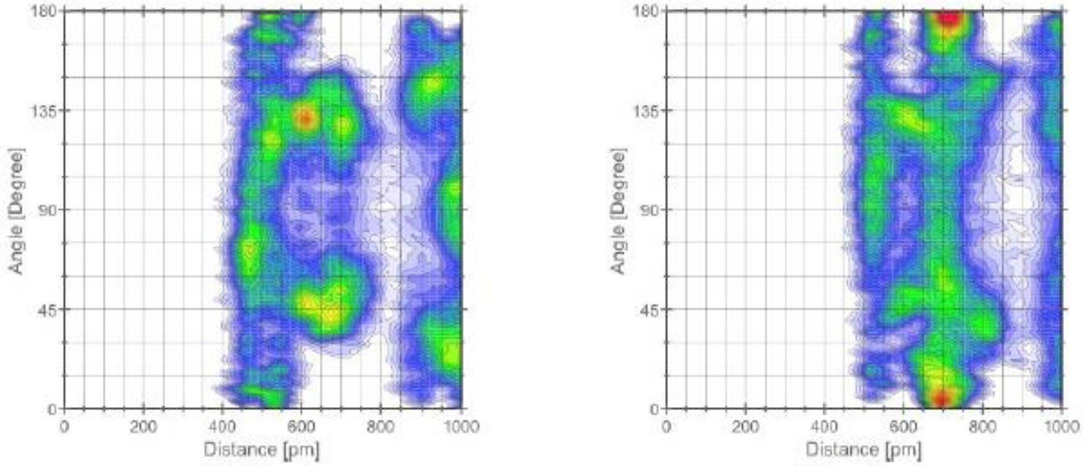

GS-Catalyzed **GS-Uncatalyzed**

Figure 6.7. CDF assessing the π^{+}-π stacking between the imidazolium cation and Ring 3 (R3) of the substrate in specific base catalyzed and uncatalyzed [BMIM][BF4] (upper) and [BMIM][PF_6] (lower) at the ground state.

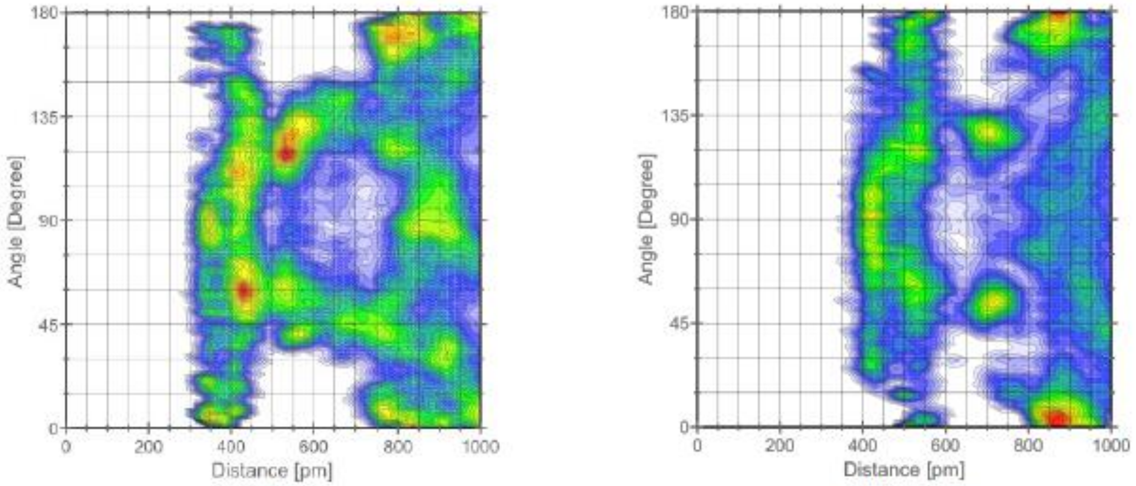

TS-Catalyzed **TS-Uncatalyzed**

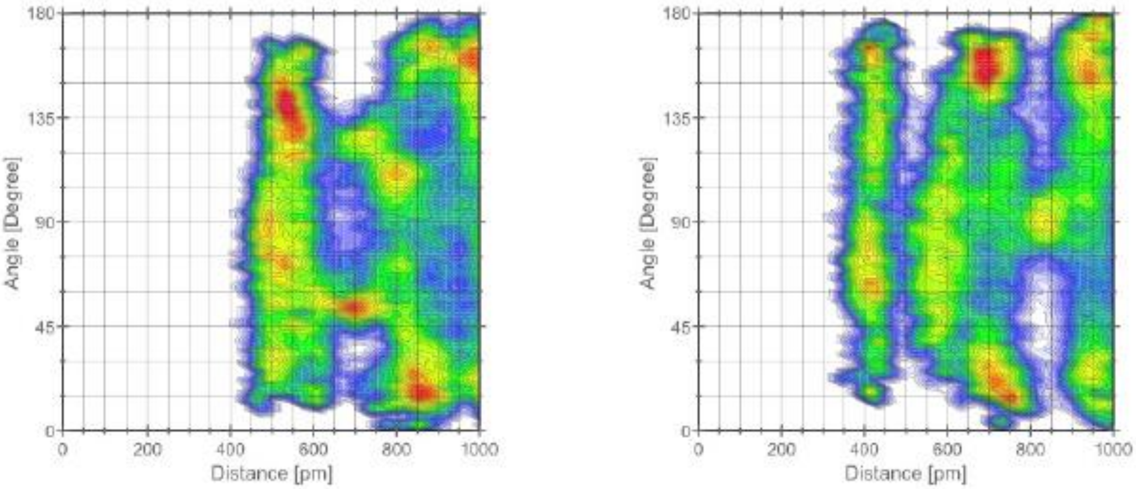

TS-Catalyzed **TS-Uncatalyzed**

Figure 6.8. CDF assessing the π^+-π stacking between the imidazolium cation and Ring 1 (R1) of the substrate in specific base catalyzed and uncatalyzed [BMIM][BF_4] (upper) and [BMIM][PF_6] (lower) at the transition state.

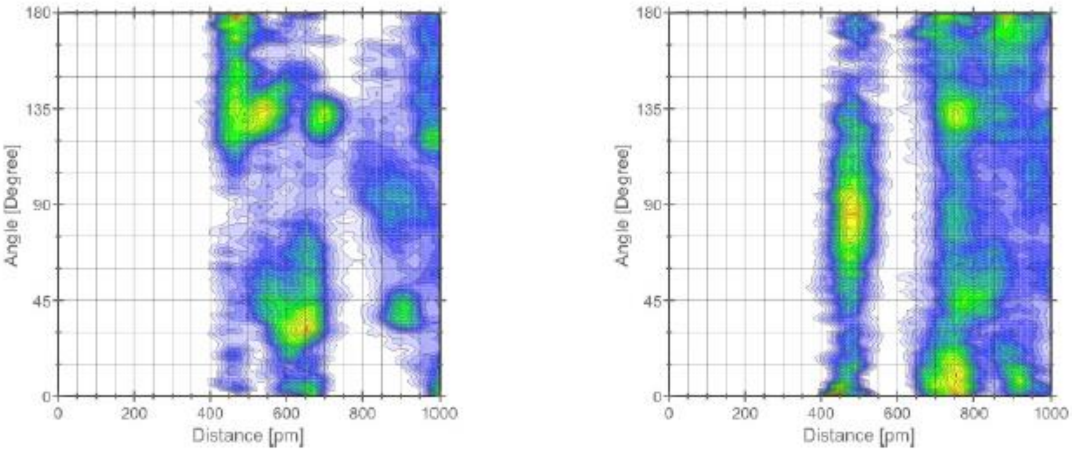

TS-Catalyzed

TS-Uncatalyzed

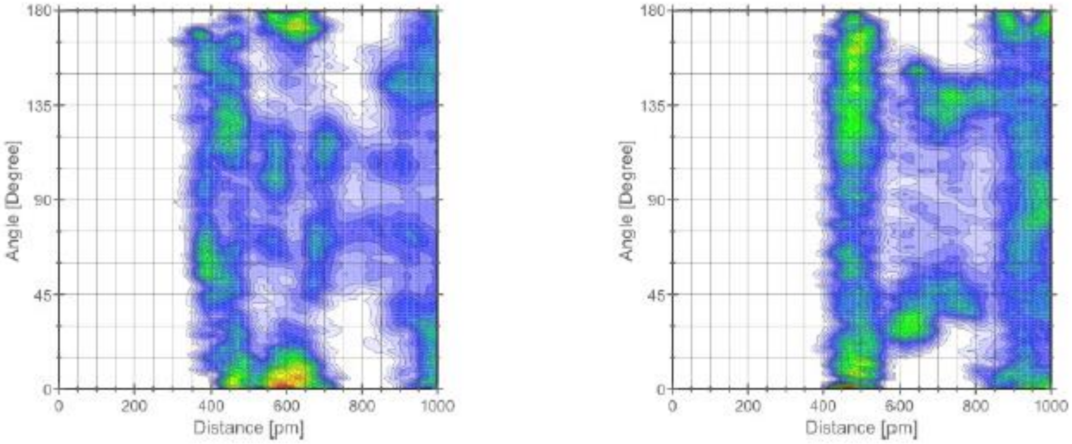

TS-Catalyzed

TS-Uncatalyzed

Figure 6.9. CDF assessing the π^{+}-π stacking between the imidazolium cation and Ring 2 (R2) of the substrate in specific base catalyzed and uncatalyzed [BMIM][BF_4] (upper) and [BMIM][PF_6] (lower) at the transition state.

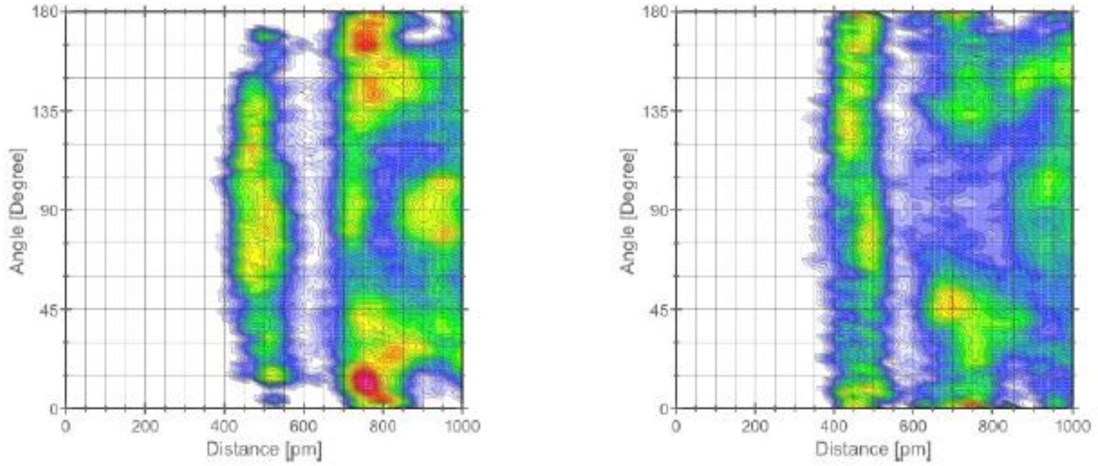

TS-Catalyzed **TS-Uncatalyzed**

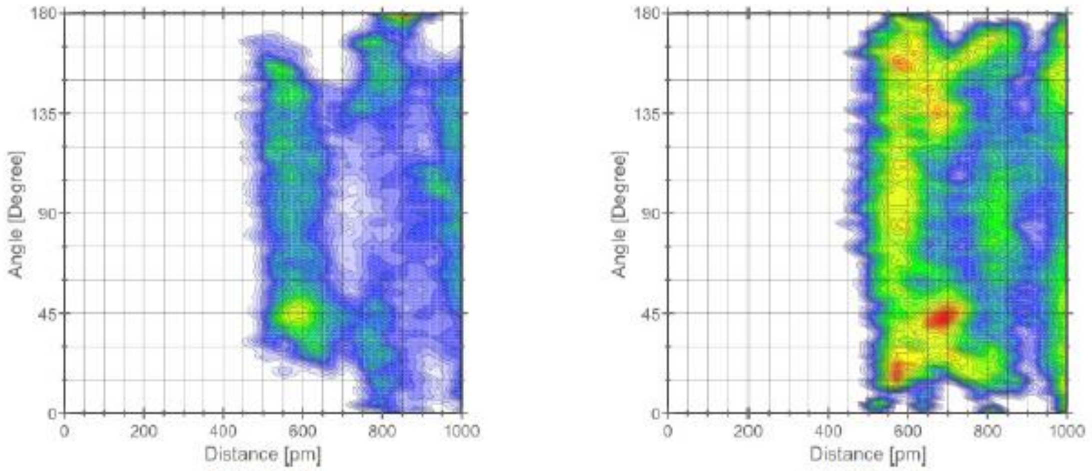

TS-Catalyzed **TS-Uncatalyzed**

Figure 6.10. CDF assessing the π^{+}-π stacking between the imidazolium cation and Ring 3 (R3) of the substrate in specific base catalyzed and uncatalyzed [BMIM][BF$_4$] (upper) and [BMIM][PF$_6$] (lower) at the transition state.

To examine the coplanarity present in the substrate as a consequence of both π^{+}-π stacking dihedral angle distributions for the solute phenyl rings were monitored over the final 20 million configurations of the QM/MM/MC/FEP simulations for both specific base-catalyzed and uncatalyzed reactant and transition state structures. Examining the three dihedral angles, ϕ_1= C-

C-C-N (magenta), ϕ_2 = C-C-C-C (red), and ϕ_3= N-N-C-C(blue) (Figures 6.11 and 6.12), for the specific base-catalyzed reactant in [BMIM][BF_4] finds the three phenyl rings to be relatively planar, i.e., approximately 0 or 180 deg, with distribution peaks for ϕ_1, ϕ_2, and ϕ_3 ranging from 0 to 30 degrees; the transition structure dihedral angles become less planar with the distribution peaks ranging from 50 to 60 degrees for ϕ_1 and $\phi_{2.}$ Figure 6.11 shows the specific base-catalyzed transition structure in [PF_6] found to be overall less planar than in the [BF_4] ionic liquid, particularly for ϕ_1 and ϕ_2 dihedral angles. The same general trend in planarity, i.e., more prevalent coplanarity in BF_4 over PF_6 ionic liquids, is found for the catalyzed rout when comparing dihedral angles distribution plots between the reactant and transition structures (Figure 6.12). This suggests that favorable π^+-π stacking interaction between BMIM and phenyl rings may induce a more constructive reaction orientation in the BF_4 ionic liquid prior to nucleophilic attack and may therefore help enhance the rate relative to PF_6.

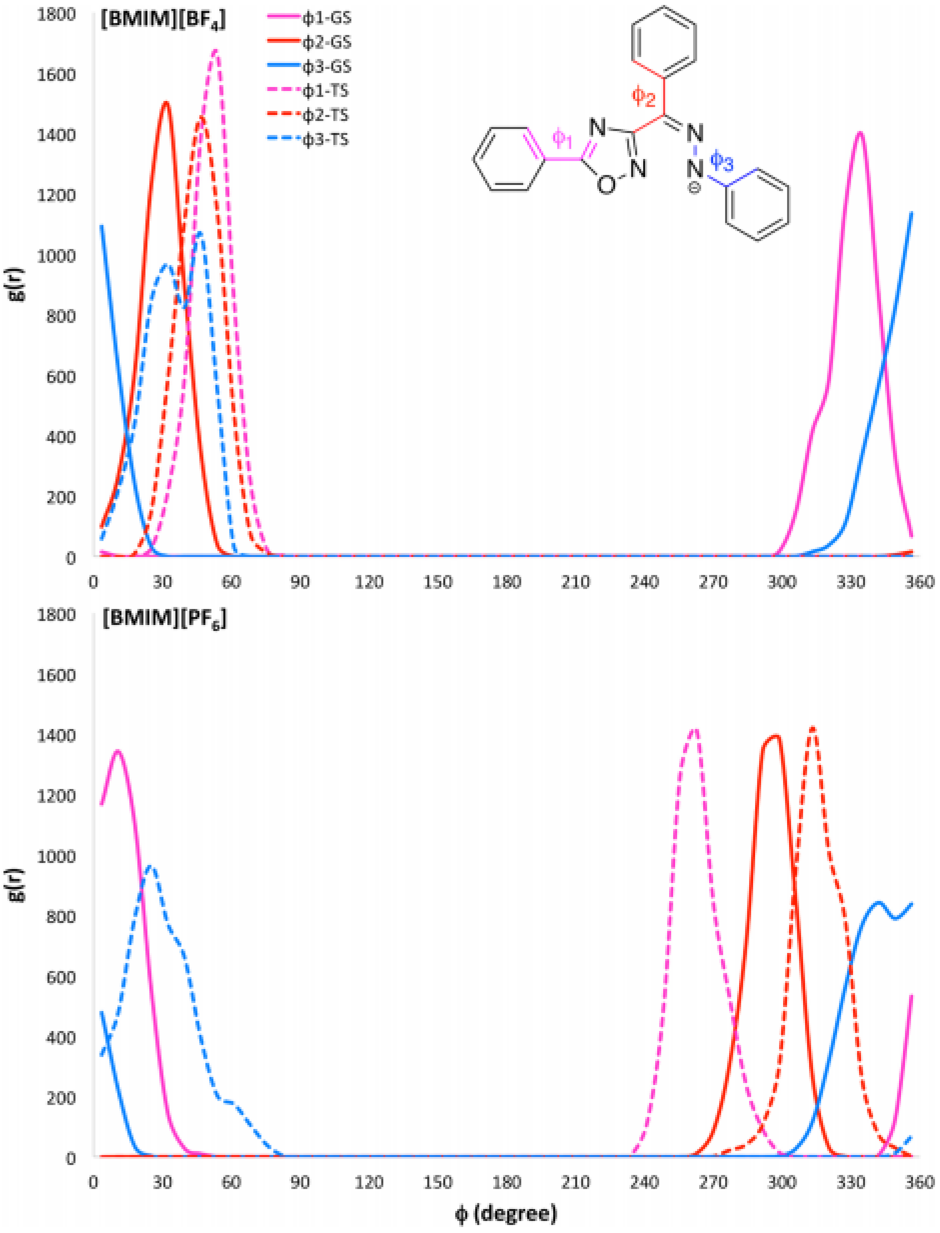

Figure 6.11. Dihedral distribution plots for the specific base-catalyzed MRH reaction ground state (GS) and transition state (TS) in the ionic liquids. Definition of torsion angles ϕ_1= C-C-C-N (magenta), ϕ_2 = C-C-C-C (red), and ϕ_3= N-N-C-C (blue).

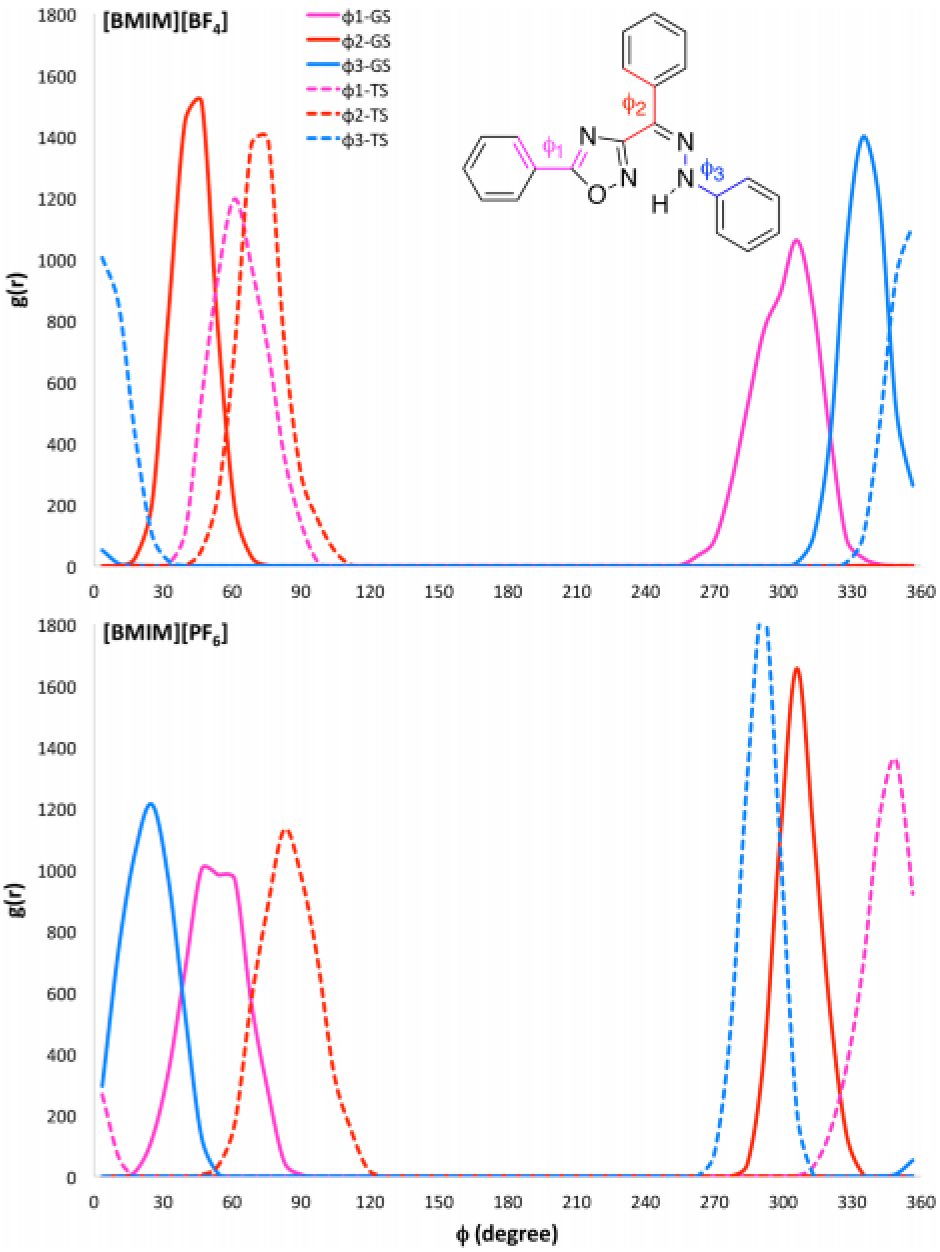

Figure 6.12. Dihedral distribution plots for the uncatalyzed MRH reaction ground state (GS) and transition state (TS) in the ionic liquids. Definition of torsion angles ϕ_1= C-C-C-N (magenta), ϕ_2 = C-C-C-C (red), and ϕ_3= N-N-C-C (blue).

In addition to the favorable π^+-π interactions between the BMIM cation and the phenyl substituents, π-stacking between BMIM and the bicyclic quasi-aromatic 10π oxadiazole/triazole reacting region should help stabilize the transition state.

Radial distribution functions for the ground and transition states from both the specific base-catalyzed and uncatalyzed reaction mechanisms in BF_4 and PF_6 are reported in Figure 6.13 and Figure 6.14. The distance between the most acidic proton on the BMIM cation, that is the H located on the 2-position carbon atom bisecting the nitrogen atoms on the imidazolium ring (pKa = 21-23)[69,70] and the hydrazonic nitrogen, oxaiozonic nitrogen, and oxadiozonic oxygen atoms on the MRH substrate were monitored over the course of the reaction with the employment of radial distribution function.

For the specific base-catalyzed reaction in BF_4, the most acidic proton on BMIM (label H1) gives large peaks centered at 250 pm with the negative charged hydrazonic nitrogen (N2) atom and the oxadiozolic nitrogen (N1) atoms at the ground state. At the transition state the electron density shifts to the oxadiozlic oxygen (O1) and, as a result, a large radial distribution peak forms between H1-O1 as the ionic liquid organizational structure adjust to stabilize the change in electron distribution. Concurrently, the H1-N2 peak diminished for the base-catalyzed transition state giving a smaller peak centered at 370 pm, reflecting the reduction in negative charge (Figure 6.13).

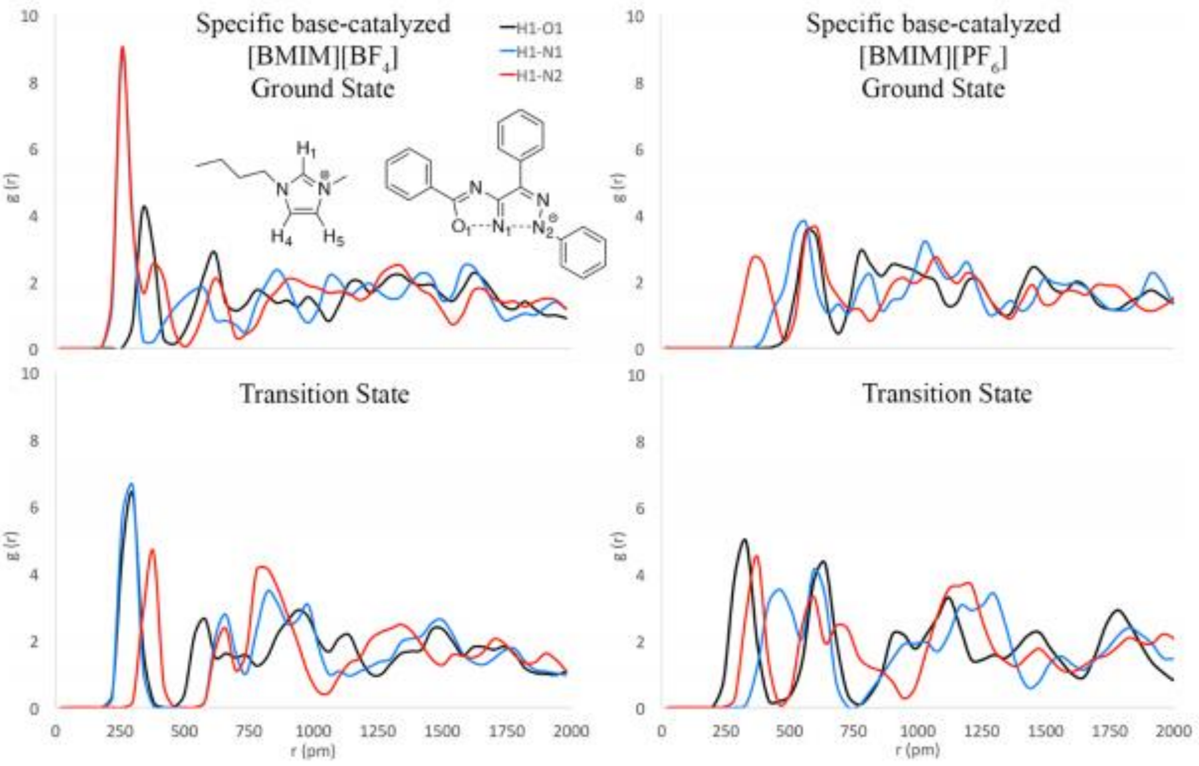

Figure 6.13. Radial distribution functions in [BMIM][BF$_4$] (left) and [BMIM][PF$_6$] (right) for the specific base-catalyzed MRH ground and transition states between the most acidic proton on BMIM and the oxadiozolic oxygen (H1-O1, black), oxadiozolic nitrogen (H1-N1, blue), and hydrazonic nitrogen (H1-N2, red).

The uncatalyzed reaction mechanism in [BMIM][BF4] gives radial distribution function that greatly differ from the specific base-catalyzed catalyzed pathway. The uncatalyzed path begins as a neutral reactant, but forms a charge separated transition structure with partial positive charge on N2 and a partial negative charge on O1 (Figure 6.14). Accordingly, the radial distribution peak centered around 310 pm for the uncatalyzed H1-N2 ground state shifts at the transition state to a distance of 500 pm with a much smaller peak as the N2 becomes more positively charged. The small H1- O1 peak centered around 360 pm for the [BMIM][BF$_4$]

ground state becomes much larger and distance decrease to 280 pm a negative charge develops on O1 at the transition structure .

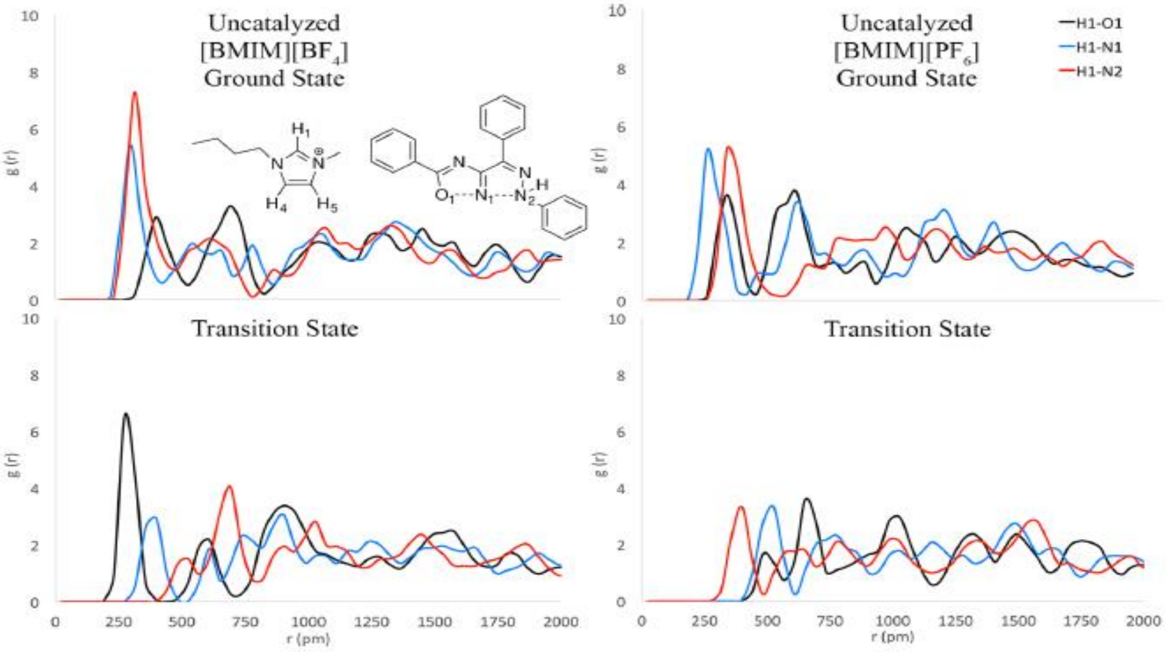

Figure 6.14. Radial distribution functions in [BMIM][BF$_4$] (left) and [BMIM][PF$_6$] (right) for the uncatalyzed MRH ground and transition states between the most acidic proton on BMIM and the oxadiozolic oxygen (H1-O1, black), oxadiozolic nitrogen (H1-N1, blue), and hydrazonic nitrogen (H1-N2, red).

In addition, the substrate interactions with H4 and H5 protons directly attached to the imidazolium carbon ring atoms nearest the side-chain N-butyl and N-methyl, respectively, were also examined. The radial distribution functions for the MRH reactant and transition state in [BMIM][PF$_6$] are given in Figure 6.15-6.18 for H4 and H5. Visual inspection of the plots finds dramatically smaller peaks between the H4 atom in BMIM and the heterocycle O and N atoms as compared to [BMIM BF$_4$] for both mechanisms. This suggests that the PF$_6$ anion severely weakens the favorable BMIM electrostatic interactions provided to the transition state.

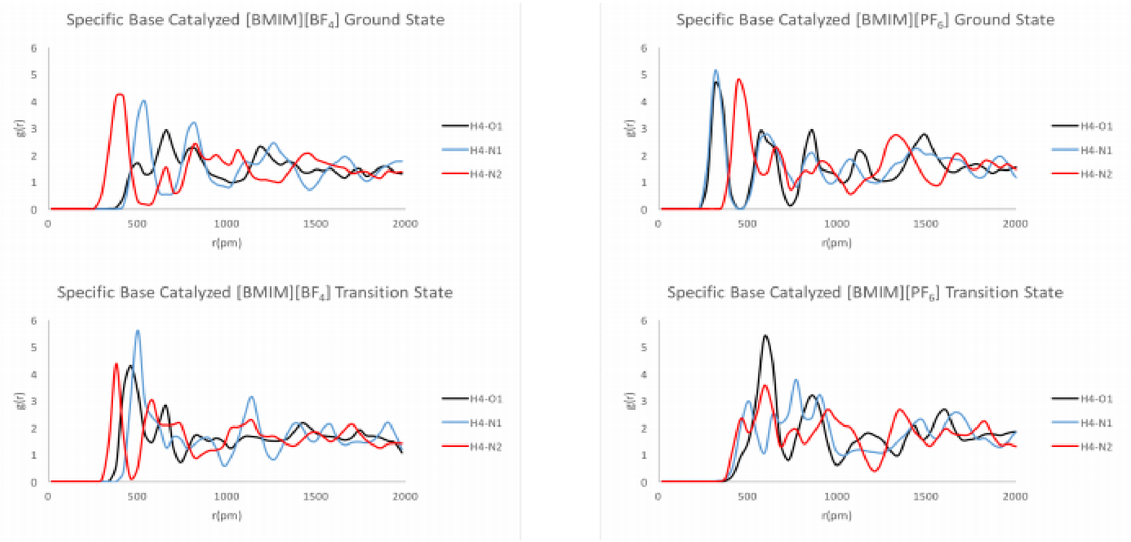

Figure 6.15. Radial distribution functions in [BMIM][BF$_4$] and [BMIM][PF$_6$] for the specific-catalyzed MRH ground and transition states between H4 on BMIM and the oxadiozolic oxygen (H4-O1, black), oxadiozolic nitrogen (H4-N1, blue), and hydrazonic nitrogen (H4-N2, red)

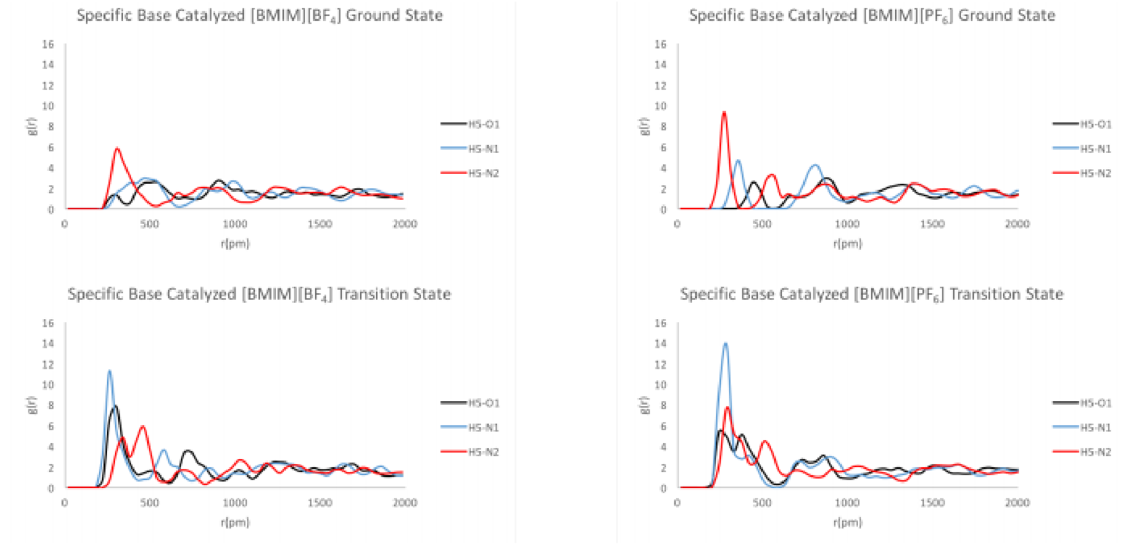

Figure 6.16. Radial distribution functions in [BMIM][BF$_4$] and [BMIM][PF$_6$] for the specific base catalyzed MRH ground and transition states between H5 on BMIM and the oxadiozolic oxygen (H5-O1, black), oxadiozolic nitrogen (H5-N1, blue), and hydrazonic nitrogen (H5-N2, red)

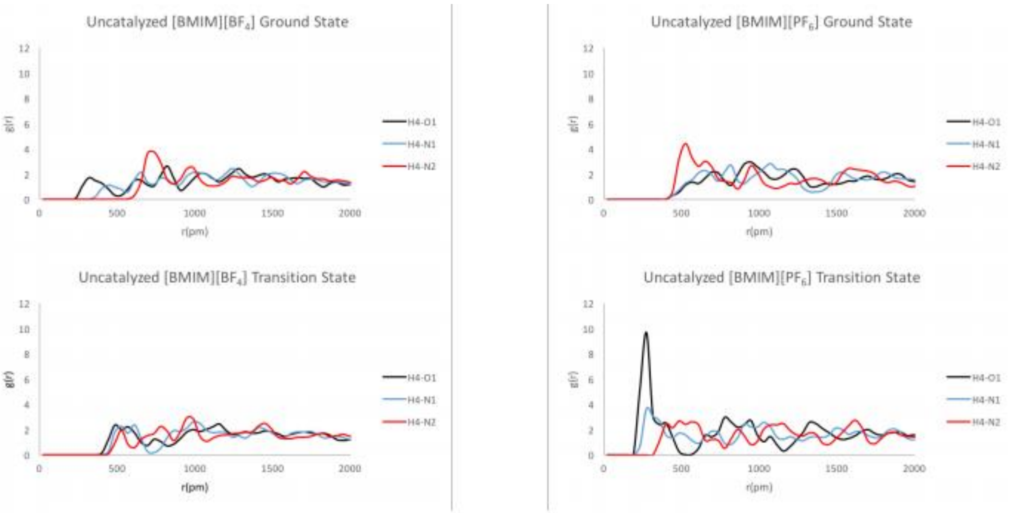

Figure 6.17. Radial distribution functions in [BMIM][BF$_4$] and [BMIM][PF$_6$] for the uncatalyzed MRH ground and transition states between H4 on BMIM and the oxadiozolic oxygen (H4-O1, black), oxadiozolic nitrogen (H4-N1, blue), and hydrazonic nitrogen (H4-N2, red)

Figure 6.18. Radial distribution functions in [BMIM][BF$_4$] and [BMIM][PF$_6$] for the uncatalyzed MRH ground and transition states between H5 on BMIM and the oxadiozolic oxygen (H5-O1, black), oxadiozolic nitrogen (H5-N1, blue), and hydrazonic nitrogen (H5-N2, red)

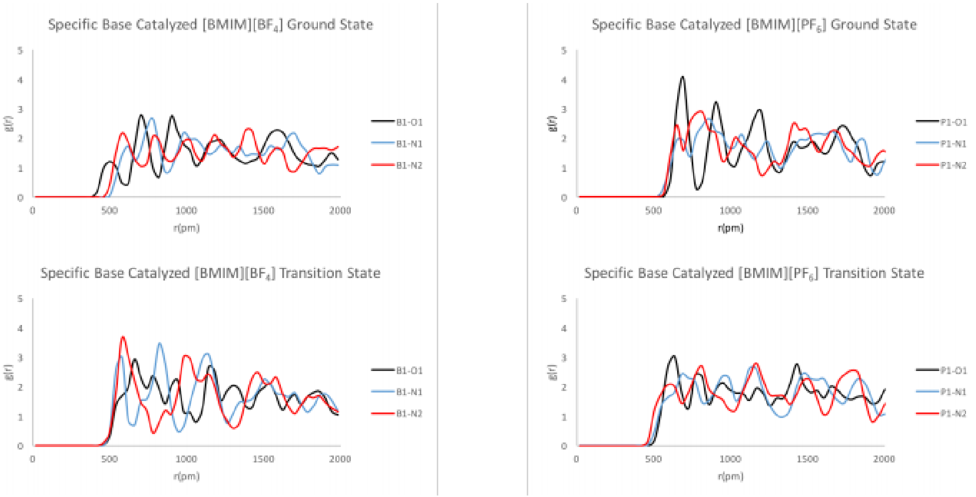

Figure 6.19. Radial distribution functions in [BMIM][BF$_4$] and [BMIM][PF$_6$] for the specific base-catalyzed MRH ground and transition states between the center atom of the anion and the oxadiozolic oxygen (B1/P1-O1, black), oxadiozolic nitrogen (B1/P1-N1, blue), and hydrazonic nitrogen (B1/P1-N2, red)

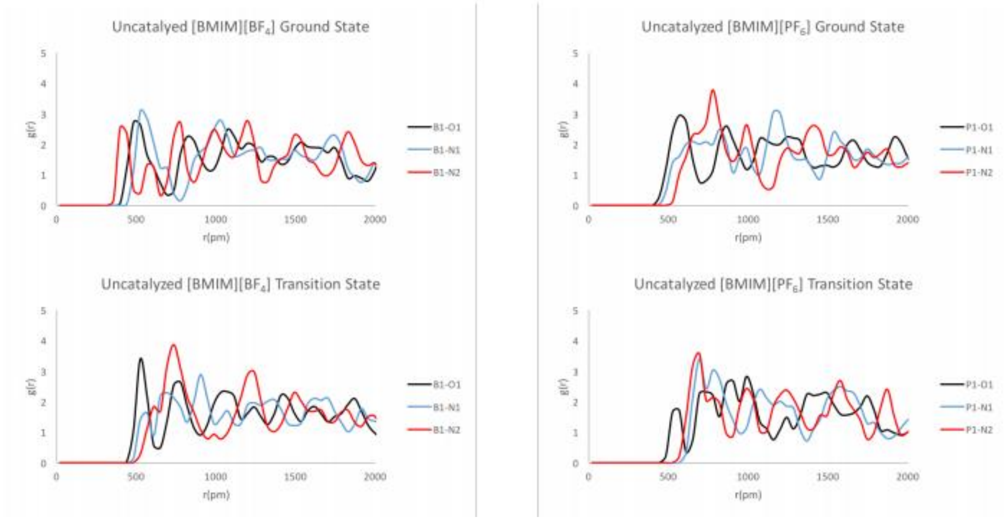

Figure 6.20. Radial distribution functions in [BMIM][BF$_4$] and [BMIM][PF$_6$] for the uncatalyzed MRH ground and transition states between the center atom of the anion and the oxadiozolic oxygen (B1/P1-O1, black), oxadiozolic nitrogen (B1/P1-N1, blue), and hydrazonic nitrogen (B1/P1-N2, red).

The solute-solvent interactions occurring over the course of the MRH reaction were assessed by computing the nearest neighbor distribution between the H1, H4, and H5 proton and the substrate O1, N1, and N2 atoms (Table 6.4 and Figures 6.21-6.27). This distribution monitor the distance between the closest cation/anion and the substrate over the final 20 million MC steps. A much tighter interactions between [BMIM] and substrate in the [BMIM][BF_4] ionic liquid was found as compared to [BMIM][PF_6] consistent with the radial distribution functions. The distance between the H1 atom and the O1, N1, and N2 atoms are 1-2 Å closer in the [BMIM][BF_4] and are indicative of greater electrostatic stabilization, particularly at the transition state (Table 4).

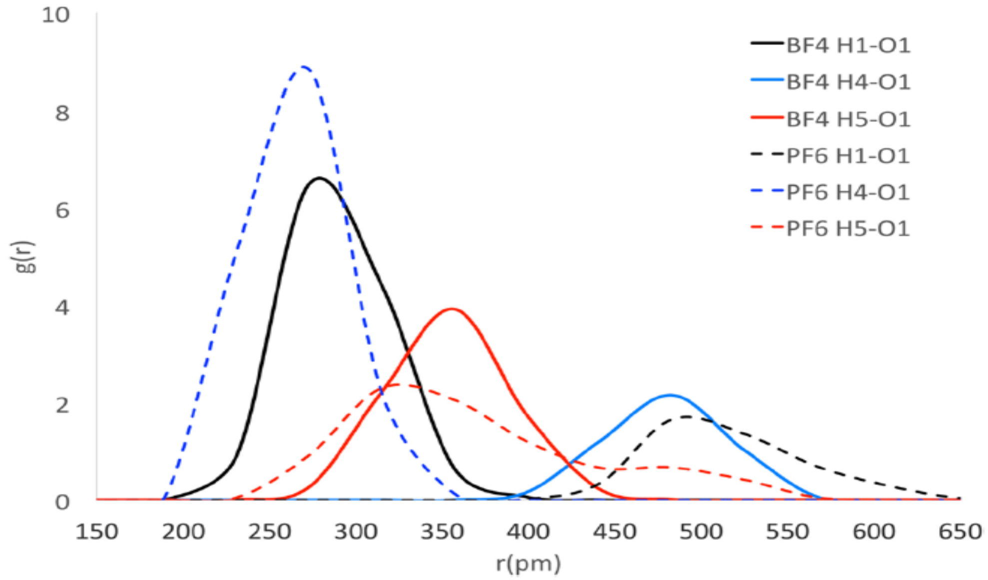

Figure 6.21. Nearest neighbor distribution in [BMIM][BF_4] (solid lines) and [BMIM][PF_6] (dashed lines) for the uncatalyzed MRH transition states between the most acidic proton on BMIM (H1, H4, and H5) and the oxadiozolic oxygen (O1).

Figure 6.21 shows a nearest distribution neighbor plot highlighting the distance between [BMIM] ring proton and the oxadiozolic oxygen on the MRH substrate for the uncatalyzed transition state. As shown in the Figure 6.21, the [BMIM][BF$_4$] ionic liquid interact with the transition structure predominantly via the most acidic BMIM proton H1 (black solid line) which is represented by highest distribution at lowest distance (~260pm). The [BMIM][PF$_6$] ionic liquid on the contrary interacts predominantly through the less acidic H4 proton (blue dashed line). This suggests a greater electrostatic stabilization in [BMIM][BF$_4$] solvent.

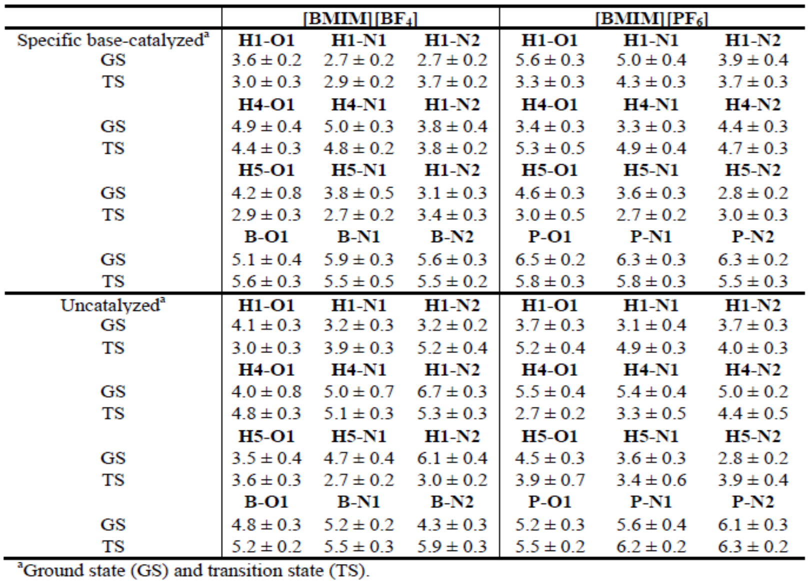

	[BMIM][BF$_4$]			[BMIM][PF$_6$]		
Specific base-catalyzed[a]	**H1-O1**	**H1-N1**	**H1-N2**	**H1-O1**	**H1-N1**	**H1-N2**
GS	3.6 ± 0.2	2.7 ± 0.2	2.7 ± 0.2	5.6 ± 0.3	5.0 ± 0.4	3.9 ± 0.4
TS	3.0 ± 0.3	2.9 ± 0.2	3.7 ± 0.2	3.3 ± 0.3	4.3 ± 0.3	3.7 ± 0.3
	H4-O1	**H4-N1**	**H1-N2**	**H4-O1**	**H4-N1**	**H4-N2**
GS	4.9 ± 0.4	5.0 ± 0.3	3.8 ± 0.4	3.4 ± 0.3	3.3 ± 0.3	4.4 ± 0.3
TS	4.4 ± 0.3	4.8 ± 0.2	3.8 ± 0.2	5.3 ± 0.5	4.9 ± 0.4	4.7 ± 0.3
	H5-O1	**H5-N1**	**H1-N2**	**H5-O1**	**H5-N1**	**H5-N2**
GS	4.2 ± 0.8	3.8 ± 0.5	3.1 ± 0.3	4.6 ± 0.3	3.6 ± 0.3	2.8 ± 0.2
TS	2.9 ± 0.3	2.7 ± 0.2	3.4 ± 0.3	3.0 ± 0.5	2.7 ± 0.2	3.0 ± 0.3
	B-O1	**B-N1**	**B-N2**	**P-O1**	**P-N1**	**P-N2**
GS	5.1 ± 0.4	5.9 ± 0.3	5.6 ± 0.3	6.5 ± 0.2	6.3 ± 0.3	6.3 ± 0.2
TS	5.6 ± 0.3	5.5 ± 0.5	5.5 ± 0.2	5.8 ± 0.3	5.8 ± 0.3	5.5 ± 0.3
Uncatalyzed[a]	**H1-O1**	**H1-N1**	**H1-N2**	**H1-O1**	**H1-N1**	**H1-N2**
GS	4.1 ± 0.3	3.2 ± 0.3	3.2 ± 0.2	3.7 ± 0.3	3.1 ± 0.4	3.7 ± 0.3
TS	3.0 ± 0.3	3.9 ± 0.3	5.2 ± 0.4	5.2 ± 0.4	4.9 ± 0.3	4.0 ± 0.3
	H4-O1	**H4-N1**	**H1-N2**	**H4-O1**	**H4-N1**	**H4-N2**
GS	4.0 ± 0.8	5.0 ± 0.7	6.7 ± 0.3	5.5 ± 0.4	5.4 ± 0.4	5.0 ± 0.2
TS	4.8 ± 0.3	5.1 ± 0.3	5.3 ± 0.3	2.7 ± 0.2	3.3 ± 0.5	4.4 ± 0.5
	H5-O1	**H5-N1**	**H1-N2**	**H5-O1**	**H5-N1**	**H5-N2**
GS	3.5 ± 0.4	4.7 ± 0.4	6.1 ± 0.4	4.5 ± 0.3	3.6 ± 0.3	2.8 ± 0.2
TS	3.6 ± 0.3	2.7 ± 0.2	3.0 ± 0.2	3.9 ± 0.7	3.4 ± 0.6	3.9 ± 0.4
	B-O1	**B-N1**	**B-N2**	**P-O1**	**P-N1**	**P-N2**
GS	4.8 ± 0.3	5.2 ± 0.2	4.3 ± 0.3	5.2 ± 0.3	5.6 ± 0.4	6.1 ± 0.3
TS	5.2 ± 0.2	5.5 ± 0.3	5.9 ± 0.3	5.5 ± 0.2	6.2 ± 0.2	6.3 ± 0.2

[a] Ground state (GS) and transition state (TS).

Table 6.4. Average Distance (Å) Calculated using a Nearest Neighbor Distribution between the Acidic Proton (H1) in BMIM, Boron (B) in BF$_4$, or Phosphorous (P) in PF$_6$ and the Oxadiozolic Oxygen (O1), Oxadiozolic Nitrogen (N1), and Hydrazonic Nitrogen (N2) from the MRH reaction mechanisms.

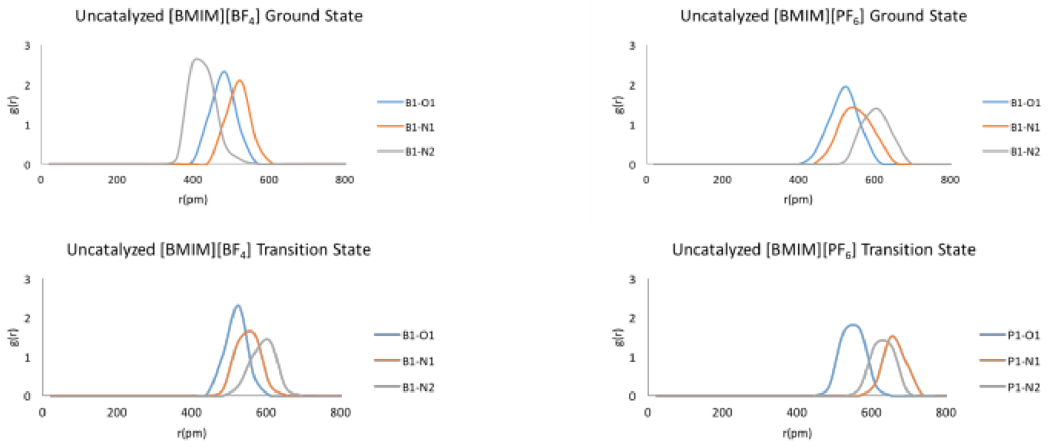

Figure 6.22. Nearest neighbor distribution in [BF$_4$] and [PF$_6$] anion and the oxadiozolic oxygen (B1/P1-O1), oxadiozolic nitrogen (B1/P1-N1), and hydrazonic nitrogen (B1/P1-N2) in uncatalyzed mechanism.

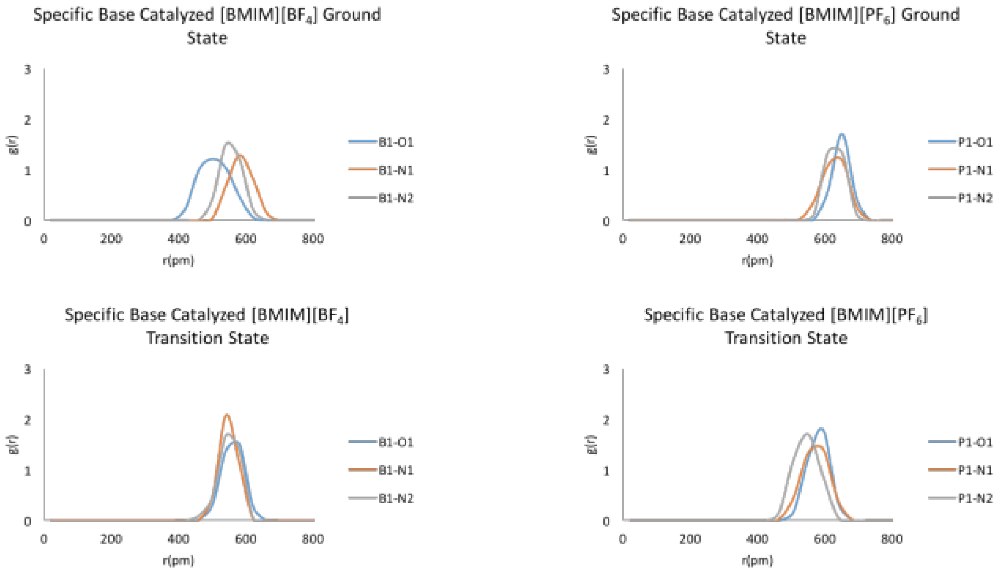

Figure 6.23. Nearest neighbor distribution in [BF$_4$] and [PF$_6$] anion and the oxadiozolic oxygen (B1/P1-O1), oxadiozolic nitrogen (B1/P1-N1), and hydrazonic nitrogen (B1/P1-N2) in specific base-catalyzed mechanism.

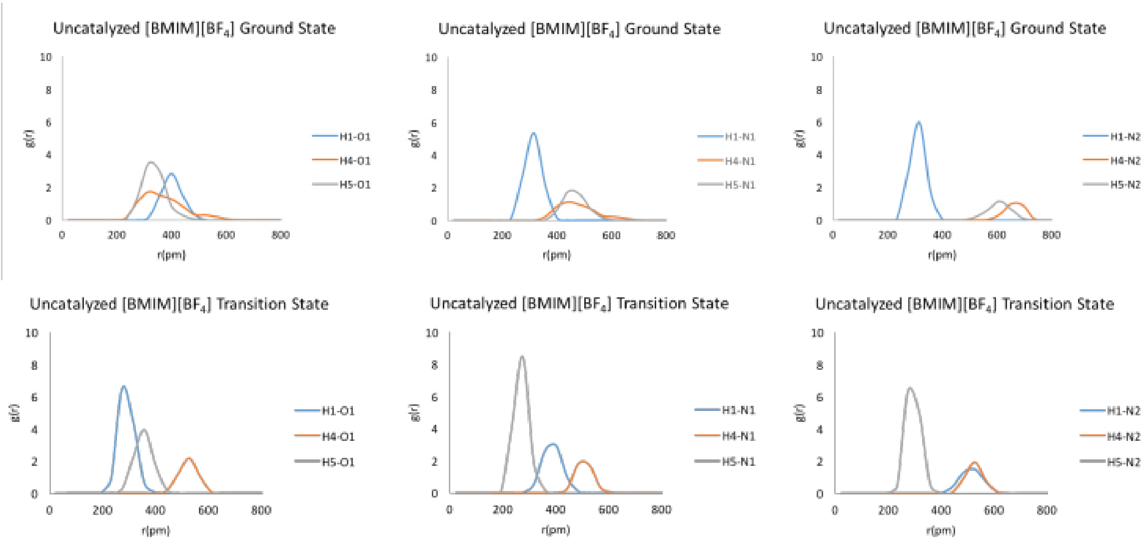
Uncatalyzed [BMIM][BF$_4$] Ground State

Uncatalyzed [BMIM][BF$_4$] Ground State

Uncatalyzed [BMIM][BF$_4$] Ground State

Uncatalyzed [BMIM][BF$_4$] Transition State

Uncatalyzed [BMIM][BF$_4$] Transition State

Uncatalyzed [BMIM][BF$_4$] Transition State

Figure 6.24. Nearest neighbor distribution between H1, H4, and H5 protons on the imidazolium ring of [BMIM] and the oxadiozolic oxygen (H-O1), oxadiozolic nitrogen (H-N1), and hydrazonic nitrogen (H-N2) in uncatalyzed [BMIM][BF$_4$]

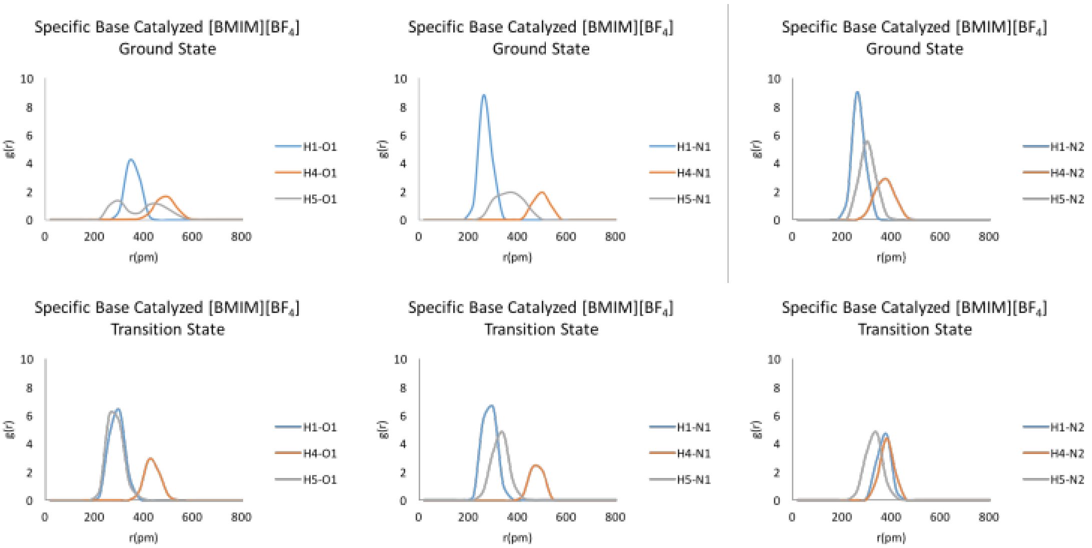
Specific Base Catalyzed [BMIM][BF$_4$] Ground State

Specific Base Catalyzed [BMIM][BF$_4$] Ground State

Specific Base Catalyzed [BMIM][BF$_4$] Ground State

Specific Base Catalyzed [BMIM][BF$_4$] Transition State

Specific Base Catalyzed [BMIM][BF$_4$] Transition State

Specific Base Catalyzed [BMIM][BF$_4$] Transition State

Figure 6.25. Nearest neighbor distribution between H1, H4, and H5 protons on the imidazolium ring of [BMIM] and the oxadiozolic oxygen (H-O1), oxadiozolic nitrogen (H-N1), and hydrazonic nitrogen (H-N2) in specific base-catalyzed [BMIM][BF$_4$]

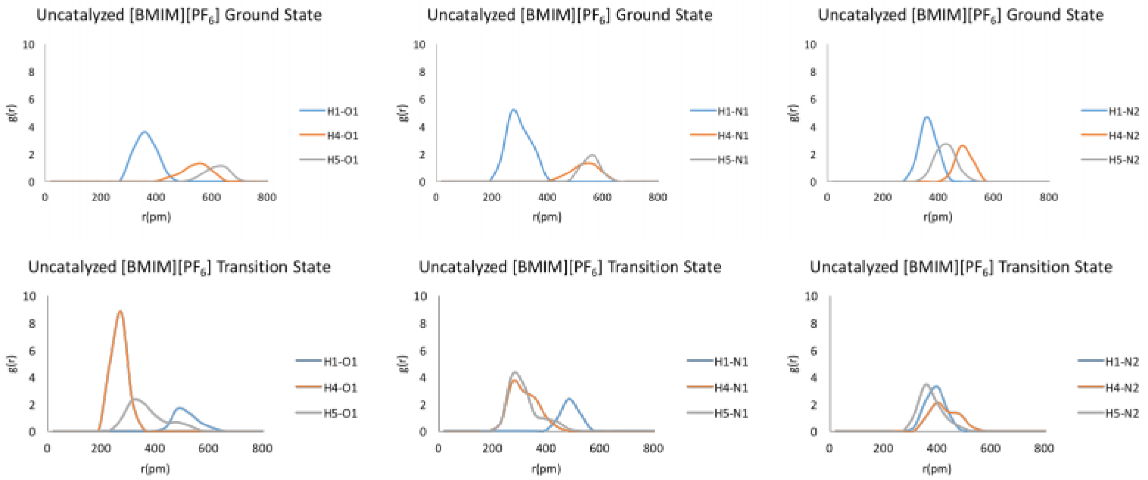

Figure 6.26. Nearest neighbor distribution between H1, H4, and H5 protons on the imidazolium ring of [BMIM] and the oxadiozolic oxygen (H-O1), oxadiozolic nitrogen (H-N1), and hydrazonic nitrogen (H-N2) in uncatalyzed [BMIM][PF$_6$]

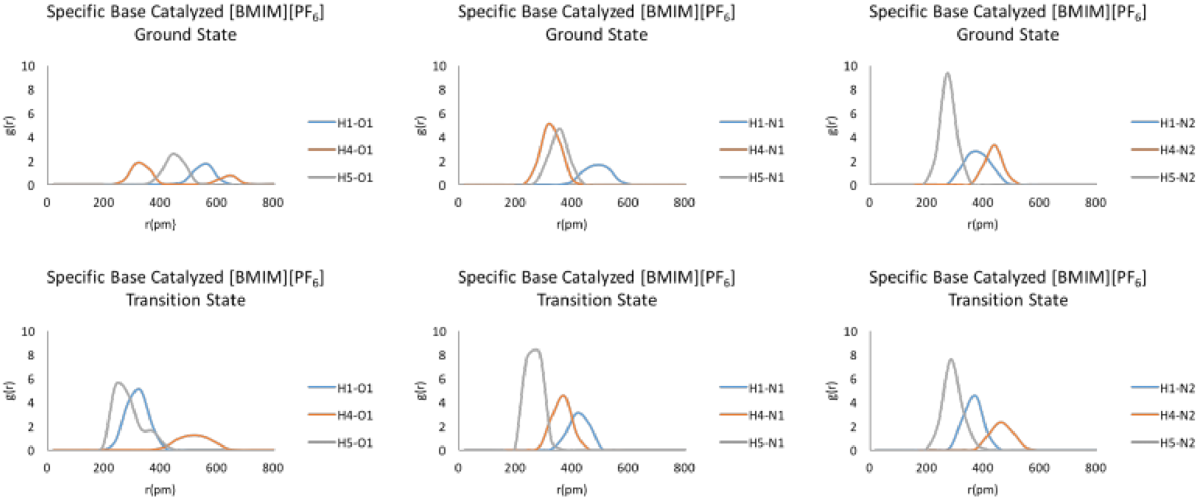

Figure 6.27. Nearest neighbor distribution between H1, H4, and H5 protons on the imidazolium ring of [BMIM] and the oxadiozolic oxygen (H-O1), oxadiozolic nitrogen (H-N1), and hydrazonic nitrogen (H-N2) in specific base-catalyzed [BMIM][PF$_6$]

6.5 Conclusions

Room temperature ionic liquids have been known to affect the reaction rate of a chemical reactions. One reaction in particular of interest was MRH reaction of the *Z*-phenylhydrazone of 3-benzoyl-5-phenyl-1,2,4-oxadiazole into 4-benzoylamino-2,5- diphenyl-1,2,3-triazole. D'Anna et al. studied the rate of MRH reaction on conventional solvents as well as on selective ionic liquids and reported a dramatic rate enhancement in the ionic liquid reaction medium [BMIM][BF_4] as compared to conventional organic solvents, including acetonitrile, methanol, and benzene.[127] Surprisingly, the group also reported significant increase in the rate for the MRH reaction in [BMIM][BF_4] as compared to [BMIM][PF_6],despite the similarities in physical properties. The two ionic liquids have comparable polarities, viscosity, and cation composition. Thus it's been difficult to rationalize the difference in the rate enhancement observed among the ionic liquids experimentally. To gain on depth understanding in the nature of the rate enhancement observed, QM/MM MC/FEP simulations were carried out for the MRH reaction of the *Z*-phenylhydrazone of 3-benzoyl-5-phenyl-1,2,4-oxadiazole into 4-benzoylamino-2,5-diphenyl-1,2,3-triazole in methanol, acetonitrile, [BMIM][BF_4], and [BMIM][PF_6]. Mixed QM/MM methodology was applied to the MRH reaction for the uncatalyzed and specific base-catalyzed pathways. Consistent with experimental results for the MRH reaction, the computation predicted lower energy barriers in the [BMIM][BF_4] solvent as compared to [BMIM][PF_6]for both uncatalyzed and specific-base catalyzed pathways. Moreover, the computed base-catalyzed route yielded lower absolute $\Delta G^{\ddagger}$ energies than that of uncatalyzed route. It has been hypothesized that the π^{+}-π interactions between the ionic liquid cation, BMIM, and the aromatic rings on 3-benzoyl-5-phenyl-1,2,4-oxadiazole impose a pre-ordered geometric arrangement that enhances the rate of reaction.[127] Accordingly, structural analyses of the simulations using combined distribution functions for the angle and distance of BMIM to the MRH substrate phenyl rings and bicyclic 10π oxadiazole/triazole transition state region confirmed significant π^+-π stacking. Dihedral angle distributions found the MRH reactants and transition structures solvated by [BMIM][BF_4] to have a greater coplanar orientation than in [BMIM][PF_6] for both catalayzed and uncatalyzed reactions, which implies maximize electronic effects exerted on the reaction route. In addition, closer average distances between the most acidic protons on the BMIM cation and the hydrazonic nitrogen, oxadiozolic nitrogen, and oxadiozolic oxygen atoms were found in [BMIM][BF_4] compared to [BMIM][PF_6]. The larger PF_6^- anion appears to reduce the favorable site-specific stabilizing electrostatic interactions at the transition state relative to BF_4^-. This could be the reason for the larger experimental $\Delta H^\ddagger$ values measured for the MRH in [BMIM][PF_6]. From all the computation and analysis of results of the current work, a better explanation to the origin of rate and reactivity of the MRH reaction in ionic liquids has been obtained.

Reference

(1) Bertram, S.; Blumenberg, M.; Michaelis, W.; Siegert, M.; Krüger, M.; Seifert, R. Methanogenic Capabilities of ANME-Archaea Deduced from ^{13} C-Labelling Approaches: Methanogenesis of ANME. *Environ. Microbiol.* **2013**, *15* (8), 2384–2393. https://doi.org/10.1111/1462-2920.12112.

(2) Conrad, R. The Global Methane Cycle: Recent Advances in Understanding the Microbial Processes Involved: Global Methane Cycle. *Environ. Microbiol. Rep.* **2009**, *1* (5), 285–292. https://doi.org/10.1111/j.1758-2229.2009.00038.x.

(3) Krüger, M.; Treude, T.; Wolters, H.; Nauhaus, K.; Boetius, A. Microbial Methane Turnover in Different Marine Habitats. *Palaeogeogr. Palaeoclimatol. Palaeoecol.* **2005**, *227* (1–3), 6–17. https://doi.org/10.1016/j.palaeo.2005.04.031.

(4) Cedervall, P. E.; Dey, M.; Li, X.; Sarangi, R.; Hedman, B.; Ragsdale, S. W.; Wilmot, C. M. Structural Analysis of a Ni-Methyl Species in Methyl-Coenzyme M Reductase from *Methanothermobacter Marburgensis*. *J. Am. Chem. Soc.* **2011**, *133* (15), 5626–5628. https://doi.org/10.1021/ja110492p.

(5) Thauer, R. K. Biochemistry of Methanogenesis: A Tribute to Marjory Stephenson: 1998 Marjory Stephenson Prize Lecture. *Microbiology* **1998**, *144* (9), 2377–2406.

(6) Bousquet, P.; Ciais, P.; Miller, J. B.; Dlugokencky, E. J.; Hauglustaine, D. A.; Prigent, C.; Van der Werf, G. R.; Peylin, P.; Brunke, E.-G.; Carouge, C.; et al. Contribution of Anthropogenic and Natural Sources to Atmospheric Methane Variability. *Nature* **2006**, *443* (7110), 439–443. https://doi.org/10.1038/nature05132.

(7) Mueller, T. J.; Grisewood, M. J.; Nazem-Bokaee, H.; Gopalakrishnan, S.; Ferry, J. G.; Wood, T. K.; Maranas, C. D. Methane Oxidation by Anaerobic Archaea for Conversion to Liquid Fuels. *J. Ind. Microbiol. Biotechnol.* **2015**, *42* (3), 391–401. https://doi.org/10.1007/s10295-014-1548-7.

(8) Che, F.; Gray, J. T.; Ha, S.; McEwen, J.-S. Reducing Reaction Temperature, Steam Requirements, and Coke Formation During Methane Steam Reforming Using Electric Fields: A Microkinetic Modeling and Experimental Study. *ACS Catal.* **2017**, *7* (10), 6957–6968. https://doi.org/10.1021/acscatal.7b01587.

(9) Johnson, K. A.; Johnson, D. E. Methane Emissions from Cattle. *J. Anim. Sci.* **1995**, *73* (8), 2483–2492. https://doi.org/10.2527/1995.7382483x.

(10) Wuebbles, D. J.; Hayhoe, K. Atmospheric Methane: Trends and Impacts. In *Non-CO2 Greenhouse Gases: Scientific Understanding, Control and Implementation*; van Ham, J., Baede, A. P. M., Meyer, L. A., Ybema, R., Eds.; Springer Netherlands: Dordrecht, 2000; pp 1–44. https://doi.org/10.1007/978-94-015-9343-4_1.

(11) Wang, F.-P.; Zhang, Y.; Chen, Y.; He, Y.; Qi, J.; Hinrichs, K.-U.; Zhang, X.-X.; Xiao, X.; Boon, N. Methanotrophic Archaea Possessing Diverging Methane-Oxidizing and Electron-Transporting Pathways. *ISME J.* **2014**, *8* (5), 1069–1078.

(12) Stocker, T.F., D. Qin, G.-K. Plattner, L.V. Alexander, S.K. Allen, N.L. Bindoff, F.-M. Bréon, J.A. Church, U. Cubasch,; S. Emori, P. Forster, P. Friedlingstein, N. Gillett, J.M. Gregory, D.L. Hartmann, E. Jansen, B. Kirtman, R. Knutti, K.; Krishna Kumar, P. Lemke, J. Marotzke, V. Masson-Delmotte, G.A. Meehl, I.I. Mokhov, S. Piao, V. Ramaswamy, D.; Randall, M. Rhein, M. Rojas, C. Sabine, D. Shindell, L.D. Talley, D.G. Vaughan and S.-P. Xie. *Technical Summary. In: Climate Change 2013: The Physical Science Basis. Contribution of Working Group I to the Fifth Assessment Report of the Intergovernmental Panel on Climate Change [Stocker, T.F., D. Qin, G.-K. Plattner, M. Tignor, S.K. Allen, J. Boschung, A. Nauels, Y. Xia, V. Bex and P.M. Midgley (Eds.)]*; Cambridge University Press, Cambridge, United Kingdom and New York, NY, USA., 2013.

(13) Lelieveld, J.; Crutzen, P. J.; Dentener, F. Changing Concentration, Lifetime and Climate Forcing of Atmospheric Methane. *Tellus* **1998**, *50B*, 128–150.

(14) Ruppel, C. D.; Kessler, J. D. The Interaction of Climate Change and Methane Hydrates: Climate-Hydrates Interactions. *Rev. Geophys.* **2017**, *55* (1), 126–168. https://doi.org/10.1002/2016RG000534.

(15) Wolf, J.; Asrar, G. R.; West, T. O. Revised Methane Emissions Factors and Spatially Distributed Annual Carbon Fluxes for Global Livestock. *Carbon Balance Manag.* **2017**, *12* (1). https://doi.org/10.1186/s13021-017-0084-y.

(16) Schwietzke, S.; Sherwood, O. A.; Bruhwiler, L. M. P.; Miller, J. B.; Etiope, G.; Dlugokencky, E. J.; Michel, S. E.; Arling, V. A.; Vaughn, B. H.; White, J. W. C.; et al. Upward Revision of Global Fossil Fuel Methane Emissions Based on Isotope Database. *Nature* **2016**, *538* (7623), 88–91. https://doi.org/10.1038/nature19797.

(17) Thauer, R. K.; Shima, S. Methane as Fuel for Anaerobic Microorganisms. *Ann. N. Y. Acad. Sci.* **2008**, *1125* (1), 158–170. https://doi.org/10.1196/annals.1419.000.

(18) Thauer, R. K. Functionalization of Methane in Anaerobic Microorganisms. *Angew. Chem. Int. Ed.* **2010**, *49* (38), 6712–6713. https://doi.org/10.1002/anie.201002967.

(19) McDonal, I. R.; Upton, M.; Hall, G.; Edwards, C.; Saunders, J. R.; Ritchie, D. A. Molecular Ecological Analysis of Methanogens and Methanotrophs in Blanket Bog Peat. *Microb. Ecol.* **1999**, *38* (3), 244–252. https://doi.org/10.1007/s002489900174.

(20) Takai, K.; Horikoshi, K. Genetic Diversity of Archaea in Deep-Sea Hydrothermal Vent Environments.

(21) Kaster, A.-K.; Goenrich, M.; Seedorf, H.; Liesegang, H.; Wollherr, A.; Gottschalk, G.; Thauer, R. K. More Than 200 Genes Required for Methane Formation from H_2 and CO_2 and Energy Conservation Are Present in *Methanothermobacter Marburgensis* and *Methanothermobacter Thermautotrophicus*. *Archaea* **2011**, *2011*, 1–23. https://doi.org/10.1155/2011/973848.

(22) Shima, S.; Krueger, M.; Weinert, T.; Demmer, U.; Kahnt, J.; Thauer, R. K.; Ermler, U. Structure of a Methyl-Coenzyme M Reductase from Black Sea Mats That Oxidize Methane Anaerobically. *Nature* **2011**, *481* (7379), 98–101. https://doi.org/10.1038/nature10663.

(23) DiMarco, A. A.; Bobik, T. A.; Wolfe, R. S. Unusual Coenzymes of Methanogenesis. *Annu. Rev. Biochem.* **1990**, *59* (1), 355–394.

(24) Ferry, J. Acetate Metabolism in Anaerobes from the Domain Archaea. *Life* **2015**, *5* (2), 1454–1471. https://doi.org/10.3390/life5021454.

(25) Vorholt, J. A.; Thauer, R. K. The Active Species of 'CO2'Utilized by Formylmethanofuran Dehydrogenase from Methanogenic Archaea. *FEBS J.* **1997**, *248* (3), 919–924.

(26) ELLERMANN, J.; HEDDERICH, R.; BÖCHER, R.; THAUER, R. K. The Final Step in Methane Formation. *FEBS J.* **1988**, *172* (3), 669–677.

(27) Thauer, R. K. The Wolfe Cycle Comes Full Circle. *Proc. Natl. Acad. Sci.* **2012**, *109* (38), 15084–15085.

(28) Rospert, S.; Linder, D.; Ellermann, J.; Thauer, R. K. Two Genetically Distinct Methyl-Coenzyme M Reductases in Methanobacterium Thermoautotrophicum Strain Marburg and ΔH. *FEBS J.* **1990**, *194* (3), 871–877.

(29) Ahn, Y.; Krzycki, J. A.; Floss, H. G. Steric Course of the Reduction of Ethyl Coenzyme M to Ethane Catalyzed by Methyl Coenzyme M Reductase from Methanosarcina Barkeri. *J. Am. Chem. Soc.* **1991**, *113* (12), 4700–4701.

(30) Kaneko, M.; Takano, Y.; Chikaraishi, Y.; Ogawa, N. O.; Asakawa, S.; Watanabe, T.; Shima, S.; Krüger, M.; Matsushita, M.; Kimura, H.; et al. Quantitative Analysis of Coenzyme F430 in Environmental Samples: A New Diagnostic Tool for Methanogenesis and Anaerobic Methane Oxidation. *Anal. Chem.* **2014**, *86* (7), 3633–3638. https://doi.org/10.1021/ac500305j.

(31) Duin, E.; Cosper, N.; Mahlert, F.; Thauer, R.; Scott, R. Coordination and Geometry of the Nickel Atom in Active Methyl-Coenzyme M Reductase from Methanothermobacter Marburgensis as

Detected by X-Ray Absorption Spectroscopy. *J. Biol. Inorg. Chem.* **2003**, *8* (1–2), 141–148. https://doi.org/10.1007/s00775-002-0399-2.

(32) Grabarse, W.; Mahlert, F.; Duin, E. C.; Goubeaud, M.; Shima, S.; Thauer, R. K.; Lamzin, V.; Ermler, U. On the Mechanism of Biological Methane Formation: Structural Evidence for Conformational Changes in Methyl-Coenzyme M Reductase upon Substrate Binding. *J. Mol. Biol.* **2001**, *309* (1), 315–330. https://doi.org/10.1006/jmbi.2001.4647.

(33) Finazzo, C.; Harmer, J.; Bauer, C.; Jaun, B.; Duin, E. C.; Mahlert, F.; Goenrich, M.; Thauer, R. K.; Van Doorslaer, S.; Schweiger, A. Coenzyme B Induced Coordination of Coenzyme M via Its Thiol Group to Ni(I) of F $_{430}$ in Active Methyl-Coenzyme M Reductase. *J. Am. Chem. Soc.* **2003**, *125* (17), 4988–4989. https://doi.org/10.1021/ja0344314.

(34) Selmer, T.; Kahnt, J.; Goubeaud, M.; Shima, S.; Grabarse, W.; Ermler, U.; Thauer, R. K. The Biosynthesis of Methylated Amino Acids in the Active Site Region of Methyl-Coenzyme M Reductase. *J. Biol. Chem.* **2000**, *275* (6), 3755–3760.

(35) Kahnt, J.; Buchenau, B.; Mahlert, F.; Krüger, M.; Shima, S.; Thauer, R. K. Post-Translational Modifications in the Active Site Region of Methyl-Coenzyme M Reductase from Methanogenic and Methanotrophic Archaea: Methanogenic Archaea Methyl-Coenzyme M Reductase. *FEBS J.* **2007**, *274* (18), 4913–4921. https://doi.org/10.1111/j.1742-4658.2007.06016.x.

(36) Nayak, D. D.; Mahanta, N.; Mitchell, D. A.; Metcalf, W. W. Post-Translational Thioamidation of Methyl-Coenzyme M Reductase, a Key Enzyme in Methanogenic and Methanotrophic Archaea. *Elife* **2017**, *6*.

(37) Grabarse, W.; Mahlert, F.; Shima, S.; Thauer, R. K.; Ermler, U. Comparison of Three Methyl-Coenzyme M Reductases from Phylogenetically Distant Organisms: Unusual Amino Acid Modification, Conservation and Adaptation. *J. Mol. Biol.* **2000**, *303* (2), 329–344. https://doi.org/10.1006/jmbi.2000.4136.

(38) Horng, Y.-C.; Becker, D. F.; Ragsdale, S. W. Mechanistic Studies of Methane Biogenesis by Methyl-Coenzyme M Reductase: Evidence That Coenzyme B Participates in Cleaving the C−S Bond of Methyl-Coenzyme M †. *Biochemistry* **2001**, *40* (43), 12875–12885. https://doi.org/10.1021/bi011196y.

(39) Goenrich, M.; Duin, E. C.; Mahlert, F.; Thauer, R. K. Temperature Dependence of Methyl-Coenzyme M Reductase Activity and of the Formation of the Methyl-Coenzyme M Reductase Red2 State Induced by Coenzyme B. *JBIC J. Biol. Inorg. Chem.* **2005**, *10* (4), 333–342. https://doi.org/10.1007/s00775-005-0636-6.

(40) Deobald, D.; Adrian, L.; Schöne, C.; Rother, M.; Layer, G. Identification of a Unique Radical SAM Methyltransferase Required for the Sp3-C-Methylation of an Arginine Residue of Methyl-Coenzyme M Reductase. *Sci. Rep.* **2018**, *8* (1). https://doi.org/10.1038/s41598-018-25716-x.

(41) Radle, M. I.; Miller, D. V.; Laremore, T. N.; Booker, S. J. Methanogenesis Marker Protein 10 (Mmp10) from *Methanosarcina Acetivorans* Is a Radical *S* -Adenosylmethionine Methylase That Unexpectedly Requires Cobalamin. *J. Biol. Chem.* **2019**, jbc.RA119.007609. https://doi.org/10.1074/jbc.RA119.007609.

(42) Meyerdierks, A.; Kube, M.; Kostadinov, I.; Teeling, H.; Glöckner, F. O.; Reinhardt, R.; Amann, R. Metagenome and MRNA Expression Analyses of Anaerobic Methanotrophic Archaea of the ANME-1 Group. *Environ. Microbiol.* **2010**, *12* (2), 422–439. https://doi.org/10.1111/j.1462-2920.2009.02083.x.

(43) Corti, S.; Molteni, F.; Palmer, T. N. Signature of Recent Climate Change in Frequencies of Natural Atmospheric Circulation Regimes. *Nature* **1999**, *398* (6730), 799–802.

(44) Scheller, S.; Goenrich, M.; Boecher, R.; Thauer, R. K.; Jaun, B. The Key Nickel Enzyme of Methanogenesis Catalyses the Anaerobic Oxidation of Methane. *Nature* **2010**, *465* (7298), 606–608. https://doi.org/10.1038/nature09015.

(45) Scheller, S.; Goenrich, M.; Thauer, R. K.; Jaun, B. Methyl-Coenzyme M Reductase from Methanogenic Archaea: Isotope Effects on the Formation and Anaerobic Oxidation of Methane. *J. Am. Chem. Soc.* **2013**, *135* (40), 14975–14984. https://doi.org/10.1021/ja406485z.

(46) Duin, E. C. Role of Coenzyme F430 in Methanogenesis. In *Tetrapyrroles*; Springer, 2009; pp 352–374.

(47) Mahlert, F.; Grabarse, W.; Kahnt, J.; Thauer, R. K.; Duin, E. C. The Nickel Enzyme Methyl-Coenzyme M Reductase from Methanogenic Archaea: In Vitro Interconversions among the EPR Detectable MCR-Red1 and MCR-Red2 States. *JBIC J. Biol. Inorg. Chem.* **2002**, *7* (1–2), 101–112. https://doi.org/10.1007/s007750100270.

(48) Goubeaud, M.; Schreiner, G.; Thauer, R. K. Purified Methyl-Coenzyme-M Reductase Is Activated When the Enzyme-Bound Coenzyme F430 Is Reduced to the Nickel (I) Oxidation State by Titanium (III) Citrate. *Eur. J. Biochem.* **1997**, *243* (1–2), 110–114.

(49) Hinderberger, D.; Piskorski, R. P.; Goenrich, M.; Thauer, R. K.; Schweiger, A.; Harmer, J.; Jaun, B. A Nickel–Alkyl Bond in an Inactivated State of the Enzyme Catalyzing Methane Formation. *Angew. Chem. Int. Ed.* **2006**, *45* (22), 3602–3607. https://doi.org/10.1002/anie.200600366.

(50) Rospert, S.; Voges, M.; Berkessel, A.; Albracht, S. P.; Thauer, R. K. Substrate-Analogue-Induced Changes in the Nickel-EPR Spectrum of Active Methyl-Coenzyme-M Reductase from Methanobacterium Thermoautotrophicum. *FEBS J.* **1992**, *210* (1), 101–107.

(51) Gräwert, T.; Hohmann, H.-P.; Kindermann, M.; Duval, S.; Bacher, A.; Fischer, M. Inhibition of Methyl-CoM Reductase from *Methanobrevibacter Ruminantium* by 2-Bromoethanesulfonate. *J. Agric. Food Chem.* **2014**, *62* (52), 12487–12490. https://doi.org/10.1021/jf505056g.

(52) Duin, E. C.; McKee, M. L. A New Mechanism for Methane Production from Methyl-Coenzyme M Reductase As Derived from Density Functional Calculations. *J. Phys. Chem. B* **2008**, *112* (8), 2466–2482. https://doi.org/10.1021/jp709860c.

(53) Ermler, U.; Grabarse, W.; Shima, S.; Goubeaud, M.; Thauer, R. K. Crystal Structure of Methyl–Coenzyme M Reductase: The Key Enzyme of Biological Methane Formation. *Science* **1997**, *278* (5342), 1457–1462. https://doi.org/10.1126.

(54) Ermler, U. On the Mechanism of Methyl-Coenzyme M Reductase. *Dalton Trans.* **2005**, No. 21, 3451. https://doi.org/10.1039/b506697b.

(55) Wongnate, T.; Ragsdale, S. W. The Reaction Mechanism of Methyl-Coenzyme M Reductase: HOW AN ENZYME ENFORCES STRICT BINDING ORDER. *J. Biol. Chem.* **2015**, *290* (15), 9322–9334. https://doi.org/10.1074/jbc.M115.636761.

(56) Jaun, B. Coenzyme F430 from Methanogenic Bacteria: Oxidation of F430 Pentamethyl Ester to the Ni(III) Form. *Helv. Chim. Acta* **1990**, *73* (8), 2209–2217. https://doi.org/10.1002/hlca.19900730818.

(57) Pelmenschikov, V.; Blomberg, M. R. A.; Siegbahn, P. E. M.; Crabtree, R. H. A Mechanism from Quantum Chemical Studies for Methane Formation in Methanogenesis. *J. Am. Chem. Soc.* **2002**, *124* (15), 4039–4049. https://doi.org/10.1021/ja011664r.

(58) Pelmenschikov, V.; Siegbahn, P. E. M. Catalysis by Methyl-Coenzyme M Reductase: A Theoretical Study for Heterodisulfide Product Formation. *JBIC J. Biol. Inorg. Chem.* **2003**, *8* (6), 653–662. https://doi.org/10.1007/s00775-003-0461-8.

(59) Wongnate, T.; Sliwa, D.; Ginovska, B.; Smith, D.; Wolf, M. W.; Lehnert, N.; Raugei, S.; Ragsdale, S. W. The Radical Mechanism of Biological Methane Synthesis by Methyl-Coenzyme M Reductase. *Science* **2016**, *352* (6288), 953–958.

(60) Kern, D. I.; Goenrich, M.; Jaun, B.; Thauer, R. K.; Harmer, J.; Hinderberger, D. Two Sub-States of the Red2 State of Methyl-Coenzyme M Reductase Revealed by High-Field EPR Spectroscopy. *JBIC J. Biol. Inorg. Chem.* **2007**, *12* (8), 1097–1105. https://doi.org/10.1007/s00775-007-0281-3.

(61) Roessler, M. M.; Salvadori, E. Principles and Applications of EPR Spectroscopy in the Chemical Sciences. *Chem. Soc. Rev.* **2018**, *47* (8), 2534–2553. https://doi.org/10.1039/C6CS00565A.

(62) Hagen, W. R. EPR Spectroscopy as a Probe of Metal Centres in Biological Systems. *Dalton Trans.* **2006**, No. 37, 4415. https://doi.org/10.1039/b608163k.

(63) Altenbach, C.; Flitsch, S. L.; Khorana, H. G.; Hubbell, W. L. Structural Studies on Transmembrane Proteins. 2. Spin Labeling of Bacteriorhodopsin Mutants at Unique Cysteines. *Biochemistry* **1989**, *28* (19), 7806–7812.

(64) Hubbell, W. L.; Mchaourab, H. S.; Altenbach, C.; Lietzow, M. A. Watching Proteins Move Using Site-Directed Spin Labeling. *Structure* **1996**, *4* (7), 779–783.

(65) Columbus, L.; Hubbell, W. L. A New Spin on Protein Dynamics. *Trends Biochem. Sci.* **2002**, *27* (6), 288–295.

(66) Duin, E. C. Introduction to Biomolecular Electron Paramagnetic Resonance Theory.

(67) Prisner, T.; Rohrer, M.; MacMillan, F. Pulsed EPR Spectroscopy: Biological Applications. *Annu. Rev. Phys. Chem.* **2001**, *52* (1), 279–313.

(68) Bobko, A. A.; Dhimitruka, I.; Zweier, J. L.; Khramtsov, V. V. Fourier Transform EPR Spectroscopy of Trityl Radicals for Multifunctional Assessment of Chemical Microenvironment. *Angew. Chem. Int. Ed.* **2014**, *53* (10), 2735–2738. https://doi.org/10.1002/anie.201310841.

(69) Duval, S.; Kindermann, M. Use of Nitrooxy Organic Molecules in Feed for Reducing Methane Emission in Ruminants, and/or to Improve Ruminant Performance, February 2018.

(70) Ellefson, W. L.; Wolf, R. S. Component C of the Methylreductase System of Methunobucterium.

(71) Becker, D. F.; Ragsdale, S. W. Activation of Methyl-SCoM Reductase to High Specific Activity after Treatment of Whole Cells with Sodium Sulfide †. *Biochemistry* **1998**, *37* (8), 2639–2647. https://doi.org/10.1021/bi972145x.

(72) Ladapo, J.; Whitman, W. B. Method for Isolation of Auxotrophs in the Methanogenic Archaebacteria: Role of the Acetyl-CoA Pathway of Autotrophic CO2 Fixation in Methanococcus Maripaludis. *Proc. Natl. Acad. Sci.* **1990**, *87* (15), 5598–5602.

(73) Gerbhardt, P.; Possot, O.; Foglino, M.; Sibold, L.; Klein, A. Construction of an Integration Vector for Use in the Archaebacterium Methanococcus Voltae and Expression of a Eubacterial Resistance Gene. *Mol Gen Genet* **1990**, *221* (2), 271–279.

(74) Argyle, J. L.; Tumbula, D. L.; Leigh, J. A. Neomycin Resistance as a Selectable Marker In. *APPL Env. MICROBIOL* **1996**, *62*, 5.

(75) Bertani, G.; Baresi, L. Genetic Transformation in the Methanogen Methanococcus Voltae PS. *J. Bacteriol.* **1987**, *169* (6), 2730–2738. https://doi.org/10.1128/jb.169.6.2730-2738.1987.

(76) Micheletti, P. A.; Sment, K. A.; Konisky, J. Isolation of a Coenzyme M-Auxotrophic Mutant and Transformation by Electroporation in Methanococcus Voltae. *J. Bacteriol.* **1991**, *173* (11), 3414–3418. https://doi.org/10.1128/jb.173.11.3414-3418.1991.

(77) Patel, G. B.; Nash, J. H. E.; Agnew, B. J.; Sprott, G. D. Methanococcus Voltae Protoplastst. *APPL Env. MICROBIOL* 5.

(78) Gardner, W. L.; Whitman, W. B. Expression Vectors for Methanococcus Maripaludis: Overexpression of Acetohydroxyacid Synthase and β-Galactosidase. *Genetics* **1999**, *152* (4), 1439–1447.

(79) Tumbula, D. L.; Bowen, T. L.; Whitman, W. B. Characterization of PURB500 from the Archaeon Methanococcus Maripaludis and Construction of a Shuttle Vector. *J. Bacteriol.* **1997**, *179* (9), 2976–2986. https://doi.org/10.1128/jb.179.9.2976-2986.1997.

(80) Hendrickson, E. L.; Kaul, R.; Zhou, Y.; Bovee, D.; Chapman, P.; Chung, J.; Conway de Macario, E.; Dodsworth, J. A.; Gillett, W.; Graham, D. E.; et al. Complete Genome Sequence of the Genetically Tractable Hydrogenotrophic Methanogen Methanococcus Maripaludis. *J. Bacteriol.* **2004**, *186* (20), 6956–6969. https://doi.org/10.1128/JB.186.20.6956-6969.2004.

(81) Moore, B. C.; Leigh, J. A. Markerless Mutagenesis in Methanococcus Maripaludis Demonstrates Roles for Alanine Dehydrogenase, Alanine Racemase, and Alanine Permease. *J. Bacteriol.* **2005**, *187* (3), 972–979. https://doi.org/10.1128/JB.187.3.972-979.2005.

(82) Jones, W. J.; Whitman, W. B.; Fields, R. D.; Wolfe, R. S. Growth and Plating Efficiency of Methanococci on Agar Media. *Appl. Environ. Microbiol.* **1983**, *46* (1), 220–226.

(83) Lyu, Z.; Chou, C.-W.; Shi, H.; Wang, L.; Ghebreab, R.; Phillips, D.; Yan, Y.; Duin, E. C.; Whitman, W. B. Assembly of Methyl Coenzyme M Reductase in the Methanogenic Archaeon *Methanococcus Maripaludis*. *J. Bacteriol.* **2018**, *200* (7). https://doi.org/10.1128/JB.00746-17.

(84) Gunsalus, R. P.; Romesser, J. A.; Wolfe, R. S. Preparation of Coenzyme M Analogs and Their Activity in the Methyl Coenzyme M Reductase System of Methanobacterium Thermoautotrophicum. *Biochemistry* **1978**, *17* (12), 2374–2377. https://doi.org/10.1021/bi00605a019.

(85) Zheng, K.; Ngo, P. D.; Owens, V. L.; Yang, X.-P.; Mansoorabadi, S. O. The Biosynthetic Pathway of Coenzyme F430 in Methanogenic and Methanotrophic Archaea. *Science* **2016**, *354* (6310), 336–339. https://doi.org/10.1126/science.aaf9070.

(86) Allen, K. D.; Wegener, G.; White, R. H. Discovery of Multiple Modified F430 Coenzymes in Methanogens and Anaerobic Methanotrophic Archaea Suggests Possible New Roles for F430 in Nature. *Appl. Environ. Microbiol.* **2014**, *80* (20), 6403–6412. https://doi.org/10.1128/AEM.02202-14.

(87) Bokranz, M.; Baumner, G.; Allmansberger, R.; Ankel-Fuchs, D.; Klein', A. Cloning and Characterization of the Methyl Coenzyme M Reductase Genes from Methanobacterium Thermoautotrophicum. 10.

(88) Soo, V. W. C.; McAnulty, M. J.; Tripathi, A.; Zhu, F.; Zhang, L.; Hatzakis, E.; Smith, P. B.; Agrawal, S.; Nazem-Bokaee, H.; Gopalakrishnan, S.; et al. Reversing Methanogenesis to Capture Methane for Liquid Biofuel Precursors. *Microb. Cell Factories* **2016**, *15* (1). https://doi.org/10.1186/s12934-015-0397-z.

(89) Prakash, D.; Wu, Y.; Suh, S.-J.; Duin, E. C. Elucidating the Process of Activation of Methyl-Coenzyme M Reductase. *J. Bacteriol.* **2014**, *196* (13), 2491–2498. https://doi.org/10.1128/JB.01658-14.

(90) Gunsalus, R. P.; Wolfe, R. S. Methyl Coenzyme M Reductase from Methanobacterium Thermoautotrophicum. *J. Biol. Chem.* **1980**, *255* (5), 1891–1895.

(91) Rouviere, P. E.; Wolfe, R. S. Component A3 of the Methylcoenzyme M Methylreductase System of Methanobacterium Thermoautotrophicum AH: *J. Bacteriol.* **1989**, *171* (9), 4556–4562.

(92) Duin, E. C.; Prakash, D.; Brungess, C. Methyl-Coenzyme M Reductase from Methanothermobacter Marburgensis. In *Methods in Enzymology*; Elsevier, 2011; Vol. 494, pp 159–187. https://doi.org/10.1016/B978-0-12-385112-3.00009-3.

(93) Yang, N.; Reiher, M.; Wang, M.; Harmer, J.; Duin, E. C. Formation of a Nickel−Methyl Species in Methyl-Coenzyme M Reductase, an Enzyme Catalyzing Methane Formation. *J. Am. Chem. Soc.* **2007**, *129* (36), 11028–11029. https://doi.org/10.1021/ja0734501.

(94) Dey, M.; Telser, J.; Kunz, R. C.; Lees, N. S.; Ragsdale, S. W.; Hoffman, B. M. Biochemical and Spectroscopic Studies of the Electronic Structure and Reactivity of a Methyl−Ni Species Formed on Methyl-Coenzyme M Reductase. *J. Am. Chem. Soc.* **2007**, *129* (36), 11030–11032. https://doi.org/10.1021/ja074556z.

(95) Martínez-Fernández, G.; Abecia, L.; Arco, A.; Cantalapiedra-Hijar, G.; Martín-García, A. I.; Molina-Alcaide, E.; Kindermann, M.; Duval, S.; Yáñez-Ruiz, D. R. Effects of Ethyl-3-Nitrooxy Propionate and 3-Nitrooxypropanol on Ruminal Fermentation, Microbial Abundance, and Methane Emissions in Sheep. *J. Dairy Sci.* **2014**, *97* (6), 3790–3799. https://doi.org/10.3168/jds.2013-7398.

(96) Reynolds, C. K.; Humphries, D. J.; Kirton, P.; Kindermann, M.; Duval, S.; Steinberg, W. Effects of 3-Nitrooxypropanol on Methane Emission, Digestion, and Energy and Nitrogen Balance of Lactating Dairy Cows. *J. Dairy Sci.* **2014**, *97* (6), 3777–3789. https://doi.org/10.3168/jds.2013-7397.

(97) Hristov, A. N.; Oh, J.; Giallongo, F.; Frederick, T. W.; Harper, M. T.; Weeks, H. L.; Branco, A. F.; Moate, P. J.; Deighton, M. H.; Williams, S. R. O.; et al. Correction for Hristov et al., An Inhibitor Persistently Decreased Enteric Methane Emission from Dairy Cows with No Negative Effect on Milk Production. *Proc. Natl. Acad. Sci.* **2015**, *112* (37), E5218–E5218. https://doi.org/10.1073/pnas.1515515112.

(98) Duin, E. C.; Wagner, T.; Shima, S.; Prakash, D.; Cronin, B.; Yáñez-Ruiz, D. R.; Duval, S.; Rümbeli, R.; Stemmler, R. T.; Thauer, R. K.; et al. Mode of Action Uncovered for the Specific Reduction of Methane Emissions from Ruminants by the Small Molecule 3-Nitrooxypropanol. *Proc. Natl. Acad. Sci.* **2016**, *113* (22), 6172–6177. https://doi.org/10.1073/pnas.1600298113.

(99) Butler, K.; Jelfs, K.; Gren, W. An Introduction To Computational Methods. **2008**.

(100) Leach, A. *Molecular Modelling: Principles and Applications*, 2nd ed.; Pearson Education Limited, 2001.

(101) Friesner, R. A. Ab Initio Quantum Chemistry: Methodology and Applications. *Proc. Natl. Acad. Sci.* **2005**, *102* (19), 6648–6653. https://doi.org/10.1073/pnas.0408036102.

(102) Hehre, W. J. *A Guide to Molecular Mechanics and Quantum Chemical Calculations*; Wavefunction, Inc: Irvine, CA, 2003.

(103) Hohenberg, P.; Kohn, W. Inhomogeneous Electron Gas. *Phys. Rev.* **1964**, *136* (3B), B864–B871. https://doi.org/10.1103/PhysRev.136.B864.

(104) Kohn, W.; Sham, L. J. Self-Consistent Equations Including Exchange and Correlation Effects. *Phys. Rev.* **1965**, *140* (4A), A1133–A1138. https://doi.org/10.1103/PhysRev.140.A1133.

(105) Christensen, A. S.; Kubař, T.; Cui, Q.; Elstner, M. Semiempirical Quantum Mechanical Methods for Noncovalent Interactions for Chemical and Biochemical Applications. *Chem. Rev.* **2016**, *116* (9), 5301–5337. https://doi.org/10.1021/acs.chemrev.5b00584.

(106) Thiel, W. Semiempirical Quantum–Chemical Methods. *Wiley Interdiscip. Rev. Comput. Mol. Sci.* **2014**, *4* (2), 145–157. https://doi.org/10.1002/wcms.1161.

(107) Pople, J. A.; Beveridge, D. L.; Dobosh, P. A. Approximate Self-Consistent Molecular-Orbital Theory. V. Intermediate Neglect of Differential Overlap. *J. Chem. Phys.* **1967**, *47* (6), 2026–2033. https://doi.org/10.1063/1.1712233.

(108) G. Parr, R. *A Method for Estimating Electronic Repulsion Integrals Over LCAO MO'S in Complex Unsaturated Molecules*; 1952; Vol. 20. https://doi.org/10.1063/1.1700802.

(109) Dewar, M. J. S.; Zoebisch, E. G.; Healy, E. F.; Stewart, J. J. P. Development and Use of Quantum Mechanical Molecular Models. 76. AM1: A New General Purpose Quantum Mechanical Molecular Model. *J. Am. Chem. Soc.* **1985**, *107* (13), 3902–3909. https://doi.org/10.1021/ja00299a024.

(110) Stewart, J. J. P. Optimization of Parameters for Semiempirical Methods II. Applications. *J. Comput. Chem.* **1989**, *10* (2), 221–264. https://doi.org/10.1002/jcc.540100209.

(111) Repasky, M. P.; Chandrasekhar, J.; Jorgensen, W. L. PDDG/PM3 and PDDG/MNDO: Improved Semiempirical Methods. *J. Comput. Chem.* **2002**, *23* (16), 1601–1622. https://doi.org/10.1002/jcc.10162.

(112) Jensen, F. *Introduction to Computational Chemistry*, Second.; 2007.

(113) Essmann, U.; Perera, L.; Berkowitz, M. L.; Darden, T.; Lee, H.; Pedersen, L. G. A Smooth Particle Mesh Ewald Method. *J. Chem. Phys.* **1995**, *103* (19), 8577–8593.

(114) de Leeuw, S. W.; Perram, J. W.; Smith, E. R. Simulation of Electrostatic Systems in Periodic Boundary Conditions. I. Lattice Sums and Dielectric Constants. In *Proceedings of the Royal Society of London A: Mathematical, Physical and Engineering Sciences*; The Royal Society, 1980; Vol. 373, pp 27–56.

(115) Acevedo, O.; Jorgensen, W. L. Quantum and Molecular Mechanical Monte Carlo Techniques for Modeling Condensed-Phase Reactions: Monte Carlo Techniques for Modeling Condensed-Phase Reactions. *Wiley Interdiscip. Rev. Comput. Mol. Sci.* **2014**, *4* (5), 422–435. https://doi.org/10.1002/wcms.1180.

(116) Winget, P.; Thompson, J. D.; Xidos, J. D.; Cramer, C. J.; Truhlar, D. G. Charge Model 3: A Class IV Charge Model Based on Hybrid Density Functional Theory with Variable Exchange. *J. Phys. Chem. A* **2002**, *106* (44), 10707–10717.

(117) van Gunsteren, W. F.; Daura, X.; Mark, A. E. Computation of Free Energy. *Helv. Chim. Acta* **2002**, *85* (10), 3113–3129. https://doi.org/10.1002/1522-2675(200210)85:10<3113::AID-HLCA3113>3.0.CO;2-0.

(118) Jorgensen, W. L. Perspective on "Equation of State Calculations by Fast Computing Machines." *Theor. Chem. Acc. Theory Comput. Model. Theor. Chim. Acta* **2000**, *103* (3–4), 225–227. https://doi.org/10.1007/s002149900053.

(119) Metropolis, N.; Rosenbluth, A. W.; Rosenbluth, M. N.; Teller, A. H.; Teller, E. Equation of State Calculations by Fast Computing Machines. *J. Chem. Phys.* **1953**, *21* (6), 1087–1092. https://doi.org/10.1063/1.1699114.

(120) Steinhauser, M. O.; Hiermaier, S. A Review of Computational Methods in Materials Science: Examples from Shock-Wave and Polymer Physics. *Int. J. Mol. Sci.* **2009**, *10* (12), 5135–5216. https://doi.org/10.3390/ijms10125135.

(121) Zwanzig, R. W. High-Temperature Equation of State by a Perturbation Method. I. Nonpolar Gases. *J. Chem. Phys.* **1954**, *22* (8), 1420–1426. https://doi.org/10.1063/1.1740409.

(122) Chandrasekhar, J.; Jorgensen, W. L. Energy Profile for a Nonconcerted SN2 Reaction in Solution. *J. Am. Chem. Soc.* **1985**, *107* (10), 2974–2975.

(123) Muhammad, N.; Man, Z.; Ziyada, A. K.; Bustam, M. A.; Mutalib, M. I. A.; Wilfred, C. D.; Rafiq, S.; Tan, I. M. Thermophysical Properties of Dual Functionalized Imidazolium-Based Ionic Liquids. *J. Chem. Eng. Data* **2012**, *57* (3), 737–743. https://doi.org/10.1021/je200710t.

(124) Sudhakar, G. K.; Bhaskar, V. K.; Verma, R. First Title: Ionic Liquids-Useful Reaction Green Solvents for the Future Second Title: Ionic Liquids Are the Replacements for Environmentally Damaging Solvents in a Wide Range of Chemical Processes. *J. Biomed. Pharm. Res.* **2012**, *1* (2), 07–12.

(125) Chapeaux, A.; Simoni, L. D.; Ronan, T. S.; Stadtherr, M. A.; Brennecke, J. F. Extraction of Alcohols from Water with 1-Hexyl-3-Methylimidazolium Bis(Trifluoromethylsulfonyl)Imide. *Green Chem.* **2008**, *10* (12), 1301. https://doi.org/10.1039/b807675h.

(126) Allen, C.; Sambasivarao, S. V.; Acevedo, O. An Ionic Liquid Dependent Mechanism for Base Catalyzed β-Elimination Reactions from QM/MM Simulations. *J. Am. Chem. Soc.* **2013**, *135* (3), 1065–1072. https://doi.org/10.1021/ja3098614.

(127) D'Anna, F.; Frenna, V.; Marullo, S.; Noto, R.; Spinelli, D. Mononuclear Rearrangement of Heterocycles in Ionic Liquids Catalyzed by Copper(II) Salts. *Tetrahedron* **2008**, *64* (49), 11209–11217. https://doi.org/10.1016/j.tet.2008.09.055.

(128) Ghosh, P. B. Preparation and Study of Some 5- and 7-Substituted 4-Nitrobenzofurazans and Their A/-Oxides ; a Retro-Boulton-Katritzky Rearrangement. *J. Chem. Soc.* **1968**, *B*, 334–338.

(129) Cosimelli, B.; Guernelli, S.; Spinelli, D.; Buscemi, S.; Frenna, V.; Macaluso, G. On the Synthesis and Reactivity of the *Z* -2,4-Dinitrophenylhydrazone of 5-Amino-3-Benzoyl-1,2,4-Oxadiazole. *J. Org. Chem.* **2001**, *66* (18), 6124–6129. https://doi.org/10.1021/jo0157270.

(130) Cosimelli, B.; Frenna, V.; Guernelli, S.; Lanza, C. Z.; Macaluso, G.; Petrillo, G.; Spinelli, D. The First Kinetic Evidence for Acid Catalysis in a Monocyclic Rearrangement of Heterocycles: Conversion of the *Z* -Phenylhydrazone of 5-Amino-3-Benzoyl-1,2,4-Oxadiazole into *N* ,5-Diphenyl-2 *H* -1,2,3-Triazol-4-Ylurea. *J. Org. Chem.* **2002**, *67* (23), 8010–8018. https://doi.org/10.1021/jo026039z.

(131) Boulton, A. J.; Katritzky, A. R.; Hamid, A. M. Heterocyclic Rearrangements. Part X. A Generaiised Monocyclic Rearrangement. 3.

(132) Crowhurst, L.; Mawdsley, P. R.; Perez-Arlandis, J. M.; Salter, P. A.; Welton, T. Solvent–Solute Interactions in Ionic Liquids. *Phys Chem Chem Phys* **2003**, *5* (13), 2790–2794. https://doi.org/10.1039/B303095D.

(133) Frenna, V.; Spinelli, D.; Consiglio, G. Mononuclear Heterocyclic Rearrangements. Effect of the Structure of the Side Chain on the Reactivity. Part 1. Rearrangement of Some 3-Arylureines of 5-Phenyl-I ,2,4-Oxadiazole into I -Aryl-3-Benzoylamino-I ,2,4-Triazolin-5-Ones in Acetonitrile, Benzene, and Dioxane-Water. *J CHEM SOC PERKIN TRANS* **1990**, 7.

(134) Frenna, V.; Vivona, N.; Consiglio, G.; Spinelli, D. Mononuclear Heterocyclic Rearrangements. Part 9.’ A Kinetic Study of the Rearrangement of the 2-Phenylhydrazone of 3-Benzoyl-5-Phenyl- I,2,4-Oxadiazole into 4-Benzoylamino-2,5-Diphenyl-I ,2,3-Triazole in Methanol, Dioxan, Ethyl Acetate, and Acetonitrile. 4.

(135) Bottoni, A.; Frenna, V.; Lanza, C. Z.; Macaluso, G.; Spinelli, D. Convergent Results from Experimental and Theoretical DFT Studies of the Intramolecular Rearrangement of *Z*- Hydrazones of 3-Acyl-1,2,4-Oxadiazoles [†]. *J. Phys. Chem. A* **2004**, *108* (10), 1731–1740. https://doi.org/10.1021/jp0309668.

(136) Swiss, K. A.; Firestone, R. A. Acceleration of Bimolecular Reactions by Solvent Viscosity [1]. *J. Phys. Chem. A* **1999**, *103* (27), 5369–5372. https://doi.org/10.1021/jp991066n.

(137) Armacost, K.; Acevedo, O. Exploring the Aldol Reaction Using Catalytic Antibodies and “On Water” Organocatalysts from QM/MM Calculations. *J. Am. Chem. Soc.* **2014**, *136* (1), 147–156. https://doi.org/10.1021/ja405614p.

(138) Jorgensen, W. L. Optimized Intermolecular Potential Functions for Liquid Alcohols. *J. Phys. Chem.* **1986**, *90* (7), 1276–1284. https://doi.org/10.1021/j100398a015.

(139) Sambasivarao, S. V.; Acevedo, O. Development of OPLS-AA Force Field Parameters for 68 Unique Ionic Liquids. *J. Chem. Theory Comput.* **2009**, *5* (4), 1038–1050. https://doi.org/10.1021/ct900009a.

(140) Thompson, J. D.; Cramer, C. J.; Truhlar, D. G. Parameterization of Charge Model 3 for AM1, PM3, BLYP, and B3LYP. *J. Comput. Chem.* **2003**, *24* (11), 1291–1304. https://doi.org/10.1002/jcc.10244.

(141) Vilseck, J. Z.; Sambasivarao, S. V.; Acevedo, O. Optimal Scaling Factors for CM1 and CM3 Atomic Charges in RM1-Based Aqueous Simulations. *J. Comput. Chem.* **2011**, *32* (13), 2836–2842. https://doi.org/10.1002/jcc.21863.

(142) Allen, C.; McCann, B. W.; Acevedo, O. Ionic Liquid Effects on Nucleophilic Aromatic Substitution Reactions from QM/MM Simulations. *J. Phys. Chem. B* **2015**, *119* (3), 743–752. https://doi.org/10.1021/jp504967r.

(143) Acevedo, O.; Jorgensen, W. L.; Evanseck, J. D. Elucidation of Rate Variations for a Diels−Alder Reaction in Ionic Liquids from QM/MM Simulations. *J. Chem. Theory Comput.* **2007**, *3* (1), 132–138. https://doi.org/10.1021/ct6002753.

(144) D’Anna, F.; Frenna, V.; Noto, R.; Pace, V.; Spinelli, D. Can the Absence of Solvation of Neutral Reagents by Ionic Liquids Be Responsible for the High Reactivity in Base-Assisted Intramolecular Nucleophilic Substitutions in These Solvents? [†]. *J. Org. Chem.* **2005**, *70* (7), 2828–2831. https://doi.org/10.1021/jo048485n.

(145) Brehm, M.; Kirchner, B. TRAVIS - A Free Analyzer and Visualizer for Monte Carlo and Molecular Dynamics Trajectories. *J. Chem. Inf. Model.* **2011**, *51* (8), 2007–2023. https://doi.org/10.1021/ci200217w.

(146) Pensado, A. S.; Brehm, M.; Thar, J.; Seitsonen, A. P.; Kirchner, B. Effect of Dispersion on the Structure and Dynamics of the Ionic Liquid 1-Ethyl-3-Methylimidazolium Thiocyanate. *ChemPhysChem* **2012**, *13* (7), 1845–1853. https://doi.org/10.1002/cphc.201100917.